WARWICK
THE UNIVERSITY OF WARWICK

**A Thesis Submitted for the Degree of PhD at the University of Warwick**

**Permanent WRAP URL:**
http://wrap.warwick.ac.uk/135021

**Copyright and reuse:**
This thesis is made available online and is protected by original copyright.
Please scroll down to view the document itself.
Please refer to the repository record for this item for information to help you to cite it.
Our policy information is available from the repository home page.

For more information, please contact the WRAP Team at: wrap@warwick.ac.uk

**warwick.ac.uk/lib-publications**

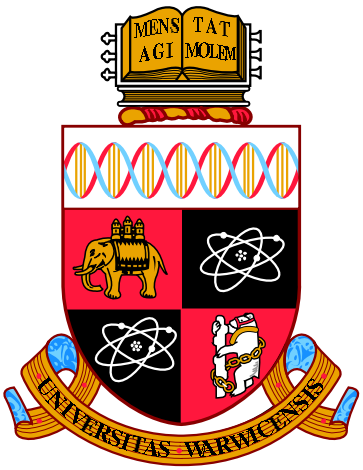


# The Dynamics of Phototaxis in Photosynthetic Microorganisms

by

**Richard Jeffery Henshaw**

**Thesis**

Submitted to the University of Warwick

for the degree of

**Doctor of Philosophy**

**Department of Physics**

June 2019

THE UNIVERSITY OF WARWICK

# Contents

# List of Tables

# List of Figures

# Acknowledgments

This thesis would not have been possible it had not been for the support of so many people along the way, too many to count, but I shall do my best! From an academic perspective, I would first like to thank my supervisor Dr. Marco Polin for giving me the opportunity and support to work on such an exciting project. Next Dr. Raphaël Jeanneret for his help (and considerable patience) during the drafting of our phototaxis paper - your support was invaluable and I'm extremely grateful for all the time you spent on it. Many thanks to Dr. Joseph Christie-Oleza for kindly supplying the initial cultures of *Micromonas pusilla* and Mr. Steve Hindmarsh for preparing the mould used for the millifluidic device.

Four years is a long time to dedicate to a single manuscript but this thesis only represents half of my time at the University of Warwick, and there are many people to thank who have made this journey the crazy one it has been. To the Cryfield gang (Ollie, Issy, Rosie, Emma, Phoebe, Sophie, Ben, Modestas, Mike), for taking an extremely quiet maths and physics student and bringing me way outside of my comfort zone - you guys helped me in so many ways that you don't know and I'm proud to know you all.

Music has always been, and always will be, my biggest passion, and has pulled me through my time here. I've had so many opportunities to perform in incredible environments alongside amazingly talented musicians and has really been the driving force of my time here. I must thank the University of Warwick Music Centre (Lucy, Lizzy, James, Paul and Lucy) for all that they have done (and continue to do) to equip Warwick with one of the most diverse and inclusive university musical experiences in the UK.

To the Wind Orchestra. Wind Orch was the first society I joined at Warwick and the one I've been most involved in - I hope that I've been able to give back a fraction of what you guys have given me. Feeling Saxy I know you will keep going from strength to strength and I'm proud to have been there at your inception. There are so many of you to thank it would be impossible to list you all, but I need to mention the "Dream Team" in particular Jenny. We've been through so much together and fought off so many bollards, I can't thank you enough for being you. Jenny, we did it.

I came to university as a wind band player and morphed into jazz, and a big part of that is thanks to Big Band. You guys made every gig incredible (well, excluding Manchester minitour), and gave me my proudest moment at university at NCBF nationals 2015. Like Wind Orch I know I've made friends for life and I hope to see you all at Reunion Ball! A special thanks has to go to Malik, Rhys, Adam, Matt Bates and James Webster for all you've done over the past 8 years, even if you didn't realise it at the time.

Sports was not something I enjoyed before university but that has completely reversed over now. Special mention to UWAC for bringing me into the fold and giving me so many opportunities to represent my university, as well as my first hangover. To the Triathlon and Road Cycling Club for taking a keen cyclist and throwing him into a pool, with special mention to Simon and Matt for all of their support over many evenings in the pub.

To my fellow physicists - you guys brought a real sense of community to what can often be a lonely and frustrating environment. A big shout out to the lunch gang, Pub Wednesday and Well-Being coffee. Thankfully I never joined the karaoke group...

To the rest of the group, it has been a pleasure working alongside you all and I wish you all the best for the future. In particular the other prisoners of P.160 - Maria and Max. You guys made the long days worth it with some truly terrible jokes and appalling banter and I will miss working with you both. Maria, thank you for giving me the opportunity to go on so many walks to the library cafe, and

Max for giving me the kick up the backside to actually start this thesis and for all of your help during the writing process, I can't say thank you enough for all your help. Simone, try to make sure Steve doesn't destroy the lab - it is in your hands now.

But the biggest thanks of all have to go to my family - especially Mum, Dad and Kirsty - for none of this would have been possible without you and your support, from putting up with my endless phone calls to keeping me on track during the rough patches. I hope I've done you proud and now you can finally tell people that I have in fact left university.

Finally, to all of those who have supported me in some way along this journey, this is for you.

# Declarations

I declare that this thesis reports my work between October 2015 and March 2019 under the supervision of Dr. Marco Polin. The studies in this thesis have not been submitted either wholly or in part to this or any other academic institution for the admission of a higher degree. Except where indicated by specific reference in the text, the work is the candidate's own work. Work done in collaboration with, or with the assistance of, others, is in is indicated below and during this thesis. Any views expressed in this thesis are those of the author.

Chapter 4 is based strongly on a prepared manuscript that will be submitted for publication:

- R. Henshaw, R. Jeanneret, M. Polin. Phototaxis of the dominant marine pico-eukaryote *Micromonas pusilla.*. *In preparation.* 2019

For this work, I was responsible for the all the experiments and analysis as well as writing the manuscript alongside Dr. Raphaël Jeanneret and Dr. Marco Polin. The original jump-diffusion simulation code was provided by Dr. Raphaël Jeanneret which was adapted by myself to produce the numerical experimental data presented in this chapter.

Chapter 5, specifically Fig 5.6 and Fig 5.10, are based on experimental data collected by Jonathan Roberts, an undergraduate summer student co-supervised between myself and Dr. Marco Polin. Experiments were carried out under my supervision, and any analysis/analytical tools/conclusions made from this data are my own.

Chapter 6 presents recent results from an ongoing collaboration with the

group of Dr. Giorgio Volpe at UCL. In this work I was responsible for preparing the microfluidic devices/cell cultures, carrying out the experiments with Manish Trivedi, then developing the tools to analyse and presenting the results from the experiments to the group.

*"Making the simple complicated is commonplace; making the complicated simple, awesomely simple, that's creativity"*
Charles Mingus

# Abstract

The motility strategies of *M. pusilla* are characterised for the first time, establishing a new variant of run-tumble motion: stop, run or reverse. This pattern bears remarkable similarities to the run-reverse motion of marine bacteria, suggesting the size of the organism dominates the choice of motility strategy. The phototaxis of *M. pusilla* is then described for the first time at both population and single cell scales. The proposed method of phototaxis - an extension of the run length when the cell is orientated towards the light stimulus - is verified with a series of jump-diffusion numerical simulations. The phototactic study was extended by demonstrating the first recorded intensity dependent step-up photophobic response of *M. pusilla*, followed by a stronger step-down response. During these responses cells switch from typically stationary behaviour to continuous swimming to escape the harmful environment. The step-up response can also be triggered chemically during an apparent cell death, leading to burst events where cells attempt to escape from a spherically diffusing source of pollutant radiating from a single cell. The similarities in these independent responses suggest there is a global avoidance strategy present in the organism to escape from harmful environments. Finally, a new experimental system is proposed to investigate phototaxis in more complicated optical landscapes and channel confinements using the model organism *C. reinhardtii*. Photoaccumulation to two Gaussian stripes is observed to impede the transport through a channel, opening up the question of what influence phototaxis could have in porous media.

In whole, the motility and phototactic behaviour of the most globally dominant pico-eukaryote *M. pusilla* has been investigated and characterised for the first time, as well the discovery of an apparently universal avoidance strategy from a variety of harmful environments.

# Chapter 1

# Introduction and Thesis Structure

## 1.1 Background

At the heart of all science is a desire to understand how and why the universe behaves as it does, from sub-atomic particles through black holes. Whilst the tools have evolved over the countless years humanity has been asking these questions have remained, at their core, the same. What has become increasingly clear however is that many of the questions facing modern science cannot be answered by one specific discipline [1]. Indeed it is not unusual for scientists to be working on the same problem from different directions without realising that in fact they only have access to half the required pieces. A prime example of this are biological systems for which, up until the mid-nineteenth century, it was commonly believed were subject to their own specialist laws that were somehow different from the underlying laws of physics. Karl Pearson introduced the term "Bio-Physics" in 1892 and noted that "*This branch of science does not appear to have advanced very far at present, but it not improbably has an important future.*" [2] and marked the birth of one of the most diverse fields in modern physics. The merging of physics and biology proved fruitful for both sides, with physiological advancements such as the discovery of the DNA double helix based on X-ray diffraction to physical advancements quantum coupling in magnetic materials based on the spatial patterns of flocking birds [3].

One such topic that has benefited from the attention of both physics and biophysics is the motility of microswimmers such as marine plankton. The long-standing views of Victor Hensen [4] that the movement of these species is dominated by the surrounding flows is now recognized as being partially incorrect. The fitness of

such organisms has a strong dependence on how they can navigate their dynamically patchy environment to maximise exposure to food sources (e.g. nutrient patches) whilst avoiding the many hazards of their environment. These ecologically vital organisms form the basis of the food web and are also responsible for approximately half of the global primary carbon production [5]. Many of these organisms are photosynthetic and are able to adapt their motion in response to light in a poorly-understood process known as phototaxis. Understanding how these organisms can respond efficiently to environmental changes and how they could adapt to change in our climate-changing world is therefore essential from both an ecological and economical standpoint.

The work presented in this thesis aims to begin to describe environmental responses such as phototaxis in a much more ecologically relevant manner. We also hope that the work presented here will provide the necessary tools and experimental systems to begin to probe biological phototaxis at a fundamental level.

## 1.2 Structure and Outline

This thesis begins by first reviewing the physical laws dominating behaviour at the micron scale in fluids in Chapter 2 which is then followed by a discussion of the current (and development of) the experimental techniques used to probe phenomena at this length scale. Chapter 3 switches focus towards a more biological perspective, focussing on the processes that support life and movement in low Reynolds environments as well as comprehensively introducing the two microorganisms that feature in this thesis: the ecologically important and globally dominant picoeukaryote *M. pusilla* and the model bi-flagellated green algae *Chlamydomonas reinhardtii*. Chapter 4 presents the first dedicated motility and phototaxis study of *M. pusilla*. Chapter 5 examines a series of novel phenomena exhibited by *M. pusilla*, namely the first reported photophobic response in the organism as well as collective events in response to apparent cell death, leading to the proposition of a global avoidance response in the organism. Chapter 6 presents more recent work involving the phototactic behaviour of *C. reinhardtii* in more complicated light environments and confined geometries. Finally Chapter 7 concludes the story, summarising the main points of this thesis before discussing the future outlook and further development of the presented material.

# Chapter 2

# Swimming at the micron scale

## 2.1 Introduction

The study of fluid dynamics is one that stretches back throughout history, with countless individuals striving to further the understanding of this inherently complex and chaotic environment. Starting with Archimedes and buoyancy all the way up to cutting edge studies such as sound wave propagation in suspensions of colloids [6], fluid dynamics has enticed, bewitched, confounded, frustrated and awed scientists from all walks of life and study. A personal favourite quote from Heisenberg encapsulates this: *"When I meet God, I am going to ask him two questions: Why relativity? And why turbulence? I really believe he will have an answer for the first"*. It is here that this thesis begins with a summary of the key principles behind the behaviour of microswimmers and the complex environment through which they move. This chapter starts with the physical laws driving the complex swimming behaviours observed in these microswimmers, followed by a summary of the principal techniques used to investigate and study phenomena at these length scales: microfluidics and optical microscopy. However before these techniques can be approached we must first establish a framework to operate in and where better to start than with one of the most famous equations in mathematics: the Navier-Stokes equation.

## 2.2 Low Reynolds number environments

### 2.2.1 Navier Stokes and the Reynolds number

In early 2000 the Clay Mathematics Institute of Cambridge (Massachusetts) established seven Prize Problems, with the aim of exposing the greatest problems faced in mathematics at the beginning of the new millennium to wider world. Each of these

problems has a prize fund of $1 million for its solution[1]. One of these problems is to prove the existence of a smooth function which solves the Navier-Stokes equation - a partial differential equation which describes the flow of incompressible fluids, developed by Claude-Louis Navier and Sir George Gabriel Stokes [7–10]. There will be no such attempt to solve this problem here (many better minds have attempted and fallen short), so rather than discussing attempts to solve this problem it is instead used to motivate the behaviour of microswimmers. To begin the Navier-Stokes equation for an incompressible Newtonian fluid [7] is:

$$\nabla \cdot \mathbf{u} = 0 \tag{2.1}$$

$$\frac{\partial \mathbf{u}}{\partial t} = -(\mathbf{u} \cdot \nabla) \cdot \mathbf{u} - \frac{1}{\rho}\nabla p + \frac{\mu}{\rho}\nabla^2 \mathbf{u} + \mathbf{f} \tag{2.2}$$

Where $\mathbf{u}$ is the relative fluid velocity, $\rho$ the density of the fluid, $\mu$ the dynamic viscosity of the fluid and $p$ the pressure. From left to right, the terms represent: the directional change of the relative fluid velocity, the effect of the divergence on the velocity, an inertial term, a viscous term and finally an external forcing term $\mathbf{f}$. Comparing the relative importance of the inertial and viscous terms leads to perhaps the most dominating dimensionless number in fluid dynamics: the Reynolds number [11–13] - the ratio of viscous and inertial forces in a fluid subject to different fluid velocities which is defined as:

$$\frac{\text{inertia}}{\text{viscous}} \sim \frac{UL\rho}{\mu} = Re \tag{2.3}$$

Where $U$ is a typical scale of the velocity and $L$ a typical length scale (over which the fluid varies). Importantly it allows to us to predict fluid flow patterns, relating quantities such as the length scales of the geometry and the viscosity of the fluid in question. At low Reynolds number the fluid moves in smooth layers/paths, known as the laminar regime. At high Reynolds numbers this structure breaks down and the fluid behaviour becomes chaotic and impossible to describe analytically. Fig 2.1a gives a practical example of this with smoke from a candle - there is a clear transition from the smooth laminar regime to the chaotic turbulent regime. This dimensionless quantity is an extremely powerful tool as it allows one to predict transition between laminar and turbulent regimes and to compare similarities between different sized systems. A prime case of this is in the design of aircraft wings, where comparisons of the Reynolds number are used to predict the behaviour of the fluid flow over the

[1] To date, only one of these prizes has been claimed - the Russian mathematician Grigori Perelman solved the Poincaré conjecture problem in 2003. The Russian recluse actually turned the prize down, and has apparently now given up mathematics.

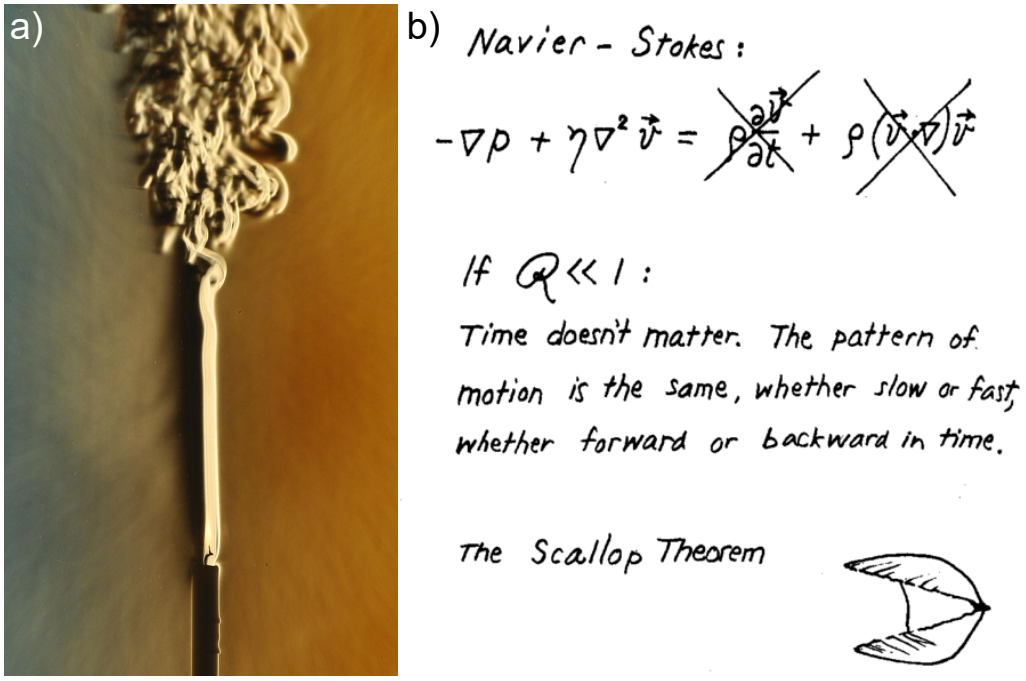


Figure 2.1: **The Reynold's number and Purcell's scallop theorem. a).** Schilieren photograph of smoke from a candle (from: [19], credit: Dr. Gary Settles) where the laminar-turbulent transition is clearly visible. **b**). An extract from Purcell's talk in 1977 [20] where the scallop theorem for reciprocal motion gets its name.

full-sized aircraft wing in order to estimate the aircraft's performance across a range of airspeed and aerofoil size. [14–18].

For context: the largest mammal on the planet is the Blue whale which will typically produce a Reynolds number on the order $10^8$, a human swimming in water is typically around two orders of magnitude less than this and a small fish will have a Reynolds number on the order 1. The humble phytoplankton cell (typically $1 - 100'$s, microns) will have a Reynolds number on the order $10^{-2} - 10^0$. To put this in layman terms -a phytoplankton swimming in water will face a comparable environment to a human swimming in treacle! At these low Reynolds numbers viscous forces dominate the behaviour of the system. This means that swimmers can no longer "coast", or explicitly ceasing to propel leads to an immediate cease in swimming. For example a micron-sized sphere travelling on the order of 10's microns per second will coast approximately $10^{-10}$ m - or the mean radius of an electron orbiting a hydrogen nucleus [20]! In essence a microswimmers velocity is determined by the motion it is undergoing at that exact moment. It is in this regime that this thesis will focus: from now forwards it is safe to assume that flows are laminar (unless

stated otherwise) and that inertia forces are negligible in comparison to viscous forces. This has significant impact on propulsion strategies of microswimmers in these low Reynolds number environments, specifically the imposed constraints on the physical motion responsible for producing the propulsive force.

### 2.2.2 Scallop Theorem - breaking time symmetry

When a body/organism is swimming it will undergo some form of cyclical deformations - i.e. in order to keep swimming the body has to at some point revert back to its original configuration before restarting the swimming cycle. When the cycle is completed the body will have travelled some distance in the fluid. However working in the low Reynolds environment puts a significant restriction on the forms this motion can take. In this regime, if a body deforms in a reciprocal cycle - that is to say, the motion is identical when time is reversed - then any motion forward is then counteracted by moving backwards during the recovery cycle. This forms the basis of the "Scallop's Theorem", famously presented by Edward Purcell [20], where the scallop was used as an example of reciprocal motion. Fig 2.1b shows an excerpt from Purcell's 1977 talk where he presented this theory, and is one of the most famous/significant papers when it comes to microswimmers.

There are countless examples of microswimmers and self-propelled particles, both naturally occurring and man-made. These range from the zooplankton [21] and phytoplankton [22] to sperm cells seeking out an ovum [23–25] to synthetically produced Janus particles [26] and even bubble-driven microjets [27]. One of the primarily methods for propulsion available to biological swimmers is by use of one or more appendages connected to the body of the swimmer such as the whip-like eukaryotic flagellum [28]. Since we are only interested in the viscous regime the swimmers here are considered as force/torque-free i.e. no net force/torque on the swimmer, with the structure and details of these flagella discussed in greater detail in Chapter 3. From a more theoretical viewpoint, by considering the forces exerted on the slender body of the flagellum as it moves through the fluid one can relate this to the swimming speed of the whole swimmer. Most biological swimmers take advantage of these slender bodies for propulsion, exploiting the fact that at low Reynolds numbers the response of a fluid to the motion of a boundary is essentially instantaneous.

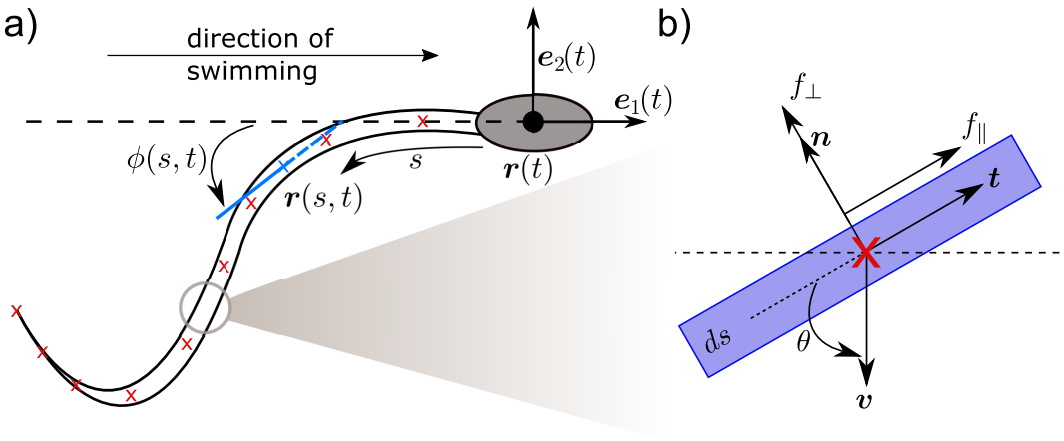


Figure 2.2: **a).** Sketch of a biological swimmer with an oscillatory flagellum, such as a sperm cell. The position of the cell body, $\mathbf{r}(\mathbf{t})$, sets a coordinate system with the orthogonal vectors $\mathbf{e}_{1,2}$. The combination of the length parameter $s$ and the angle made between each point of the flagellum ($\mathbf{r}(s,t)$) given by $\phi(s,t)$ describes the position of all points of the flagellum. **b).** The flagellum can be thought of as a series of connected cylinders with length $ds$, with an orientation described by the local tangent/normal ($\mathbf{t}, \mathbf{n}$ resp.) and travelling with some velocity $\mathbf{v}$ at an angle $\theta$ with respect to the tangent. The drag per length can be separated into perpendicular/parallel components labelled as $f_\perp, f_\parallel$ respectively.

### Drag-based thrust

Let us consider a biophysical example as shown in Fig 2.2: a biological swimmer that is propelled by a single flagellum which "whips" back and forth on an oscillatory wave-like (but non-reciprocal) deformation cycle e.g. sea-urchin spermatozoa [29]. A coordinate system can be set by the position of the cell body, using the orthogonal vectors $\mathbf{e}_j(t), j = 1, 2$. The cell body has position $\mathbf{r}(t)$, and the flagellum has a length parameter $s$ which allows the position of each point along the flagellum (with length $L$) to be described by $\mathbf{r}(s,t)$. Finally, the angle the tangent of each point of the flagellum makes with the cell body orientation $\mathbf{e}_1(t)$ is described by $\phi(s,t)$. We can then write the translational velocity of the cell body as:

$$\dot{\mathbf{r}}(t) = v_1\mathbf{e}_1(t) + v_2\mathbf{e}_2(t) \tag{2.4}$$

Where $v_j(t)$ is the speed in the $j$th direction at a time $t$. Similarly we can write a rotational velocity:

$$\begin{aligned}\dot{\mathbf{e}}_1(t) &= \Omega(t)\mathbf{e}_2(t)\\ \dot{\mathbf{e}}_2(t) &= -\Omega(t)\mathbf{e}_1(t)\end{aligned} \tag{2.5}$$

Assuming the flagellum is an asymptotically slender filament, the motion of the filament is opposed by a (local) viscous drag per unit length:

$$\mathbf{f}(s,t) = \zeta_{\perp}\mathbf{v}_{\perp}(s,t) + \zeta_{\parallel}\mathbf{v}_{\parallel}(s,t) \tag{2.6}$$

Where $\zeta_{\perp}, \zeta_{\parallel}$ are defined as the perpendicular/parallel drag coefficients respectively. For drag-based thrust to work as a method of propulsion we require that there is some drag anisotropy (i.e. $\zeta_{\perp} \neq \zeta_{\parallel}$) which provides a means of generating force perpendicular to the direction of motion and that there is some non-zero time-averaged propulsion - the motion is non-reciprocal as per the scallop theorem. A beating flagellum can be thought of as the sum of a series of connected straight cylinders, each moving with velocity $\mathbf{v}$ at some angle $\theta$ to the direction of the local tangent at that point (Fig 2.2b). We can write the drag per length components as:

$$f_{\perp} = -\zeta_{\perp}v_{\perp} = -\zeta_{\perp}v\sin(\theta), \qquad f_{\parallel} = -\zeta_{\parallel}v_{\parallel} = -\zeta_{\parallel}v\cos(\theta) \tag{2.7}$$

In the isotropic case the friction coefficients are equal and therefore the force on the flagellum and its velocity have the same direction. However in the anisotropic case the drag per unit length now includes a third component which is perpendicular the direction of the velocity, which is the propulsive force on the body:

$$\mathbf{f}_p = (\zeta_{\parallel} - \zeta_{\perp})v\sin(\theta)\cos(\theta)\mathbf{e}_1 \tag{2.8}$$

From this our second condition is met: in order to generate the non-reciprocal motion we need both $v$ and $\theta$ to vary in periodically in time. Doing so satisfies the scallop's theorem and we are left with a self-propelled microswimmer. Now that the force at a particular point is known the resultant force and torque (and therefore velocity) on the swimmer's body can be calculated by remembering that in these low Reynold's number environments swimmers are considered as being force/torque-free:

$$\begin{aligned} \mathbf{F}(t) = 0 &= \mathbf{F}_{body}(t) + \int_0^L \mathbf{f}(s,t)ds \\ \mathbf{M}(t) = 0 &= \mathbf{M}_{body}(t) + \int_0^L \mathbf{f}(s,t) \times \mathbf{r}(s,t)ds \end{aligned} \tag{2.9}$$

### 2.2.3 Long-range hydrodynamics

#### Oseen Tensor and Stokeslets

Up to this point only short-range hydrodynamics have been considered, such as the drag-force on the flagellum. Now we turn our attention to long-range hydrodynamics

and their implications for microswimmers. As mentioned before, the dynamics of an incompressible fluid is governed by the Navier-Stokes equations (Eq 2.2). In the viscous regime (low Reynolds) the non-linear terms can be neglected, resulting in the linearised Navier-Stokes equation:

$$\rho\frac{\partial \mathbf{u}}{\partial t} = \mu\nabla^2\mathbf{u} - \nabla p + \mathbf{f} \tag{2.10}$$

With sufficiently low Reynolds number this reduces to the Stokes equation:

$$\nabla p - \mu\nabla^2\mathbf{u} = \mathbf{f} \tag{2.11}$$

In the case of an unbounded system with an external force field $\mathbf{f}(\mathbf{r}, t)$ these linearised equations can be solved analytically [30]. In the case of Stokes flow [31] (i.e. time-independent $\mathbf{f}(\mathbf{r})$) this can be shown to give a velocity field of the form:

$$\mathbf{u}(\mathbf{r}) = \int d^3r'\mathbf{H}(\mathbf{r} - \mathbf{r}') \cdot \mathbf{f}(\mathbf{r}', t') \tag{2.12}$$

Where $\mathbf{H}(\mathbf{r})$ is known as the Oseen tensor, which has Cartesian components:

$$H_{ij}(\mathbf{r}) = \frac{1}{8\pi\eta r}\left[\delta_{ij} + \frac{r_i r_j}{r^2}\right] \tag{2.13}$$

Where $i, j$ denote the coordinate $(x, y, z)$, $\delta_{ij}$ the Dirac delta function and $r = |\mathbf{r}|$. This fundamental solution is known as a stokeslet [32], which physically represents the flow field due to a point force. From this tensor we can see that the velocity field will decay as $1/r$, but more interestingly is the directional anisotropy that is a result of this field. If there is some force $\mathbf{F}$ applied to the fluid, then evaluating the velocity parallel/perpendicular to the direction of the force gives:

$$u_{\parallel} = \frac{|\mathbf{F}|}{4\pi\eta r}, \qquad u_{\perp} = \frac{|\mathbf{F}|}{8\pi\eta r} \tag{2.14}$$

Respectively. In essence for the same force the flow field in the perpendicular direction is half the magnitude of the flow field in the parallel direction. From the Oseen tensor we can obtain the complete set of singularities for viscous flow by differentiating the fundamental solution [33]. Combinations of these solutions can then be used to exactly describe the flow field generated from a wide range of geometries, such as the dipole swimmer.

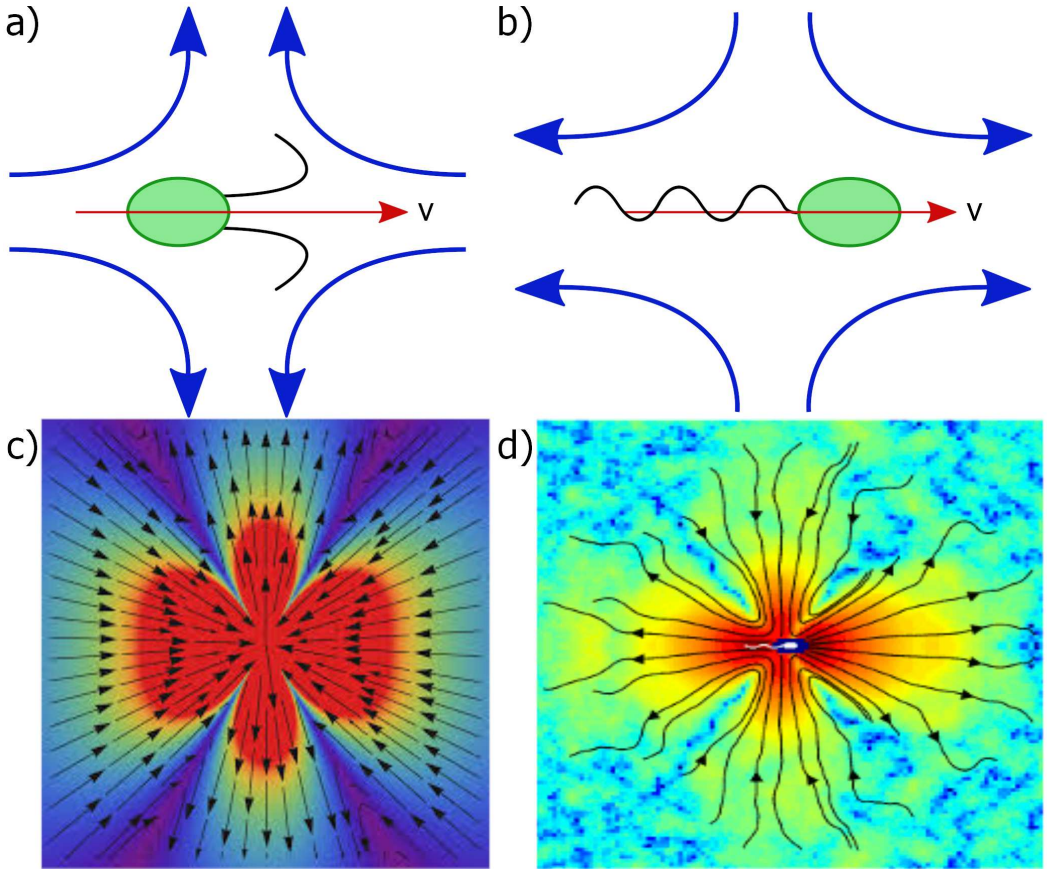


Figure 2.3: **Pusher-puller dipole swimmers**. **a).** Puller-type dipole swimmer. The fluid is pulled towards the cell along the direction of travel and expelled perpendicular to the direction of travel. **b).** Pusher-type dipole swimmer. A mirror image of the puller-type swimmer: fluid is drawn in towards the cell perpendicular to the direction of travel and is pushed in front/behind the cell body. [34]. **c).** Simulated streamlines around an artifical swimmer [35]. We can clearly see the characteristics of a pusher-dipole, where the fluid is pulled in from the front/back and expelled from the sides. **d).** Experimental flow field of the pusher swimmer *Escherichia coli* [36]. In this we can clearly see the fluid flow reproducing the sketched behaviour in (b). Both of these flow fields are in bulk conditions i.e. far from walls and other swimmers.

### Dipole swimmers

Hydrodynamically speaking a force dipole represents the flow field resulting from two close point forces with opposite directions. Mathematically, a force dipole located at $\mathbf{r}_0$ can be described by considering two opposing forces of equal magnitude at positions $\mathbf{r} = \mathbf{r}_0 \pm \mathbf{d}/2$. Expanding this to leading order [37] gives the following for the flow field induced by the force dipole:

$$\mathbf{u}_{\mathrm{fd}}(\mathbf{r}) = \frac{f_0 d}{8\pi\eta r^3}\left[-1 + 3\frac{(\mathbf{r}\cdot\hat{\mathbf{e}})^2}{r^2}\right]\mathbf{r}, \qquad \mathbf{f}_0 = f_0\hat{\mathbf{e}}, \qquad \mathbf{d} = d\hat{\mathbf{e}} \tag{2.15}$$

Where $\hat{\mathbf{e}}$ gives the axial direction of the force dipole. From this expression we can see that the flow field will decay as a $1/r^2$ and also see from that changing the sign of the point forces will reverse the direction of the flow field. If we have a system with an active "head" whilst dragging a passive "tail" through a fluid then forces act to pull fluid in towards the head and out from the sides (Fig 2.3a). Vice-versa, if the tail is actively pushing the head through the fluid, then fluid will be pushed away from the head/tail and pulled in from the sides (Fig 2.3b). These two classes are known as "pusher/puller" swimmers respectively. Fig 2.3cd shows two such cases: firstly the simulated flow field for an a stokeslet in a weak nematic fluid [35] and secondly the experimental flow field for the pusher-type bacteria *Escherichia coli* [36].

**Introducing surfaces**

Introducing surfaces into the mix adds a significant level of difficulty but it can be dealt with by considering the image of the force dipole [37]. There are three main consequences of a force-dipole moving close to a solid boundary or surface, demonstrated by the bacteria *Escherichia coli*. In bulk conditions this organism swims in an approximately straight line but near a boundary the trajectories begin to spiral and become circular (Fig 2.4a) [38]. Retaining the no-slip condition at the boundary requires the introduction of an image of the swimmer on the opposite side of the boundary.

Consider a force dipole at a height $z_{fd}$ above a solid (planar) boundary, and then let the image of the force dipole be at $-z_{fd}$, i.e. below the boundary. At the surface ($z = 0$), the perpendicular component of the velocity field vanishes. Near to the surface the dipole experiences an attractive force to the wall, given by the $z-$component of the flow field of the image dipole at the position of the physical dipole [37]:

$$u_{\mathrm{wall,z}}(z_{fd}) = -\frac{f_0 d}{\gamma z_{fd}^2}\left[1 - 3(\hat{\mathbf{e}}\cdot\hat{\mathbf{e}}_z)^2\right] \tag{2.16}$$

Where $\gamma$ is some numerical constant containing the viscosity. In the case of a non-slip boundary condition the flow field is essentially the same - it retains the same dependency on distance and angle from the boundary but there is a change to $\gamma$.

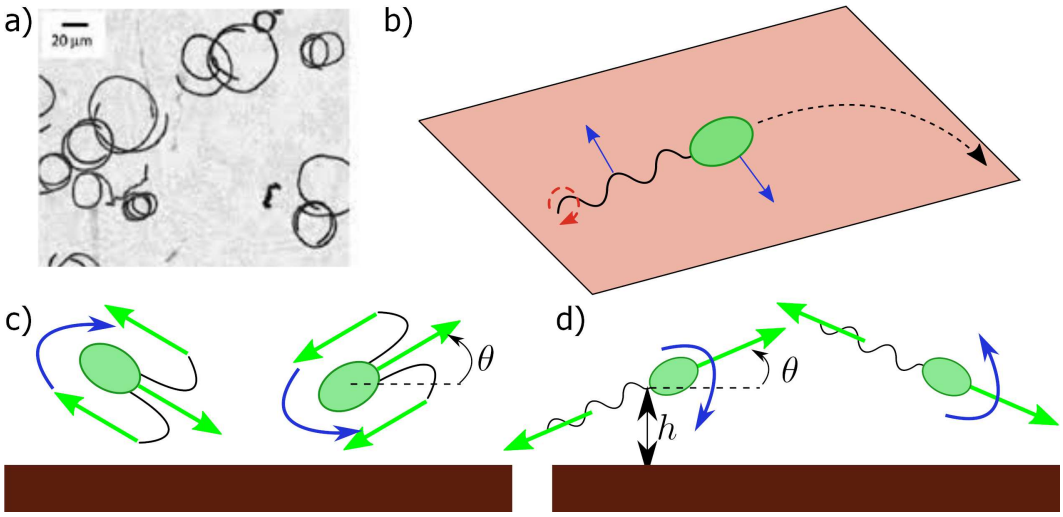


Figure 2.4: **Effects of a force dipole near a solid boundary. a).** Experimentally recorded trajectories of bacteria swimming near a solid boundary, where the trajectories transition from approximately straight trajectories to circular ones [38]. **b).** Sketch of the underlying mechanism responsible for the circular trajectories. Rotation of the swimmer flagellum near the boundary (red dotted line) induces a force on the flagellum perpendicular to the direction of motion, and an equal but opposite force on the cell body (blue arrows). The result of this is the body rotates perpendicularly to the wall, creating the circular trajectories. **c).** Puller force-dipole swimmer near a solid boundary, inducing a reorientation towards perpendicular to the surface. **d).** Pusher force-dipole swimmer near a solid boundary which induces a reorientation towards parallel to the solid boundary.

Importantly these effects will decay as $1/z^2$ with distance from the surface, so at large enough distances they become negligible.

In the case of swimming with helical flagella, such as *E. coli*, the rotation of the flagellum near a surface introduces a force on the cell perpendicular to the direction of motion and parallel to the surface (Fig 2.4b). Since the swimmer is in a force-free environment, an equal but opposing force is applied to the opposite end of the cell. This introduces a wall-based torque onto the swimmer and leads to circular trajectories.

A more general consequence of solid boundary is the impact on the swimming speed. Section 2.2.2 showed that there were two anisotropic drag coefficients $\zeta_{\perp,\parallel}$ denoting the perpendicular and parallel drag coefficients respectively. As the swimmer approaches the wall these coefficients increase but the perpendicular component increases faster than the parallel component leading to an increase in the swimming speed. Alternatively, if the swimmer maintains the same power then the

swimming speed will drop [39].

The final consequence to be discussed here is the effect that the solid boundary has on the reorientation of the swimmer. The necessary presence of an image on the other side of the boundary has been discussed briefly, but now consider if the swimmer was moving at an angle $\theta$ between the surface normal vector and the swimming direction at a height $z$ above the surface (Fig 2.4cd). It can be shown [40] that this introduces an angular velocity:

$$\Omega_r(\theta, z) = -\frac{3P\cos(\theta)\sin(\theta)}{64\pi\mu z^3}\left[1 + \frac{(\gamma^2 - 1)}{2(\gamma^2 + 1)}(1 + \cos^2(\theta)\right] \tag{2.17}$$

Where $\mu$ is the viscosity, $P$ the dipole strength and $\gamma$ the aspect ratio of the swimmer. This introduces a distinct difference between a pusher type swimmer and a puller. For a puller-type swimmer the hydrodynamic interactions are repulsive when swimming parallel to the surface, but the opposite is true for a pusher-type swimmer. In other words, the puller wants to align perpendicular to the wall and the pusher wants to align parallel to the wall, as shown in Fig 2.4cd respectively.

These hydrodynamic concepts will become important when considering the motility the two principal organisms of this thesis: *Chlamydomonas reinhardtii* and *Micromonas pusilla*. Up to this point we have only considered when the swimmers are moving, so now attention turns to when the swimmers are not swimming and how the random nature of their environment impacts their short and long-term behaviour.

## 2.3 Brownian Motion and anomalous diffusion

### 2.3.1 Brownian Motion

Micron-sized particles suspended in a fluid can be seen to undergo a random walk where the particles appear to "jitter" instead of remaining stationary. This jittering motion is the result of the cell being buffeted by the surrounding fluid molecules and is known as Brownian motion. Named after the biologist Robert Brown who in 1827 noted the random walk undertaken by pollen particles in water [41] and later confirmed by Albert Einstein in 1905 [42], this well-studied phenomena has many and far-reaching implications ranging from the motion of a simple sphere in a fluid to financial applications [43]. The mathematics supporting Brownian motion are largely due to Norbert Wiener [44] (who the Wiener process, or standard Brownian motion, is named after) who proved that the trajectory of a Brownian particle is almost everywhere continuous but nowhere differentiable

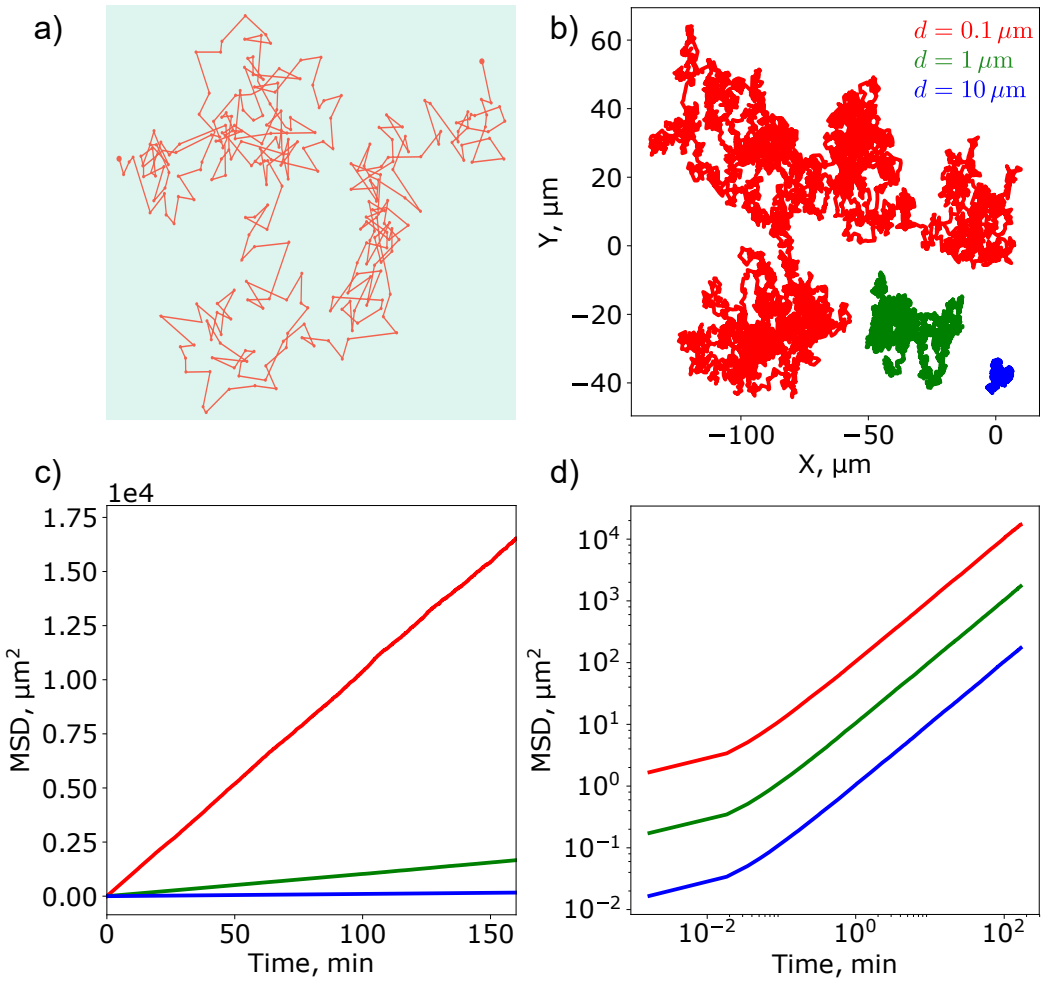


Figure 2.5: **Examples of Brownian particles. a).** The original observations of Robert Brown in 1827 of the trajectory of microscopic particles suspended in a fluid [41]. **b).** Three simulated Brownian particle trajectories for spheres with radius $0.1, 1, 10\,\mu$m (red, green, blue respectively). **c).** Ensemble-averaged mean squared displacement as a linear function of time. **d).** Ensemble-averaged mean squared displacement for each particle diameter plotted on a log-log scale. Here we see despite the different particle sizes they all follow the same power law behaviour described by Eq. 2.23 for purely Brownian motion.

Limiting the focus to particles in a fluid it is clear that attempting to follow the short term behaviour of the particle trajectory is going to be essentially pointless, instead it is better to focus on the averaged behaviour of the trajectory over longer time scales. Due to the nature of the problem several elements can be assumed: the resultant force from the molecular collisions is random with zero mean, and because it is random we can assume no correlation between the force at two different times.

Finally if the particle has a non-zero velocity then there will be a frictional force acting to bring the particle to rest proportional to the velocity of the particle. Newton's second law then produces the Langevin equation [45]:

$$m\frac{dv}{dt} + \beta v = F(t), \qquad < F(t) >= 0, \qquad < F(t)F(t') >= 2D\beta^2\delta(t-t') \quad (2.18)$$

Where $m$ is the mass of the particle, $v(t)$ the velocity with damping coefficient $\beta$ and $F(t)$ the resultant force from the molecular collisions. Since we are working in the low Reynolds number regime (where inertial effects are negligible), the mass can be neglected and hence:

$$\frac{dx}{dt} = \frac{1}{\gamma}F(t) \equiv \xi(t) \quad (2.19)$$

By integrating Eq. 2.19:

$$x(t) = \int_0^t \xi(t')dt' \quad (2.20)$$

We can see that since $< \xi(t) >= 0$, $< x(t) >= 0$. More interesting is the behaviour of the average mean-squared displacement $< x(t)^2 >$:

$$< x(t)^2 >= \int_0^t \int_0^t < \xi(t')\xi(t'') > dt'dt'' \quad (2.21)$$

Remembering from Eq. 2.18 that $< \xi(t)\xi(t') >= 2D\delta(t-t')$, we recover the famous linear relationship of the time-evolution of the mean-squared displacement [46]:

$$< x(t)^2 >= 2Dt \quad (2.22)$$

Where $D$ is the diffusion coefficient of the particle with units of area per unit time. Finally, this generalises to $d-$dimensions:

$$< \mathbf{x}(t)^2 >= 2dDt \quad (2.23)$$

For a Brownian particle the diffusion coefficient is given by the following relation [42]:

$$D = k_b T b \quad (2.24)$$

Where $k_b$ is the Boltzmann coefficient, $T$ the absolute temperature and $b$ the constant mobility of a particle, defined by the steady velocity (angular velocity) produced by a steady unit force (torque). For a spherical particle with radius $a$ in a

fluid with viscosity $\mu$, the translational/rotational mobilities ($b_t, b_r$ respectively) are obtained using Stoke's law [11]:

$$b_t = \frac{1}{6\pi\mu a}, \qquad b_r = \frac{1}{8\pi\mu a^3} \tag{2.25}$$

From Eq. 2.25 it is clear that the size of the particle will play a significant part in its diffusive behaviour. To illustrate this significance Fig 2.5a shows three simulated trajectories for three different particle radii (keeping temperature/viscosity etc constant): $0.1, 1, 10\,\mu$m (red, green, blue respectively). The particles trajectories were generated with a timestep of 0.1 s for $10,000$ timesteps, with a randomly generated step taken in both the $x$ and $y$ directions at each timestep. In Fig 2.5b, $10,000$ of these particle trajectories were averaged and the mean-squared displacement calculated as a function of time. Despite the apparent differences in behaviour, plotting the same data on a log-log scale in Fig 2.5c reveals the expected power law behaviour expected from purely Brownian motion.

A way of checking if particles are in fact Brownian is to calculate $D$ from the log-log plot (Fig 2.5) and compare this with the theoretical radius calculated from Eq. 2.24. Fitting a straight line to the mean-squared displacement for a Brownian particle should give a line of unity gradient with a $y-$intercept equal to the diffusion coefficient $D$.

### 2.3.2 Anomalous diffusion and jump-diffusion processes

Sadly the real world is never a convenient place to model and it would be far too simple if all diffusive behaviour could be described using Eq. 2.23. Throughout nature there are plentiful examples of diffusion that do not obey the linear relationship described in Eq. 2.23, ranging from semiconductors [47] to more recently ion channels in the plasma membrane [48]. These non-Brownian diffusive processes are described by anomalous diffusion, which has been a field of study since Lewis Richardson's studies on turbulent behaviour in the atmosphere [49]. Anomalous diffusion processes are ones which follow a non-linear relationship similar in form to Eq. 2.23 but now as a power law relationship between the mean-squared displacement and time:

$$< \mathbf{x}(t) >= 2dDt^{\alpha}, \qquad \alpha > 0 \tag{2.26}$$

Which separates into three distinct regimes: sub-diffusion ($\alpha < 1$), Brownian motion ($\alpha = 1$) and super-diffusion ($\alpha > 1$). A classic example of anomalous diffusive behaviour is the experiment of Solomon, Weeks and Swinney [50]. In this exper-

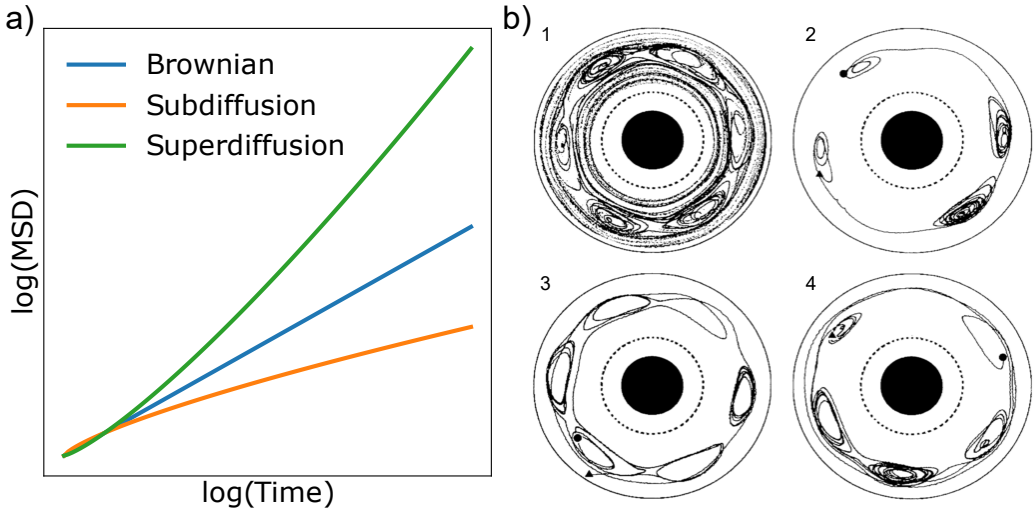


Figure 2.6: **Anomalous diffusion. a).** Three regimes of anomalous diffusion: sub-diffusion ($\alpha < 1$), Brownian diffusion ($\alpha = 1$) and super-diffusion ($\alpha > 1$) with $\alpha = 0.75, 1, 1.25$ respectively in this example. **b).** A classic experiment [50] showing the difference between normal and anomalous diffusive behaviour. Water is pumped into/out of an annulus generating a turbulent flow, in which the trajectory of many tracer particles are tracked. Far from equilibrium, particle orbits are generally "trapped" inside turbulent eddies or follow long paths, crossing vast distances in a single step.

iment they pumped fluid into and out of an annulus to generate a turbulent flow in the annulus, then recorded the position of neutrally buoyant tracer particles in this fluid. Fig 2.6b shows some example trajectories, which can be seen to separate (broadly speaking) into two categories. Some particles are trapped in the vortices formed in the fluid and so remain confined for periods of time resulting in dense trajectories with small displacement at each timestep. Other particles follow long orbits/paths where large distances are crossed in single steps, leading to a superdiffusive behaviour.

Another method of producing anomalous diffusion follows in a similar vein to the above experiment: what if particles no longer relied solely on diffusive properties to spread, but rather could travel on ballistic trajectories for short periods of time? These jump-diffusion processes are the underlying basis for many species foraging/spatial exploration strategies from large birds down to single bacteria [51]. These processes can be described as a combination of the two Lévy processes: the Wiener process (i.e. Brownian motion) and the Poisson process.

### Jump-diffusion processes

As mentioned previously in §2.3.1, the formal mathematical process describing standard Brownian motion is called the Wiener process. It is a Gaussian process with the following requirements [52]:

**Definition 2.3.1.** A Gaussian process $W(t), 0 \leq t \leq \infty$, is a *Wiener process* if and only if it satisfies:

$$\begin{aligned} \mathbb{E}[W(t)] = 0, \quad t \geq 0; \\ W(0) = 0; \\ W(t+s) - W(t)\ \mathcal{N}(0,s) \end{aligned} \tag{2.27}$$

In essence this definition states that for each increment $t$, the expected value ($\mathbb{E}$) of that increment is 0 and the process starts at $t = 0$. Finally, whilst this is clearly a non-stationary process, each increment is itself independent and stationary with a normal mean and variance. This variance can be related to the effective diffusion coefficient for the random walk. The resultant path from this process is a continuous but nowhere differentiable path due to the fact that correlations between two nearly points are, in general, too small. Hence this process can be used to describe the position of a Brownian particle but not the velocity of said particle. Fig 2.7a gives an example of a one-dimensional Wiener process for three different diffusion coefficients where at each time step the value of the function will move up/down by some normally distributed value related to the diffusion coefficient.

The second process required to build a description of jump-diffusion behaviour is the Poisson process, named after the French mathematician Siméon Denis Poisson. This stochastic counting process describes rate of occurrence of independent events, characterised by the Poisson distribution[2] More specifically, a Poisson process has the following definition and properties [53]:

**Definition 2.3.2.** A counting process $N(t), t \geq 0$ is a *Poisson process with rate* $\lambda$ if the process is such that:

$$\begin{aligned} N(0) = 0; \\ P[N(h) = 1] = \lambda h + \mathcal{O}(h); \\ P[N(h) > 1] = \mathcal{O}(h) \end{aligned} \tag{2.28}$$

[2] An interesting historical tidbit: Poisson never actually studied the Poisson process, and the Poisson distribution appears exactly once in his works. His most important works were actually focussed on electricity, celestial mechanics and most important definite integrals and Fourier analysis.

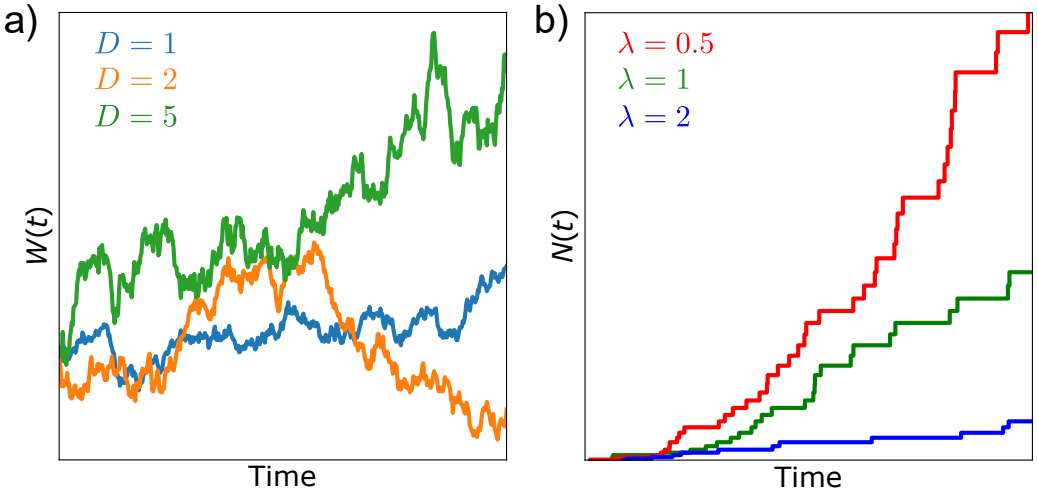


Figure 2.7: **Example of a Wiener process and a Poisson process. a).** Example of three different Wiener processes with diffusion coefficients $D = 1, 2, 5$, where the distance travelled at each timestep is some normally distributed value related to the diffusion coefficient. The total distance travelled by some time $t$ is given by $W(t)$. **b).** Poisson processes with rate parameters $\lambda = 0.5, 1, 2$, with an insert to show the individual jumps at different timesteps, with $N(t)$ being the number of events to occur by the time $t$. We see as the rate parameter decreases, the frequency of events increases.

In addition, $N(t)$ must have stationary and independent increments. $h$ here is an integer number of events.

To summarise, the second requirement states the probability of a single event occurring in a short period of time, and the third requirement that events happen singularly. These four conditions can then be shown to imply that the number of events in a time interval of length $t$ has a Poisson distribution with mean $\lambda t$. More formally: If $N(t), t \geq 0$ is a Poisson process with rate $\lambda > 0$, then for all $s, t \geq 0$:

$$P[N(t+s) - N(s) = x] = \frac{e^{-\lambda t}(\lambda t)^x}{x!}, \quad x = 0, 1, 2, \ldots \tag{2.29}$$

It is important to note that these (unit) jumps occur instantaneously, i.e. if the value of $P(t)$ jumps at a time $t_k > 0$, then $P(t_k^+) = P(t_k^-) + 1$ (this leads to $P(t)$ as being right-continuous). Fig 2.7b gives examples of three Poisson point processes with rates $\lambda = 0.5, 1, 2$ respectively. Clearly, as the rate parameter $\lambda$ is lowered there is an increase in the jump rate of the process.

Using these two processes we can build an example of a jump-diffusion process. Imagine a Brownian particle suspended in a fluid which instead of undergoing

purely diffusive behaviour described by the Wiener process, the particle also has a probability of switching to a ballistic behaviour for short periods of time. This will lead to so-called "jumps" in the trajectory of the particle. Assuming these jumps are independent we can model them as being a Poisson process with a fixed rate $\lambda$. This allows us to describe the times between the jumps, which can be shown to be exponentially distributed [54]:

Let $P(t)$ be a Poisson process with fixed rate $\lambda > 0$, let $T_j$ denote the jth jump-time and $\Delta t$ the fixed timestep. Then, the distribution of the interjump-time $\Delta T_j \equiv T_{j+1} - T_j$ for $j = 0, 1, 2, \ldots$, defining $T_0 \equiv 0$ conditioned on $T_j$, is

$$\Theta_{\Delta T_j(\Delta t)} = P[\Delta T_j \leq \Delta t | T_j] = 1 - e^{-\lambda \Delta t} \tag{2.30}$$

This combination of processes can be used to describe one of the most ubiquitous methods of self-propulsion in low-Reynolds number environments: run-and-tumble motion, i.e. periods of ballistic "runs" interspersed by periods of diffusive (or diffusive-like) behaviour. There are several distinct variants of this type of motion but this will be discussed in Chapter 3 when reviewing swimming and foraging strategies of biological microswimmers. Studying these run-tumble variants (and other motility behaviours) can be easily achieved by the combination of two now-standard techniques: optical microscopy and microfluidics.

## 2.4 Imaging life at the micron scale

### 2.4.1 Historical motivation

The use of lenses to study small objects is one that stretches back thousands of years to the early Greeks who used water-filled spheres, and so both microscopy is one of the oldest scientific methods and at the same time one of the newest. The term "microscope" was coined by Faber in 1625 [55] and nearly 400 years later we are still advancing the field with new techniques such as focal modulation microscopy [56] and light sheet fluorescent microscopy [57]. In the last century the field has expanded exponentially with developments in electron microscopy, phase contrast microscopy, confocal microscopy and optical tweezers[3], using cutting-edge optic designs to delve deeper into outstanding biological problems facing scientists today. This section briefly describes the three principal microscopy techniques that will be used later in this thesis.

[3] Numerous Nobel prizes have been awarded in this field over the last 50 years including most recently in 2018 (in Physics) Gérard Mourou and Donna Strickland for their work on laser pulses and Arthur Ashkin for his work in developing the field of optical tweezers

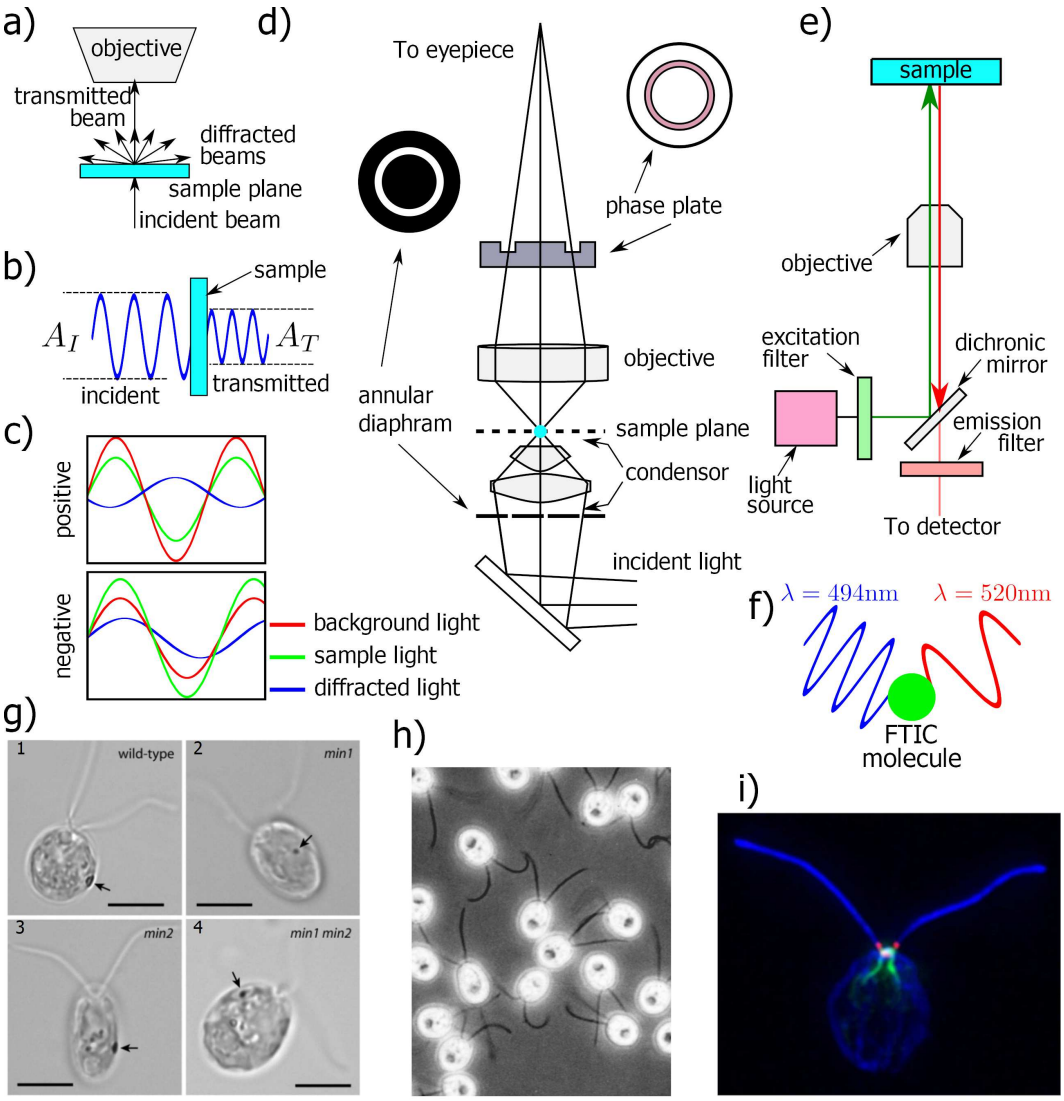


Figure 2.8: **Examples of optical microscopy. a-b).** Brightfield microscopy, where an incident beam travels through the sample and the transmitted beam captured by the objective. Image features are determined by light being absorbed/scattered by the sample, reducing the intensity of the transmitted beam. **c-d).** Phase contrast microscopy, the scattered/background/light passing through the sample have their wavelengths shifted to introduce constructive/destructive interference in order to increase the contrast of the image. There are two types of phase contrast: positive and negative, which produce bright/dark features on a dark/bright background respectively. **e-f).** Example of epi-illumination, where the sample is excited with one specific wavelength and emits a second larger wavelength which is then captured, allowing for detection of features that cannot be resolved by normal optical methods. **g).** Brightfield images of *Chlamydomonas reinhardtii* [58] highlighting different eyespots for different strains (scale bar = 5 $\mu$m). **h).** Phase contrast image of *C. reinhardtii*, credit: Steve L'Hernault (Emory University), source [59]. **i).** Fluorescent image of *C. reinhardtii* showing location of a Fa2p enzyme at the base of the flagellum. Credit: Dr. Lynn Quarmby, from: [60].

### 2.4.2 Brightfield microscopy

The first standard method is brightfield illumination, one of the simplest forms of optical microscopy. First described by August Köhler [61], it forms the foundations supporting most other forms of (transmitted) optical microscopy and requires some degree of absorption of energy by the sample being imaged. The sample is illuminated with a wide-beam that is as uniform as possible, then by absorbing the light beams the transmitted beam is reduced in amplitude but maintains the same phase as the incoming incident beam. Any sudden changes in the refractive index of the sample, such as feature boundaries etc., will result in diffracted beams radiating outwards from the sample with different phases.

The result from this technique is seen in Fig 2.8g: objects appear dark on a bright background. For small objects/objects with fine structures/objects with low contrast this technique suffers from a lack of resolution and will blur features together. If the goal is to, for example, image low-contrast structures within a biological cell then we need to use a different technique that does not rely purely on a decrease in the light amplitude.

### 2.4.3 Phase contrast microscopy

Many samples such as biological cells are unable to produce large variations in their image intensity when subjected to brightfield microscopy. Different structures in the sample however will have different refractive indexes so will in turn introduce subtle phase shifts into their transmitted beams. This can be taken advantage of by utilising interference to increase the contrast amplitude and as such increase the resolution of the final image in a technique called phase contrast microscopy [62]. [4]Here we will just consider the case of transparent cells which within themselves contain regions of differing optical densities and/or differing optical densities with their environment, such is the case with biological samples.

Fig 2.8b demonstrates this technique. Light is transmitted through a phase annulus in the condenser such that the sample is illuminated by an annulus of light of wavelength $\lambda$. In the sample itself different optical density regions of the sample will introduce differing shifts in their respective transmitted beams. These are collected by the objective at the other end of the light path which is fitted with a phase plate - the complement of the phase annulus. This introduces a further $\lambda/4$ phase shift in the incoming light outside of the ring relative to the light passing through

[4]Phase contrast presented such an improvement to the microscopy field that the inventor of the technique, Frits Zernkie, would be awarded the Nobel Prize in Physics (1953) for this work.

the phase ring, enhancing any interference caused by the sample. Through constructive/deconstructive interference the image is then created from these diffracted beams, with the shifts in interference giving the variation inside the cell therefore producing more detail in the image. Fig 2.8h gives an example of this, where the flagella of *C. reinhardtii* are immediately more visible than compared to the bright-field images (Fig 2.8g).

### 2.4.4 Epi-illumination/fluorescence microscopy

Contrasting with the above two methods is epi-illumination. Here instead of illuminating through the sample, light is passed up through the objective and the reflected/emitted light is collected back by the objective. There are two main uses for it - imaging samples that are optically opaque or for fluorescence microscopy [63,64].

Fluorescence microscopy utilises the property of fluorescent molecules known as fluorophors, which when excited by the correct incident wavelength will subsequently emit light of a different wavelength. This combined with epi-illumination forms the fundamental principles of fluorescence microscopy. The stimulating light is passed through an excitation filter then a dichromic mirror to select a specific wavelength (for example by use of a filter cube or laser) which passes through the objective and is focused onto the sample. Fluorescent molecules in the sample absorb this wavelength and release a longer (here red) wavelength which is collected by the objective. The dichromic mirror then reflects any reflected excitation light but allows the emitted longer wavelength through, which is further filtered before imaging.

Fluorescent microscopy is an extremely powerful and essential tool in biological studies and there are countless applications of this technique. For example it can detect particles below the resolution limit of standard optical microscopy (detect not necessarily resolve), and also used in the labelling and tracking different biological specimens including microtubules [65] which form the transport network of cells and using chloroplast autofluorescence as a measure of photosynthetic activity in plant cells [66]. There are drawbacks with this technique with problems such as photobleaching [67] but on the whole these can be worked around and the advantages in this case far outweigh the disadvantages of the technique.

This concludes a (brief) overview of some of the optical microscopy techniques available. To use these techniques effectively, there needs to be a means of experimentally confining swimming cells in liquid environments which leads to the field of microfluidics and micron-scale experimentation.

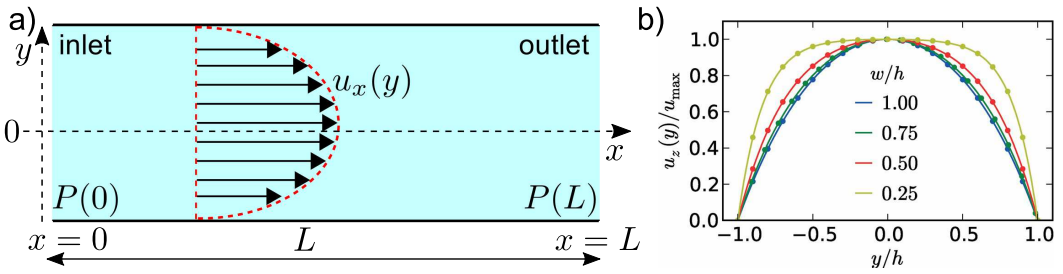


Figure 2.9: **Poiseuille flow in a cylinder - pressure driven flow. a).** Schematic of Pouisseuille flow in a cylinder of length $L$. A pressure $P(0) = p + \Delta p$ is applied at the inlet, and at the outlet there is a pressure of $P(L) = p$. The velocity profile is described by $u_x(y)$ and is parabolic in shape with no-slip conditions at the boundaries of the cylinder. **b).** Flow profile in a rectangular channel (from: [72]). As the aspect ratio tends towards 1 (i.e. to a square channel) the flow profile becomes increasingly similar to the cylindrical flow case, with the flow profile flattening out as the channel becomes increasingly rectangular in cross-section.

## 2.5 Microfluidics

Microfluidics is both a science and technology focussed on studying the behaviour of fluids/particles at the micro/nano-scale, working on fluid scales down to the femtoliter. There are several major advantages to working at these scales, the obvious one being that only minuscule volumes of sample are needed which cuts laboratory costs by orders of magnitudes. Other advantages are the fast analysis and efficient detection [68] such systems offer. Perhaps the most interesting and applicable use of microfluidics is the development of lab-on-a-chip style devices (LOC) [69–71], a developing field aiming to design and develop compact easy to use single-use devices which have a broad range of potential applications such as medical diagnostics and drug administration. It is the aim of this section to give an overview of the physical laws underlying fluid flows in these micro-channels and to describe the fabrication and implementation of the devices. To start with, we revisit to the Navier-Stokes equation to describe the behaviour of flow in such a micro-channel.

### 2.5.1 Pressure-driven flow/Poiseuille flow

The beginning of this chapter introduced the Navier-Stokes equation (Eq 2.2) and noted that there is not currently a general analytical solution for this family of equations. However in very specific cases it is possible to write down an exact analytical solution - one such example of this is pressure-driven steady state flows in channels, known as Poiseuille flows. Assuming 1) incompressibility, 2) Newtonian

behaviour at low Reynolds number, and 3) no additional forcing on the fluid we can reduce the Navier-Stokes to the previously mentioned Stokes equation (Eq 2.11). Fig 2.9a describes the problem: a cylindrical channel of radius A and length L aligned along the $x-$axis, with a pressure $P(0) = p + \Delta p$ at one end of the channel and $P(L) = p$ at the other. In this case the velocity field is invariant in the $x$ direction at low velocities [68]. Combining this with the Stokes equation leads to:

$$\mathbf{u}(\mathbf{r}) = u_x(y, z)\mathbf{e}_x \tag{2.31}$$

$$\nabla P = \mu\nabla^2[u_x(y, z)\mathbf{e}_x] \tag{2.32}$$

Recognising that the pressure only varies in the $x$ direction:

$$\eta\left[\frac{\partial^2}{\partial y^2} + \frac{\partial^2}{\partial z^2}\right] = \frac{\partial P(x)}{\partial x} \tag{2.33}$$

Since the left-hand side is a function of $(y, z)$ and the right-hand side a function of $(x)$ we can set Eq 2.32 to be constant. This implies a constant pressure gradient which in turn means that the pressure must vary linearly with $x$, and hence from the pressure boundary conditions:

$$P(\mathbf{r}) = \frac{\Delta p}{L}(L - x) + p \tag{2.34}$$

This allows us to form a set of partial differential equations to describe the flow field $u$, volumetric flow rate $Q$ and hydrodynamic resistance $R$. This flow resistance is heavily geometry/aspect ratio dependent on the channels themselves. By definition the volumetric flow rate (for an incompressible fluid) is given by:

$$Q = \frac{\Delta p}{R} = \int_C u_x(y, z)dydz \tag{2.35}$$

With $C$ denoting the cross-sectional area. This has been solved/approximated for a series of different geometries, for example in the case of a cylindrical channel it is relatively straightforward to show that the velocity field and volumetric flow rate are [73]:

$$\begin{aligned} u_x(y, z) &= \frac{\Delta p}{4\eta L}(A^2 - y^2 - z^2) \\ Q &= \frac{\pi A^4}{8\eta L}\Delta p \end{aligned} \tag{2.36}$$

As described in Fig 2.9a, the flow field has a parabolic shape with a maximum at the middle of the channel and zero at the edges of the channel which satisfies the no-slip boundary conditions. The volumetric flow rate is (as expected) independent of the $x-$direction, although it is worth pointing out at this stage that for a compressible fluid we would also need to consider the mass flow rate given by the integral of the density multiplied by the flow field, but as we are assuming incompressibility this can be ignored.

However most techniques in micro-channel production result in rectangular cross-sections for which the flow field is significantly more complicated to calculate. For a cross-section with width $w$ and height $h$ It is possible to calculate an approximation for the volumetric flow rate which improves rapidly as the aspect ratio $h/w$ decreases[5]. For a rectangular cross-section it can be shown that [68]:

$$\begin{aligned} u_x(y,z) &= \frac{4h^2\Delta p}{\pi^3\eta L}\sum_{n,\,\text{odd}}^{\infty}\frac{1}{n^3}\left[1-\frac{\cosh(n\pi\frac{y}{h})}{\cosh(n\pi\frac{w}{2h})}\right]\sin\left(n\pi\frac{z}{h}\right) \\ Q &\approx \Delta p\cdot\frac{h^3 w}{12\eta L}\left[1-0.63\frac{h}{w}\right], \quad \text{for} \quad h>w \end{aligned} \tag{2.37}$$

Which is shown in Fig 2.9b for a range of aspect ratios [72]. A final note on the hydrodynamic resistance $R$: drawing an analogy with electricity circuits it is possible to combine resistances of different size/shape connected channels as in done using Kirchhoff's laws. For two channels with hydrodynamical resistances $R_1, R_2$ respectively the combined resistance $R$ is given by:

$$\begin{aligned} R &= R_1 + R_2, && \text{for channels connected in series} \\ \frac{1}{R} &= \frac{1}{R_1}+\frac{1}{R_2}, && \text{for channels connected in parallel} \end{aligned} \tag{2.38}$$

This concept can be used to a channel designer's advantage: by using capillaries (i.e. channels with small cross-sectional area) as flow resisters it is possible to produce stable flow fields with very low velocities whilst maintaining a low hydrodynamical resistance in the main channel.

### 2.5.2 Fabrication of microfluidic devices: soft photolithography

Prior to the late 1990's microfluidics was hampered by the fact that it was difficult to develop new devices - prototyping was both time-consuming and expensive, two

[5]This approximation is much more laboured than derivation of the analytical solution for the cylindrical case, using the Riemann zeta function along the way to the final approximation. In the case of a square this approximation gives an error of around 13% but a decrease to an aspect ratio of a half ($h = w/2$) reduces the error down to 0.2% already [68]

substantial blocks for the development of any new technology. This all changed in 1998 when the group of Whitesides [74] developed a method of soft-lithography which could design, fabricate and implement new devices in a day. Soft lithiography is a broad terminology used to describe a range of techniques by which structures are replicated from a master mould onto "soft" (elastomeric) materials. The material of choice here is polydimethylsiloxane (PDMS) for short which has a range of useful and important qualities that make it an idea choice for working with both biological and microfluidic systems.

The procedure is outlined in Fig 2.10 and goes as follows. First the channels are designed in CAD software then the channel structures are built onto a silicon wafer to form a master mould. PDMS is then poured over this mould, left to cure then is cut away from the mould which can then be reused. The PDMS is cut into individual devices which then have their inlets/outlets punched out before being bonded to a glass coverslide using an oxygen plasma to form the final microfluidic device. This technique produces completed single-use devices quickly with an extremely high level of consistency between the devices which can be easily disposed of once after use.

### Creating the master mold

The first stage of developing a new device is to design the channel structure to meet the experimental requirements of the device. This needs to take various details into account such as channel width, inlet/outlets locations, wall thickness and any features such as pillars and nozzles. The minimum feature size is realistically determined by the resolution of the printed photomask - for extremely high resolution these can be printed onto quartz but these are extremely expensive and fragile. More commonly masks can be printed on high grade transparency sheet masks which are significantly cheaper and quicker to produce but are limited to a minimum feature size of approximately 15 microns. These are printed using a high grade laser printer with a resolution on the order of $10^4$ dots per inch, and need to be kept in a clean dust-free environment. Since any dust/airborne debris caught up making the master mould will introduce imperfections into all future casts from that mould, the master moulds are produced in clean-rooms to improve the quality of the mould.

The next component is the wafer itself. The silicon wafers used are of test/mechanical grade quality, with higher grade available for even more specialized processes. The wafer generally has one polished side and have a thickness of approximately 400 microns depending on the size of the wafer (generally use 3 inch diameter wafers). The wafer is typically spin-coated with a photoresist - a UV light

sensitive chemical. A negative photoresist is usually used, which hardens upon exposure to UV, but positive resists are also available. The height of the photoresist layer is determined by the speed of the spin coating, where for a given viscosity of photoresist a specific RPM will produce a specific layer height.

Once the wafer has been spun and baked for a period of time, a mask aligner is used to bring the mask into contact with the coated wafer. The closer the mask can be to the wafer the better the final resolution due to diffraction of the UV around the boundaries of the features on the mask. The wafer/mask combo is then exposed to a strong UV source, such as a vapour lamp, which (for our negative resist) hardens the photoresist in the transparent areas of the mask. A solvent (developer) is used to remove the photoresist that has not hardened, leaving a positive relief of the channels of the same height as the spun-layer of photoresist initially deposited on the wafer. This is now ready to be used as a master mould to produce single-use microfluidic devices. Depending on the height required, preparing a wafer can take as little as an hour in a clean-room for relatively thin devices, showcasing the rapid prototyping this process lends itself to.

### PDMS

PDMS is a visoelastic material that when mixed with a cross-linker and cured over heat forms a hydrophobic elastomer. Depending on the ratio of PDMS to cross-linker (usual practice is a $10:1$ mass ratio) the flexibility of the elastomer can be tweaked. More importantly PDMS is transparent to the UV/visible spectrum so it does not hinder imaging the sample with optical microscopy techniques. It is also gas-permeable which has two main uses. Firstly, oxygen can diffuse into the sample meaning any biological organisms in the channels won't suffocate - this also can be used to set gas-gradients in the medium, for example during aerotaxis studies [75]. Perhaps more importantly however is that if air bubbles get trapped in the device during filling, by simply pressurising the device (making sure to stay below a pressure that will delaminate the device, usually $25-30\,\mathrm{psi}$ in PDMS), the fluid pressure will push the air out of the device through the PDMS, resulting in a fully filled channel. This is important since the presence of bubbles with dramatically alter the behaviour of the device such as blocking features or changing the direction/magnitude of the flow in the device. It also means that once the cross-linker has been mixed in the complete solution can be put under vacuum to draw the air bubbles out of the liquid before it is poured onto the mould, greatly improving the optical transparency of the final device.

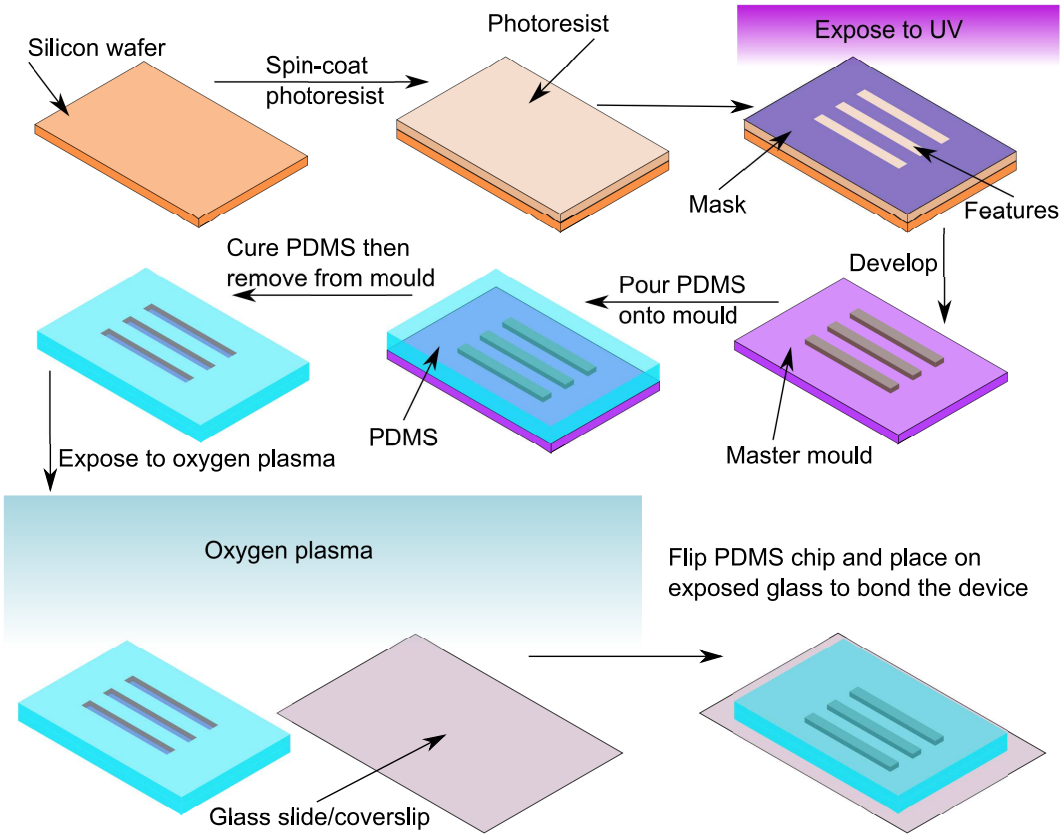


Figure 2.10: **Fabrication of microfluidic master mould and devices.** A silicon wafer is spin-coated with a photoresist, with the RPM and viscosity of the photoresist determining the height of the final layer. A mask of the desired features (here three simple straight channels) is placed on top of the photoresist and then exposed to UV. The wafer is then developed to remove excess photoresist, leaving the master mould with positive reliefs of the desired features. PDMS is then mixed in a 10:1 ratio, poured onto the mould then cured under heat until it hardens. This is then cut and peeled away from the mould, leaving a PDMS chip with negative reliefs of the desired features. The chip and a glass slide/coverslip is then exposed to an oxygen plasma which, when the two parts are brought into contact, forms a covalent bond which can be strengthed by heating the device for a few minutes.

### Bonding and sealing the device

The final stage before the device is usable is to seal the device, which is a simple task with PDMS and glass. Exposing both the PDMS and a glass cover slide to an oxygen plasma removes hydrocarbon groups, leaving silanol and OH groups on the PDMS/glass respectively. When brought into contact these form strong Si-O-Si covalent bonds in seconds, which can be further strengthened by heating the device for a few minutes on a hot plate.

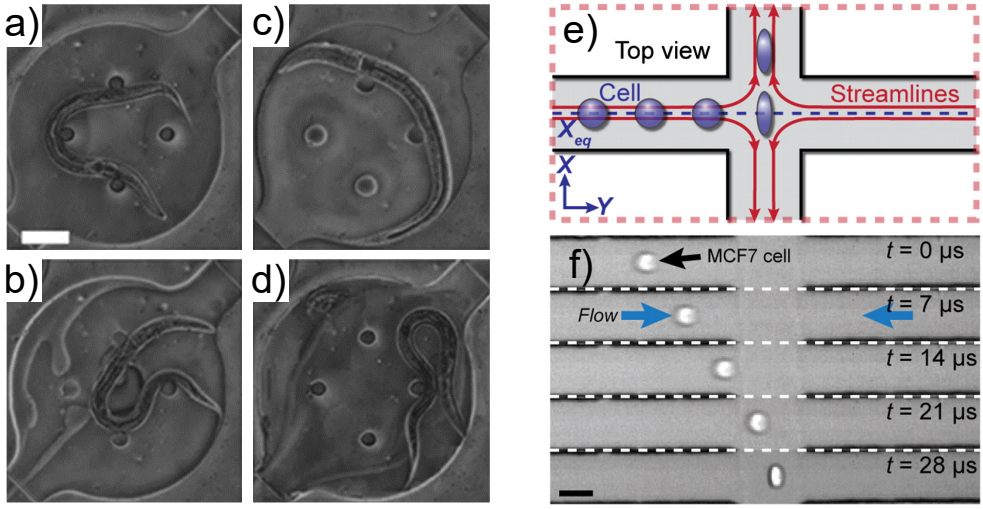


Figure 2.11: **a-d).** Microfluidic trapping of *C. elegans* [76]. An example of the complete device cycle where: (a) cells arr cultured/suspened in the device; (b) bacteria are introduced into the device; (c) the device is warmed to trigger the worm immobilization; (d) device is allowed to cool and is then flushed out. Scale bar represents 60 mm. **e-f).** Hydrodynamic stretching of single cells for large population mechanical phenotyping [77]. Cells are delivered to the extensional region of flow and their subsequent deformation measured.

The device is now ready for use - this entire procedure from original concept to having a device can be completed on the timescale of a couple of days (provided there is an available printer for the mask!) and producing more devices from the same mould takes only a few hours of lab time, the majority of which is spent waiting for the PDMS to cure fully.

### 2.5.3 Examples of microfluidic applications

A prime example of the biological applications of microfluidics are studies of the nematode *C. elegans* (Fig 2.11a-d). This worm is a particularly interesting organism as it has a complete nervous system despite being considered a relatively simple organism. However live cell imaging previously required the cells to be immobilized mechanically or chemically which is potentially harmful for the organism as well as being time consuming for the researchers. This changed when it was realised that microfluidics provided a means of trapping a single cell for live imaging without harming the cell [78] and this has opened up whole new avenues of research in the last decade, with breakthroughs being made in all manner of areas such as studying embryonic development [79].

Many biological processes rely on the detection and/or regulation of chemical gradients, such as bacterial chemotaxis towards food sources or cell migration [80]. Controlling chemical gradients in large scale flows is extremely difficult however in microfluidic devices it is fairly straightforward to setup/maintain/dynamically adapt chemical gradients in the device. Importantly these gradients are reliable and repeatable in addition to be finely tunable both spatially and temporally. One such example is the microinjector design [81] which creates a "plume" of chemical in the middle of a micro-channel which can be fine-tuned by simply changing the flow ratios in the device using standard syringe pumps.

One of the main driving forces in developing microfluidic technology is the medical world - the need for fast efficient and simple "lab on a chip" (LOC) style device which can be analysed quickly for diagnosis purposes for example. One such example of a microfluidic device developed for clinical purposes is the work of Gossett et al [77] (Fig 2.11e-f). This assay takes advantage of the different mechanical properties of different types of cells (e.g. cancer cells vs healthy cells) and uses hydrodynamics to deform the cells, allowing them to characterize the cell populations in a patient's sample at a rate of $2,000\,\text{cells.s}^{-1}$. The device allows for collecting as much data in a day as opposed to years with previous methods of single cell stretching and is a prime example of how the underlying physics can be combined with clever microfluidic design to advance cutting edge clinical work.

## 2.6 Summary

This chapter has described behaviour of fluid systems at the micron scale, and experimental methods of investigating these systems with optical microscopy and microfluidic techniques. In broad summary:

- The fluid flow of a system is described by the Navier-Stokes equation, which can be solved in very specific cases. In low Reynolds number systems, where the viscous forces dominate the inertial forces in the system, microswimmers in these environments have had to develop non-reciprocal motion in order to self-propel, often utilising drag-based thrust for this.
- Micron-sized particles suspended in a fluid are subject to thermal noise which introduce translational and rotational fluctuations into the particle. Over long periods of time these fluctuations follow a linear mean-squared displacement law which can be fitted to obtain a measure on the diffusive properties of the system.
- Experimenting at the fluid micron-scale requires two main experimental techniques: optical microscopy and microfluidics. The field of microfluidics has exploded since the development of photolithographic techniques and allows for rapid prototyping and development, using clever geometries to probe this complex environment. Optical microscopy is one of the oldest yet newest experimental methods, and there are a wide range of methods available including phase contrast and fluorescent microscopy to investigate the behaviour of swimming cells.

# Chapter 3

# Microscopic life

## 3.1 Introduction

Just as all matter can be constructed from basic building blocks (protons, neutrons etc.), living matter has a fundamental building block: the cell. Unlike protons and neutrons however, cell structure and types vary wildly between different organisms, from the simple unicellular bacteria up to the trillions of cells that make up the human body. Despite this all cells fall into one of two broad categories: eukaryotic or prokaryotes. This thesis will focus primarily on two eukaryotic organisms: *Chlamydomonas reinhardtii* and *Micromonas pusilla*. These photosynthetic algae have both been become model organisms for a variety of systems which will be explored in this chapter. Several of these systems, such as chemotaxis (directed motion along a chemical gradient) have a large literature basis with prokaryotes, so first we familiarise ourselves with eukaryote and prokaryote cell structures, before briefly summarising a variety of methods of propulsion (linking back to the hydrodynamical discussions in Chapter 2). After this we then look at the previous work concerning *M. pusilla* and *C. reinhardtii* before establishing the main experimental questions that this thesis will look to answer.

## 3.2 Living cell: structures and processes

For the purpose of this thesis we will be examining cell motility and how it changes given different environmental conditions, which means a significant amount of attention does not need to be dedicated to the inner cell structures and processes. This section instead will address the biophysical phenomena relevant to this study: photosynthesis, methods of swimming and dissolved matter in marine systems.

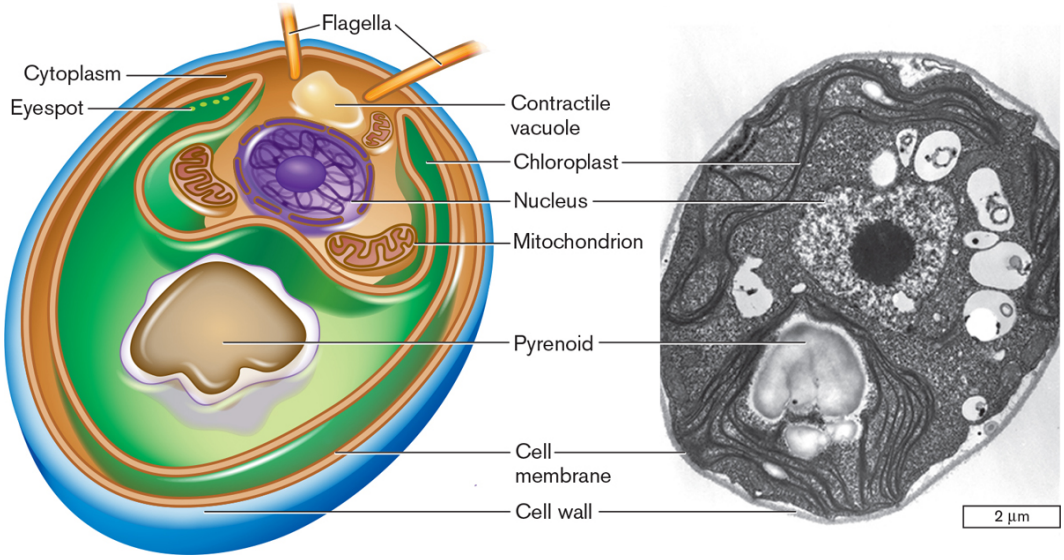


Figure 3.1: **Eukaryotic cell structure.** Cartoon/cut-through of the eukaryotic cell *Chlamydomonas reinhardtii* with the major cell structures labelled (from [82]). The main structures of interest here are: the flagella, the eyespot, the chloroplast and the pyrenoid.

### General cell structure

Almost every cell is different its shape and arrangement but there are shared characteristics between cells. All cells can be though of as a membrane holding containing a gel-like substance called a cytoplasm which fills the cell and gives it its shape. This cytoplasm contains genetic material which governs the role of the cell and how it should perform its task. The role of a membrane is to hold all of this together whilst also providing a protective barrier between the genetic material and the outside environment.

As previously mentioned, cells can be separated into one of two classes: eukaryotic and prokaryotic. Apart from their relative sizes (eukaryotes are typically larger than prokaryotes), the principal structural difference between the two is that eukaryotes have a nucleus and other organelles whereas prokaryotes[1] do not. An organelle is a membrane-housed specialised-structure which performs a specific task in the cell. For example, mitochondria[2] converts oxygen and other nutrients into adenosine triphospate (ATP) which is used as a source of chemical energy to power the various metabolic activities in the cell. Eukaryotic cells can be divided into two further sub-categories: plant and animal cells. Fig 3.1 shows an example of

[1] In fact the word prokaryotic translates from Greek to "before nucleus"
[2] Colloquially referred to as the "powerhouse of the cell"

an eukaryote - the green alga *Chlamydomonas reinhardtii*, a model organism which will be discussed in more detail later in this chapter. There are numerous structural differences between these two types of cells but the main differences are: plant cells have a cell wall, chloroplast and other specialised membrane-bound organelles (called plastids) such as a central large vacuole that are absent in animal cells. These structural differences allow for plant cells to maintain a rigidity that enables them to grow up and out, seeking out sunlight for photosynthesis which is enabled by the chloroplast.

### 3.2.1 Photosynthesis

The importance of photosynthesis cannot be understated - it is the process that provides energy to the entire biosphere and is the basis of life on Earth. The process can be generalised as: the absorption of a photon by a pigment molecule to excite an electron in order to reduce a chemical substance and form "energy-rich" molecules such as ATP [83]. These are used to form more complex molecules, and the electron lost from the pigment is replaced by an electron from the environment. The energised electron can be used to reduce a range of inorganic substances such as carbon dioxide ($CO_2$). For example, plants use water as the electron source in a processes known as oxygenic photosynthesis which can be traditionally divided into two stages: light and dark reactions, and is how all plant and algae cells undertake photosynthesis. In the light reactions, absorbed light is used to produce organic energy molecules which are used by the dark reactions in the absence of a light source. The dark reaction uses these organic energy molecules to produce other energy molecules to be used by the cell. Importantly, if the cell is starved of light for too long the dark reactions begin to fail as it relies on the output of the light reaction in order to function. At the heart of photosynthesis are the reaction centres where the main processes that form photosynthesis are carried out. In oxygenic photosynthesis there are two separate reaction centres that work in series, which are called *photosystem II* and *photosystem I* (or PSII and PSI respectively). These are the function structures responsible for carrying out photosynthesis and are found in the chloroplasts of plants and algae.

The first stage of photosynthesis is the absorption of light. The two different photosystems are only capable of absorbing light in the $680-700\,\text{nm}$ range, so cells have developed means of extending this range. An array of pigment molecule and proteins known as light-harvesting complexes (or antennas) are used to improve the photosynthetic efficiency - effectively increasing the potential absorption spectrum to $400-700\,\text{nm}$. The principal pigment responsible for this is chlorophyll, which has

main variants which are all slightly structurally different. This alters the absorption spectrum between different pigments, improving the usable absorption spectrum available for the plant. Two of the primary chlorophyll pigments are chlorophyll *a* and chlorophyll *b*, each with their own different spectra [84]. It is because of chlorophyll that plants have their green colour, whereas another major pigment class - the carotenoids - are mainly yellow/orange/reddish in colour. Photosynthesis starts with a pigment molecule absorbing an incoming photon to form an exciton (excited electron and hole combination) which typically takes on the order of femtoseconds ($10^{-15}$ s). This is then passed to the reaction centres where the bulk of the photosynthetic processes are carried out. The entire absorption-and-transfer process is incredibly efficient - it is estimated that approximately 90% absorbed energy is transferred from the antenna to the reaction centres in under $10^{-10}$ s [85]!

The two reaction centres (PSII and PSI) work in series, with PSII using light energy to oxidise water and reduce plastoquinone which is passed to PSI - plastoquinone is used to as a carrier in the electron/energy carrier transport chain. The electron transport is used to establish a proton electrochemical gradient to drive the (uphill) conversion of electrochemical energy into chemical free energy in the form of ATP. Plants and algae use this ATP reduce $CO_2$ to carbohydrates/sugars which can then be used as a food source for the organism.

### 3.2.2 Algae and phytoplankton

The term "algae" (or the singular "alga") has been used several times in this chapter but so far it has not been properly defined. Algae are photosynthetic eukaryotic organisms but have distinct differences to plants. Principally they lack the diversification of plant cells - roots, stems, leaves, and algae can be unicellular whilst plants are exclusively multicellular organisms. There are over $100,000$ species of algal in a wide range of environments such as soil, freshwater and oceans. These species come in all shapes and sizes, ranging from the microscopic *Ostrecoccus tauri* ($< 0.8$ $\mu$m) up to giant 50 m kelp structures. Algae are not just a layer of green scum to be scooped off of the pool - they have a myriad of biotechnical applications and are a crucial part of the global ecosystem. Such applications include: biofuel production (e.g. biodiesel and bioethanol), pollution indicators, biomass production, hydrogen production and even cosmetics [86–90]! A huge industrial attraction for algae is that they can be grown commercially in almost any environment and so provide an almost unparalleled conversion rate of solar energy to carbon rich molecules whilst exerting an almost negligible pressure on arable land.

These organisms have, as one might expect, a huge environmental and eco-

logical significance, but perhaps the most famous example of their environmental impact however is a negative one - harmful algal blooms. A bloom occurs when the population of algae (occurs in both freshwater and marine environments) increases rapidly. The majority of algae are not harmful to their environment but there is a small percentage which are known to be harmful or toxic. One example is a harmful algae bloom in 2004 off the coast of Florida which killed over 100 dolphins [91]. The largest bloom currently on record occurred in 1991 affecting over 1000 kilometres of the Darling River [92, 93]. Many algae species form part of the phytoplankton community - aquatic photosynthetic microorganisms that are estimated to be responsible for over half of the global oxygen production on the planet [94]. In oceanic systems phytoplankton form the primary food source for nearly all other aquatic life from zooplankton upwards. Most phytoplankton are considered passive - they rely on currents for their movement, but are also able to move vertically in order to improve their access to light and nutrients [95]. Some phytoplankton are capable of active movement enabling them to actively swim and explore their environments, for example in search of for food sources.

**Dissolved organic matter**

The global carbon cycle describes the exchange of carbon between four major systems: the atmosphere, ocean, land and fossil fuels. Current estimates put the net primary productivity of the global oceans at approximately $50\,\mathrm{Pg.C.yr^{-1}}$, or approximately 50 *billion* metric tonnes of carbon every year [96], which is roughly 50% of the primary productivity of the entire biosphere. Living organisms in the ocean contribute to a total carbon mass of roughly the $1 - 2\,\mathrm{Pg.C}$ of which approximately a quarter are phytoplankton [97]. Dissolved organic matter (DOM) makes up the majority of the non-living organic carbon, currently estimated to be at least $1000\,\mathrm{Pg.C}$ [98]. Defining what DOM actually is can be tricky as the operational definition for "dissolved" is that any material that can pass through a given filter counts as dissolved. Matter that does not pass through is called particulate organic matter (POM), and whilst establishing a definitive boundary between the two phases is tricky it remains that DOM remains a major store of carbon in the oceans. Dissolved organic carbon (DOC) is estimated to be in the same range as the quantity of carbon in the atmosphere - on the order of hundreds of Pg.C [99].

As well as being critical component of the global carbon cycle DOM is also an important food source for many marine microorganisms. Part of this is due to the fact that DOC does not sediment (unlike particulate carbon) so it remains a food source at a variety of heights in the water column. Phytoplankton significantly

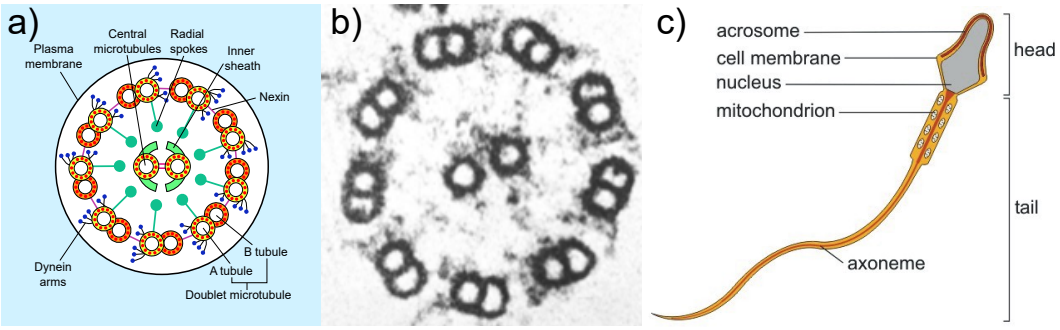


Figure 3.2: **The eukaryotic flagellum. a).** The axonemic structure that forms the core of the flagellum. Nine pairs of microtubules surround a pair of single microtubules, which are connected by dyenin motor proteins which introduce bending/wave patterns into the flagellum motion (from [100]). **b).** An electron micrograph cross-section of a sperm tail (from [101]). **c).** One of the most well-known examples of a flagellum: the mammalian sperm cell, where the flagellum is approximately 50 microns in length. Image from [102], courtesy of Thomas Gensrch (Forschungszentrum Jülich).

influence DOM in the oceans by being able to release it into the surrounding aquatic environment through a number of ways. These vary from release from virus lysis which can theoretically move approximately $10^9$ tonnes of carbon every day and cell death, but perhaps more significantly from extracellular release due to photosynthesis.

Many algae/phytoplankton are motile and so are able to explore their environments, hunting for nutrient patches or seeking optimal light environments. There are a variety of methods available for these organisms to propel themselves, and the choice of motility pattern will have a significant bearing on the fitness of the organism.

## 3.3 Methods of propulsion at the micron scale

Chapter 2 discussed the physics underlying motility in low Reynolds number environments. Principally Purcell's scallop's theorem which shows that reciprocal motion will not produce any net motion in the viscosity-dominated regime - there needs to be some breaking of the time-reversibility in order for the organism to swim. There are a range of methods that biological microswimmers have evolved to overcome these physical restraints, starting with the eukaryotic flagellum.

### 3.3.1 The eukaryotic flagellum

The term "flagellum" derives from the 19th century, based on the Latin diminutive *flagrum* or "scourge". In a more biological context, the term flagellum refers to to slender whip-like appendages which are generally used for movement by microscopic cells. There are three different classes of flagellum: bacterial, eukaryotic and archaeal flagellum, but for the scope of this thesis we are only concerned with the eukaryotic case.

The eukaryotic flagellum has a very distinctive structure, shown in Fig 3.2a. The main bundle consists of nine pairs of microtubules (doublets) which surround a central pair of two single microtubules (singlets). This classic "9+2" structure forms the core of the flagellum and is called an axoneme. The outer doublets are linked by dynein, a set of motor proteins which are capable of moving along microtubules in cells, and occur at regular intervals along the length of the axoneme. When the motor is activated it attempts to walk along the microtubules which would be expected to produce sliding motion, but the presence of the other structural links in the axoneme converts this motion to a bending motion instead, inducing waves or beating patterns when the flagellum moves. The outer doublets are linked to the inner singlets by a set of radial spokes comprised of at least 23 proteins that contribute to the regulation of the flagellum motility [103]. The entire bundle is enclosed in the flagellum membrane - an extension of the cell membrane and is rooted at the cell body by a structure known as the basal body. One popular example of the eukaryotic flagella comes from the mammalian sperm cell (Fig 3.2c), where the flagellum beats out oscillatory waves which themselves rotate about an axis [104]. Single swimming human spermatoza propel themselves at approximately one body length per second ($\approx 50\,\mu\text{m.s}^{-1}$), although in viscoelastic fluids the cells can swim collectively faster [105].

It is worth mentioning that flagella are not just tools to enable cell motility. Cilia are structurally idenitical to flagella but tend to be much shorter - they are named differently for the sole reason that they were both named before their individual structures were investigated. The only functional difference is that flagella tend to "beat" and produce oscillatory wave patterns, whereas cilia have a power stroke/recovery phase, but this should not be used as a strict differential between the two structures. These ciliated cells are used for a variety of other processes, for example large populations of ciliated cells - over $10^7\,\text{mm}^{-2}$ [100] - transport fluid and material (such as mucus) along respiratory passages. This transport is achieved by the production of metachronal waves along an array of cilia, which is an order of magnitude more efficient than the entire cilia population beating in phase with

each other [106]. Non-motile cilia (also known as primary cilia) play a sensory role in the body, for example in hearing and the regulation of signal transduction in the brain [107, 108].

The two organisms of focus in this thesis are both eukaryotic and propel themselves by use of one (or more) eukaryotic flagella. However, this is naturally not the only means of propulsion available to microswimmers (both biological and non-biological swimmers) as will now be briefly discussed.

### 3.3.2 Prokaryotic flagellum

The prokaryotic flagellum does not share the same previously described eukaryotic structure. Instead of the 9+2 structure we are now familiar with, the bacterial flagellum is a 20 nm hollow tube and has a helical shape. The flagellum has a "hook" to join it to the cell body [113] (Fig 3.3a), and it is this sharp bend that directs the flagellum away from the cell body - otherwise the flagellum would point normally to the cell body. This would present a significant problem for a bacterium as many bacterial cells have many flagella (for example, *E. coli* has $8 - 20$ flagella) so directed motion would not be possible if the flagella could not be orientated with respect to the cell body. A series of proteins rings act as bearings for the shaft that runs between the hook and cell membrane. The hook is rotated by a motor which rotates the helical flagella like a screw to propel the cell, which will be discussed in Section 3.4.1 when discussing the run-tumble motion of bacteria such as *E. coli*.

### 3.3.3 Swarming

Swarming can be almost thought of as an elevated form of bacterial swimming. It is defined as being the rapid multicellular bacterial surface movement powered by rotating flagella [114], or more simply a rapid population migration across a surface of flagellated bacteria. Swarming was first reported in 1972 [115], and generally forms fractal-like patterns radiating out from a central spot (Fig 3.3b). Swarming requires flagellated bacteria, and often excessively flagellated cells. During swarming, cells form large rafts (or islands) in which the encapsulated cells hardly move [116]. Swarming motility has extremely important implications in a wider biological setting, namely the formation of biofilm production on surfaces. Biofilms provide a safe haven for bacteria to survive antibiotics and other hostile environments and have been reported to improve antibiotic resistance dramatically in comparison to planktonic bacteria [117].

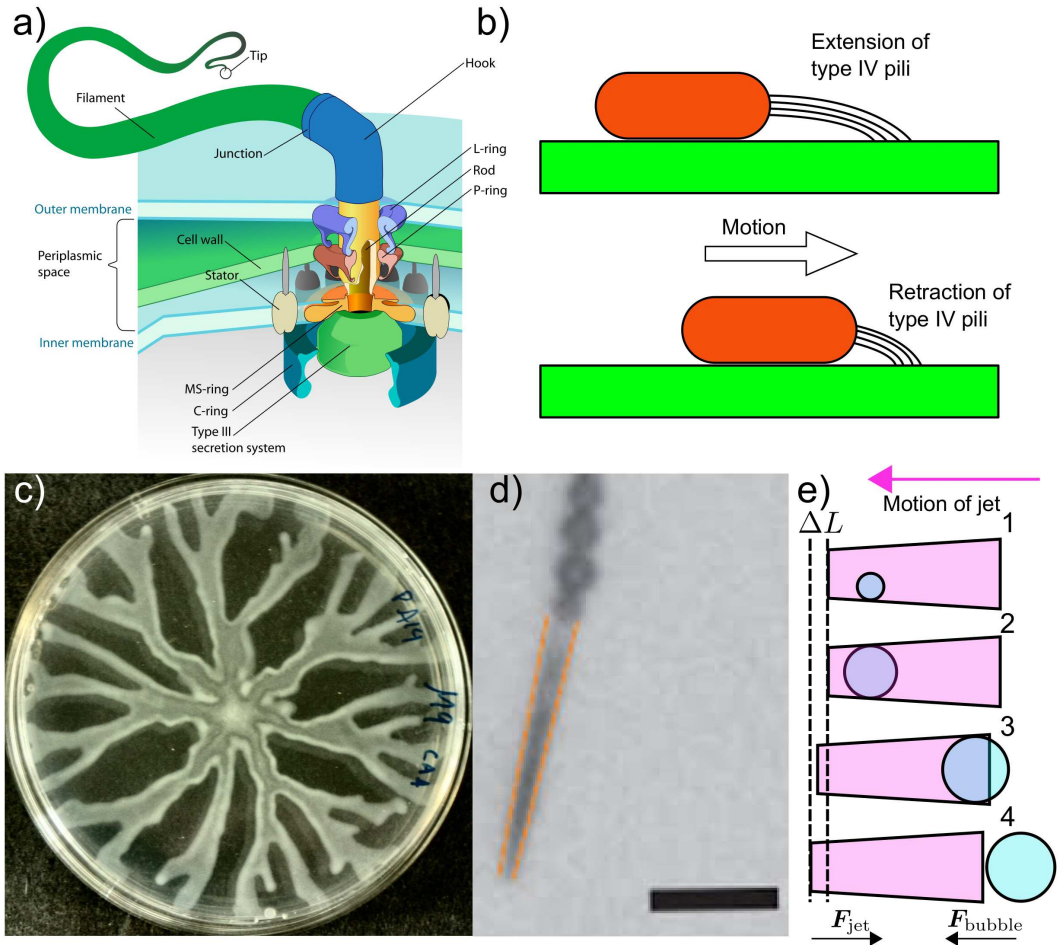


Figure 3.3: Examples of other propulsion methods availabe to a range of microswimmers. **a).** The prokaryotic flagellum, which consists of a slendar filament rotated by motor and hook combination in the cell body. Image from [109]. **b).** Gliding motion along a surface, where multiple pili are extended/retracted in a grappling hook motion. Image based from [110]. **c).** Bacterial swarming along a surface, producing characteristic fractal patttern on the surface as the fronts propagate. Image from [111]. **d).** A catalytic microjet which is propelled by a source of bubbles generated and travelling through the body of the tube. Image from [112]. **e).** The mechanics propelling the microjet: (1) a bubble is formed inside the conical body; (2) this expands to fill the available height; (3) force imbalance moves the bubble down the tube, expanding as it moves, and an equal force is exterted on the tube to move it through the medium ; (4) the bubble exits and the microjet will cease to move whilst there is not a bubble moving through the body.

### 3.3.4 Gliding

Gliding motility, in contrast to the above propulsion methods, is one that does not necessary require any dedicated propulsion apparatus such as flagella. In general,

it is defined as being the smooth translocation of cells over a surface by an active process that requires the expenditure of energy [118]. In general, it follows the long axis of the cell body which tends to produce cell colonies that have long/thin spreading fronts (Fig 3.3c). This smooth motion is similar to but not the same as twitching motility[3], where cells use pili (a hair-like appendage associated with bacterial adhesion [122]) like grappling hooks to pull themselves across a moist surface. There currently is not an agreed upon mechanism responsible for gliding motility as this may change between species, but is a subject of much debate due to linking gliding motility with biofilm formation and development.

### 3.3.5 Catalytic jet engines

The final stop on this whirlwind tour of motility methods is quite an unconventional one. When the term "jet engine" is used the immediate thought is of aviation, but advances in technology in the last decade or so have brought this term to the world of microswimmers. These micromachines are able to self-propel by converting chemical fuel to kinetic energy using a catalyst. Named microjets, these "swimmers" consist of a rolled-up microtube with the inner surface coated in a catalyst [27, 123]. Catalysing hydrogen peroxide to decompose it into (gaseous) oxygen and water inside the tube produces a bubble that expands and fills the available height. A force imbalance then pushes this along the tube (towards the wider opening), which in turn exerts a force on the microtube, propelling it through the medium (Fig 3.3de). The result is a "swimmer" that can propel itself up to $2\,\mathrm{mm.s^{-1}}$ (50 body lengths per second!) that leaves a trail of bubbles in its wake. The trajectories can be controlled by introducing a layer of iron and tuning an external magnetic field, but it is hoped that that this microjet technology could lead to advancements in drug delivery as well improving our knowledge of the mechanistic workings of catalytic micromachines.

## 3.4 Swimming and Directed Motion

Moving the emphasis away from the propulsion methods of microswimmers to what advantages microswimmers would get from being motile - there is clearly some evolutionary pressure for organisms to swim otherwise swimming organisms would be a lot scarcer. Here we will be considering force-free swimmers as previously discussed in Chapter 2, with the emphasis on flagellated swimmers. These can be

[3]This terminology was first described in 1961 by Lautrop [119] to describe the surface motility of *Acinetobacter calcoaceticus*, a bacterial species which is part of the human intestinal flora [120, 121]

broadly subdivided into two classes: cells who swim continuously (or for extended periods of time) and cells whose trajectories resemble a random walk. We start with the later and where better to start than the seminal work of Howard Berg and his studies of the bacterium *Escherichia coli*.

### 3.4.1 Run-tumble motion

*E. coli* is perhaps one of the most well-known microorganisms on the planet, often associated with food poisoning and urinal tract infections ($75-95\%$, [127, 128]). Typically found in the intestines, it is simple and inexpensive to cultivate harmless strains of this organism in a laboratory setting which has helped *E. coli* become the most widely studied prokaryotic organism for a variety of systems/phenomena.

An electron micrograph of the cell is shown in Fig 3.4a: a typically 2 micron rod-shaped cell, propelled by a bundle of multiple prokaryotic flagella dispersed randomly over the surface of the cell. In 1972 Howard Berg and Douglas Brown [125] published the first description of the motility of this organism which they describe as *"...an alternating sequence of intervals during which changes in direction ar gradual or abrupt..."*. An example of one the trajectories they analysed is shown in Fig 3.4b, where the two phases are highlighted. This style of motion has been called "run-and-tumble", where periods of ballistic-style swimming (runs) are interspersed with a period of diffusion (tumbles)[4] in which the cell reorientates some angle $\theta$ (see Fig 3.4 for a sketch of this style of motion). If these reorientations were truly random then on average $\theta = 90^\circ$, but in this work they observe a skewness towards small angles. They were able to show that the two phases of the cycle follow Poisson distributions - the probability of end of a run and the probability of the end of a tumble (per unit time) are constant.

Later studies of the flagellum dynamics of *E. coli* unveiled the mechanisms responsible for this behaviour [129] (Fig 3.4d). During a run, the flagella dispersed over the cell body all rotate counter-clockwise (CCW), causing the flagella to bundle together to form a single helical bundle which propels the cell. During a tumble, one or more of these flagella begin to rotate clockwise (CW), causing an unbundling of the flagella bundle and a change in the handedness of the flagellum [37]. Whilst this is ongoing the cell undergoes a reorientation caused by a combination of the active motion of the flagella and the passive rotational diffusion the cell will be subject to at this length scale. After a short period of time the flagella bundle reforms and the cell swims off in the direction of its new orientation.

[4] As a side note, in this paper they call the tumbles "twiddles", sadly this name did not catch on as well as tumble.

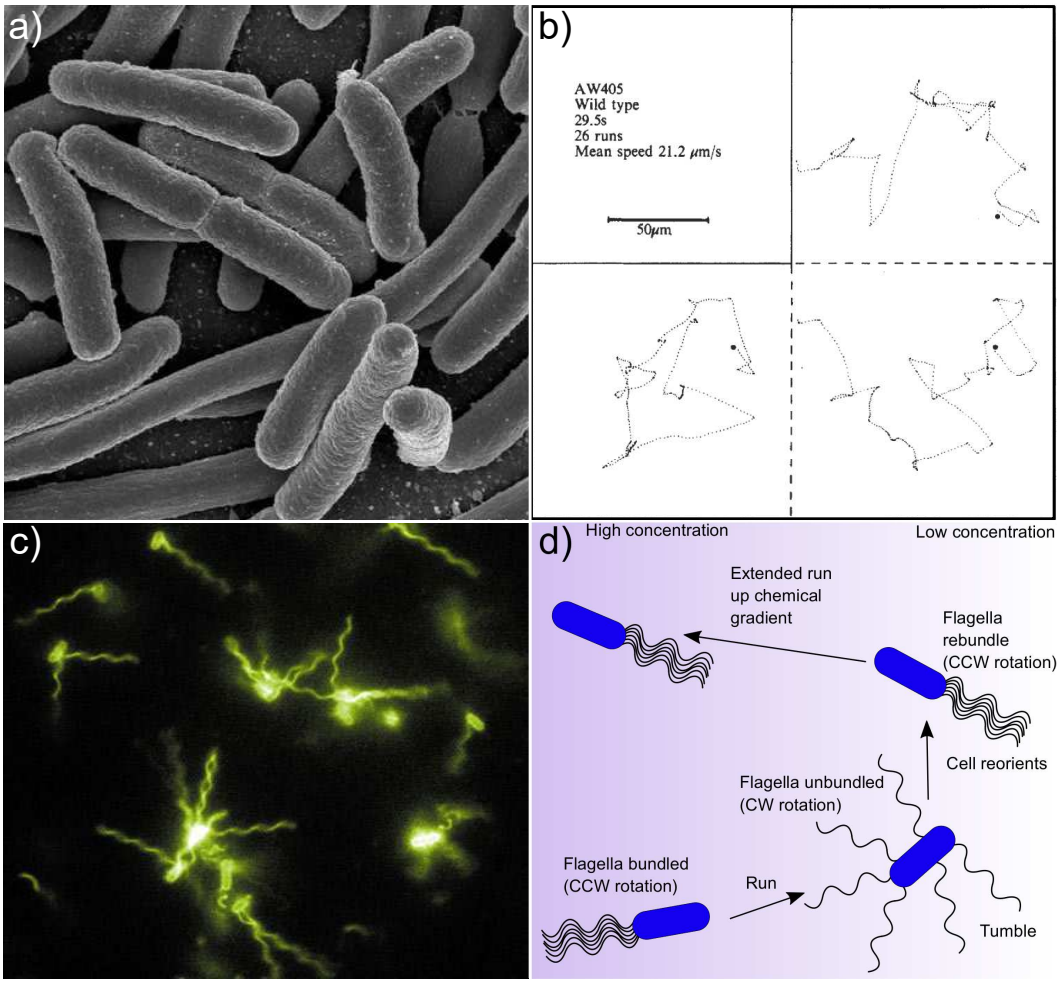


Figure 3.4: **Run-tumble motion of the model bacterium *Escherichia coli*. a).** An electron micrograph of the rod-shaped *E. coli* [124]. Credit Wikipedia Commons. **b).** Examples of the original run-tumble trajectories analysed by Howard Berg in his original work involving the chemotaxis of *E. coli* [125]. **c).** Stained *E. coli* examined in a fluorescent microscope to highlight the behaviour of the flagella in motile cells [126], clearly showing examples of the flagella bundled and unbundled for the different motility phases. **d).** Sketch describing the run-tumble motility of *E. coli* and the flagella behaviour during this. In the presence of a chemoattractant the run lengths are extended to produce a biased random walk up the chemical gradient.

### 3.4.2 Chemotaxis

The original purpose of investigating the motility dynamics of *E. coli* was in effort to better understand how the organism moves along chemical gradients. Regulating motility to respond to a chemical signal is a process known as chemotaxis, which has

been intensely studied since its first description in 1884 by Pfeffer when investigating bracken fern spermatozoa (followed by Leber in 1888 and studies of mammalian leukocytes responding to a focus of injury [130]). This specific form of "taxis" (directed motion) is an important mechanism for a variety of biological processes such as immune reactions and the feeding of marine microorganisms. One of the model organisms for chemotactic studies is *E. coli*, which will extend its run length along chemical gradients to produce a biased random walk which introduces an effective net drift in the trajectory [131].

*E. coli* using a temporal sensing mechanism to make comparisons of the chemical environment it is swimming through. If the conditions deteriorate a tumble will be triggered, whereas if the conditions become more favourable the cell will typically extend its run length. In order to do carry out this style of sensing mechanism the cell needs to be capable of measuring its current environment and remembering what the conditions were like in its previous position. Many studies have been devoted to this understanding this process and its limitations (e.g. chemical sensitivity) though, at the molecular level, there is still work to be done to understand features such as the dynamics between receptor complexes for which *E. coli* remains a model organism due to its relatively simple sensory network.

### 3.4.3 Run-reverse motion

An interesting question arises when expanding the scope of chemotaxis - can uniflagellated swimmers perform chemotaxis, and if so how? Since the organism cannot unbundle its flagellum, the reorientation method of the cell will be significantly different to that of *E. coli* where the tumbles are initiated by reversing the direction of rotation of one or more flagella. Hydrodynamically speaking an uniflagellated swimmer was to reverse the direction of rotation of its flagellum, the cell would only be able to reverse its direction (aside from thermal reorientation). So called "run-reverse" motion is the most common form of motion in marine isolates, being exhibted by over 70% of the population [134, 135]. An example of such an organism is the marine bacteria *Vibrio alginolyticus* (Fig 3.5a), known to cause wound infections in humans [136]. This organism undergoes a run-tumble style of motion but with some key differences to the classical behaviour of *E. coli*. In bulk conditions the motility pattern is formed of a three-step cyclical process, sketched in Fig 3.5b. The cell swims forward, then reverses the motor in order to carry out an 180° reorientation (a "reversal"). This change from forward to backward swimming is extremely fast, taking typically less than 1/30 s. However the next transition (backwards to forwards) can be up to three times longer. During this longer changeover,

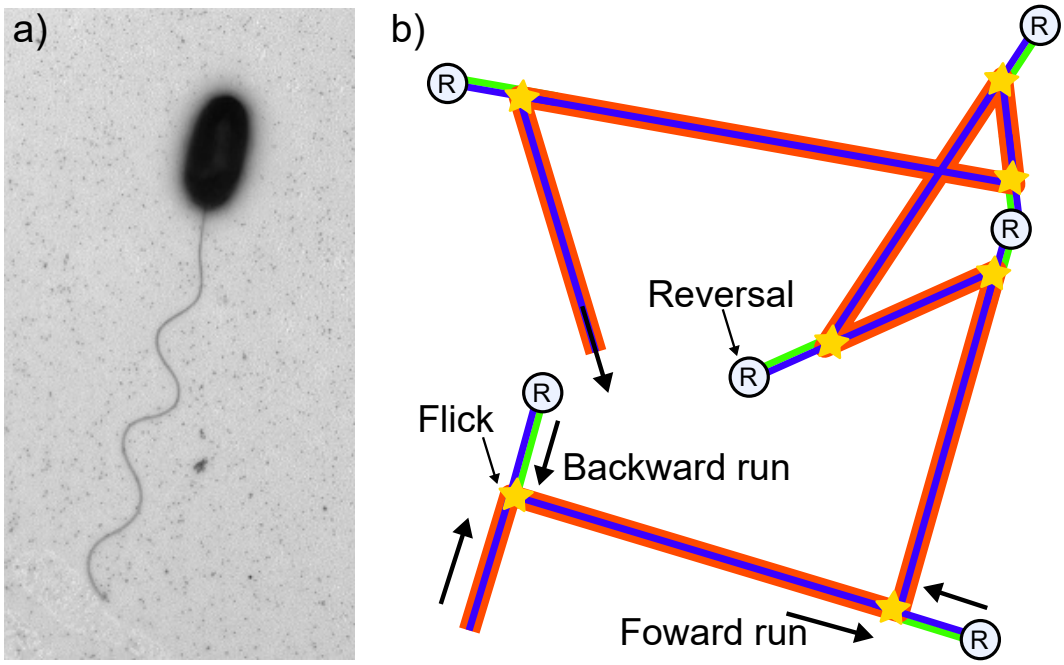


Figure 3.5: **Run-reverse-flick motion of *Vibrio alginolyticus*. a).** A TEM image of *Vibrio alginolyticus*, clearly showing the single polar flagellum extending out of the cell. Image from [132], credit: Kwangmin Son, Jeffery S Guasto and Roman Stocker, Stocker Lab, CEE, MIT. **b).** Sketched trajectory, adapted from [133]. The cell swims forward (blue), reverses (green) then flicks the flagellum to introduce a sharp reorientation into the trajectory.

the flagellum forms a small kink which results in the body and flagellum no longer being coaxial. Amplification of this by rotation of the flagellum results in a fast and efficient mean reorientation of $90°$ in less than a tenth of a second whilst the body only translates less than half a body length. After this "flick" the flagellum realigns with the cell body and the cell begins to swim forward in this new orientation.

This three-step process forms a hybrid motility pattern [133] which is a combination of a run-reverse pattern and random tumble caused by the flick. Whilst this is a costly method of exploring an environment [133], *V. alginolyticus* is in fact three times more efficient at chemotaxis than *E. coli*. Modelling of variations of run-tumble motion around a nutrient patch in shear conditions [137] show that run-reverse styles of motion are orders of magnitude more efficient for maintaining the cell in the local nutrient patch than conventional run-tumble motion. Interestingly they show that some noise in the rotational diffusion of the cell actually improves the residence time in the nutrient patch for certain flows, which could motivate why many organisms such as *V. alginolyticus* have developed flicks/variants

of run-reverse motion to improve their hunt for microscale nutrient patches.

### 3.4.4 From chemical stimulus to light stimulus - phototaxis

There are a plethora of other forms of directed motion, such as responses to: gravity (gravitaxis), temperature (thermotaxis), magnetic fields (magnetotaxis), viscosity gradients (viscotaxis) electric field (electrotaxis), and mechanical stimuli (mechanotaxis). The taxis that this thesis will focus on however is directed motion in response to an external light stimulus: phototaxis. This relies on organism being able to a) detect the direction of the external light source and b) adjust its motility to respond to this stimulus. Phototactic responses can be split into two broad categories: positive and negative responses - motion towards/away from the light stimulus respectively. This directed motion was first reported for photosynthetic prokaryotes in 1883 [138] although it is believed that eukaryotes first evolved the ability to track a light source in three-dimensions in water [139].

In contrast with chemotaxis, phototaxis is a woefully understudied response given its obvious ecological implications. For example, a photosynthetic organism could use phototaxis to gain a significant fitness advantage by manipulating its motility to remain in optimal light conditions for longer periods of time. Historically, phototactic "studies" were limited to describing how the cell motility changed in response to different illumination conditions. In the past few decades this has begun to change, in particular in the last 10 years where interest in phototaxis has spiked. Phototaxis has been reported in a number of flagellates such as *Euglena gracilus* and *Volvox*, but there is one organism that has risen above to be the model system for phototactic studies: the green alga *Chlamydomonas reinhardtii*.

## 3.5 *Chlamydomonas reinhardtii:* the model organism

*Chlamydomonas reinhardtii* is an unicellular bi-flagellated photosynthetic green algae, first described by Dangeard in 1888 [143], that has firmly established itself as a model organism for an extremely wide range of systems. These include cell structure, flagellum dynamics, photosynthesis and phototaxis. As a result of *C. reinhardtii* establishing itself as a model organism: its complete genome has been sequenced [144], many mutant strains have been isolated/characterised and are easily available from algal collections, cell cultures can be easily synchronised in a diurnal chamber and the organism is extremely simple to grow in laboratory conditions [145]. *C. reinhardtii* has been incredibly well-documented, including a detailed three volume review entitled *The Chlamydomonas Sourcebook* [146].

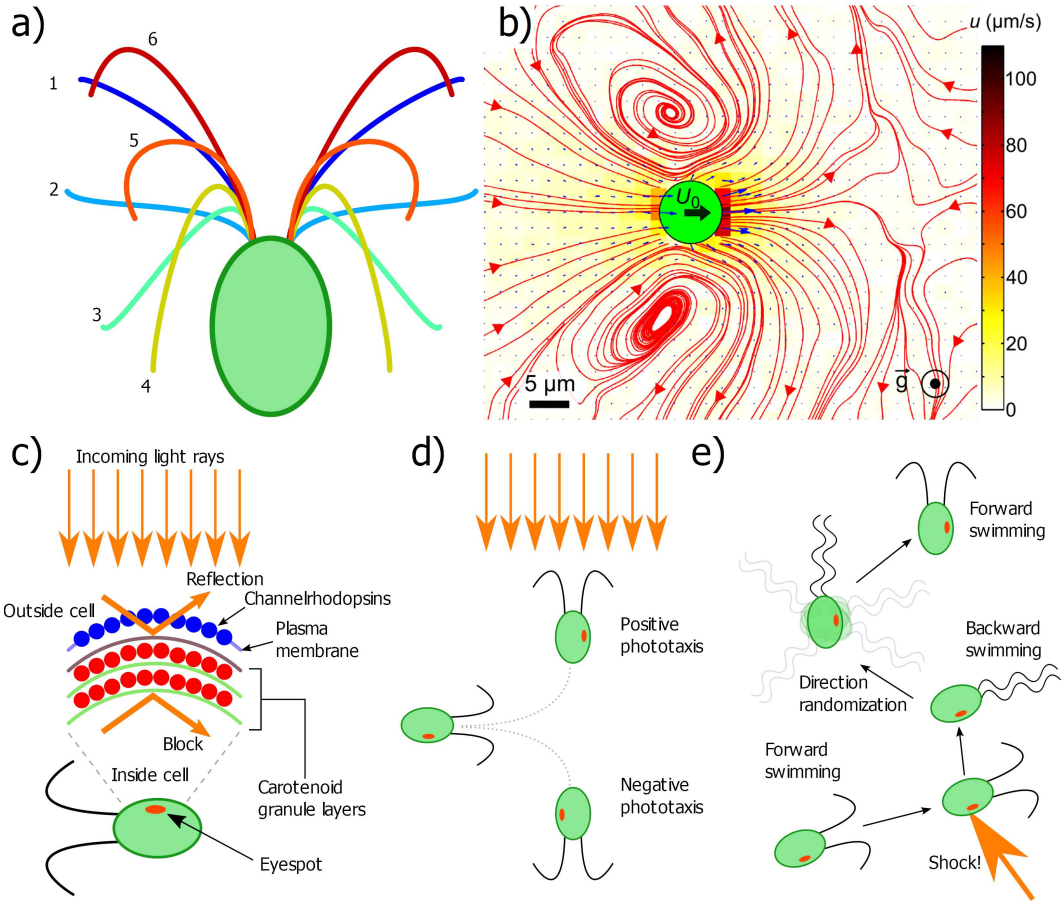


Figure 3.6: **Motility and photoresponses of the model eukaryote *Chlamydomonas reinhardtii*. a).** Flagella beat pattern of *C. reinhardtii* resembles a ciliated beat pattern - a power stroke followed by a recovery stroke back to original flagella position, producing a breaststrokes swimming behaviour. **b).** Experimental flow field produced by *C. reinhardtii* [140] **c).** The structure of the eyespot, highlighting how the carotenoid layers shield the channelrhodopsin photoreceptors from light transmitting through the cell (Adapted from [141]). **d).** Positive and negative phototaxis, where the cell steers towards/away from the light respectively. **e).** A photoshock response of *C. reinhardtii*, where the cell stops motion, swims backwards, reorientates and swims off in a new direction after a sudden step-up in light intensity (Adapted from [142]).

### 3.5.1 Cell description and motility

The basic cell structure of *C. reinhardtii* is shown in Fig 3.1, a 10 $\mu$m standard eukaryotic cell. A single chloroplast is located near the basal portion of the cell, with a single pyrenoid near the rear of the cell which provides the carbon dioxide rich environment required for photosynthesis. On the equator of the cell there is a

single orange-coloured eyespot which the cell uses to undertake phototaxis. Fig 3.6c sketches the structure of the eyespot which has two main components: a high-density region of channelrhodopsin and the stigma. Channelrhodopsin are light-gated ion channel proteins which are sensitive to the $450 - 700\,\text{nm}$ spectral range [145]. In nature, channelrhodopsins act to couple incoming light to the flagellar motion in order to keep the organism in optimal light conditions [147]. These photoreceptor proteins are layered on top of the stigma: an area of the chloroplast which is comprised of stacks of carotenoid-rich granules. These reddish pigments act as a dielectric mirror reflect the longer wavelengths away from the outside of the cell whilst simultaneously blocking light travelling through the back of the cell (which would be a problem due to the transparency of the cell) [147, 148]. This is currently estimated to improve the light signal to the cell by approximately a factor of 80 [149].

*C. reinhardtii* swims with two flagella at the front the cell body as a puller swimmer which are named as the cis- and trans-flagella for the flagella closest/furthest from the eyespot respectively. High-speed flash photography revealed that the flagella beat in a similar fashion to cilia [150] with the beat separated into two strokes: a power stroke and a recovery stroke. Fig 3.6a outlines this pattern: during the power phase (steps 1-4) the flagella remain relatively straight, bending at the base as the travel towards the cell body. In the recovery stroke (steps 4-6) a bending wave propagates along the flagellum, producing the non-reciprocal motion necessitated by the scallops theorem. Tracking of the eyespot reveals that the cell body rotates counterclockwise during swimming and traces out a helical trajectory due an asynchrony in the flagella beat patterns [151]. The asynchronous beating pattern also introduces stochastically distributed sharp turns (under dark conditions) into the cell trajectory which produces an eukaryotic version of run-tumble behaviour [152]. On average *C. reinhardtii* swims at around $100\,\mu\text{m.s}^{-1}$ and rotates‘ with a frequency on the order of $2\,\text{Hz}$. The hydrodynamic flow fields of *C. reinhardtii* have also been studied (Fig 3.6b) [140], showing that it is equivalent to a three-Stokeslet model with force magnitudes of $F/2$ and $F$ for each flagellum/cell body respectively.

### 3.5.2 Phototaxis of *Chlamydomonas reinhardtii*

The eyespot of *C. reinhardtii* provides the cell with a direct tool for measuring the direction of an external light stimulus. As the cell swims and rotates the eyespot will act as a “reverse-lighthouse” - instead of sending out beams of light from a spinning source the cell will “see” a uniform source as distinct flashes as the eyespot aligns then rotates past the light axis. The two principle photoresponses of *C. reinhardtii* are summarised in Fig 3.6de: phototaxis and photoshock. At moderate

light intensities the organism will, in general, swim towards a light source (positive phototaxis). At higher intensities the cell will swim away from the light (negative phototaxis), which can be thought of a rudimentary means of photoprotection to defend the cell from potentially harmful light intensities [153]. The sign of phototaxis in *C. reinhardtii* has been linked to many different variables, from the age of the culture [154], the light-shielding properties of the carotenoid layer in the eyespot [141] and the photosynthetic activity of the cell [155]. Phototaxis can be used to accumulate the cells into high density regions [155] (photoaccumulation) and has even been used in place of centrifugation to improve cell densities in experiments. Accumulation here is defined as the directed motion of cells which acts to increase the cell population around an external stimulus - for example a light patch in the case of photoaccumulation. A similar effect can be achieved by the second class of photoresponse: a photoshock (or photophobic stop response). These responses are triggered by a sudden and large change in light intensity, during which the cell will: stop moving, reverse for a short time then attempt to swim off in a new direction. The reversal is achieved by moving the flagella to the front of the cell and introducing a different beating wave down the flagella, as shown in Fig 3.6e. It should be noted that this can be thought of as a form of accumulation but to be more precise: the photoshock will increase the residence time of the cell in the area affected by the stimulus (or even causing the cell to become stuck in the affected area), thus appearing to actively increase the cell population in the affected vicinity, which is subtly different to the "classical" photoaccumulation to a light source.

The transmission of the signal from the eyespot to the flagella motor apparatus is a complicated one but in essence the photoresponses are mediated by the flux of calcium ions ($Ca^{2+}$) in the cell. For both responses (taxis and shock) [156] incoming light activates the channelrhodopsins in the eyespot which in turn triggers a flux of $Ca^{2+}$ into the cell body. This causes a depolarisation across the cell which, if strong enough, floods the flagellum with $Ca^{2+}$ that is then detected and produces the changes in the flagellar waveform responsible for photoshock. If this depolarisation is not sufficient to produce the photoshock response it instead introduces fluctuations in the interflagellar $Ca^{2+}$ which when detected lead to brief changes in the flagella to produce the phototactic steering.

*C. reinhardtii* has a impressive wealth of studies focused on it spanning all manner of topics from molecular cell biological to biophysical phenomena. This contrasts heavily with another phototactic eukaryote which will be the main experimental focus of this thesis: *Micromonas pusilla.*

## 3.6 *Micromonas pusilla*: the dominant marine pico-eukaryote

*Micromonas pusilla* is today recognised as the most dominant marine organisms [157], and currently one of the smallest known eukaryotic organism on Earth. In fact, due to its size it can be described as a pico-eukaryote: planktonic eukaryotes which are less than 3 microns in size. This organism has an interesting history of being studied for a wide range of topics such as virus dynamics, evolution of green algal cells and its photosynthetic machinery. Despite this it is a surprisingly under-researched organism, indeed from the very beginning this has been a complex organism which has a nasty habit of throwing a spanner in the works - starting with its initial genus classification.

### 3.6.1 Discovery

The story begins in 1952[5] with R.W.Butcher who undertook a study of classifying pico/nano-scale planktonic organisms [159]. One of the organisms classified in this study was a $1 - 1.5\,\mu$m diameter, uniflagellated brownish cell. It appeared to be presented in a wide body of samples from multiple locations around the UK (Conway, Cornwall and Essex), but it was difficult to assign a taxonomic position to the organism. Under light microscopy, the simple nature of the cell combined with the green/brownish colour in suspension and the variety in shape suggested that it fell under the *Chromulina* genus, and so the species was named *Chromulina pusilla*. This species stood out as being one of the smallest known algal cells and its presence in many different marine environments [160] bookmarked it for further study. Later that decade further observations by Irene Manton and M. Parke made it clear that this organism could not be classified into the *Chromulina* genus and formed a new genus called *Micromonas*, with *Micromonas pusilla* being the type species with aim of safeguarding *M. pusilla* from any future name change if the genus required any subdivision in the future.

### 3.6.2 Morphology and structure

Later that decade Manton decided to investigate the structure of this organism under an electron microscope, a standard established procedure with ciliated plant cells. Fig 3.7 shows the general morphology of the organism - a pear/comma shaped body that is a similar size to the bacteria in the sample (Fig 3.7a). The flagellum

[5]There is actually an earlier reference from 1951 (Knight-Jones) who introduce the organism but they do in fact reference Butcher's paper which was in press at the time.

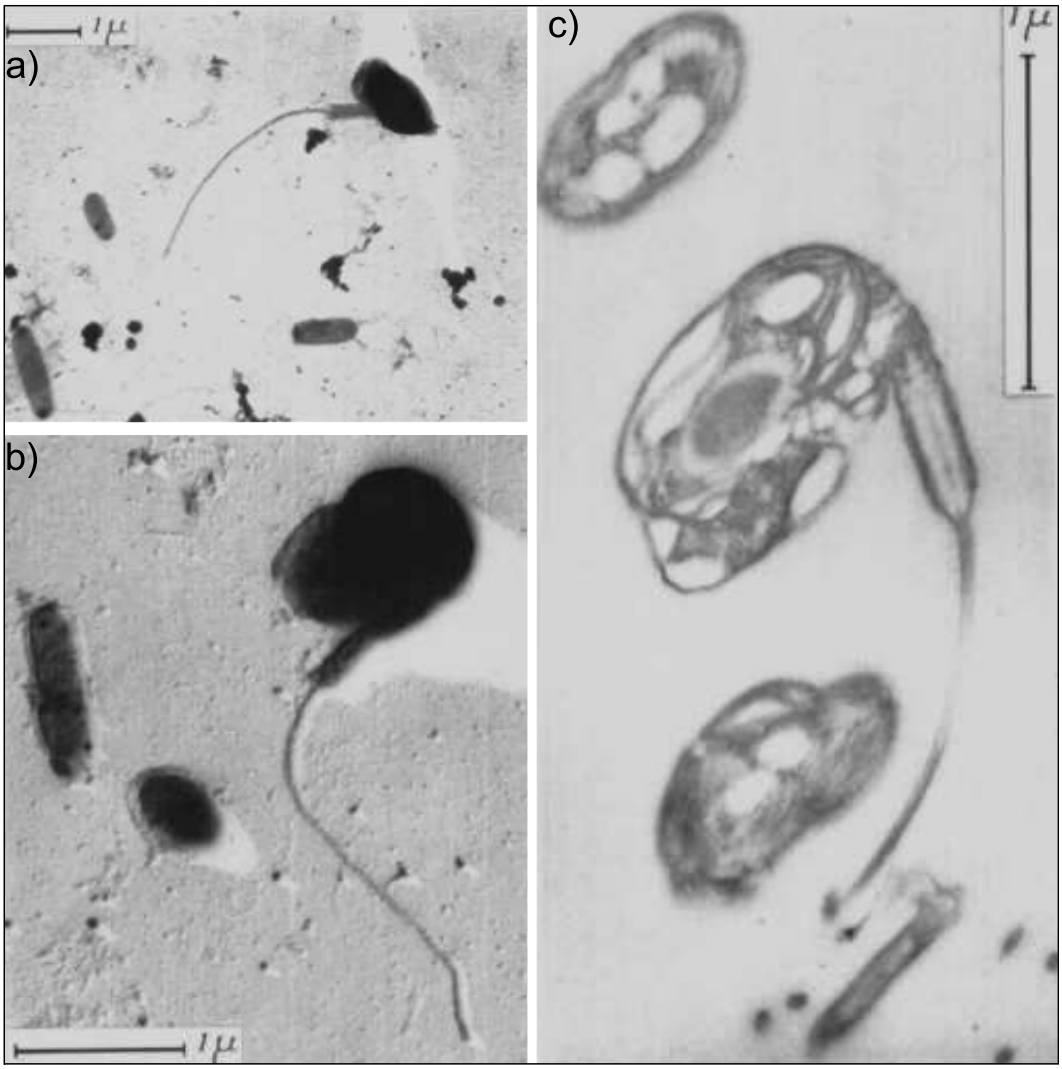


Figure 3.7: **First reported images of *M. pusilla* (then *Chromulina pusilla*)** [158]. **a).** Shadow-cast whole mount of the flagellate, prepared in 1953 and re-examined in 1957 with a Philips microscope, showing one cell of the organism and one bacterium. Direct descendent from the type culture of Butcher 1952 and original isolated from the Conway esturay by Knight-Jones. **b).** A cell and bacteria from a culture, isolated from the English Channel. **c).** A section through a cell showing the two parts of the flagellum and internal cell contents which include the plastid and pyrenoid with a part of the nucleus.

protrudes from the side of the cell body, with a short wide section less than a micron in length (the basal section) with a slender extension (called the distal portion) another $2-3$ microns in addition. These lengths are variable but in general the first wider section is always significantly shorter than the slender extension that

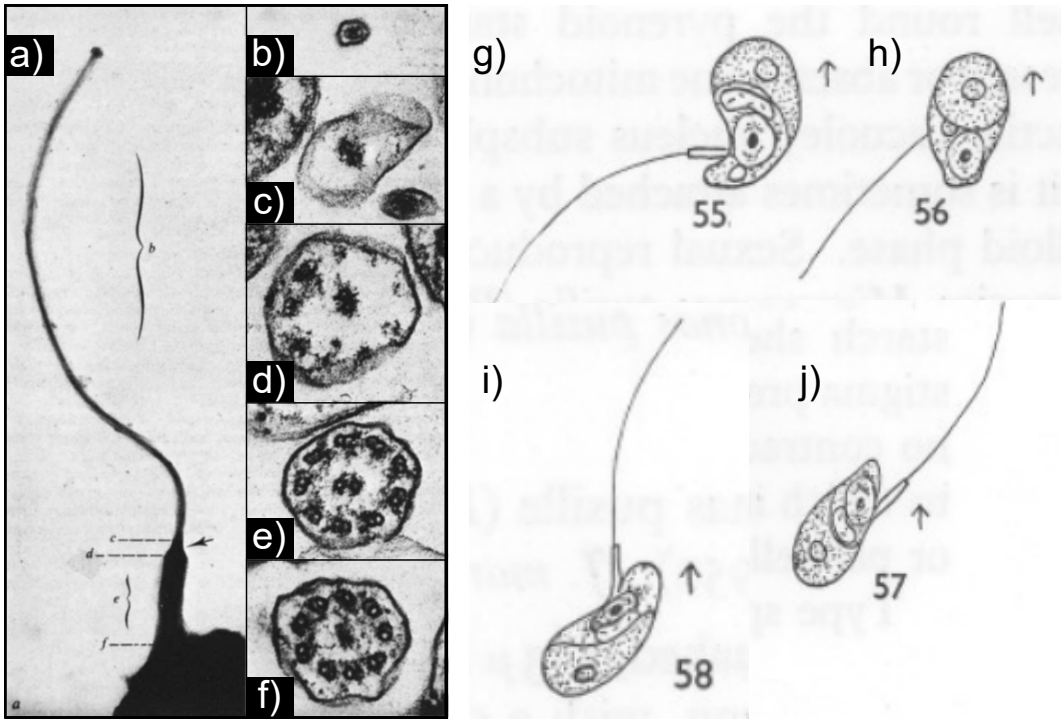


Figure 3.8: **The flagellum of *M. pusilla* (originally *C. pusilla*)** [161, 162] **a).** Elctron micrograph of a negatively stained *M. pusilla*. The distal protion of the flagellum beyond the arrow is about 70 nm in diameter and is too thin to contain the usual '9 + 2' axoneme. The dotted lines and brackets labelled b-f indicate the approximate levels of the corresponding cross-sections. **b).** Cross-section through distal portion of the flagellum where on the central tubules remain. Note that the membrane closely surrounds the two trubules, which seem to be closer to each other than in the usual 9 + 2 structure. **c).** Cross-section through the flagellum just distal to the point where the peripheral tubules have terminated. **e).** Cross-section through the proximal portion of the flagellum, showing the typical '9 + 2' axoneme. **f).** Cross-section at the base of the flagellum, showing the axosome just promximal to the origin of the central tubules. **g-h).** [161] (55-56). Individuals with the flagellum and body in position characteristic for the species during rapid swimming. **i-j).** Individuals swimming slowly with flagellum directed forwards.

completes the flagellum. This width difference is more prominent in Fig 3.7bc.

### The flagellum

The flagellum is the first feature of interest here - at first it is not clear if it follows the typical 9 + 2 structure of standard eukaryotic flagella, but closer examination of a cut-through of the flagellum confirmed that in the first section of the flagellum it does indeed contain the standard structure, with the central pair extending past

this to form the distal portion of the flagellum. This was studied in more detail 20 years later by Omoto et. al [162], who realised that this extension allowed for direct observation of the central pair behaviour. Fig 3.8 shows an electron micrograph of the flagellum of *M. pusilla* and its internal structure. Here they show clearly how the $9 + 2$ structure stops in the shorter stub and how the flagellum extends the central pair (or $0 + 2$ structure to be specific). This flagellum can be viewed under dark-field microscopy, where it becomes apparent that the distal portion takes on a left-handed helical structure. In free-swimming cells the basal section seems to beat back-and-forth, but also the distal section rotates its helical structure to propel the cell [163]. The last point to note about this flagellum is that interestingly enough the cell is able to orientate it either in front of the cell or behind the cell, meaning the organism can swim as both a puller and pusher-type swimmer [161] shown in Fig 3.8g-h.

### The plastid

The plastid is the largest organ in the cell, the most conspicuous component of which is the pyrenoid which is large enough to dominate almost every cross-sectional view of the cell body. In this case we avoid going into detail about this region of the cell apart from to note that it provided the first two clues as to an incorrect original classification - the arrangement of lamella (a thin layer or membrane) and the fine structure of the single mitochondrion.

### Morphological implications on the classification

*M. pusilla* provides a very interesting insight to the developmental structure of plant cells. Firstly, it contains the bare minimum of each necessary component to point that it would be almost impossible to further reduce the cell size/layout without significantly altering the structure of the organelles themselves. Even the flagellum, despite its disproportionate ratio between the basal and distal section sizes, is not meaningfully different from the standard eukaryotic structures once the size differences between organisms is taken into account. Pigment analysis [6] showed that there was no trace of chlorophyll *b*, which was the final proof that the species needed to be removed from the genus *Chromulina* and class Chrysophyceae, and reclassed as a Prasinophyceae.

[6] this was in the form of a personal communication between Parke (Plymouth) and Kennedy (Sheffield)

### 3.6.3 Motility

Since 1951 there has been a multitude of work involving *M. pusilla* apart from the motility/navigation strategies of *M. pusilla*. Excluding the small body of work on the flagellum, description of the cell motility are limited to brief passages in various papers such as the initial observations of Knight-Jones [160] where they report swimming speeds of up to 50 body lengths per second ( $100\,\mu\mathrm{ms}^{-1}$). Actual measurements of the swimming velocities/motility patterns are extremely limited - it comes down to effectively to a handful studies [160, 164, 165]. To date the most "complete" description of the motility of *M. pusilla* remains the original work of Manton and Parke [161]. They describe how the cell predominately travels as a pusher-type swimmer, with the flagellum perpendicular to the body before bending behind the cell body (Fig 3.8gh). When the cell is orientated as a puller, the speed is lower and this is a less frequent mode of propulsion. They also pick up on the "dithering" behaviour of the cell - the organism tends to spend a large amount of time stationary before swimming rapidly. They claim the population can be divided into a motile and non-motile phase where the non-motile cells are larger than the motile phase. Outside of these brief descriptions however the underlying motility of the organism remains unclear.

#### Directed Motion

If the underlying swimming behaviour of *M. pusilla* is poorly understood, then understanding directed motion and taxis behaviour i.e. chemotaxis, phototaxis etc. of this organism is order of magnititudes worse. Claims of *M. pusilla*'s phototactic behaviour appear to stem from a statement from the original work of Manton and Parke where they state: *"The species is strongly phototactic and is not toxic to fish (tested by Mrs B. Hepper)'.* Grateful as we are to Mrs Hepper for clarifying the species lack of toxicity, there is a distinct lack of empirical evidence supporting the phototaxis in the organism.

Comparatively, chemotaxis of *M. pusilla* has a goldmine of literature to refer to - a single paper by Seymour [166] where they investigate the chemotaxis of multiple species to dimethlysulfoniopropionate (DMSP), (Fig 3.9). DMSP is a phytoplankton produced solute which can constitute up to 10% of total cell carbon contents [167]. Released during certain events, such as cell lysis, these sources act as a source of carbon and sulphur which have been linked to grazing-deterrence in phyotplankton [168] as well as (via a transformation) a foraging cue for a range of higher organisms such as birds, penguins and seals [169]. In this paper they use a

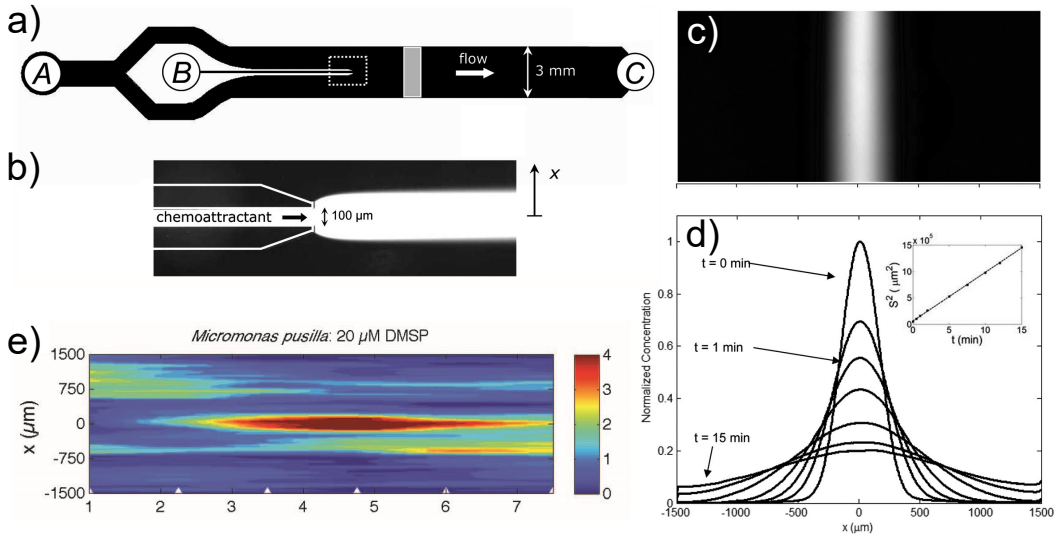


Figure 3.9: **Chemotaxis of *Micromonas pusilla*. a).** Schematic of the microinjector developed by Seymour et al [81]. Cells suspended in media are injected at A, and the chemical stimulus at B. Inlet B leads to a 100 $\mu$m wide tip (b), and by controlling the ratio of the flow rates the width of the diffusive plume can be controlled. **c).** The diffusive plume, imaged using fluorescent microscope and a fluorescent dye at inlet B. **c).** Once the flow is switched off, the plume will diffuse laterally over time as shown in (d). **e).** The accumulation of *M. pusilla* over time to a central plume of DMSP, with normalized cell concentration denoted by the colour [166].

microfluidic device which they developed and tested extensively a couple of years prior to this study [81], shown in Fig 3.9a. This device allows for the fast and relatively straightforward creation of controllable chemical gradients based on the ratio of of the flow rates at inlets A and B. The device forms a diffusive plume along the length of the device which, when the flow is switched off, will diffuse perpendicularly to the direction of flow (Fig 3.9d). In this paper they show there is a clear and fast chemotactic response of *M. pusilla* to DMSP (Fig 3.9e) where the cells collect in the middle of the channel where the DMSP concentration is at its highest.

### 3.6.4 Diversity

To this point perhaps a biased picture has been painted of *M. pusilla* - the lack of motility studies do not mean that this organism has been ignored by the scientific community. It is widely considered to be the most dominant species in a wide range of marine and coastal environments such as; the Arctic [170–172], North Pacific Ocean [173], Barents Sea [174], Mediterranean Sea [175], the English Channel [157] and coastal waters off of Brazil [176] to name but a few. The largest collective

body of work with *M. pusilla* involves the study of host-virus systems, for which *M. pusilla* has established itself as a model organism.

### 3.6.5 Host-virus dynamics

#### Discovery of the *Micromonas pusilla* virus (MPV)

In 1979 Mayer kick-started this field of study by reporting the presence of a lytic virus infecting *M. pusilla* [177] [7]. At this point in time not much was known about *Micromonas pusilla* - the main studies available by this point were previously mentioned works of Manton and Parke, Butcher and Throndsen [158, 159, 161, 164]. Consequently all that was known about the cell prior to this was the fact it was an extremely small photosynthetic microorganism, present in large numbers in both marine and coastal environments, and that cell did not have a cell wall - known as a "naked cell". The virus was tested across 35 species from 5 different classes, but only induced lysis in *M. pusilla*, hence was given the name of "*Micromonas pusilla* virus" (MPV).

This discovery had several major implications. It was the first reported case of viral destruction of a marine phytoplankton, and secondly the entry method of the virus into the cell was unlike anything else reported at the time. Other algal viruses required penetration of the cell wall in order to infect a cell, but the naked nature of the cell means that this is not possible with *M. pusilla*. At the time of this study the virus's presence was only confirmed in natural seawater from Washington state and British Columbia [178] but it was clear that this was a dynamical system that required much more detailed study. Since this time there have been numerous studies isolating a variety of virus infecting and lysing with *M. pusilla*, highlighting how this organism has become a model organism for this dynamical system.

Three years later after the work of Mayer, Waters and Chan [179] took up the mantle of this work, identifying many key physiological events during the host-virus cycle. By using a light-dependent drop in chlorophyll *a* fluorescence in infected host cells as a metric they were able to characterize the total virus growth cycle, determining a 14 hr total lytic cycle. More interesting however was how mutants of *M. pusilla* would develop resistance to one strain of the virus only to become susceptible to a different strain. Certain virus-resistant strains could not be kept alive which suggests a lethal mutation in the virus, but the fact that all of the strains of *M. pusilla* host cells were susceptible to lysis from a strain of MPV suggests a

[7] This is perhaps not strictly true - in 1976 Pienaar reported the presence of virus-like particles in three species of phytoplankton, but did not confirm their virus nature at the time [178]

specific virus reproductive cycle (specifically lytic compared to lysogenic).

### Impacts on the oceanic carbon cycling

Since this original work there have been several detailed studies into the dynamics of this host-virus system and its ecological implications. Cottrell and Suttle [180, 181] showed that the virus infection rates had a dependent on the illumination conditions of the host cells, as well showing a equivalence between the virus production rates and the growth rate of *M. pusilla*. This suggests a balanced and stable coexistence between host and virus explaining perhaps how *M. pusilla* has remained a dominant organism despite having an apparently specific virus targeting the species and its mutations. More importantly however is the ecological implication of this work: lysis of phytoplankton is a prominent source of nutrients, such as dissolved organic carbon (DOC) (also known as dissolved organic matter (DOM)), in marine systems as studied by Lonborg et al in 2013 [182]. DOC is defined as the fraction of total carbon that can pass through a (typically) $0.22 - 0.7\,\mu$m filter, and accounts for roughly 20% of all organic carbon [183]. It acts as a food source for microorganisms and so forms an important part of the microbial food web in marine environments. Viral lysis acts to release cell content in a regenerative manner to the foodweb, theoretically moving $10^9$ tonnes of organic carbon *per day* from host cell biomass into DOM. Lonborg et al [182] used *M. pusilla* and MPV to investigate viral lysis could impact DOC in marine environments, choosing *M. pusilla* due to its ecological relevance and global prominence. One of the main sources of DOC is extracellular release from photosynthesis but in this study they show that the increases in DOC due to viral lysis are significantly faster ($2.5\times$) and larger ($4.5\times$) compared with photosynthesis extracellular release. Viral lysis also produces trace metals and other organic nutrients which are important for supporting microorganism populations, and as such forms a crucial part of the recycling of nutrients in oceanic environments.

### Phytochromes and photosynthesis

Whilst both algae and plants use photosynthesis as a fuel source there are fundamental differences in their methods, primarily due to how different wavelengths of light will attenuate in water. Land plants use a phytochrome photoreceptor which are activated by red/far-red light. The phytochrome is also responsible for a range of regulatory processes in land plants such as seed germination and dispersal. Whilst absent in many other green algae, it was found that *M. pusilla* also contains a phytochrome [184]. This is surprising since red light is rapidly attenuated with water

depth and so it would not be expected that *M. pusilla* has the need for a phytochrome. However it was shown that in this case the *Micromonas* phytochrome has a strong blue-shift, allowing for the detection of longer wavelengths that will not be attenuated as strongly in water. This is reinforced by earlier work which showed that the algal phytochrome can indeed span almost the entire visible spectrum [185]. This work on the phytochromes of *M. pusilla* is in its early stages but the global dispersal of the organism in a variety of aquatic (and optical) environments presents *M. pusilla* as a model organism for studying the adaptive responses to different environmental conditions by the phytochrome.

This is showcased by the work of Halsey et al in 2014 [186] which compared the photosynthetic energy utilization in two ecologically significant prasinophytes: the now-familiar *M. pusilla* and *Ostrecoccus tauri*. *O. tauri* is a unicellular green algae and is currently the smallest eukaryote known to man with a typical cell body size of $\approx 0.8\,\mu$m. Both of these organisms are common marine organisms, with the strain of *O. tauri* studied here being isolated from the euphotic zone - the layer of water close enough to the surface such that photosynthesis is possible - maintains a high light absorption capacity. Between this and a previous study [187] (involving two other ecologically significant microalgae *Dunaliella tertiolecta* and *Thalassiosira weissflogii*) it was found that the net carbon production was roughly half in *M. pusilla* compared to the other four species. This result indicates that *M. pusilla* has been able to evolve a high gross-to-net photosynthetic conversion efficiency - i.e. a high efficiency of converting the captured solar radiation into chemical energy. The conversion efficiency is shown to be dependent on the growth rate of *M. pusilla*, in particular during nitrogen limited growth where cells become "primed" to respond to nitrogen-rich nutrient patches in their environment. This fast response time allows *M. pusilla* to almost immediately benefit from entering a high-nutrient patch, and it is proposed that the for *M. pusilla* the cost of maintaining a high light harvesting capacity is more than balanced by the potential benefits associated from motility.

## 3.7 Summary

The key points were:

- There are a variety of propulsion methods available to microscopic biological swimmers, though a common method is the use of one or more flagella/cilia beating/rotating in a non-reciprocal manner. Many organism are able to perform "taxis" - directed motion in response to an external stimulus e.g. chemotaxis, phototaxis.

- Some swimmers use run-and-tumble motion to navigate and explore their environment, which consists of ballistic runs interspersed with periods of reorientation (tumbles). Organisms such as *E. coli* are able to modulate this motility to perform chemotaxis up/down chemical gradients.

- Many photosynthetic organisms are able to direct their motion in response to an external light source in a poorly understood process known as phototaxis. The bi-flagellated eukaryote *C. reinhardii* has established itself as a model organism for phototactic studies for a variety of reasons including a well-defined eyespot and the ease at which the organism can be cultured. *C. reinhardtii* exhibits two different photoresponses: phototaxis and a photophobic (photoshock) response.

- *Micromonas pusilla* is one of the smallest pico-eukaryotes currently known and can be found in virtually all coastal and marine environments. *M. pusilla* has previously been reported to be phototactic but there is a lack of any motility and phototactic studies for this organism.

Phototaxis, despite increased interest in recent years, remains a poorly understood response and has been limited to model systems such as *C. reinhardtii* which do not have much significant ecological impact. These studies have also been limited to simplistic photolandscapes - uniform light sources or Gaussian patches of light. In the upcoming chapters this will be expanded by firstly discussing the motility and photoresponses of the ecologically significant *M. pusilla*, then presenting a new experimental method for phototaxis in more complicated photolandscapes with the model phototactic organism *C. reinhardtii*.

# Chapter 4

# Motility and phototaxis of *Micromonas pusilla*

Disclaimer: This chapter is strongly based on the prepared manuscript: R. Henshaw, R. Jeanneret, M. Polin. Phototaxis of the dominant marine pico-eukaryote *Micromonas pusilla*. *In preparation*. 2019

## 4.1 Introduction

Photosynthetic microorganisms are fundamental primary producers - they are at the base of major food webs (i.e. oceanic environments) and contribute to approximately half of global carbon fixation despite only making up $\approx 1\%$ of the Earth biomass [5, 188]. They are also currently one of the most promising systems for biofuel development [189], with an unparalleled conversion rate of solar energy to carbon-rich molecules with negligible pressure on arable land. Many of these organisms (including bio-technologically relevant ones) are motile, which has a direct impact on the fitness of the organism when it comes to matters such as locating/aggregating around food source whilst at the same time avoiding predators and other hazardous situations. To do this, these micro-organisms have developed a wide variety of tools and mechanisms to navigate their environments in response to different stimuli and growth conditions. These directed motion, or *taxis*, involve cells directly reorientating/modulating their behaviour in response to an external stimulus. The classical example is chemotaxis, the response to chemical gradients, and is famously demonstrated by Howard Berg with studies of chemotaxis in *Escherichia coli* [125]. Other prominent taxis include: rheotaxis (response to fluid velocities), viscotaxis (fluid viscosities), gravitaxis (gravitational fields) and mag-

netotaxis (magnetic fields) [190–193]. In this chapter I will focus on the ability to adapt motility in directed response to an external light stimulus: the poorly understood process of phototaxis. Phototaxis will in turn modulate the intensity and spectral composition of light captured by the chloroplast, thereby determining the photosynthetic activity of the organism and providing a strong selective advantage to photosynthetic organisms which are also phototactic. Phototaxis has a considerable and significant impact on aquatic environments, namely contributing to the largest biomass migration on the planet: diel vertical migration [95,186]. These single cell-responses can in turn lead to patchiness of microbial populations which are capable of developing blooms which can have both global (e.g. climate regulation) and local (e.g. tourism) impacts. As such these taxis processes are being increasingly studied to improve our limited understanding of these systems, especially in ecologically relevant systems.

Perhaps one of the most dominant marine species is the green alga *Micromonas pusilla*, found in marine and coastal environments alike, from the Caribbean Sea to Norwegian fjords and Arctic waters [164, 170]. Despite its prominence, research involving this organism (and specifically its motility) is extremely sparse in comparison to other prominent organisms such as *E. coli*. The first major works by Manton and Parke [161] describe in detail the morphology and some qualitative features of its motility remain the main motility study of this organism, and the statement "...strongly phototactic and not toxic to fish..." remain to date the sole literature on the phototaxis of this organism. Outside of this topic, works highlighting *M. pusilla* have included: host-virus dynamics involving a RNA virus which infects the cell, its chemotactic behaviour towards important chemicals such as DMSP, its phagotrophic behaviour, central-pair rotation of the flagellum and last but not least the recent sequencing of its genome which has provided great insights into the evolution of green algae [162, 166, 172, 194, 195].

Despite these important and fundamental discoveries, there is very little known about the motility, foraging strategy and single-cell response to stimuli. To summarize [161], the cell has a $1 - 2\mu m$ sized comma-shaped body (making it the smallest known eukaryote on Earth) along with a single flagellum of length $\approx 5\mu$m which protrudes from the concave side of the cell, propelling it with speeds up to 50 body lengths per second [160]. It apparently changes its swimming direction frequently but the mechanism behind this is currently unclear. The cell can orientate itself to swim as either a pusher or puller-class swimmer, and more recently has been shown [163] that contrasting with normal eukaryotic bending/wave propagation, the flagellum of *M. pusilla* rotates similarly to bacteria flagellum. Phototaxis

has only been briefly mentioned with this organism [161] and so the range of wavelengths/intensities that trigger this behaviour as well as the single-cell responses leading to it remain unknown. The fact that *M. pusilla* can undergo phototaxis is itself surprising since the organism does not have a dedicated eyespot to determine the direction of the stimulus.

Here we start to fill the experimental gaps of this organism by shedding light on the motility and single-cell phototaxis of this globally important species. First we characterise the single-cell motility in controlled conditions using particle tracking velocimetry. Next we investigate the net population phototactic response to a wide range of stimulating light intensities and wavelengths, then model this net drift as a one-dimensional drift diffusion problem to extract a phototactic drift from the system. After this we look more closely at the single-cell trajectories to determine the spatial asymmetries in the run lengths responsible for the observed population behaviour, verifying them by incorporating the cell motility parameters into a series of jump-diffusion simulations. Finally we propose a hypothesis for the light detection mechanisms in the cell before drawing this chapter to a close.

## 4.2 Experimental setup

All of the results presented here were obtained using the following experimental setup, a sketch of which is shown in Fig 4.1. For all experiments a Nikon TE 2000U inverted microscope with a longbandpass filter (765nm cut-off, wavelength, Knight Optical UK) was used to limit any phototactic behaviour from the imaging light. Cells were filmed using a 40× air objective and an Allied Vision Pike F-100b camera, with the settings optimised to reduce the required imaging intensity to limit thermal convection in the sample. A cuboid polydimethysiloxane (PDMS) chamber was cast with internal dimensions 10mm × 10mm × 4mm, with a PDMS wedge insert added at the far edge to reduce any coherent back-reflection into the sample. The PDMS insert was made by casting a sacrificial device and cutting out the walls of the device, then dividing this in two to produce two triangular wedge-shaped pieces per wall. One of these pieces was then glued inside the chamber using Norland Optical Adhesive and sealed with a thin layer of adhesive followed by PDMS to prevent any leakage behind the wedge. Once the insert was set, the PDMS device was then bonded to a glass cover-slip using a Harrick oxygen plasma cleaner. The advantages of PDMS were discussed in Chapter 2, but briefly PDMS is a biologically inert material which has excellent optical qualities in the visible spectrum, making it an extremely suitable material choice for the experimental

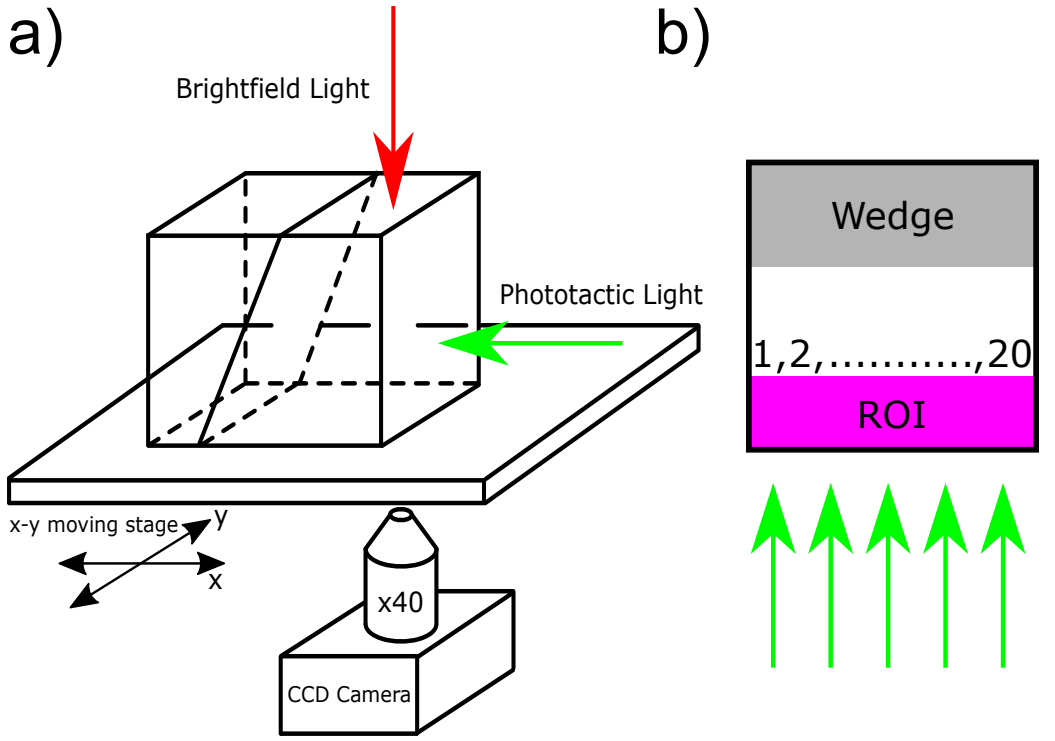


Figure 4.1: **Experimental setup for the cell motility and phototaxis experiments of *M. pusilla*. a).** Cells were loaded into a PDMS cuboid with a PDMS wedge insert to prevent coherent reflection back into the sample. The millifludic device was mounted on a computer-controlled x-y stage and images were taken with brightfield illumination with 765nm wavelength light. Phototaxis stimulus was directed perpendicular to the stage from a series of collimated LED sources. **b).** Region of interest in the chamber, viewed from the top. The population counts were sampled at 20 locations within 185 microns of the boundary closest to the stimulus (shown in magenta). The sites were sampled in a cyclical manner: $1-2-...-20-1-2-...$ etc. until each site had been sampled for 88 minutes.

chamber. Prior to filming the sample had been left to sediment for several hours. The external light stimulus was generated from one of four LEDs (then collimated) with peak wavelengths $\lambda = 470\text{nm}, 530\text{nm}, 595\text{nm}$ and 625nm. The stimulating light intensity was measured with a Spectrum Technologies Field Scout light sensor reader.

### Culturing

Initial cultures of *M. pusilla* strain RC827 were generously provided by Dr. Joseph Christie-Oleza. These cultures were grown and swapped between two media to promote cell growth - Keller (K) medium [196] and Gulliard's f/2 medium [197]. These

were prepared using artificial seawater in 500ml quantities excluding the sodium-glycerophosphate to reduce precipitation. The cultures were cultivated in a diurnal chamber on a 16/8 hour light/dark cycle maintained at 20°C at a light intensity of $100\mu E.m^{-2}.s^{-1}$ from fluorescent strips. All experiments took place with the cells growing in f/2 medium.

## 4.3 Characterising the cell motility of *Micromonas pusilla*

### 4.3.1 Particle tracking velocimetry (PTV)

Particle tracking velocimetry (PTV) is a technique used to measure the velocity of particles suspended in a fluid. In contrast to particle image velocimetry (PIV), this Lagrangian approach relies on tracking individual particles in either two or three-dimensions. Here, two-dimensional PTV is used to investigate the cell motility and phototaxis of *Micromonas pusilla*. PTV can be broken down into two stages of analysis: pretracking to find the particle positions followed by a tracking algorithim to link those positions together to form trajectories of single cells. The algorithms and MATLAB files used for both stages are readily available [198], and are based on the IDL Particle Tracking software developed by Grier, Crocker and Weeks [199]. These MATLAB functions will be indicated in italics when each function is used in the particle tracking process.

#### Pretracking

Fig 4.2 demonstrates the process of pretracking the images to find the particle positions for that specific frame. The sample image here is a brightfield image of *M. pusilla* taken at 40× magnification so that the individual cells appear as dark spots on the image. After this the image is passed through a spatial bandpass filter (*bpass.m*) with user-defined length scales of the background noise and the feature size - here the diameter of the cells as they appear in the image. This filter smooths out the features and removes the noisy background from the image, resulting in Fig 4.2b. After the image has been filtered the next task is to find local maxima to pixel accuracy (*pkfnd.m*) which will give a rough approximation of the particle's location. This is further refined by taking this list of positions and calculating the centroid (*cntrd.m*) of each feature to locate (as best as possible) the centre of each feature to sub-pixel accuracy (Fig 4.2c). Repeating this across all the detected features with the correct parameters, located by trial-and-error, gives Fig 4.2d: the location of each cell in the image down to sub-pixel accuracy.

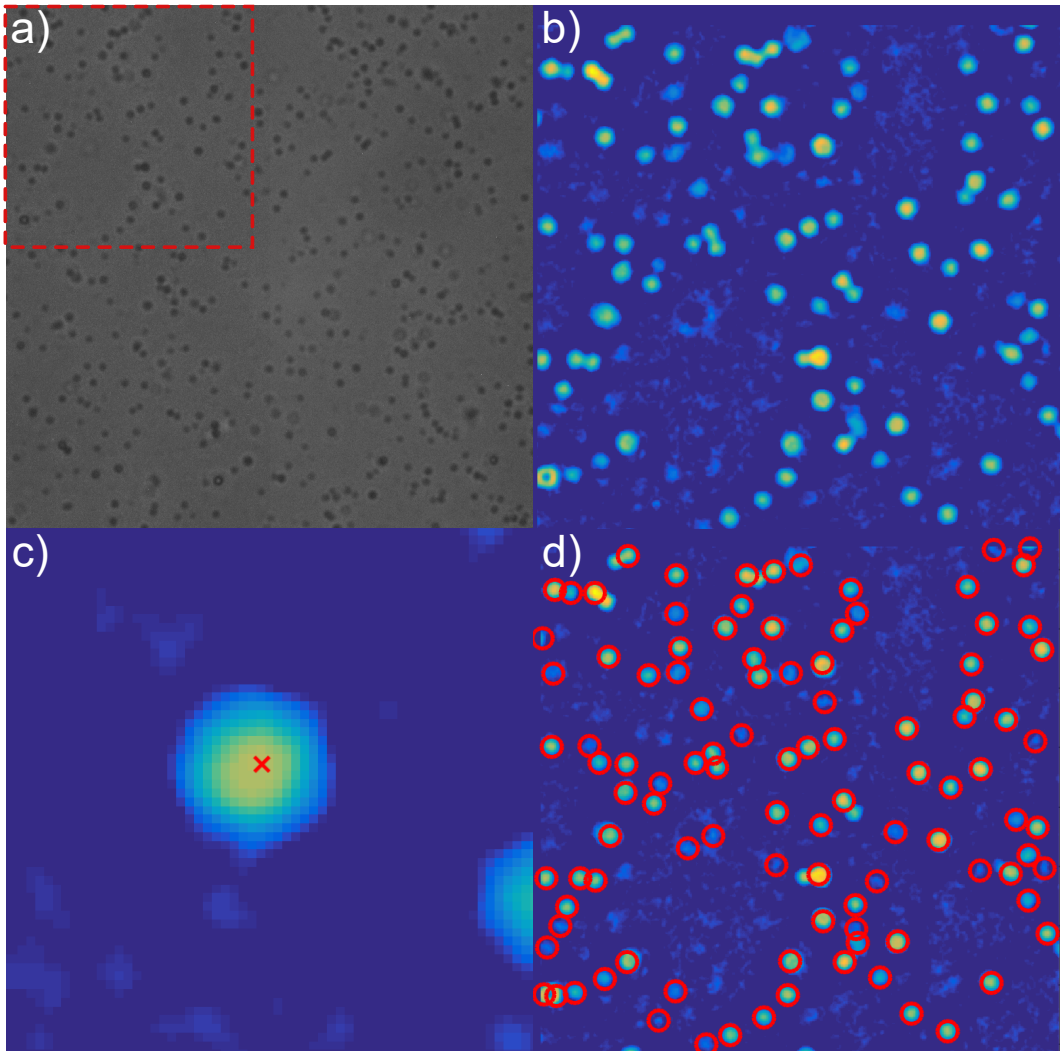


Figure 4.2: **Example of pretracking. a).** The original brightfield image (40× magnification) where cells appear as dark spots. **b).** The image is inverted to make the particles bright on a dark background, then passed through a spatial band-pass filter to smooth the image and remove the background. Shown here is a the highlighted red region from (a). **c).** Features are located on the image based on the average feature size and brightness, located to initially to pixel accuracy before being refined to find the centroid (plotted red x) of each feature. **d).** Tuning the various parameters allows accurate location of particles which can then be used to reconstruct the trajectories. Feature location is extremely robust once the correct parameters have been found although if two particles are overlapping this can occasionally lead to errors in particle identification. As such it is safer to stay at a cell density such that there is sufficient distance between any two particles at a given time to avoid misidentification.

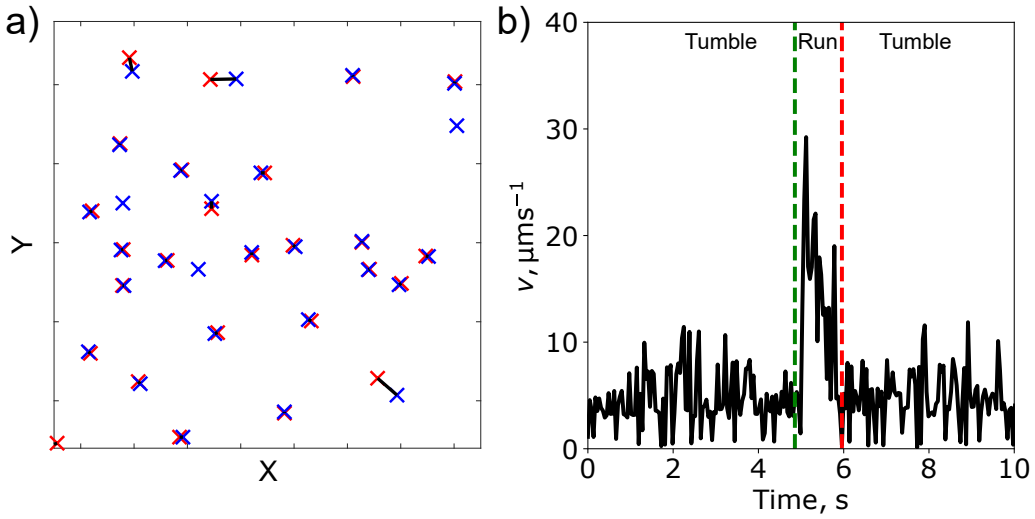


Figure 4.3: **Example of particle tracking. a).** Example of linking the particle positions from frame 1 (blue) to the particle positions in frame 2 (red), with the linking bonds labelled in black. **b).** From the particle trajectories we can extract the instantaneous particle velocity, and use this to locate the run events in a run-tumble trajectory by observing that in the instantaneous cell speed the run velocity greatly exceeds the Brownian noise.

### Tracking algorithim

Once the particle locations have been found for every frame in the experiment (and compiled into a list), these can then be linked together to form individual particle trajectories. Following the steps of Crocker and Grier, we first define the location of the $i$th particle (out of $N$ particles) at a time $t$ as $\mathbf{r}_i(t)$ and the time evolution of the particle distribution:

$$\rho(\mathbf{r}, t) = \sum_{i=1}^{N} \delta(\mathbf{r} - \mathbf{r}_i(t)) \tag{4.1}$$

The goal is to match locations of particles in one frame with the next frame, taking care when working with multiple particles to send each particle to the next correct (and most likely) position in the next frame. To do this we aim to find the a set of connections between the $N$ particle locations in the two images that is the most probable set of connections. This can be motivated by considering Brownian motion. For an ensemble of $N$ Brownian particles with diffusion coefficient $D$, the probability distribution where the $i$th particle will diffuse a distance $\delta_i$ in a time $\tau$ is given by the product of each individual particle probability distribution:

$$P(\delta_i|\tau) = \left(\frac{1}{4\pi D\tau}\right)^N \exp\left(-\sum_{i=1}^{N}\frac{{\delta_i}^2}{4D\tau}\right) \tag{4.2}$$

By maximising this probability distribution we can find the most likely connection of particle locations between subsequent frames (equivalently by minimising the exponent). Calculating this for all possible connections is a task that will scale as $N!$ which is extremely impractical for any reasonably sized system, so we impose that all connections must be shorter than some characteristic length scale $L$, i.e. $\max(|\delta_i|) = L$. Provided the particle separation is such that there is a value of $L$ which limits the number of possible connections of each particle to single connections (or small numbers of connections), the trajectory linking scales more as $N\ln(N)$ instead of $N!$ as before. Finally it is worth noting that linking particle trajectories is only achievable if the single particle displacement $\delta_i$ is sufficiently smaller than the typical interparticle separation. This is a simple limit to maintain experimentally for diffusing particles, as for colloids on the scale of microns will diffuse less than their diameter at reasonable framerates (i.e. less than 60 frames per second). When considering swimming particles however the density must be more carefully controlled to maintain good tracking of the particles.

During the implementation of the tracking algorithm (*track.m*), there are two parameters in addition to the typical displacement of a particle between frames that can be set to improve the quality of the particle tracking. Firstly a parameter can be set to eliminate trajectories shorter than a specific length (i.e. 100 frames) to remove short "blinking" trajectories. Particles can also be allowed to disappear from the field of view for a maximum (defined) number of frames and be identified as the same particle if it reappears in time, but this does greatly increase the computational cost of the algorithm. Once the trajectories have been acquired there is a variety of motility data that can be acquired such as swimming speed, direction of motion etc. Analysing a run-tumble particle adds a level of complexity to this analysis, namely in the identification of the two phases of motion. Fig 4.3a shows an example of the implementation of the tracking algorithm between frame one (blue) and frame two (red), with the linked positions connected with black lines. This can be used to follow the trajectory of a single cell for prolonged periods of time regardless of its swimming behaviour, for example organisms which swim continously such as *Chlamydomonas reinhardtii* or a run-tumble organism such as *M. pusilla*. For a run-tumble organism the individual runs can be located by examining the instantaneous swimming speed of the cell (Fig 4.3b), noting that during the run-phase the instantaneous swimming velocity greatly exceeds that of the Brownian noise.

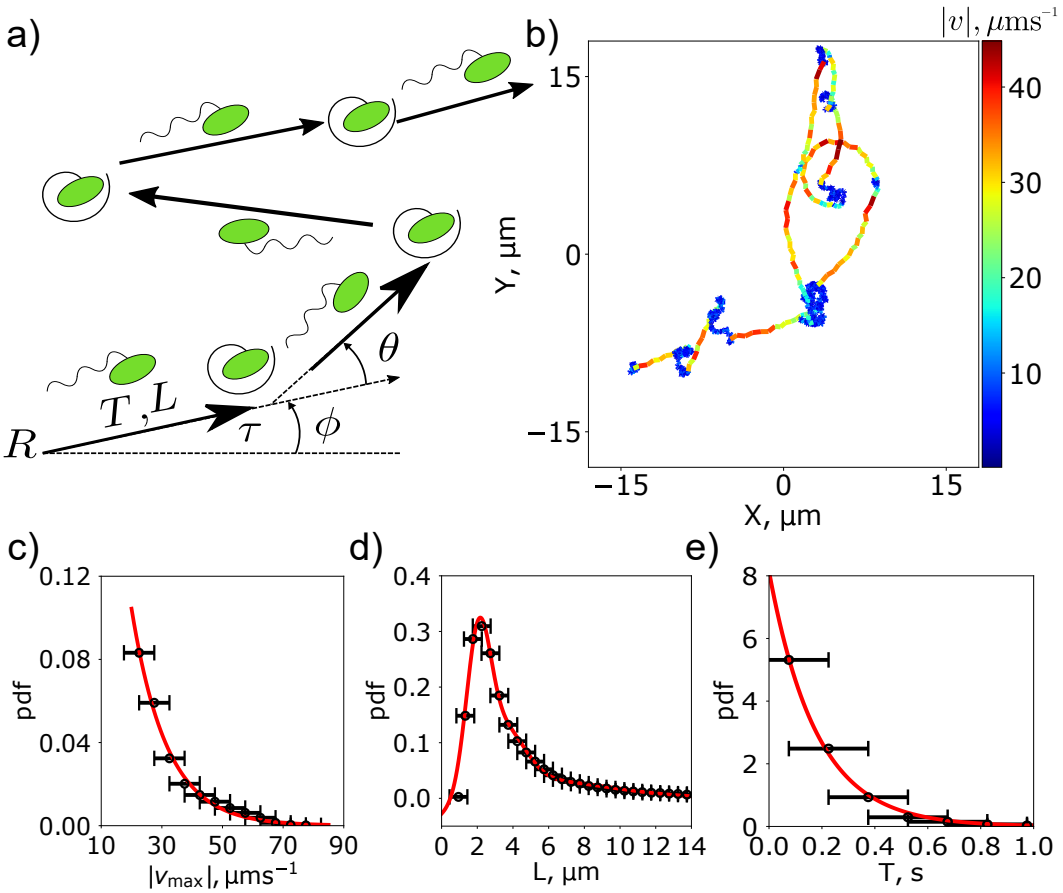


Figure 4.4: **Motility of *M. pusilla* a).** Sketch of stop, run-reverse motion, noting in particular the reorientatation angle $\theta$ measured counter-clockwise from the previous run, which has a run angle of $\phi$ measured relative to the $x-$axis as labelled. **b).** Examples of *M. pusilla* trajectories, colour-coded by the instanteous velocity (see colormap). A cell alternate between stop phases (blue) and forward or backward runs (red). **c).** Peak run speed of individual trajectories. We have also observed extrememly rare cases of the speed exceeding $100\mu\text{ms}^{-1}$ which are not recorded here. **d).** Run length. **e).** Run duration. The vast majority of the runs last for less than a second, but there are rare cases of these runs lasting tens of seconds. **f).** Tumble duration (stopping duration), which are exponentially distributed. Similar to the run duration, there are extremely rare cases where the tumbling duration will exceed tens of seconds.

### 4.3.2 Cell motility

Before characterising any single cell phototactic behaviour, we must first characterise the motility of *M. pusilla* in control conditions - i.e. without any light stimulation. Some typical trajectories are shown in Fig 4.4b, demonstrating how the cell alternates between phases of active swimming in straight runs and phases of apparent

passivity during which reorientation takes place. This motility pattern bears striking resemblance to the run-stop motion of *Rhodobacter sphaeriodes*, a marine bacterium which has a single polar flagellum. To quantify the motility fully we extract various parameters based on the run pattern of *M. pusilla* (Fig 4.4a): the run time ($T$), the run length ($L$), the run direction ($\phi$) given by the angle between the x-axis and the swimming direction, the stopping (tumble) time ($\tau$) and the reorientation angle ($\theta$), with the average values of these parameters are given in Table 4.1.

As discussed in Chapter 2, the switching events between running to stopping (and vice versa) both follow Poisson processes. This is illustrated by the distributions of the run times $T$ and tumble times $\tau$ as shown in Fig 4.4 which are well fitted by simple exponentials with switching rates $\kappa_{\text{run}} = 1/ < T >= 5 \pm 1\text{s}^{-1}$ and $\kappa_{\text{stop}} = 0.95 \pm 0.04\text{s}^{-1}$. During a run the cells do not swim at a constant velocity (as seen by the trajectories in Fig 4.4a), instead there are phases of acceleration/deceleration at the beginning/end of runs respectively. This is most likely due to conformal changes of the flagellum, and it has been noted [161] that the flagellum does curl under the body during reorientation which would agree with the observed behaviour of the run velocities. Peak run speeds can be in excess of $80\mu\text{ms}^{-1}$ with an average run speed of $22.89 \pm 0.02\mu\text{ms}^{-1}$ (or $\approx 11\,\text{bodylengths.s}^{-1}$), giving an average run length of a few body lengths $< L >= 4.54 \pm 0.01\mu\text{m}$.

### 4.3.3 Description of the reorientation angle distribution

Once the runs have been located in the experimental data, it is a relatively straightforward task to determine the reorientation angle $\theta$ of the cells and then use this to help characterise the type of run-tumble motion. In order to measure this a trajectory needs to consist of a minimum of a run followed by a tumble then another run. In every case the reorientation angle is measured counter-clockwise relative

Table 4.1: Mean values of the cell motility parameters in control conditions (i.e. no external light stimulus).

| Motility Parameter | Control |
|---|---|
| Run Length $\langle L \rangle$ ($\mu$m) | $4.54 \pm 0.01$ |
| Run Duration $\langle T \rangle$ (s) | $0.20 \pm 0.04$ |
| Stop Duration $\langle \tau \rangle$ (s) | $1.05 \pm 0.04$ |
| Peak Speed ($\mu\text{m.s}^{-1}$) | $31.53 \pm 0.02$ |
| Run Speed ($\mu\text{m.s}^{-1}$) | $22.89 \pm 0.02$ |

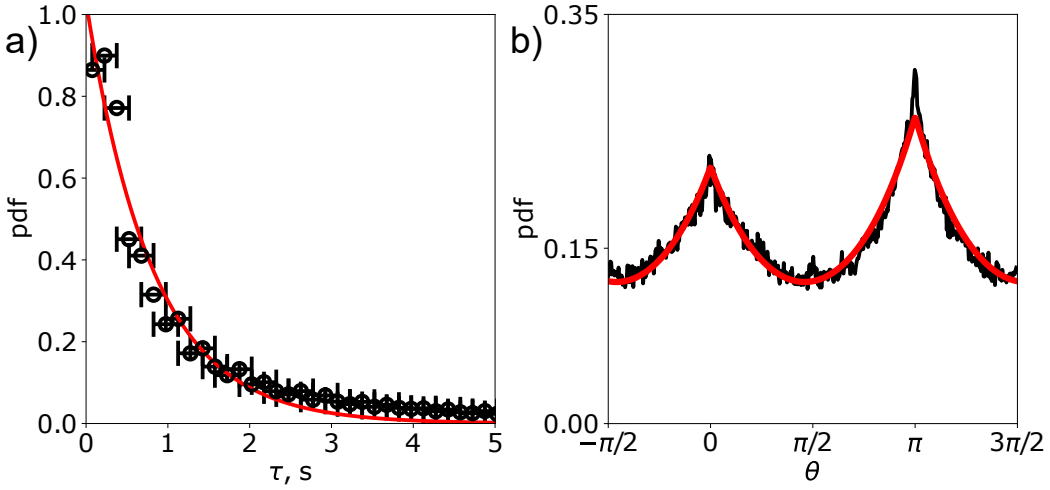


Figure 4.5: **Reorientation distribution of *M. pusilla*. a).** Exponential distribution of the tumbling duration $\tau$ for *M. pusilla*. **b).** The experimental distribution of $\theta$ (black). There are clearly two peaks in the distribution at $\theta = 0, \pi$, meaning that on average cells will either continue in the previous run-direction or reverse their path, similar to the run-reverse motion of marine bacteria. This is fitted (red) with the function described in Eq 4.8.

to the previous run direction, as shown in Fig 4.4a. Since in the experiments it is impossible (in this case) to measure how the cell reorientates during a tumble, $\theta$ will be bounded in a $2\pi$ interval where as in reality theta can take any real value as the number of cell rotations during a tumble is unknown. This means any theoretical description of the reorientation angle distribution will need to be wrapped over the unit circle (Fig 4.5b), producing the wrapped probability distribution as a $2\pi$ periodic sum.

From Fig 4.5b, there are two clear peaks in the reorientation angle distribution at $\theta = 0, \pi$. Physically speaking this means that after a run, the cell is more likely to either continue in the same direction ($\theta = 0$) or back upon itself ($\theta = \pi$). This bears a striking resemblance to the run-reverse strategies of marine bacteria, but is interesting as *M. pusilla* is a eukaryote not a prokaryote. Care needs to be taken here with convention: it is unclear whether these 180° turns are a result of the cell physically changing its orientation or if the cell is simply reversing its direction - a "reversal" in the conventional sense. Either of these options are possible especially given that is has also been reported that *M. pusilla* can swim as both a pusher and a puller type swimmer [161], which would enable a classical reversal. Since we are unable to track the flagellum and therefore the orientation of the cell, it is unclear which of these mechanisms is taking place. For ease of discussion, these

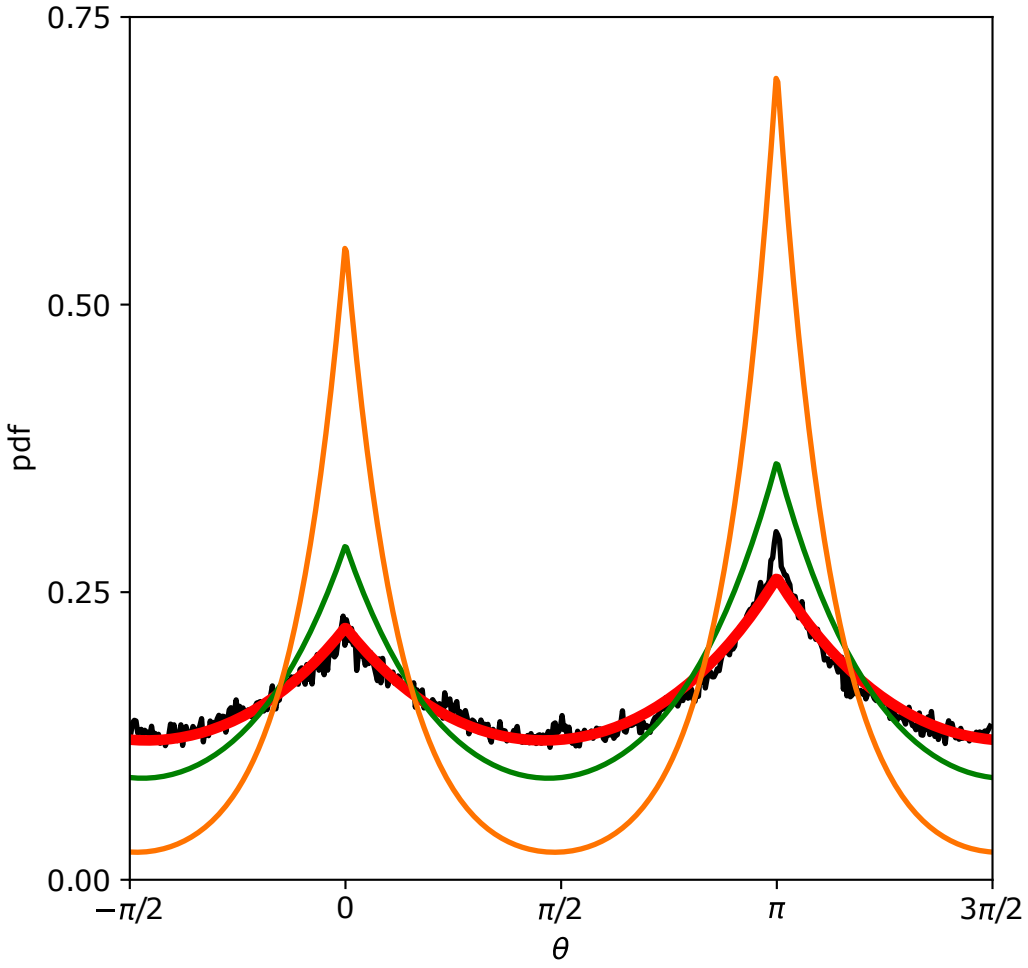


Figure 4.6: **Comparison of theoretical reorientation distributions.** As shown previously, the experimental/fitted distributuions for $\theta$ are shown in black/red respectively. Exponential distribution of the tumbling duration $\tau$ for *M. pusilla*. Shown in green/orange are the theoretical $\theta$ distributions for a passive sphere with radius $1\,\mu$m and $\approx 0.63\,\mu$m respectively ($D_{rot} \approx 0.15, 0.6\,\text{rad.s}^{-1}$ respectively). The later is chosen as this is the equivalent spherical radius if we consider that the cell as a prolate ellipsoid with semi-principal axis $1\,\mu$m and $0.5\,\mu$m, a reasonable approximation for *M. pusilla*. The clear differences in these two theoretical distributions compared to the experimental distributions suggests an active component to the reorientation during a tumble as opposed to reorientation purely from rotational diffusion.

turns will be referred to as reversals from here forwards, but the true nature of these reorientation events remains an open question.

Due to the erratic stopping nature of the cell, i.e. combinations of short

and long tumbles, this novel motility strategy is named as *stop, run-reverse*. Given all this information about the reorientation distribution it is possible to derive a theoretical distribution based on of the knowledge that $\theta$ has two peaks in its distribution, which goes as follows. Consider a run-tumble particle with an exponentially distributed tumble duration with characteristic time $\tau_d$:

$$P_{\text{exp}}(\tau) = \frac{1}{\tau_d} \exp\left( - \frac{\tau}{\tau_d} \right) \tag{4.3}$$

The particle is going to be subject to Brownian reorientation with the probability distribution function, with a peak reorientation angle of $\theta_p = 0$, described by the probability distribution:

$$P_{\text{therm}}(\theta) = \frac{1}{\sqrt{4\pi D_{\text{rot}}\tau}} \exp\left( - \frac{(\theta - \theta_p)^2}{4\pi D_{\text{rot}}\tau} \right), \qquad \theta \in (-\infty, \infty) \tag{4.4}$$

Where $D_{\text{rot}}$ is the rotational diffusion coefficient and the particle reorientates an angle $\theta$ in time $\tau$. Combining these two distributions and summing over all values of the tumble duration gives the probability distribution:

$$P(\theta) = \int_{\tau=0}^{\infty} \frac{1}{\tau_d} \exp\left( - \frac{\tau}{\tau_d} \right) \frac{1}{\sqrt{4\pi D_{\text{rot}}\tau}} \exp\left( - \frac{(\theta - \theta_p)^2}{4\pi D_{\text{rot}}\tau} \right) d\tau, \tag{4.5}$$

Two modifications need to be made to apply this to *M. pusilla*. Since we are only capable of experimentally measuring $\theta \in [-\pi/2, 3\pi/2]$, $P(\theta)$ needs to be wrapped to form the circular distribution $P_w(\theta)$ by:

$$P_w(\theta) = \sum_{k=-\infty}^{\infty} P(\theta + 2\pi k) \tag{4.6}$$

Secondly we need to account for the twin peaks of the experimental distribution of $\theta$. This is done by combining two probability distribution with a parameter $\Gamma$, noting that if $P_1(x), P_2(x)$ are normalized probability distributions then:

$$P(x) = (1 - \Gamma)P_1(x) + \Gamma P_2(x), \qquad \Gamma \in [0, 1] \tag{4.7}$$

Produces the normalized probability distribution $P(x)$. Combining the two modifications of Eq 4.6, Eq 4.7 with our original probability distribution Eq 4.5, with $\theta_{p1,2} = 0, \pi$, we obtain:

$$P_w(\theta) = \sum_{k=-\infty}^{+\infty} \int_{\tau=0}^{+\infty} \Big[ (1-\Gamma) \frac{\mathrm{e}^{-\tau/\tau_d}}{\tau_d} \frac{\mathrm{e}^{-(\theta+2k\pi)^2/(4D_{\mathrm{rot}}\tau)}}{\sqrt{4\pi D_{\mathrm{rot}}\tau}} + \Gamma \frac{\mathrm{e}^{-\tau/\tau_d}}{\tau_d} \frac{\mathrm{e}^{-(\theta-\pi+2k\pi)^2/(4D_{\mathrm{rot}}\tau)}}{\sqrt{4\pi D_{\mathrm{rot}}\tau}} \Big] d\tau \tag{4.8}$$

**Fitting to the experimental data**

The final step is to optimise the theoretical distribution to best fit the experimental data. This can be done by minimising the Kullback-Leibler divergence (or K-L divergence) [200]. The K-L divergence is a measure of how different two probability distributions are from each other. Crucially it is not a measure of distance since it is not symmetric, but rather a measure of the relative entropy between the two distributions. It provides a means of (effectively) measuring the information lost by approximating one distribution with another, for example measuring the divergence of an experimental distribution $p(x)$ from the model distribution $q(x)$. From definition, the K-L divergence is:

$$D_{KL}(p(x)||q(x)) = \sum_{x \in X} p(x) \ln \left( \frac{p(x)}{q(x)} \right) \tag{4.9}$$

In this case the model distribution is $q(x) \equiv P_w(\theta)$ and the experimental data is $p(x)$. The best fit will be given by minimising the K-L divergence, which results in the following parameters: $\Gamma = 0.55, D_{\mathrm{rot}} = 2.1\,\mathrm{rad.s}^2$ and $\tau_d = 0.8\,\mathrm{s}$, indicating with this value of $\Gamma$ the cell is slightly more likely to undergo a reversal than continue in the same direction, and the theoretical tumble time is in good agreement with the experimental tumble duration of $< \tau >= 1.05 \pm 0.04\mathrm{s}$. The resulting distribution is shown in Fig 4.5b as the red line overlaying the experimental data (blue) and is clearly in strong agreement with the experimental distribution of $\theta$.

**Insight to the reorientation mechanisms**

Playing with this analytical description allows us to make some conjectures about the reorientation mechanism of *M. pusilla*. We can use the Stokes-Einstein relation (Eq. 2.24-2.25) to estimate an effective radius ($R_{Brown}$) for a sphere at the same temperature in the same medium:

$$R_{Brown} = \left( \frac{8\pi\mu D_{rot}}{k_b T} \right)^{\frac{1}{3}} \tag{4.10}$$

Using the this relation the fitted rotational diffusion coefficient gives an equivalent spherical radius of $R_{Brown} = 0.414 \pm .06\mu$m. Likewise, approximating the cell body of *M. pusilla* as a prolate ellipsoid with average semi-principal axis $a = 1\mu\text{m}, b = 0.5\mu$m gives an equivalent spherical radius of $0.63\mu$m. This results in a Brownian rotational diffusivity approximately a third the magnitude of $D_{rot}$ taken from the fit of $P_w(\theta)$. Keeping $\tau_d, \Gamma$ the same as in the fit of $P_w(\theta)$, plotting the resulting theoretical distributions for the sphere and prolate-ellipsoid gives the green and orange curves in Fig 4.5b respectively. These are obviously far off the experimental fits and the difference will only grow as the non-spherical nature of the cell body is taken into account, for example by introducing Perrin friction factors [201]. These multiplicative adjustments are used to determine the diffusion coefficients of a rigid spheroid, using information from spheres of equivalent volumes.

Comparing the differences between the theoretical passive reorientation distributions with the experimental distribution it is clear that there must be some active element to the reorientation of *M. pusilla* to increase the rotational diffusivity of the cell (evident in the flatter experimental distribution). Interestingly a similar conclusion was made by Rosser et al [202] when studying the run-tumble motility of *Rhodobacter sphaeroides*, an organism with striking similarities to *M. pusilla*. Both organisms have a single flagellum, and in the case of *R. sphaeroides* reorientations are caused by stopping the flagellum motor rather than unbundling as is the case in the classical run-tumble of *E. coli* [203]. *R. sphaeroides* uses "run-stop" motion, with the reorientation angle peaked around $\theta = 0$. In their work it is proposed that the active contribution to the reorientation could arise from slow motion of the flagellum during a stop or perhaps rapid transformations of the flagellum during the transition from a stop to a run. These seem promising with *M. pusilla* as it is known that the flagellum "curls" slowly under the cell body during a stop [161] but more work and dedicated experiments are needed to unravel the reorientation dynamics of this organism.

## 4.4 Translational diffusion coefficient

As previously discussed in Chapter 2, it is possible to determine the translational diffusion coefficient $D_t$ from the time evolution of the mean-squared displacement. We recall the following relationship for anomalous diffusion in a two-dimensional system:

$$< \mathbf{x}^2(t) >= 4D_t t^{\alpha}, \qquad \alpha > 0 \tag{4.11}$$

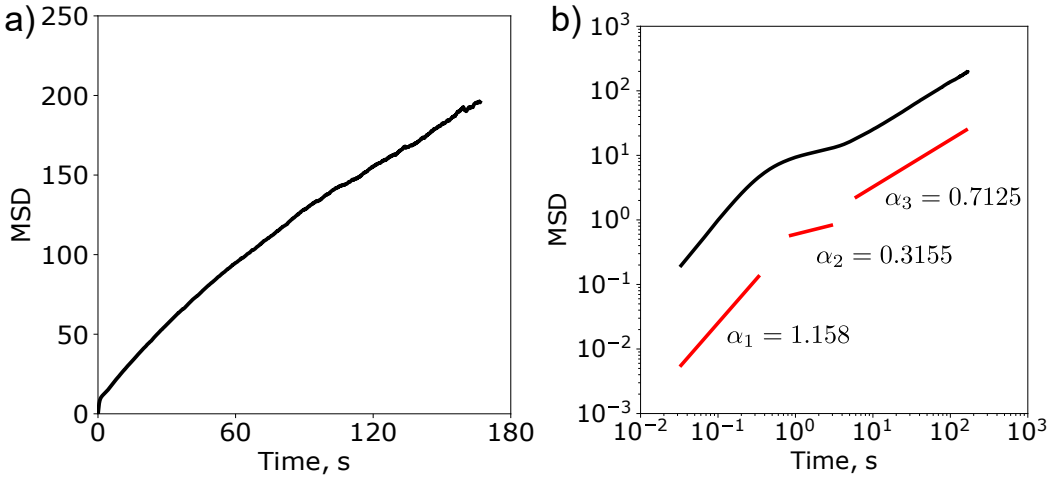


Figure 4.7: **Mean-squared displacement of *M. pusilla*.** Experimentally measured values of the MSD for *Micromonas pusilla* on **(a)** linear scales and **(b)** logarithmic scales. There is a change in diffusive behaviour at the long-time scales, with apparent sub-diffusion with an exponent of $\alpha_3 = 0.7125$ and $D_t = 1.17\mu\text{ms}^{-2}$.

Where the exponent $\alpha$ gives three regimes: diffusion, subdiffusion and superdiffusion ($\alpha = 1, \alpha < 1, \alpha > 1$ resp.). With the run-tumble nature of *M. pusilla* we expect the MSD to display anomalous behaviour [204] at both the short and long time scales. Fig 4.7b shows this behaviour - at short timescales the behaviour is superdiffusive ($\alpha_1 = 1.158$) but at long time scales this becomes subdiffusive ($\alpha_3 = 0.7125$). This subdiffusion was not expected but is believed to be simply the consequence of the limited field of view of the experiments ($185\mu$m). This could be tested in theory by changing the field of view (i.e. by changing the magnification used for example) but this will impact the accuracy of the particle tracking. At higher magnifications there will be insufficient sampling time as particles will leave the field of view too quickly, and at lower magnification the particle location becomes less reliable due to the small size of the cell. Despite this it is still possible to extract an estimate on the value of the diffusion coefficient at long-time scales of $D_t = 1.17\mu\text{ms}^{-2}$.

## 4.5 Population phototaxis

Any taxis motion will eventually manifest itself as a net drift at the populations scale. To quantify the phototactic response we first measured the accumulation of cells at the edge of the chamber nearest the light source (within $185\mu$m of the boundary) over an 88 minute exposure time for wide range of light intensities and wavelengths. This was done by sampling at 20 equally spaced sites covering the

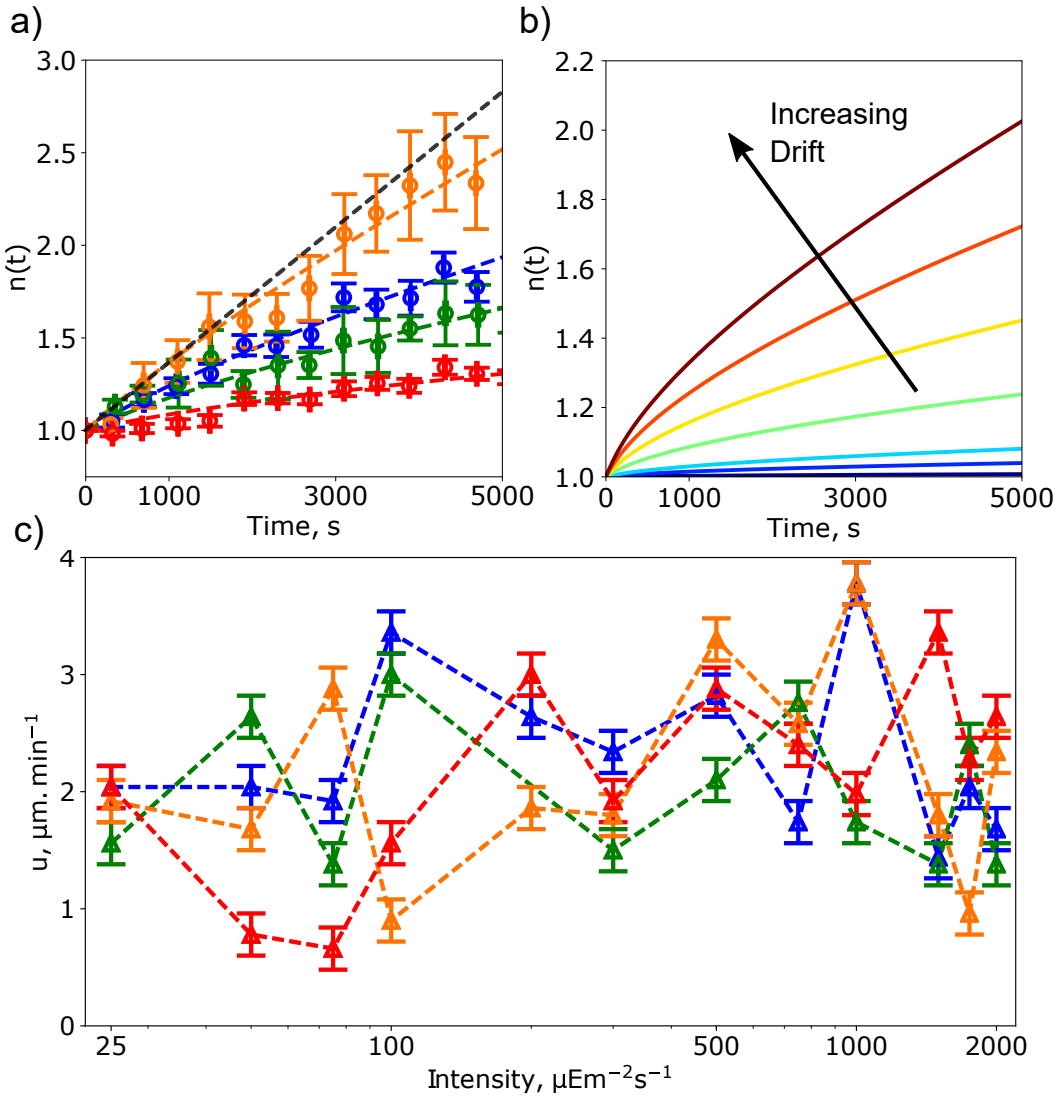


Figure 4.8: **Population scale phototaxis of *M. pusilla*. a).** Evolution of the number of cells (normalized by initial cell count) within the field of view close to the light source at $I = 75\mu\text{E.m}^{-2}.\text{s}^{-1}$ for the four wavelengths (circle) examined together with the best fit from the drift-diffusion solution (dotted lines). Blacked dashed line is a linear extrapolation of the initial population growth where drift dominates diffusion. **b).** Example of the drift diffusion model behaviour for a fixed diffusion constant but with increasing drift velocities. **c).** Phototactic response quantified by the drift velocity $u$ as a function of intensity $I$ for the four wavelenths examined. the phototactic drift is always positive showing a positive phototactic response for every parameter tested.

width of the chamber as shown in Fig 4.1, using a computer controlled microscope stage to move between the sites in a cyclical manner (i.e. sites were sampled in

the order $1-2-3\cdots-20-1-2-3\ldots$ etc.). Effectively, each site is sampled every 230 s then the twenty sites averaged to measure the cell count as a function of time. The evolution of the number of cells in that region, $n(t) = N(t)/N_0$ where $N_0$ is the initial number, for the four wavelengths examined with fixed intensity $I = 75\mu\text{E.m}^{-2}.\text{s}^{-1}$, is plotted in Fig 4.8a where we see a clear accumulation. Since *M. pusilla* displays diffusive behaviour on long time scales from the run-tumble behaviour, we can expect the accumulation dynamics to be well described by a one-dimensional drift-diffusion model.

### 4.5.1 One-dimensional drift diffusion

The run-tumble behaviour of *M. pusilla* can be described in the long-term as a diffusive behaviour with diffusion coefficient $D_t$. Any bias in the cell's swimming behaviour will result in a net population drift at long time scales, akin to subjecting purely diffusive particles to a net drift with the particles confined in some region of space (for example, the microfluidic device). Since the light stimulus will be assumed to be collimated i.e. there is a single well defined light axis, we can model this problem as a one-dimensional confined drift-diffusion problem. This has been studied, in particular by [205], and here present the main results from that paper. This is included for completeness and accessibility of the material - for a more rigorous and complete discussion please see the source material.

#### Model

Consider a colloidal suspension whose number density at a time $t$ is given by $n(x,t)$ with the $x$-coordinate restricted to the interval $0 \leq x \leq h$. Given constant drift velocity $u$ and Einstein coefficient $D$, the particle current $J$ is described by

$$J = un - D\frac{dn}{dx} \tag{4.12}$$

The density and current satisfy the conservation equation and also the zero current condition at the boundaries

$$\frac{\partial J}{\partial x} + \frac{\partial n}{\partial t} = 0, \qquad J(0) = 0 = J(h) \tag{4.13}$$

Combining these, we obtain the diffusion equation for the number density

$$\frac{\partial n}{\partial t} = D\frac{\partial^2 n}{\partial x^2} - u\frac{\partial n}{\partial x} \tag{4.14}$$

For convenience, we introduce the dimensionless variables

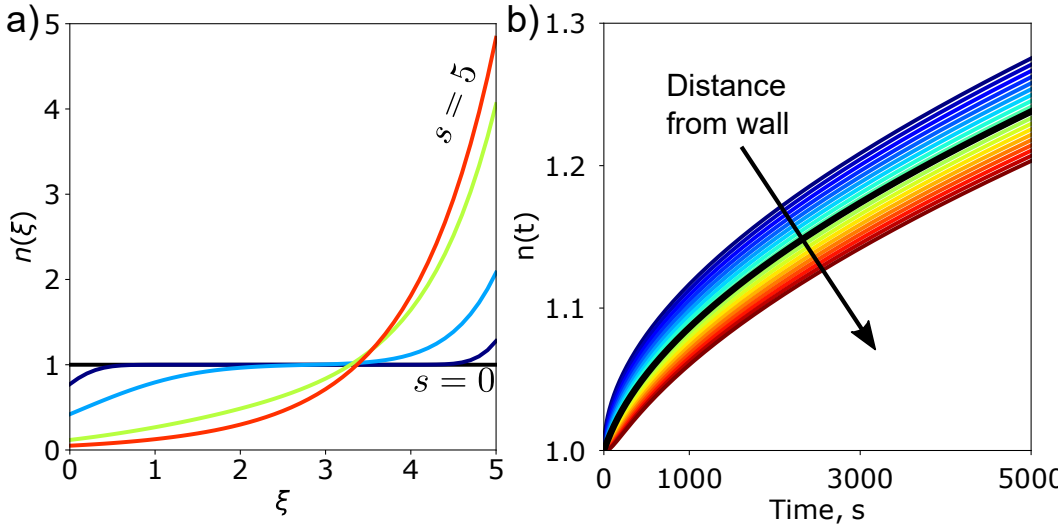


Figure 4.9: **Model of confined one-dimensional drift-diffusion with constant drift and diffusion. a).** The evolution of the exponential equilibrium distribution across the length of the interval, using the dimensionless variables $\xi, s$ to represent length and time respectively. Shown here: $s = 0, 0.05, 0.5, 2.5, 5$. **c).** The population evolution as a function of distance from the boundary. Given a window of size $B$, the evolution of the population in that viewing window can be described by the average of the population evolution at all points in that interval, denoted by the black line.

$$s = t\frac{|u|}{l}, \qquad \xi = \frac{x}{l}, \qquad \xi_0 = \frac{h}{l} \tag{4.15}$$

Where $\xi_0$ is in fact the Péclet number of particle diffusion. Using these variables, our original diffusion equation becomes

$$\frac{\partial n}{\partial \tau} = \frac{\partial^2 n}{\partial \xi^2} + \frac{\partial n}{\partial \xi} \tag{4.16}$$

With $u < 0$ so the particles are driven towards the left boundary at $x = 0$. This direction of current is chosen arbitrarily, we could equally choose $u > 0$ such that the current is driven to the right boundary of $x = h$, in which case we simply set $\xi = \xi_0 - \frac{x}{l}$ and continue with the methodology.

For the general initial distribution of particles, define the Greens function of the process $g(\xi, \xi_1; s)$ which is the probability for a particle located position $\xi_1$ at time $s = 0$ to be found at position $\xi$ at time $s$. From this, the time evolution of the initial distribution $n(\xi, 0)$ is described by evaluating

$$n(\xi, s) = \int_0^{\xi_0} g(\xi, \xi_1; s) n(\xi_1, 0) d\xi_1 \tag{4.17}$$

Substituting Equation 4.17 into Equation 4.16, the Greens function can be shown to satisfy the dimensionless diffusion equation (Equation 4.16).

Solving for the Greens function is a fairly arduous process, but the final form is given by

$$\begin{aligned} g(\xi, \xi_1; \tau) =& \frac{e^{-\xi}}{1 - e^{-\xi_0}} \\ &+ e^{-\xi} \sum_{k=-\infty}^{\infty} e^{-k\xi_0} E(2k\xi_0 + \xi_1 + \xi, s) \\ &+ e^{-(\xi - \xi_1)/2} \sum_{k=-\infty}^{\infty} \sum_{\pm} w(2k\xi_0 + \xi \pm \xi_1, s) \end{aligned} \tag{4.18}$$

Where the functions $E, w$ are defined as

$$w(\xi, s) = \frac{1}{2\sqrt{\pi s}} e^{-\frac{s^2 + \xi^2}{4s}}, \qquad E(\xi, s) = \frac{1}{2} \operatorname{erf}\left(\frac{s - \xi}{2\sqrt{s}}\right) - \frac{1}{2} \tag{4.19}$$

In the long time limit, the Green's function tends to the stationary probability distribution

$$g_{eq}(\xi) = \frac{e^{-\xi}}{1 - e^{-\xi_0}} \tag{4.20}$$

For an initial constant density $n(\xi, 0) = n_0$, Equation 4.17 becomes

$$n(\xi, s) = n_0 \int_0^{\xi_0} g(\xi, \xi_1; s) d\xi_1 \tag{4.21}$$

By integrating the Green function term by term, an expression for the time evolution of a flat original density can be found as:

$$\begin{aligned} n(\xi, s) = n_{eq}(\xi) + n_0 \sum_{k=-\infty}^{\infty} \Big\{ & e^{-\xi/2} W(2k\xi_0 + \xi, s) \\ & - e^{(\xi_0 - \xi)/2} W[(2k+1)\xi_0 + \xi, s] \Big\} \end{aligned} \tag{4.22}$$

Where the function $W$ and equilibrium value $n_{eq}$ are defined as

$$\begin{aligned} W(\xi, s) =& 2sw(\xi, s) \\ &+ e^{-\xi/2}(s - \xi + 1)E(\xi, s) + e^{\xi/2}E(-\xi, s) \end{aligned} \tag{4.23}$$

$$n_{eq}(\xi) = n_0\xi_0 \frac{e^{-\xi}}{1 - e^{-\xi_0}} \tag{4.24}$$

Finally, changing back to the original variables brings the equilibrium distribution to the form

$$n_{eq}(x) = n_0 \frac{h}{l} \frac{e^{-x/l}}{1 - e^{-h/l}} \tag{4.25}$$

This model is demonstrated by Fig 4.9. From an initially uniform distribution the model tends towards a steady exponential solution $n_{eq}$ (Fig 4.9a). Fig 4.9b shows the evolution of the number density distribution close to the $x = 0$ boundary. As the distance from the boundary increases there is an expected decrease in the population accumulation (as there is still distance remaining for the particles to drift). Since in any experiment the field of view will span some length and not just a single point in space, this differing behaviour as a function of distance from the wall will have a significant effect on any fitting of experimental data. Across some field of view with size $B$, the resultant population behaviour can be described as the average of the population distribution at each point encompassed in that field of view, defined as $N_{Beq}(t)$:

$$N_{Beq}(t) = \frac{1}{B} \sum_{i=1}^{B} n(x_i) \tag{4.26}$$

Where $N_{Beq}(t)$ is the evolution of the average number density of the population within a fixed distance of the boundary, where $B$ is determined by the size of the observation window. This is demonstrated in Fig 4.9b as the solid black line, denoting the average population value of the plotted range of $x$ values.

A few points should be raised here. Firstly, this is only valid at sufficiently low particle concentrations such that hydrodynamic interactions between particles can be ignored. For semidilute suspensions the diffusion coefficient can be augmented to account for collective diffusion with steric/hydrodynamic interactions. Finally, the diffusion coefficient used in these calculations are assumed to the be the diffusion coefficient of a Brownian particle. This is not the case with *M. pusilla*, but since neither particle size or interactions feature explicitly in the model it is a reasonable assumption to treat the cells as particles of a size such that the diffusion coefficients are equivalent, retaining the validity of the model.

### 4.5.2 Fitting to the experimental data

Fitting this model to the experimental data shown in Fig 4.8a with a fixed value of the diffusion coefficient ($D_t = 1.17\mu\text{ms}^{-2}$) gives remarkable agreement for the evolution of the particle number density in the region near the boundary. Leaving the drift velocity $u$ as a free-fitting parameter the phototactic response can now be quantified across a range of intensities and wavelengths examined. Fig 4.8c gives the fitted phototactic drift velocity $u$ for these experimental conditions. There is a positive response for all the combinations of wavelength/intensity, but the strength of the response does not appear to have any clear dependency on either variable. The only noticeable trait is the weaker response to the red light stimulus at low intensity compared to the blue/green wavelengths.

From these experiments it is confirmed qualitatively that *M. pusilla* is indeed a strongly phototactic organism as previously noted [161] but the magnitude of the response is quite low: $u$ never exceeds $4\mu\text{m.min}^{-1}$. The next step is to establish the cell motility parameters and how variations in these microscopic parameters can lead to the observed population behaviour.

## 4.6 Individual cell phototaxis

Having established the presence of phototaxis at the population, there must be some changes to the single cell swimming behaviour in response to the light stimulus. This took a significant amount of work and data collection to realise - over a million trajectories were analysed in efforts to locate the modulation in swimming behaviour responsible for the observed phototaxis. Cells were stimulated at a specific wavelength and intensity ($\lambda = 625\text{nm}, I = 300\mu\text{E.m}^{-2}\text{.s}^{-1}$) along the $x$-axis (equivalent to a run angle of $\phi = 0$) and recorded between $0 - 45$min (referred to as "short"

Table 4.2: Mean values of the cell motility parameters for three different data sets with standard errors. Control: no external stimulus. Short: $0 - 45$ mins exposure. Long: $90 - 120$ mins exposure.

| Motility Parameter | Control | Short exposure | Long exposure |
|---|---|---|---|
| Run Length $\langle L \rangle$ ($\mu$m) | $4.54 \pm 0.01$ | $4.55 \pm 0.02$ | $4.45 \pm 0.01$ |
| Run Duration $\langle T \rangle$ (s) | $0.20 \pm 0.04$ | $0.20 \pm 0.04$ | $0.20 \pm 0.04$ |
| Stop Duration $\langle \tau \rangle$ (s) | $1.05 \pm 0.04$ | $1.035 \pm 0.04$ | $1.05 \pm 0.04$ |
| Peak Speed ($\mu\text{m.s}^{-1}$) | $31.53 \pm 0.02$ | $31.22 \pm 0.03$ | $31.47 \pm 0.02$ |
| Run Speed ($\mu\text{m.s}^{-1}$) | $22.89 \pm 0.02$ | $22.59 \pm 0.02$ | $22.66 \pm 0.02$ |

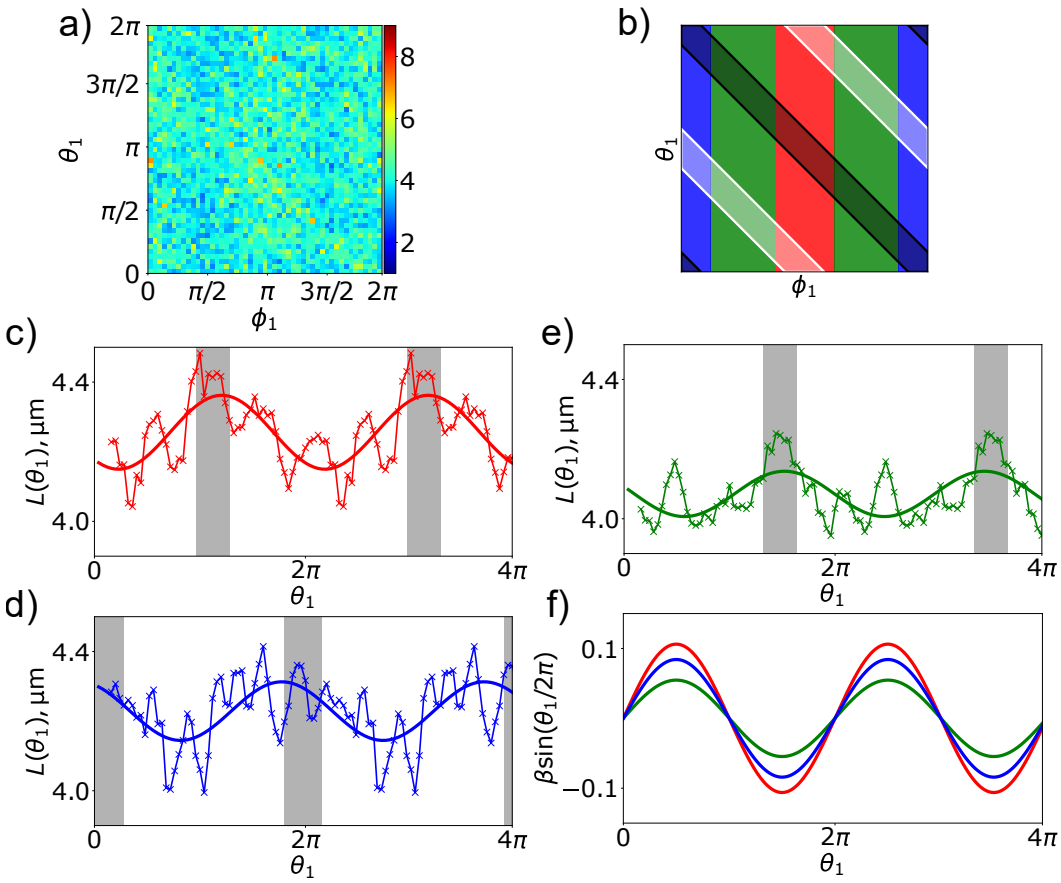


Figure 4.10: **Single-cell phototaxis of *M. pusilla*. a).** Distribution of the run length $L(\phi_1, \theta_1)$ - the run length following a run of angle $\phi_1$ and reorientation $\theta_1$. **b).** This can be separated into three regions where the previous runs ($\phi_1$) were directed: away (red), towards (blue) and perpendicular (green) to the light source. Runs that reorientate towards/away from the light fall in the grey/white areas respectively, referred to as zones. **c-e).** The distribution of $L(\phi_1, \theta_1)$ for the three light conditions with the signal repeated and fitted with a sinusoidal curve to highlight the trends. Runs reorientated back towards the light are highlighted with grey zones, which are longer than runs in other directions. **f).** Magnitude of the sinusoidal fits, showing a stronger response in the cases where the cells undergo a reversal back towards the light (red).

exposure). Surprisingly almost none of the microscopic cell motility quantities (run angle, run length, reorientation angle, run duration etc.) noticeably change apart from a small drop in the tumble duration $\tau$. The lack of change in the run length distribution as a function of $\phi$ instead suggests that it is small spatial asymmetries that produce the phototactic motion. Trajectories were also studied for stimulation times of $90 - 120$mins (referred to as "long" exposure) to investigate any saturation

of response. Table 4.2 gives the motility parameters for these three (control, short, long exposure) data sets and as is readily apparent there is no meaningful change between any the of the motility parameters between the different stimulations.

### 4.6.1 Considering the full-cycle

To fully determine the phototactic method we need to instead consider the full run-tumble-run cycle. In particular, the run length $L(\phi_1, \theta_1)$ where $\phi$ is the *previous* run angle and $\theta$ the subsequent reorientation and $L$ is the run length of the *following* run. Fig 4.10a shows the distribution of $L(\phi_1, \theta_1)$, with the value of $L(\phi_1, \theta_1)$ given as the colour, where we can see that it is not uniform. Going further, we divide this plot into three regions as shown in Fig 4.10b: previous runs orientated away from the light (red), previous runs orientated towards the light (blue) and previous runs orientated orthogonal to the light (green). The forward/backward regions were chosen by selecting runs that were within $\pi/4$ of the light axis, then runs outside of this were assigned to the orthogonal regions. Labelled on top of these regions are grey/white zones which define zones where the combination of $\phi_1, \theta_1$ orientate the subsequent run towards/away from the light respectively. We will refer to these zones as the "phototactic zones".

Averaging over $\phi_1$ gives $L(\theta_1)$ for each of the three zones, which are shown in Fig 4.10d-f, where the signal has been plotted over two full periods to better show any signal modulations. The positive phototactic zones have been labelled in grey shading, and the signals fitted with a simple sinusoidal function $L = \gamma + \beta \sin(\theta_1 - \delta)$, plotted as solid lines over the data. In each case we see that $L(\theta_1)$ is maximal when the cell reorientates towards the light stimulus. Fig 4.10f shows only the fits with the phase and average value removed. Here we see that the runs that undergo a reversal and move back towards the light (red) have a stronger response than both those that continue towards the light (blue) and ones which were originally orthogonal.

### 4.6.2 Jump-diffusion simulations

Having identified a spatial asymmetry in the trajectories, the last step is to confirm that these can reproduce the observed population trajectories. To do this we ran a series of numerical experiments based on the two-dimensional jump-diffusion simulations of Jeanneret et al. [206] which built on the framework of Wiener/Poisson processes described in Chapter 2. In essence, we model the two-dimensional projection of the stochastic trajectory of a cell, $(x(t), y(t))$ as being:

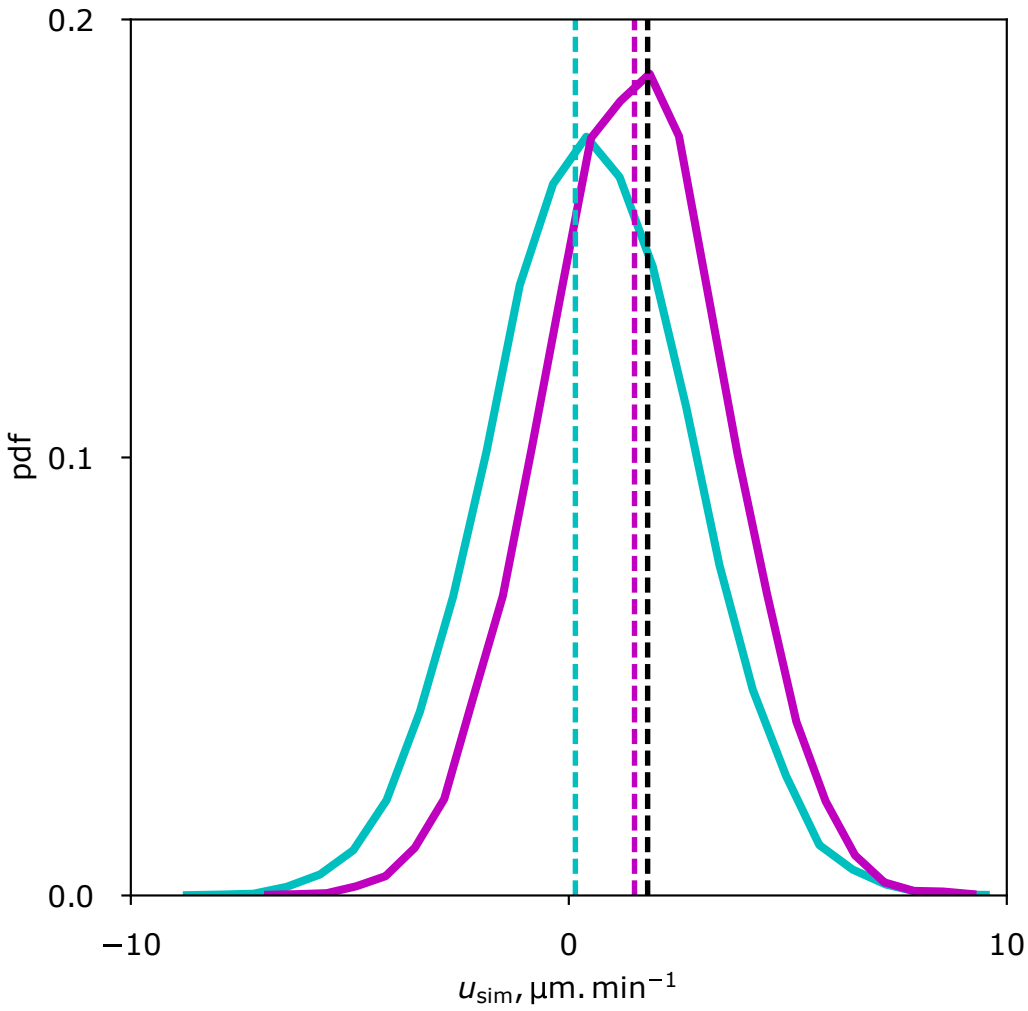


Figure 4.11: **Jump-diffusion simulation drift distributions.** Distribution of the drift velocities (full lines) and average drift velocities (dashed) for the jump diffusion simulations with and without light (magenta/cyan) respectively. The simulations with light stimulation reproduce the experimental population drift for this set of intensity/wavelength (black dashed line).

$$\begin{aligned} dx(t) &= \sqrt{2D_W}dW_x(t) + L\cos(\phi)dP(t) \\ dy(t) &= \sqrt{2D_W}dW_y(t) + L\sin(\phi)dP(t) \end{aligned} \tag{4.27}$$

Which combines a standard Wiener process $dW_{x,y}(t)$ with some diffusivity $D_W$, with a Poisson process for the jumps, $dP(t)$, which is characterised with an average time interval between the jumps $\tau$. At each timestep $\Delta t$, the particle undergoes a random walk with diffusivity $D_W$. To include the Poisson process, at

each timestep a random number in the (open) interval $(0, 1)$ is drawn. This open interval is partitioned into a centered interval of length $\lambda\Delta t$, where $\lambda = 1/\tau$, and the complement of this centered closed interval. If the randomly generated number is inside this closed centered interval then a run is started, else if the number is in the complement then a run does not start. To be precise, if: $a \in (0, 1)$ is in the closed centered interval $[(1 - \lambda\Delta t)/2, (1 + \lambda\Delta t)/2]$, a run starts. Once a run has started it has a fixed run duration and a second run cannot start whilst a run is in progress nor can the particle diffuse in this time. After the run has been completed, the procedure repeats with a new random number picked to choose between a random step or a run and thus continues the jump-diffusion process.

**The modifications**

These simulations were modified to incorporate the specific motility responses of *M. pusilla*. In both the control and phototactic cases, $2,000$ particles were simulated for a duration of $t_{end} = 5400$s with a timestep of $\Delta t = 0.004$s. Particles were given a previous run direction $\phi_0$ and reorientation $\theta_0$ sampled randomly from $[0, 2\pi)$ to give the initial run angle $\phi_1$. Each jump length is sampled randomly from the distribution of run lengths as a function of the previous run angle/reorientation - i.e. for the $i$th jump, we sample from $L(\phi_{i-1}, \theta_{i-1})$. After each run the particle samples a waiting time based on the exponential tumble distribution (Fig 4.5), then during this time it diffuses both rotationally ($D_{rot} = 2.1\text{rad}^2.\text{s}^{-1}$) and translationally ($D_{Brown} = 0.34\mu\text{m}^2.\text{s}^{-1}$, chosen as this is the equivalent spherical radius $R = 0.63\mu$m for the particle). The rotational diffusion during this waiting time coupled with the probability of undergoing a reversal ($\Gamma = 0.55$) produces the reorientation angle $\theta_1$. From $\phi_1, \theta_1$ the run length for the next run can then be sampled and the process repeats for the duration of the simulation. During a jump a particle cannot diffuse or start another jump. From these simulations, we can then define a drift velocity of each simulated cell as $u_{\text{sim}} = (x(t_{end}) - x(0))/t_{end}$.

Fig **??** presents the results of these simulations. In cyan we see in the control case there is no average drift along the light axis, whereas when the light stimulus is switched on (magenta) there is a clear bias towards the light with a simulated average drift of $< u_{\text{sim}} >= 1.5 \pm 0.02\mu.\text{min}^{-1}$, which is very close to the experimental value of $u_{exp} = 1.8 \pm 0.3\mu.\text{min}^{-1}$ for this wavelength and intensity.

## 4.7 Light detection hypotheseses - link to photosynthetic activity

Up to this point we have established that *M. pusilla* is indeed a strongly phototactic organism that is able to modulate its run length to produce a net population drift towards the light stimulus. Compared to other organisms classically studied for phototaxis such as *Chlamydomonas reinhardtii* however, *M. pusilla* does not have a dedicated eyespot for light detection which begs the question: how does *M. pusilla* detect the light source? One possible answer could be related to cell lensing [207] but this will be discussed in Chapter 5. Here we propose the hypothetical mechanism: that the phototactic response is mediated by the photosynthetic activity of the cell, which takes place in the chloroplast located in a plastid in the front of the cell [161]. In such case, the decrease/increase of the photosynthetic activity during a run away from/towards the light might trigger an increase/decrease of the swimming speed as the organism reverse. In the case where the cell runs in a path approximately perpendicular to the stimulus direction the photosynthetic activity would not change substantially, thus preventing the organism from effectively determining the direction of the light stimulus. This could be a way of explaining why in the case where the previous run is perpendicular to the light source, the increase in the run length is reduced in comparison to runs that were initially on the light axis (Fig 4.10f). Despite this being a plausible mechanism given the experimental data presented here, further investigation should aim to understand the complex biochemical processes taking place upon photo-stimulation as well as the flagellum, apparatus dynamics.

### 4.7.1 Phototaxis vs. sedimentation

The overlying question however is why does *M. pusilla* undergo phototaxis. The drift is extremely slow so the cell would be, in theory, unable to respond to small variations in the local light intensity efficiency or effectively. It has previously been suggested that *M. pusilla* uses its phototaxis to counter-balance the effects of sedimentation to keeps its vertical position in the water column [95]. Preliminary measurements of the sedimentation speed of *M. pusilla* support this hypothesis but more experimentation is needed to fully confirm if phototaxis can indeed be used to maintain the cell's vertical position.

## 4.8 Conclusion

Previous studies have reported the existence of phototaxis amongst the dominant marine pico-eukaryote *M. pusilla*, no clear picture of both the magnitude and the microscopic origins of this response has yet been established. Here by combining population-level and single-cell tracking as well as numerical simulation we have shown that this globally important species is capable of regulating its motility in response to directed light stimuli, thus confirming the presence of phototaxis.

By examining a total of $1,163,617$ single-cell tracks both with and without light stimulation, we have shed light on both the strategy *M. pusilla* uses to navigate and explore its environment and the way it manages to drift towards a light source. Interestingly, the cells perform a type of motion never reported before, which we name as "*stop-run or reverse*" (although a similar motility pattern has been reported in *E. coli* after forced body elongation [208]). This name reflects the fact that the cells frequently stop in order to partially reorientate via seemingly enhanced-rotational diffusion while they "choose" afterwards to move forwards ("run") or backward ("reverse") with respect to their previous run direction. Depsite variants of run-reverse motions being common amongst marine prokaryotes this is (to the best of our knowledge) the first case of such behaviour in marine eukaryotes.

The motility strategy is most certainly a consequence of the comparatively simple propulsion mechanism of the cell - a single rotating flagellum - which does not allow the cell to actively steer towards any controlled direction, despite the data presented here suggesting an active enhancement of the stochastic reorientation process. This contrasts with most other algae which do have dedicated eyespots to detecting light stimulus, such as *Chlamydmonas reinhardtii* and *Euglena gracilis*. Instead, the phototactic drifts experienced by *M. pusilla* originates from subtle directional asymmetries in run lengths. By examining the average run length for given values of the reorientations as a function of the previous run angle we observe increases/decreases in runs that are reorientated back towards/away from the light source respectively. This strategy is validated by incorporating the experimentally observed motility patterns into a series of jump-diffusion simulations and measuring the simulated population drifts that this produces.

The phototactic drift here is very faint, with a maximum fitted speed at the population level of $u \approx 4\mu\text{m.min}^{-1}$. This contrasts with previous studies on the chemotactic responses of this species where drifts were observed to be on the order of $\mu\text{ms}^{-1}$ [166]. The phototaxis observed here could be a method of counter-acting the sedimentation of the organism, in order to remain a the same position in the

water-column. Indeed the magnitude of the phototactic drifts obtained here agree with measurements of the sinking speed of the cells when no light stimulus is imposed anywhere. Most importantly however, is the fact that the phototactic response is always positive - i.e. directed towards the light stimulus. This is regardless of the wavelength/intensity of the source, even when it could have been expected to be harmful for the cell, for example via photo-oxidative stress. This again contrasts with other classical phototactic organisms such as *C. reinhardtii* which switch to photophobic behaviours at high intensities in order to prevent photodamage (i.e. from photoxidative stress). Despite the response being positive, the phototactic drift does not follow any wavelength-dependent scaling laws, suggesting that the cells use several distinct phytochrome photoreceptors whose activation depends on light intensity. Finally, *M. pusilla* is less sensitive to red than blue/green wavelengths at low intensities ($< 100\mu\text{E.m}^{-2}\text{s}^{-1}$). This most likely reflects the natural conditions of light in the oceans, where red wavelengths do not penetrate to depths greater than a few meters. As a consequence the peak sensitivity at low intensity would be shifted towards smaller wavelengths in order for the cells to keep track of the light when deeper in the water layer.

## 4.9 Key points:

The key points from this chapter are:

- *Micromonas pusilla* is perhaps the most globally dominant marine pico-eukaryote, with a cell body of $1 - 2\mu m$ and a single flagellum of length approximately $5\mu$m. It has previously been studied for host-virus systems and eukaryotic flagellum, but there has not been a dedicated motility or phototaxis study despite previous claims in literature of the cell being "strongly phototactic"

- We find that *M. pusilla* undergoes a novel motility strategy we call "stop, run or reverse" where the organism can tumble for long periods of time, followed by either continuing the previous run direction or reverse its direction. This is most likely linked to the fact that the cell can orientate its flagellum either in front or behind itself to swim as a puller/pusher-type swimmer respectively.

- At a population level *M. pusilla* is positively phototactic to a wide range of intensities across the visible spectrum with no obvious wavelength/intensity scaling laws. This can be modelled as confined one-dimensional drift-diffusion, and fitting the solution of this model to the population curves near a boundary gives a measure of the phototactic drift velocity.

- At the single-cell level, there is a directional run asymmetery where runs that reorientate back towards the light source are larger than those reorientated away from the light source. Using jump-diffusion simulations we verify that this can reproduced the experimental population drift by incorporating the cell motility parameters directly into the simulations.

- Further work should look to identify if a). the organism is capable of negative phototaxis and b). how the cell is able to detect the light source despite the absence of a dedicated eyespot. Our leading hypothesis is that the phototaxis is mediated by the photosynthetic activity of the cell, which is a valid explanation given our current experimental data.

# Chapter 5

# Universal avoidance response of *Micromonas pusilla*

Declarations: The raw experimental data shown in Fig 5.6 comes from experiments filmed by Jonathan Roberts during a summer research project which I co-supervised. Any data processing/analysis/modelling/discussions presented here is my own work.

## 5.1 Introduction

The previous chapter presented the first dedicated motility and phototaxis study of the dominant marine pico-eukaryote *Micromonas pusilla*. As a brief recap: *M. pusilla* is a $2\,\mu$m photosynthetic organism with a single flagellum which utilises a form of run-tumble motion to explore its environment. The run directions are not random - during a reorientation the cell will preferably reorientate to either continue in the previous run direction or in the opposite direction (run-reverse behaviour). It was shown that *M. pusilla* undergoes a slow positive phototactic drift towards a wide range of intensities and wavelengths across the visible spectrum. However there was not any evidence of a negative phototaxis response or photophobic response, which is the first goal of this chapter. We will then move onto a chemical response, likely attributed to cell death, and link the two responses to the existence of a global avoidance response of *M. pusilla* to harmful environments.

## 5.2 Step-up/step-down photo-responses of *Micromonas pusilla*

### 5.2.1 Initial discovery: attempting microlensing of *M. pusilla*

The principal open question from Chapter 4 was how can *M. pusilla* detect the light source given that it does not have a dedicated eyespot. This contrasts the classical eukaryotic phototaxis of *Chlamydomonas reinhardti*, where the cell has a dedicated eyespot with photoreceptors to detect the light source directly and change its motion accordingly. However there are other examples of phototactic microorganisms which do not have a dedicated eyespot, such as the cyanobacteria genus *Synechocystis*. Cyanobacteria, sometimes called "blue-green algae" are a phylum of bacteria which are also capable of photosynthesis. *Synechocystis* cells are not flagellated but rather use a "gliding" motility to propel themselves along surfaces. The physical mechanisms responsible for gliding motion remain unclear but there are several proposed mechanisms such as extension and retraction of pili in a "grappling hook" style of motion [118]. The phototaxis of *Synechocystis* was investigated in 2016 [207] which found that the cell morphology acted as a micro-lens to focus an image of the light source onto an internal photoreceptor. The cell can then use this to steer towards the light source, producing a positive phototactic behaviour[1]. It is possible that *M. pusilla* utilizes a similar mechanism to direct its phototaxis in absence of a dedicated eyespot, a phenonemena which can be investigated by using fluorescent microscopy (described in more detail in Chapter 2) but with the stimulating wavelength parallel to the sample plane.

Cells such as *M. pusilla* have an intrinsic natural fluorescence, more commonly referred to as autofluorescence. Fig 5.1a shows an example of the autofluorescence of *M. pusilla* imaged at 150× using an oil-immersion objective, stimulated with green light (G-2a Nikon filter cube, excitation wavelength $510 - 560\,\text{nm}$ and collecting emissions in the orange through to the near-infrared wavelength spectra (with a longpass cutoff filter of 590 nm). The cell imaged here is travelling horizontally (i.e. with a run angle of $\phi = 0$ with respect to the x-axis) and the fluorescent profile of the cell, measured at angles $\theta$ with respect to the swimming direction $\mathbf{v}$, is shown in Fig 5.1b. In this case, the cell is swimming sufficiently slowly that it is possible to measure the fluorescent profile over multiple rotations to build up a picture of fluorescent emissions over the surface of the cell. Fig 5.1c shows the

[1] Technically speaking the cell moves away from the detected light source which is in the opposite direction to the physical light stimulus, so the positive phototactic response is in fact a negative response to an image of the physical light source.

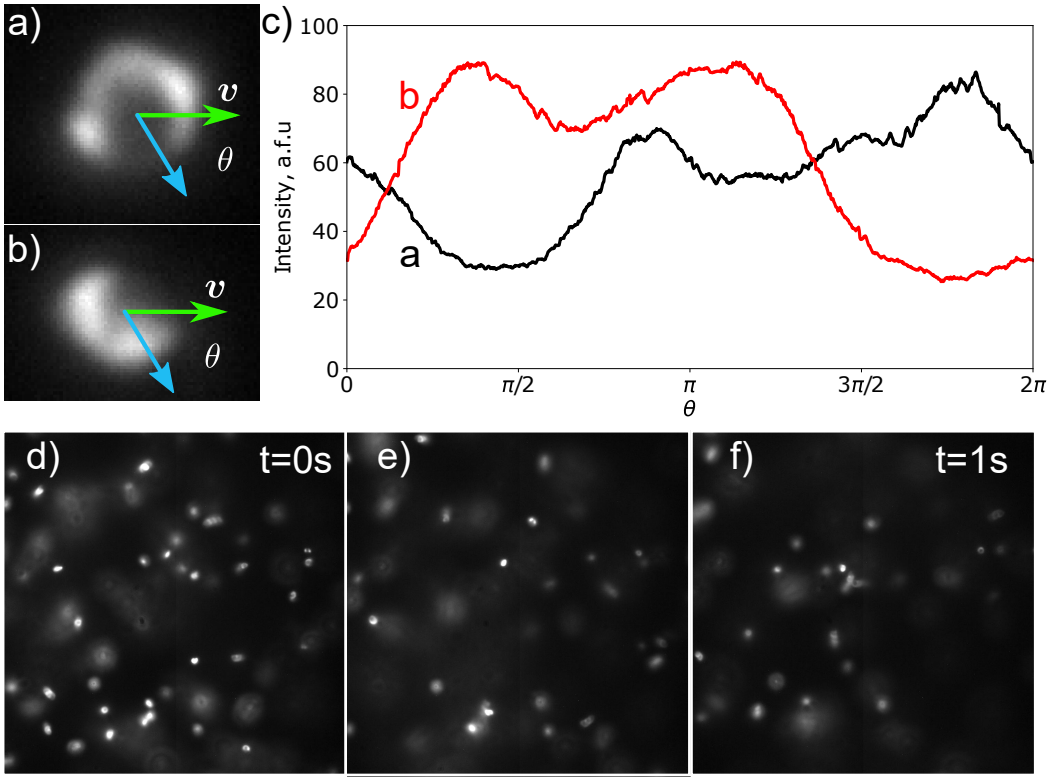


Figure 5.1: **Autofluorescence and photophobic response of *M. pusilla*. a-b).** Fluorescent profile of the cell at two different time steps, swimming in the marked direction, taken at 150× magnification. During swimming the cell rotates, exposing a different fluorescent profile at each step. **c).** The average fluorescent profile of the cell for the two time steps shown plotted as a function of $\theta$ measured clockwise around the cell. **d-f).** Photophobic response of *M. pusilla* to blue excitation. In less than a second the cell population has dramatically decreased, in complete contrast to the normal behaviour where the population should remain roughly constant in this time interval. This is due to cells switching to a continuous mode of swimming which results in cells rapidly escaping the field of view.

fluorescent intensity profile for phases of the rotation cycle, where we see that the fluorescence is (as expected) focussed in different regions of the cell

During the above experiments investigating the fluorescence of *M. pusilla* it was found that with a blue filter (FTIC), the cells would switch from their usual run-tumble/dithering behaviour and suddenly all become active and attempt to escape the stimulating light source. Fig 5.1d-f demonstrates an example of this where in less than a second the cells have swum out from the field of view when exposed to the excitation source, whereas in normal brightfield conditions the cells would not be affected. This is the first recorded instance of photophobic behaviour in *M.*

*pusilla*, and contrasts with the purely positive responses shown in Chapter 4. These responses have been labelled photophobic since they act to reduce the exposure of the cell to the light stimulus, though it should be noted that this response could equally be described as a photoactivation, where cells are "activated" in response to sharp light conditions. For the purpose of this thesis these responses will be referred to as photophobic, and it is hoped that future work should look to confirm the true nature of this novel photoresponse. The next step now is to characterise this behaviour and determine if there is any dependence on the wavelength and/or intensity of the excitation source. To do this we combine investigations of the bulk population response with single-cell studies to build a description of this response.

### 5.2.2 Step-up response leads to a population depletion

#### Methods

*M. pusilla* cells cultured in f/2 medium (an augmented artificial seawater growth medium [197]) were loaded into 400 $\mu$m thick glass capillaries and sealed with petroleum jelly to prevent flows due to evaporation. Images were taken with brightfield illumination and light stimulation was provided through the objective using a FITC filter cube ($513 - 556$ nm, $467 - 498$ nm emission/excitation wavelengths respectively) to stimulate with blue light, as shown in Fig 5.2a. The light stimulus encompasses the entire field of view, as per standard epi-illumination techniques. In the experiments of Fig 5.2 a 40× Ph1 objective filmed with Grasshopper3 camera (Flir, formally Point Gray). Light intensity is measured before the objective as labelled in Fig 5.2a. Filming and stimulation start at $t = 0$, with the cells being recorded at 3 frames per second for 206 s and the population counted at each time step (normalised to the population at $t = 0$). Light intensity was kept constant for the duration of filming. Each intensity was repeated at least 20× with fresh capillaries to ensure cells were not subject to multiple exposures.

Results here are presented in terms of *the intensity measured before the objective*, as with the available sensors this is the most reliable measurement that can be made, but the power projected onto the sample will be significantly greater than the powers used in the phototaxis experiments of Chapter 4.

#### Results

As seen previously, exposing *M. pusilla* to a sharp, intense light stimulus triggers a photophobic response in the cells where they switch from their "normal" run-tumble style of behaviour to a continuous swimming mode in an attempt to flee the harmful

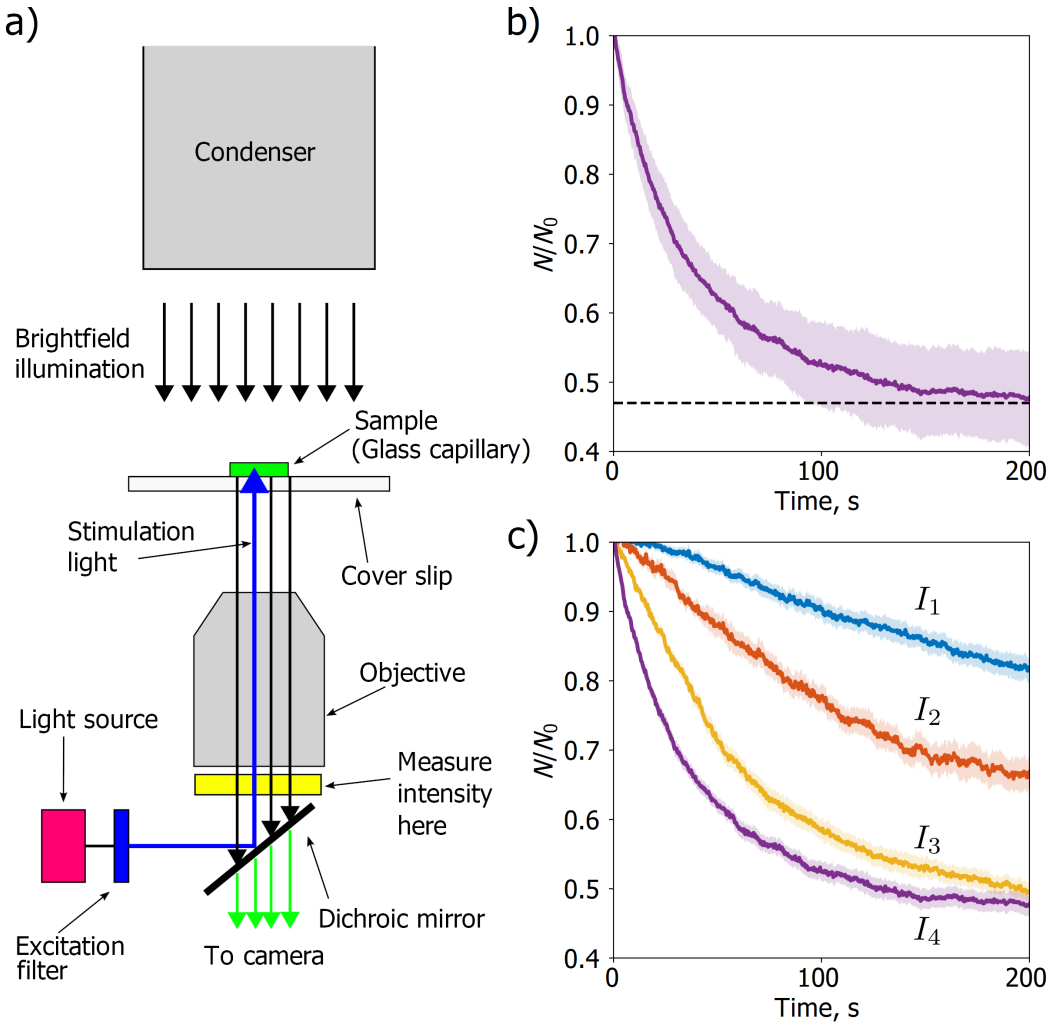


Figure 5.2: **Population depletion due to a photophobic response. a).** *M. pusilla* were loaded into a glass capillary then imaged with a combination of bright-field to film the cells and epi-illumination to stimulate the cells. In these experiments the imaging (and stimulation) is from a 40× Ph1 objective with a FITC cube to select the excitation wavelength. The filming and stimulation both begin at $t = 0$, and the population in the field of view is recorded. **b).** Population response for $23.3\,\mathrm{W.m^{-2}}$ with a standard error shaded. The population quickly decays to approximately $0.47N_0$ where only the non-responsive cells remain in the field of view. **c).** Population responses for different intensities of the same wavelength ($I_{1,2,3,4} = 2.2, 8.5, 20.2, 23.3\,\mathrm{W.m^{-2}}$). There is a clear dependence on the stimulation intensity, with a seemingly maximum fraction of the population able to respond to the stimulation. For lower powers we see that there is a brief lag phase before the population depletion begins to become noticable.

light stimulus. A measure of this response can be taken from the speed at which the population escapes the area of effect of the light stimulus. Fig 5.2b plots this for stimulation intensity of $23.3\,\mathrm{W.m^{-2}}$, where $t = 0$ marks both the start of filming and the beginning of the exposure of the stimulus. Here we see a rapid decay to a under half the original population count, meaning that approximately only half of the cells exhibit this step-up response to the light stimulus.

This was then repeated for four following intensities ($I_{1,2,3,4}$) as shown in Fig 5.2c. Here we see there is an obvious dependence on the stimulation intensity where the speed of decay is much faster at higher intensities compared to lower ones. Indeed, for the lower intensities there is observe a brief lag phase before the population begins to decay. This is due to the fact that the rate of activation (or rate of response) at these intensities is much slower than at higher intensities, which introduces a lag before the swimming cells begin to exit the field of view in significant quantities. In all of the examined intensities there is always a significant portion of the population that do not exhibit this step-up response for the duration of the experiment.

### 5.2.3 Existence of a step-down response

Having confirmed a clear intensity-dependence on the step-up response, the scale is changed to study the single cell dynamics that form this response. The same physical experiments as previous were used but now the cells are filmed at a higher framerate (of 30 frames per second) for three 45 s periods: before illumination, during illumination and after illumination. A normalized instantaneous frame velocity is calculated which is defined as the average instantaneous velocity of all the cells in the field of view during that frame normalized by the average frame velocity without any stimulation ($v_B$). Fig 5.3a shows a sketch of the anticipated behaviour we would expect to see: a constant activity before illumination (blue) followed by a jump in the activity as cells begin their step-up response (green). During the stimulation period there is a slow decay as activated cells begin to escape the field of view then in the final phase when the light is switched off (red) there is a decay back to the original activity levels as cells start to deactivate.

This however was not the observed behaviour, as shown in Fig 5.3b. The first two experimental phases demonstrate the behaviour we expect: constant activity followed by a sharp jump and a slow decay as cells are activated and begin to escape the field of view. However when the light is switched off (red), there is a brief but sharp spike in the average instantaneous velocity of the cells where a high proportion of cells in the field of view - importantly including those who did not exhibit the

first response - become active for a short period of time (approximately $5 - 10\,\mathrm{s}$). After this step-down response the activity then decays back to the original constant activity. The novel step-down response of *M. pusilla* is an unexpected discovery - the existence of the step-up response, whilst novel, can be explained as a means of escaping harmful light environments (which can be thought of as a motility-based means of photoprotection), but it is currently unclear why *M. pusilla* would have the need to evolve a step-down response.

One striking difference between the two responses is that cells that did not demonstrate the step-up response are capable of the step-down response. This is shown in Fig 5.4, which shows the active fraction (i.e. cells with an instantaneous speed above $15\,\mu\mathrm{m.s}^{-1}$, $N_{Active}$) to the current total number of cells in the field of view ($N_{Total}$), where the cells were stimulated for one minute. Both the step-up and step-down responses have the same activation rate (green and red curves respectively), with a constant activity without any stimulus (blue). However, looking back to Fig 5.2b, the step-down response has already depleted the population by approximately so intuitively it would be expected that the more "responsive" cells would have already left the field of view. The fact that the same proportion of cells exhibit the second response suggests that there is indeed some cross-over between the two responses, though further experimentation is needed to decouple those cells that exhibit both responses from cells that just undergo one of the two responses.

**Time-dependence of the step-down response**

Taking the step-down response a step further, we then investigated if the strength of the response for different exposure durations - i.e. changing the duration of the second phase of Fig 5.3b to see if there is any affect on the strength of the response during the third phase. For these experiments the setup was as per Fig 5.2a but a $20\times$ objective was used instead to increase the field of view to reduce the escape rate of the cells from the field of view. Three different exposure durations were chosen: $5, 10, 15\,\mathrm{s}$. First we measure the population depletion during the step-down response for these three different exposure durations, shown in Fig 5.3c. For the first two exposure durations less than 5% of the cells escape the field of view, but for a slightly longer exposure of $15\,\mathrm{s}$, nearly 20% of the population of *M. pusilla* escape due to the step-down response. This helps explains the initial decay of the step-down response of Fig 5.3b: the strength of the response decays in a similar manner as that of the step-up response due to the activated cells escaping the field of view as a result of the response.

Focussing instead on the cell activity due to the step-down response (Fig

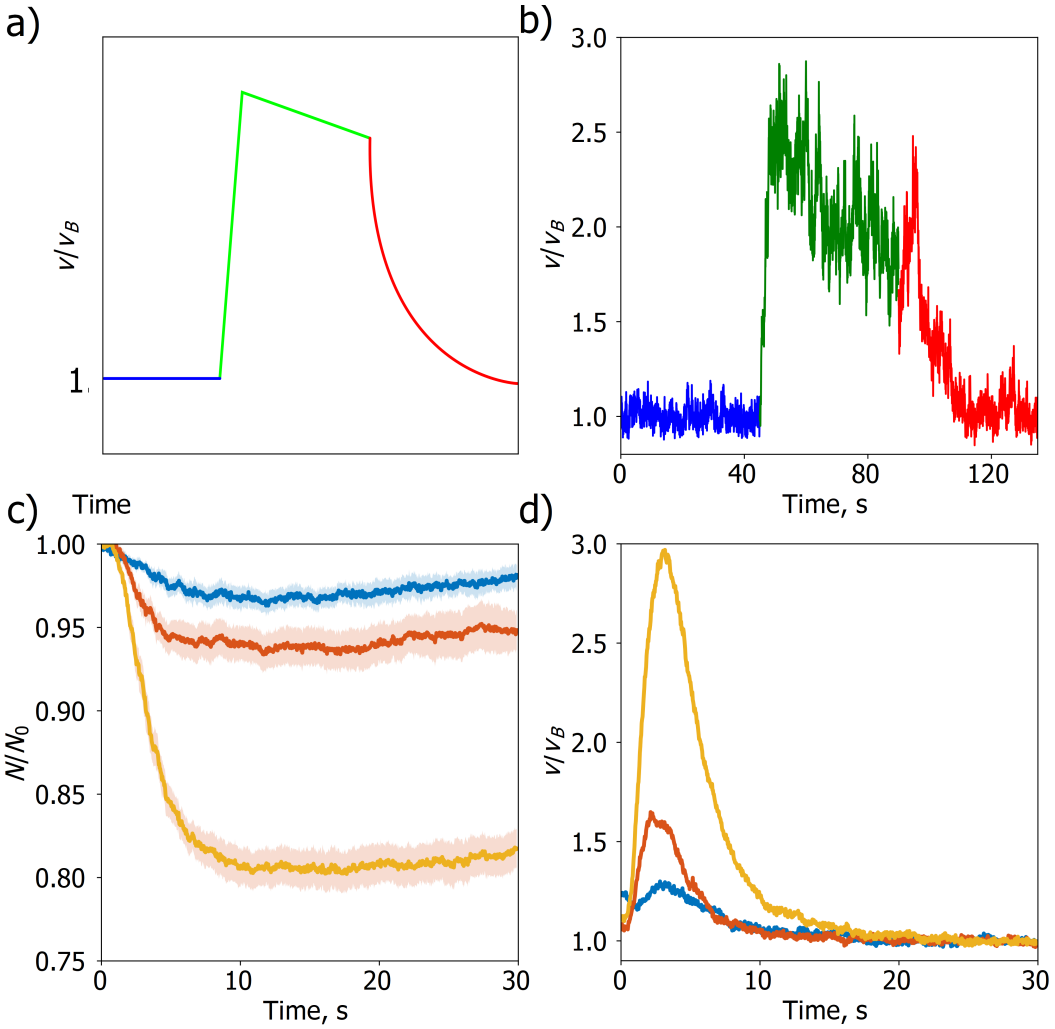


Figure 5.3: **Step-up/down photoresponses of *M. pusilla*. a).** Expected behavioural response of the step-up response: a constant level of activity before exposure (blue) follwed by a sharp jump upon exposure (green) which decays as cells escape the field of view, followed by a decay back to the original population activity as cells "deactivate". **b).** Cell response curves, normalized by the background velocity $v_B$. For the first two phases (before/during exposure, blue/green resp.) the behaviour is as expected, but after exposure (red) almost the entire cell population becomes active for a brief period of time ($5-10\,\mathrm{s}$). **c).** Population depletion due to the step-down response for the three exposure durations: $5, 10, 15\,\mathrm{s}$. This demonstrates the differing response strengths given the change in exposure durations, with only $1-5\%$ of cells escaping the field of view due to the step-down response for an exposure of $< 10\,\mathrm{s}$ compared to the $\approx 20\%$ of cells that escape after an exposure of $15\,\mathrm{s}$. **d).** Strength of the step-down response. For the shorter two exposures the subsequent step-down respoinse is relatively weak in comparison to the response of (b), but for slightly longer exposure durations the duration of response is comparable.

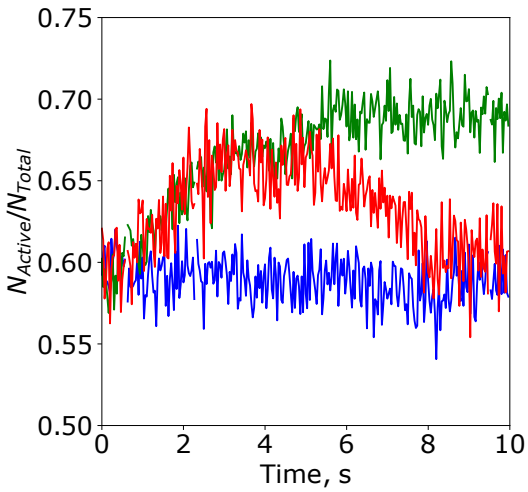


Figure 5.4: **Fraction of the cell population active during the step-up/down responses**. Active fraction (where $N_{Total}$ is the current total number of cells in view, and $N_{Active}$ those swimming above 15 $\mu$m.s$^{-1}$) at that instant. The two responses (red/green) have similar initial activation curves though we see the step-down response (red) starts to decays back to the background activation levels after a few seconds. Importantly, the majority of the cells affected by the step-up response have already left the field of view before the step-down response is triggered, so whilst the active fraction of the population looks similar between the two responses in reality many of the step-down cells will not have been affected by the step-up response.

5.3d) we see the reason for the sharp population drop in the 15 s exposure case, with a clearer dependence on the strength of the response based on the exposure duration. For the 15 s case the cell activity decays back to the original value after approximately 10 s, which is consistent with the duration of the step-down response observed in Fig 5.3b, where the cells had been exposed for 45 s. The fact that there is a sudden increase in the strength of the response after $10 - 15$ s of exposure but effectively no change between $15 - 45$ s of exposure suggests that whilst the response is dependent on some minimum exposure duration $\tau_{\text{stim}}$, it is very much an "all-or-nothing" style of response: once the response has been triggered it is not modulated by the cells, instead it is more of a binary response to the drop in light intensity.

The photobehaviour here is in stark contrast to the phototaxis discussed in Chapter 4, but it would not be the only instance of a phobic-response with *M. pusilla*. We now describe a similarly phobic response but one that is entirely chemically-driven, and apparent triggered by individual cell death events.

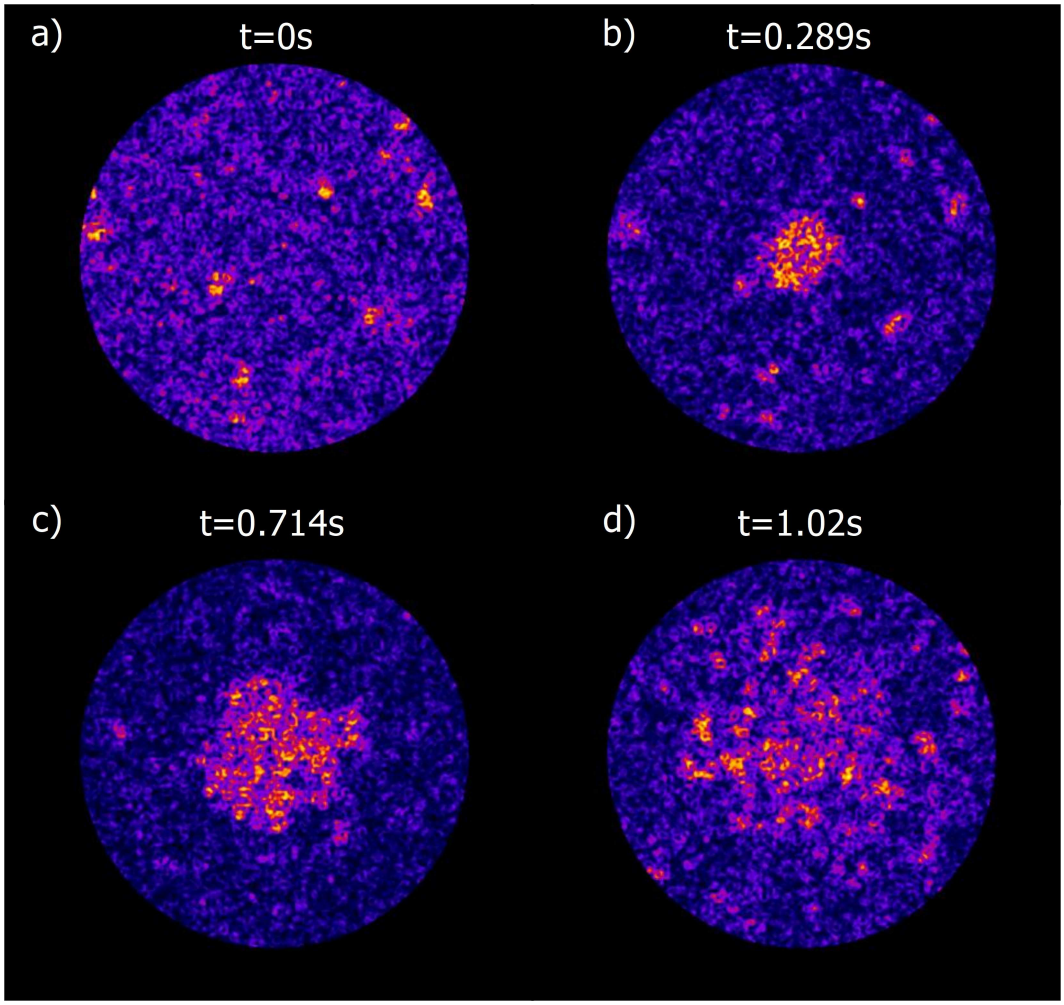


Figure 5.5: **Sample of a burst event**. In these figures a bright (yellow) value corresponds to a low correlation with the same pixel location in the previous frame so that any motion will appear bright in these plots. **a).** $t = 0$, a frame before the event begins. **b-c).** A small concentrated area of high cell motility appears and radiates outwards, "activating" more cells. **d).** At a certain point cells stop being activated by this "activation pulse" and the affected cells move away from the area causing the motility to eventually disperse and return to more normal conditions. The entire event lasts for only a few seconds.

## 5.3 Burst events

### 5.3.1 Initial discovery

In true physics fashion, this was a serendipitous discovery during the cell motility experiments of Chapter 4. In those experiments the majority of cells in the field of view would not be moving at the same time - cell movement would be seemingly

randomly distributed in the field of view. However, in an older sample, a strange collective event was observed where - starting from a single point - cells would be "activated" in a radially expanding manner and begin to swim continuously, not unlike the photoshock response discussed previously. Fig 5.5 shows an example of such an event. Here the frames are correlated with the following frame and adjusted using ImageJ to best show the motion of the cells - any motion between frames appears as a bright value against a dark background. In Fig 5.5a we see the typical case - a few cells are moving but there is not any sign of any collective response. A few frames later (Fig 5.5b) there is a small concentrated patch of movement in the centre of the field of view. Progressing a few frames further (Fig 5.5c) this area of cell motility has increased, until $1-2\,\mathrm{s}$ after the start of the event (Fig 5.5d) no more cells are activated and the motile cells begin to disperse from the local region.

This is a completely new phenomenon that has not been reported before in any microorganism, and represents an undocumented environmental response in an ecologically significant microorganism. To begin characterising this novel response we start with investigating the rates of these events to shed some insight on potential triggers of this response.

### 5.3.2 Methods

Cultures of *M. pusilla* were maintained in Gulliard's f/2 medium, prepared using artificial seawater (Sigma) in 500 ml quantities excluding the sodium-glycerophosphate to reduce any precipitation in the media. The cultures were grown in a diurnal chamber on a 16/8 hour light/dark cycle at a constant temperature of 20° C. A Nikon TE 2000U inverted microscope with an longbandpass filter (765 nm cutoff wavelength, Knight Optical UK) was used to limit any phototactic behaviour from the cells due to the imaging light. Cells were filmed at a variety of magnifications but typically at 20× magnification, enabling a wide field of view ($370\mu m$) whilst still maintaining individual particle recognition. Cells were loaded into a cuboid polydimethysiloxane (PDMS) chamber with internal dimensions $10\,\mathrm{mm}\times 10\,\mathrm{mm}\times 4\,\mathrm{mm}$ bonded to a glass cover slide with a Harrick oxygen plasma cleaner and sealed with petroleum jelly to prevent flows due to evaporation. Prior to filming the sample had been left to sediment for several hours.

#### Event frequency experiments

When characterizing the event frequency, the samples were filmed in four minute intervals for approximately 40 minutes spaced over a two hour period. During

these experiments the frame rate was lowered (to 10 frames per second) and the magnification decreased to produce a larger film duration and field of view. Events were identified by viewing the films back at an enhanced playback speed, and the approximate event start time extracted from the frame timestamps file generated by the camera.

#### Characterising the events

Contrasting with the above experimental methods, when characterizing the event dynamics a higher framerate and magnification was used (i.e. 30 frames per second, 20× magnification) to improve both the temporal and spatial resolution of the dynamics. A complete description of the analytical tools developed for analysing these events are described in detail later in Section 5.3.4.

### 5.3.3 Event description

Due to these events representing a completely novel phenomenon, there are a series of immediate questions to be answered about the dynamics of the event in order to gain insight into a potential event trigger. The logical starting point is to examine how the rate of these events change under different experimental conditions.

#### Frequency of events under different conditions

The fact that one of these events was not observed during the motility studies of Chapter 4 suggests that the event rate is so low that the probability of observing an event is extremely low. The question is does the fact that an event is observed later mean that the event rate is either extremely low or does it increase with time, increasing the probability of observing an event? It is reasonable to assume the latter for a number of reasons. Firstly, the experimental conditions around the cell are (where possible) maintained constant - the cells are maintained in the same growth media, filmed under the same illumination conditions in a temperature controlled environment and the PDMS walls of the chamber are constant. This last point is important as the thickness of the PDMS walls will mediate gas transport both into and out of the liquid surrounding the cells. The density of cells is roughly constant between experiments, and not high enough that cell-cell interactions are a likely event trigger. There are experimental elements outside of our control - such as the exact chemical/nutrient composition in each of the cell cultures, but for the purpose of the work here we assume they are constant, given cells were grown and sampled in a uniform manner using the same medium. Eliminating any

thermo/photo/mechanical triggers means that the most likely stimulus responsible is a chemical one. The fact that events are not observed at short time scales implies that there is not a sufficient concentration of this stimulus, or equivalently there are larger concentrations of this chemical at longer time scales. Given the experiments are as chemically isolated from the outside environment as possible (barring gas exchange through the PDMS), any changes in the chemical composition in the media will be due to the cells themselves - for example from metabolic waste [209]. If this is the case we should expect the rate of events to increase the longer the cells are contained in the millifluidic device, and that the rate of events should be larger when the cells are more active (i.e. during periods of higher cell activity due to photosynthesis in the day cycle for example). Likewise, cells recently diluted in fresh media should have a lower rate of events compared to cells in their original media.

Two experiments were carried out to investigate the event rates. In both experiments two chambers were recorded simultaneously with cells taken from the same culture with one chamber acting as a control. Firstly cells were centrifuged gently to form a dense pellet then, after removing the supernatant, the cells were washed and resuspended in fresh medium (Guillard's f/2). For the controls, the exact same centrifugation/supernatant removal procedure was carried out but the supernatant was simply put back into the sample instead of fresh medium. In the second experiment the control chamber was kept isolated from light sources whereas the second chamber was kept under constant illumination. The events were treated as random, independent events that occur at a constant rate $\lambda$ over a time interval of length $T$. Such events can be described by the Poisson distribution [210], where the probability of observing $k$ events in a time interval $T$ is given by:

$$P(N = k) = \frac{\lambda^k}{k!} e^{-\lambda} \tag{5.1}$$

Fig 5.6a plots the cumulative number of events over time for the case of cells in their original media (red) and resuspended in fresh media, and Fig 5.6b the fitted Poisson parameter $\lambda$ for each experimental time period taking $T = 120\,\mathrm{s}$ as the time interval (with standard error marked). Similarly, Fig 5.6cd plot the same data for the illuminated/dark chambers. The chambers were left to sediment for 2 hours in their respective conditions before filming. In both control cases (black), $\lambda$ is approximately constant for the first two time intervals with an significant increase in the last time interval. For the first experiment, where the cells have been washed and resuspended in fresh media (red, Fig 5.6ab), we see the fresh media has reduced the rate of events at longer time scales. This supports the hypothesis that there is

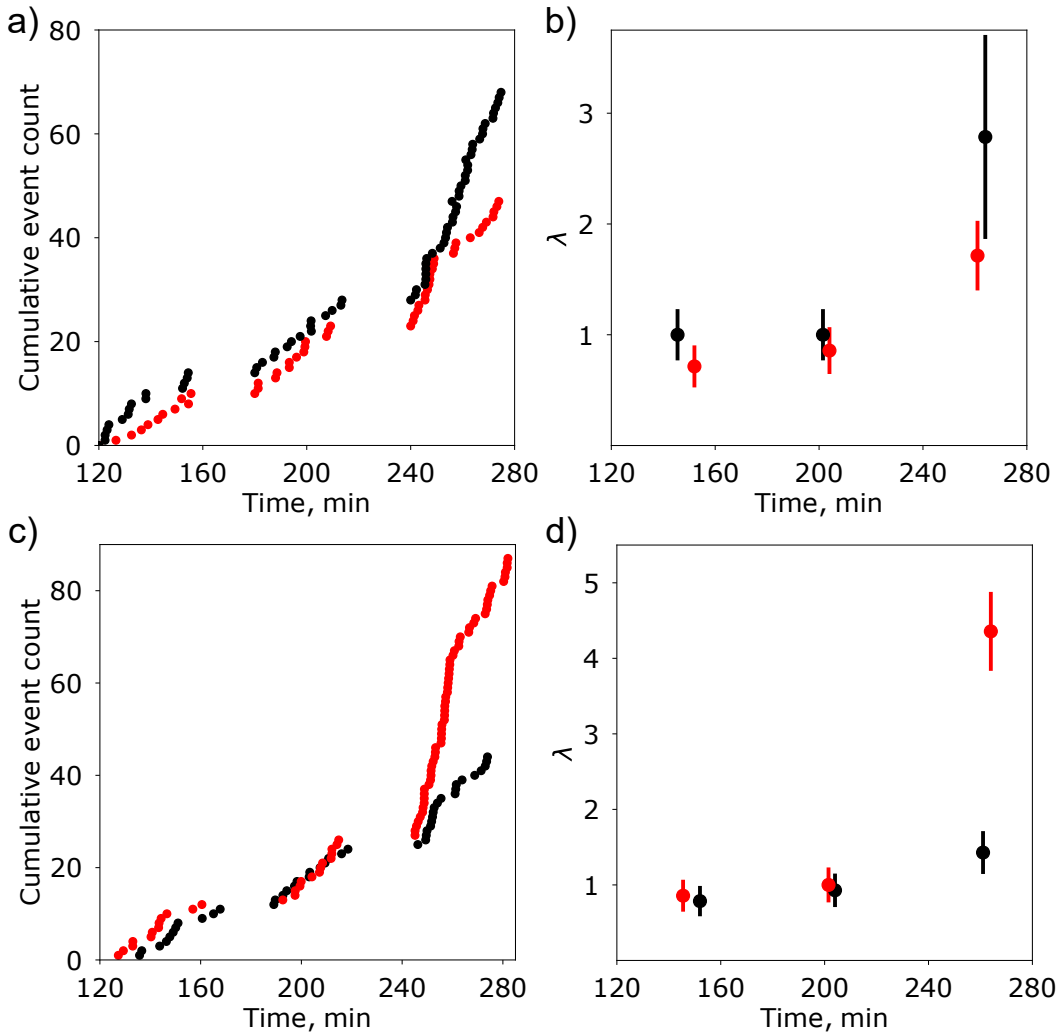


Figure 5.6: **Burst event frequency. a).** The culumlative event count with cells in their original media (black) and resuspended in fresh media (red). **b).** Fitted Poisson rates $\lambda$ for the three experimental time periods shown in (a), with a time interval of 120 s. There is a reasonable decrease in the event rate for the cells suspended in fresh media compared to those in the original media. **c).** Culumulative event count for cells constantly exposed to an external light stimulus (red) and those starved of light (black). **d).** Fitted Poisson rates for the three experimental periods shown in (c), with a time interval of 120 s. The cells that are constantly illuminated than the cells maintained in dark conditions show a dramatic increase in the event rate at later times in comparison.

a chemical trigger whose production is related to the presence of the cells as this is the only experimentally significant change between the two chambers.

A more dramatic change occurs in the illumination experiments. When the

cells are subject to constant illumination (red, Fig 5.6cd) the event changes by roughly a factor of 4 in the last time interval compared to the dark control chamber (black). Clearly $\lambda$ depends both on the duration the cells are confined for as well as a dependence on how active the cells are during this confinement. Given how during these responses the affected cells change to a continuous mode of swimming, not dissimilar to the previous photophobic response, we propose that there is a cell-produced signal/chemical that, when present in high enough concentrations, triggers the same style of avoidance response as if the cells were exposed to a harmful light stimulus.

**Event trigger**

During these experiments the cells are reasonably isolated from the outside world - barring gas exchange through the PDMS wall and any instability in the media (which we discard as a potential trigger), the most significant chemical change inside the device will be from the cells themselves. As previously discussed (primarily in Chapter 3), *M. pusilla* is one of the most dominant marine microoragnisms on the planet and is preyed upon by a wide range of organisms and viruses, including the *Micromonas pusilla* virus. It is logical to assume that *M. pusilla* could have evolved some defensive mechanisms in order to have reached its current global dispersal - there is evidence of this in the photophobic response previously discussed in this chapter. In the photophobic response cells begin to swim continuously to escape the harmful conditions they have been exposed to, similar to the individual behaviour in the burst event. However in these events the cells appear to be activating from a radially expanding cell-generated chemical source at apparently random spatial locations in the sample. Given the rate cells are lysed/predated upon in nature we propose that the chemical source is in fact a single cell that has burst/leaking into its local environment, and that the observed collective response is in direct response to a cell death. Fig 5.7 presents a sketch of the proposed mechanism. A single cell (Fig 5.7a, red) bursts - either from viral lysis or from a predator - and releases a nutrient patch into its immediate vicinity. This patch begins to diffuse outwards (Fig 5.7b, shading) and nearby cells detect this pollutant. The cells interpret this chemical signal as that a nearby cell has died and attempt to escape the local area by swimming continuously, not dissimilar to the photophobic response. The patch diffuses further and activates more cells (yellow) who all undergo this response. The initial patch distribution (i.e. Gaussian) will diffuse radially as shown in Fig 5.7d, which in combination with the detection threshold of the cells will define the radius of the detected patch at a given time (Fig 5.7d insert). Over longer period

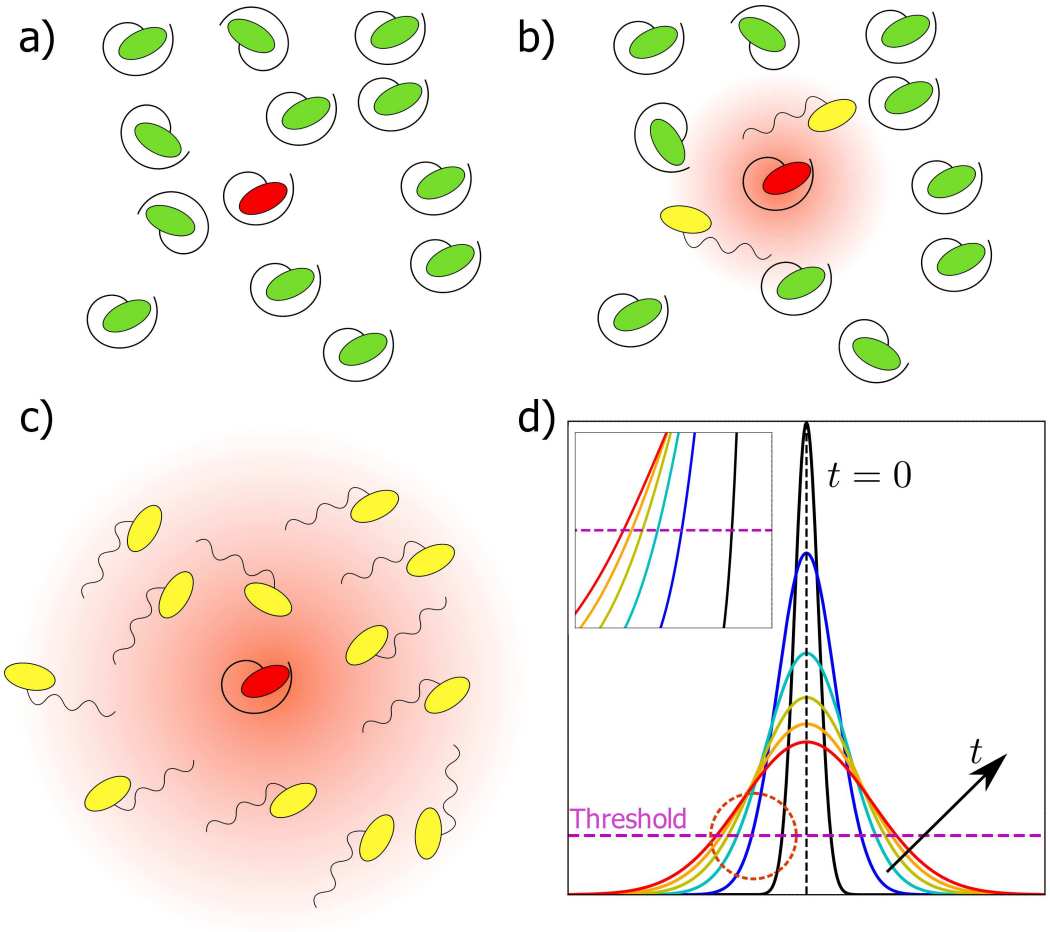


Figure 5.7: **Proposed mechanism of cell death leading to the burst response of *M. pusilla*. a).** $t = 0$ of an event - a single cell (marked as red), referred to as the "trigger cell" bursts/lyses/begins to leak etc. a pollutant into the surrounding media occupied by other cells (green). **b).** This pollutant patch (denoted by the orange shading) diffuses radially outwards from the trigger cell. When the concentration of this pollutant is above a certain threshold value around another cell, it is activated (yellow cells). These cells begin to swim continuously. **c).** The patch spreads further until all nearby cells are activated, creating a local patch of high cell motility. **d).** A diffusing patch with an initial Gaussian distribution at $t = 0/$. **Insert.** Defining a detection threshold $\Gamma$ (pink), we determine the radius from the trigger cell at which the concentration is high enough to activate surrounding cells.

of time the background concentration of this pollutant will rise, effectively lowering the detection threshold. Due to this a smaller perturbation (for example a slower cell leakage) is required to start an event and so the event rate $\lambda$ increases over time. In theory this can be verified by comparing the evolution of the event radius with the radius of a diffusing nutrient patch. To do this a number of tools were developed

to characterise the evolution of the event radius and the event duration, with care being taken to distinguish event front propagation due to moving cells and activated cells.

### 5.3.4 Characterising events

#### Measuring the radius of the event

#### Grid-correlation to determine the origin of the events

To measure the radius of the event we first need to determine the origin of the event. Fig 5.8a shows a typical bright-field image of a relatively dense population of *M. pusilla*, where the cells appear as dark spots in the image. The image was divided into a 10×10 square grid, then each grid square was correlated with the same grid but a number of frames further on (dependent on the frame rate, but typically a lag of 5 frames was used). There are a range of ways to calculate a correlation coefficient of a two-dimensional data set, but here we follow the approach of Dikbas et al. 2017 [211] to define two correlation coefficients based on the horizontal and vertical correlation respectively. Since the detection of the event relies on cell response, if there is (for example) an event starting at a point where there is a lack of cells in one direction/axis, by calculating a horizontal and vertical correlation coefficient maintains robustness in the analysis in case of any significant inhomogeneities in the local particle distribution. For events that expand symmetrically there should be little difference between the two coefficients. Firstly for a $m \times n$ matrix $\mathbf{A}$, the horizontal (vertical) variance is given by $\mathrm{Var_h}(\mathbf{A})$ ($\mathrm{Var_v}(\mathbf{A})$) where:

$$\begin{aligned} \mathrm{Var_h}(\mathbf{A}) &= \frac{\sum_i \sum_j \left(\mathbf{A}_{ij} - \bar{\mathbf{A}}_i\right)^2}{m \times n} \\ \mathrm{Var_v}(\mathbf{A}) &= \frac{\sum_i \sum_j \left(\mathbf{A}_{ij} - \bar{\mathbf{A}}_j\right)^2}{m \times n} \end{aligned} \tag{5.2}$$

Which gives us a measure of how the values of a matrix vary in both rows and columns. Next we define the respective covariance terms, which is a measure of how independent two variables are. For the two $m \times n$ matrices $\mathbf{A}, \mathbf{B}$, we define the horizontal (vertical) covariance as:

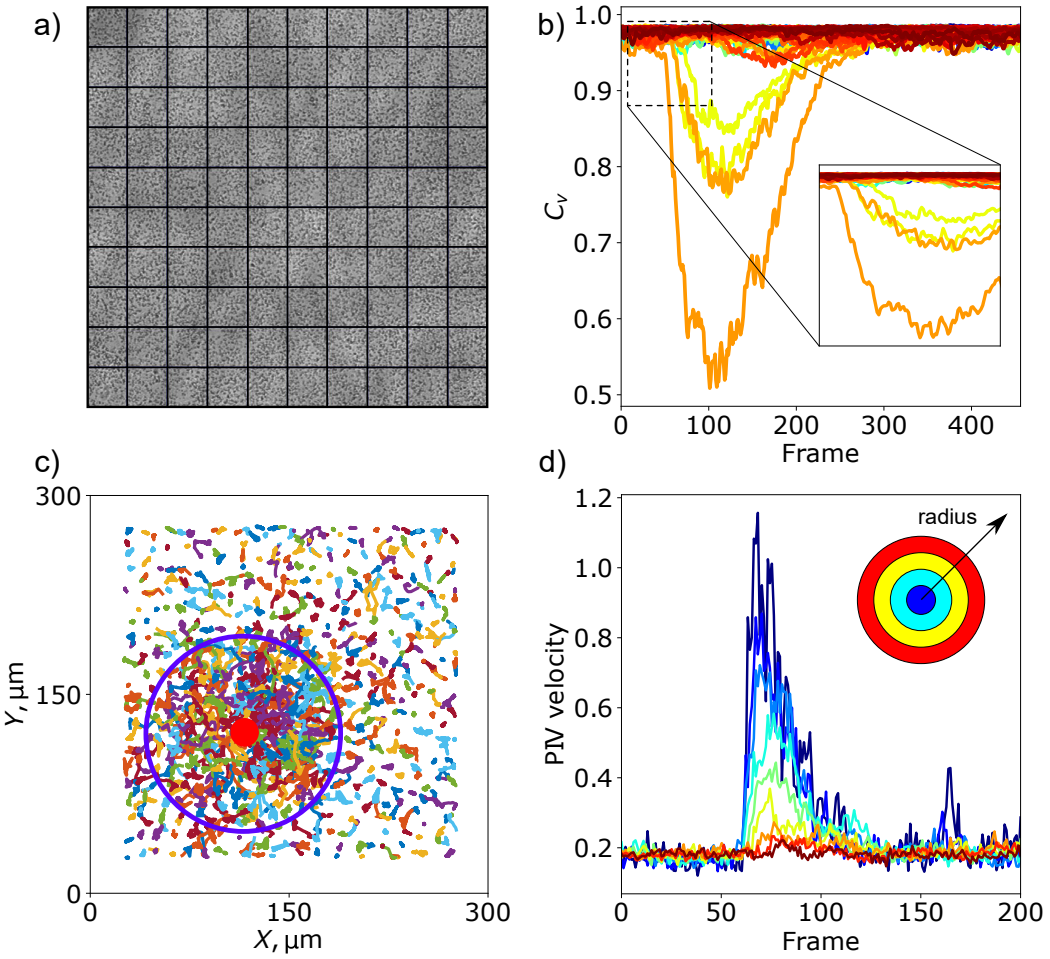


Figure 5.8: **Original methods for tracking the event front propagation. a).** A dense population of *M. pusilla*, where the image is divided up into a uniform $10 \times 10$ grid. **b).** Each grid square is correlated with itself with a separation of a few frames (typically 5 at $20 - 30$ frames per second), with the first large drop in the correlation coefficient $C_v$ pinpointing the origin of the event. **Insert.** A rough estimate of the event propagation can be obtained by analysing the subsequent drops in adjacent grid squares. **c).** PTV analysis, where the origin of the event is shown with the red dot. Tracking the density of trajectories can, for specific particle densities, give an accurate measurement of the event radius. **d).** Analysis of the PIV velocity field in concentric rings from the centre of the event provides a reasonable estimate of the event trajectory at high particle densities.

$$\begin{aligned} \mathrm{Cov_h}(\mathbf{A},\mathbf{B}) &= \frac{\sum_i \sum_j \left(\mathbf{A}_{ij} - \bar{\mathbf{A}}_i\right)\left(\mathbf{B}_{ij} - \bar{\mathbf{B}}_i\right)}{m \times n} \\ \mathrm{Cov_v}(\mathbf{A},\mathbf{B}) &= \frac{\sum_i \sum_j \left(\mathbf{A}_{ij} - \bar{\mathbf{A}}_j\right)\left(\mathbf{B}_{ij} - \bar{\mathbf{B}}_j\right)}{m \times n} \end{aligned} \tag{5.3}$$

Which allows us to define the correlations $C_{\mathrm{h}}, C_{\mathrm{v}}$ as the correlation values between two matrices $\mathbf{A}, \mathbf{B}$ as:

$$C_{\mathrm{h}} = \frac{\mathrm{Cov_h}(\mathbf{A}, \mathbf{B})}{\sqrt{\mathrm{Var_h}(\mathbf{A})\mathrm{Var_h}(\mathbf{B})}}, \qquad C_{\mathrm{v}} = \frac{\mathrm{Cov_v}(\mathbf{A}, \mathbf{B})}{\sqrt{\mathrm{Var_v}(\mathbf{A})\mathrm{Var_v}(\mathbf{B})}} \tag{5.4}$$

Using this definition of the correlation coefficients $C_{h,v}$ were calculated for each grid square, where $\mathbf{A}$ would be the grid square at time $t$, and $\mathbf{B}$ the same grid square at time $t + \Delta t$. Since the events involve large numbers of particles, this should result in a large drop in the correlation value of that grid square. Finally, since the events are apparently spherically symmetric, $C_{h,v}$ should be mostly similar and identify in which grid square the event starts, as this will be the grid square that contains the majority of the event. Fig 5.8b plots the evolution of $C_v$ over time for the grid squares in Fig 5.8a, and it gives us two crucial pieces of information: the initial grid square from the first (and in theory largest) drop in correlation, and an approximate measure of the event spread by subsequent drops in the surrounding grid squares (Fig 5.8b insert). With the principal grid square identified the process is repeated with both a decreasing box size and $\Delta t$ until a square is found such that height of the square is the diameter of the event in the second frame. The centre of this square is taken as the origin of the event.

Having established the origin of the event, the next step is to measure the radius of the event as it expands. This proved to be both an interesting and frustrating problem as the particle density was not constant between events, and had a major impact on the analysis methods used. Below there are two methods briefly summarised which were used in very specific examples to get an estimate of the radius/duration of events, followed by a more general method for a more consistent analysis of the event behaviour.

### PTV analysis

The first method trialled to measure the radius of the event utilised the individual particle trajectories that comprise the event. Fig 5.8c shows the plot of the particle trajectories in the vicinity of the event where there is a significantly higher density of trajectories around the origin of the event (marked with a red dot). For approximately the first second of the event this method does accurately follow the expanding radius of the event to the point that the moving cells begin to escape the area of effect of the event. The disadvantage of this method is that it relies on the particle density being within a very narrow band - dense enough that there are enough trajectories to extract a reliable estimate of the radius from, but not so

dense that PTV becomes almost impossible to rely upon. At low densities identifying the start location/time of an event reliably becomes extremely difficult, so these are discarded those and instead focus on the higher particle density events.

### PIV analysis

At higher particle densities PTV techniques become cumbersome and unreliable due to the combinatorics involved in the track algorithim. These limits require a different technique called particle image velocimetry (PIV). PIV is a flow visualisation technique that is able to measure instanaenous features of a flow such as velocity and vorticity. Standard PIV experiments involve the tracking of suspended tracer particles but can be used in this instance to determine features such as the starting frame of the event and in theory the expansion of the event. Analysing one of these events with PIV produces a velocity field for each time step which has a local maximum around the centre of the event. Examining the average PIV velocity in concentric rings of the image centred on the origin of the event should give a spike in velocity when the event front reaches each ring. An example of this is shown in Fig 5.8d, where the first ring (blue) gives the largest amplitude followed by subsequent delayed peaks as the event front propagates through the culture. The velocity is reduced in subsequent rings as the rings are defined with a radius width, therefore for larger rings will contain more values to average over in each ring.

Combining this method with the grid-analysis method it is possible to get a more accurate and reliable estimate on the total event duration, defined here as the time taken from the event starting for the activity in the affected area to return to normal background conditions. However using this tool to measure the radius produced some inconsistencies - the velocity field is highly sensitive to the grid size used in the PIV analysis, and was only reliable in high densities of particles. This still leaves the problematic regime of having too many particles for PTV to be effective but not enough that PIV was reliable, which unfortunately was the regime of many of the recorded events.

The last major drawback of each of these methods was the computational time. The analysis time per event was, on average, at least a day per event, and even then the results were not always reliable. With over 100 recorded events this was not a particularly efficient analysis routine given the unreliability of some of the event tracking. As such, a third method was developed which gives a dramatic improvement to both the efficiency and accuracy of the radius tracking, built off of the principles underlying the previous methods, which will now be described.

**Image summation leads to general method**

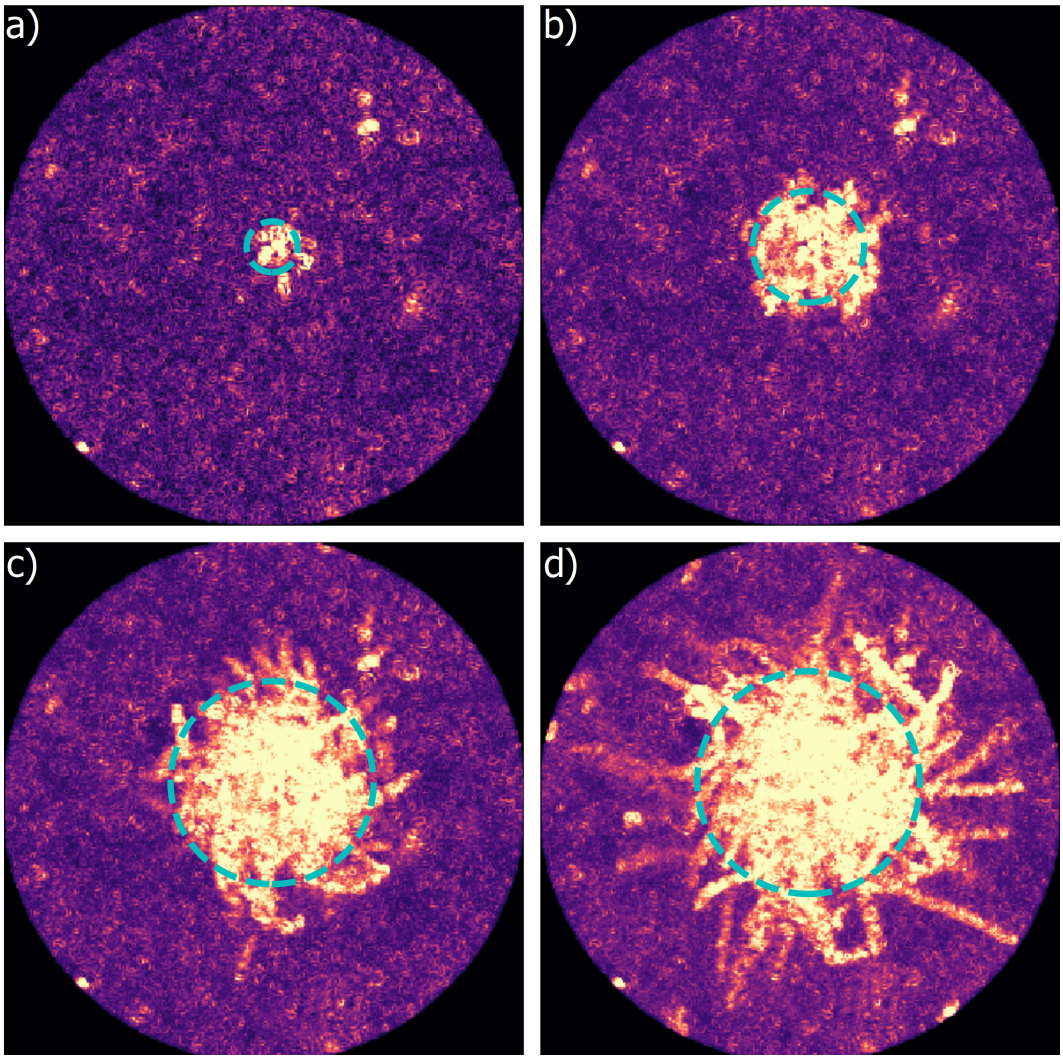


Figure 5.9: **Tracking the event front propagation.** Each pixel is set to the maximum value it achieves in all of the previous frames, where a bright value indicates that motion has occurred at that location. **a).** Two frames after the start of the event, and the event front has clearly formed in the center of the frame. **b).** More frames one, and the event is still broadly circular in appearance, with a sharp boundary between the event and the background. **c).** The event front begins to stall as new particles are not being activated, and the outwards motion is now predominately due to escaping cells. **d).** The event front has barely changed and now the motion is driven entirely by particles escaping the field, with their trajectories easily identifiable.

Looking back at the correlated images of Fig 5.5, there is a clear boundary in

these images (at least while the event is still expanding) between the event and the background. The main difficulty in tracking this boundary in fact stems from the behaviour of the centre of the event, which returns to normal before the boundary. Feature location is extremely difficult in this case as the characteristics of the event front will change substantially between time steps and events. This constant change means employing a circular feature recognition algorithm will result in the erroneous detection of multiple event boundaries per time step, which can be fixed by taking into account the event history leading up to this point. Since an image can be represented by a matrix whose the elements relate to the pixel intensity, we define a matrix $\mathbf{M}_{ijt}$ where $\mathbf{M}_{ijt}$ is the two-dimensional matrix representing the image at a time $t$. From this we can then define the following three-dimensional matrix $\mathbf{V}_{ijk}$ where the elements are defined as:

$$\mathbf{V}_{ijk} = \max(\mathbf{M}_{ijt} | t \in [0, k]) \tag{5.5}$$

Or explicitly the $ij$ values of $\mathbf{V}$ are equal to the maximum value they attain in any of the previous timesteps. This ensures that the event stays bright in the centre thus eliminating the fading seen in Fig 5.5. Fig 5.9 demonstrates this for a different event, where we can clearly see across the four timesteps shown that the event does indeed remain bright for the duration of the event. An interesting side effect of this method is that any moving cells will leave a clear path marking where they have travelled, so opens up the possibility of using this as another method of PTV that does not rely on the heavy combinatorics currently required.

By supplying this method with the start position of the event, the event front can now be easily tracked. This method follows the event front extremely robustly whilst the event remains "contained", i.e. the expansion is due to cells being activated not purely from the ballistic motion of the swimmers (Fig 5.9a-c). The breakdown in the method occurs when the event front is broken up by cells escaping the area of effect of the event as well as new cells no longer being activated, Fig 5.9d.

## 5.4 Modelling with spherical diffusion patch

### 5.4.1 Model

When modelling a pollutant patch spreading from a cell, we need to consider the spherical diffusion equation. For the function $u(r, \theta, \phi)$ (i.e. in spherical coordinates) , the spherical diffusion equation is given by:

$$\frac{\partial u}{\partial t} = \alpha \nabla^2 u = \frac{\alpha}{r^2}\frac{\partial}{\partial r}\left(r^2 \frac{\partial u}{\partial r}\right) + \frac{\alpha}{r^2 \sin(\theta)}\frac{\partial u}{\partial \theta}\left(\sin(\theta)\frac{\partial u}{\partial \theta}\right) + \frac{\alpha}{r^2 \sin(\theta)}\frac{\partial^2 u}{\partial \phi^2} \tag{5.6}$$

Here we are considering the evolution of a patch diffusing radially outwards from some symmetrical initial distribution so any dependence on either $\theta$ or $\phi$ can be ignored. Hence we can write the spherically symmetric diffusion equation:

$$\frac{\partial u}{\partial t} = \alpha \frac{1}{r^2}\frac{\partial}{\partial r}\left(r^2 \frac{\partial u}{\partial r}\right), \qquad u = u(r,t), \qquad 0 \leq r \leq R \tag{5.7}$$

Where the concentration of the chemical at a distance $r$ from the initial source at a time $t$ is given by $u(r,t)$. The initial distribution is given by $u(r,0) = u_0(r)$, and at a distance $R$ from the origin the concentration is given by $u(R,t) = u_R(t)$. Setting the general initial boundary conditions as:

$$u(r,0) = u_0(r), \qquad \left.\frac{\partial u}{\partial r}\right|_{r=0,t} = 0, \qquad u(R,t) = u_R(t) \tag{5.8}$$

This can be easily solved by a combination of separation of variables and a trial solution of the form (for the radial component of the solution):

$$P(r) = A\frac{\sin(\lambda r)}{r} + B\frac{\cos(\lambda r)}{r} \tag{5.9}$$

Where $A, B$ are constants. In order to retain finite solutions at the origin we require the cosine term in Equation 5.9 to vanish. Bringing the general solution together with the constants merged into one ($D$) gives:

$$v(r,t) = P(r)T(t) = D\exp(-\alpha\lambda^2 t)\frac{\sin(\lambda r)}{r} \tag{5.10}$$

We require from the original initial conditions for $v(r,t)$ to be equal to zero when $r = R$, which requires:

$$\lambda R = n\pi \qquad => \qquad \lambda_n = \frac{n\pi}{R} \tag{5.11}$$

Hence we can write $v(r,t)$ as the sum of all the eigenvalue solutions multiplied by corresponding constants $D_n$. This gives us an expression of $u(r,t)$:

$$u(r,t) = \sum_{n=1}^{\infty} D_n \exp(-\alpha\lambda_n^2 t)\frac{\sin(\lambda_n r)}{r} + u_R \tag{5.12}$$

All that remains is to find an expression for $D_n$, which can be done by considering the initial boundary conditions:

$$u_0(r) = u(r,0) = \sum_{n=1}^{\infty} D_n \frac{\sin(\frac{n\pi r}{R})}{r} + u_R \tag{5.13}$$

We can take advantage of the orthogonal nature of the problem to derive an expression for $D_n$ by recognising that eigenfunctions of the form $\frac{\sin(\frac{m\pi r}{R})}{r}$ form a complete orthogonal set in the interval $0 \leq r \leq R$, with a weighting factor of $r^2$ included in the integral. Multiplying both sides of Equation 5.13, integrating over $r$ and rearranging gives an expression for $D_n$ reliant solely on the initial conditions:

$$D_n = \frac{\int_0^R r[u_0 - u_R]\sin(\frac{n\pi r}{R})dr}{\int_0^R \sin^2(\frac{n\pi r}{R})dr} = \frac{2}{R}\int_0^R r[u_0 - u_R]\sin\left(\frac{n\pi r}{R}\right)dr \tag{5.14}$$

With this we now obtain the full solution by substituting the initial and boundary conditions into Eq 5.14 to get expressions for $D_n$. From this we have a description of how the mass of pollutant will diffuse out from the initial mass profile. From here forward the patch radius $\mathbf{r}(t)$ refers to the radius which at time $t$ contains 95% of total pollutant mass and it is this radius that will be used in fitting the experimentally measured radius.

**Initial conditions**

For simplicity we define the initial patch as having a Gaussian profile with a full width half maximum (FWHM) of $1.5 \times 10^{-6}$ m, approximately the size of *M. pusilla*. We assume an instantaneous mass release, and set the background concentration to 0 ($u_R = 0$), as an increased background concentration can be thought as effectively shifting the detection threshold $\Gamma$ of the cells.

$$u(r,0) = u_0(r) = \frac{M}{\sqrt{2\pi}\sigma}\exp\left(-\frac{r^2}{2\sigma^2}\right), \quad \sigma = \frac{\text{FWHM}}{2\sqrt{2\ln 2}} = \frac{1.5\times 10^{-6}}{2\sqrt{2\ln 2}} \tag{5.15}$$

Unfortunately we do not know the specific particulate responsible for triggering the burst event, but we can make some realistic estimates on $M, \Gamma$ and $D$. DMSP (dimethlysulfiopropionate) is a solute released by plankton as a specific point source such as cell lysis and grazing [167], and we know for phytoplankton populations the concentration of this in cells similar to *M. pusilla* is $46.5 \pm 73.7$ fg/cell [212]. Assuming *M. pusilla* takes the average value and all of this mass is released at

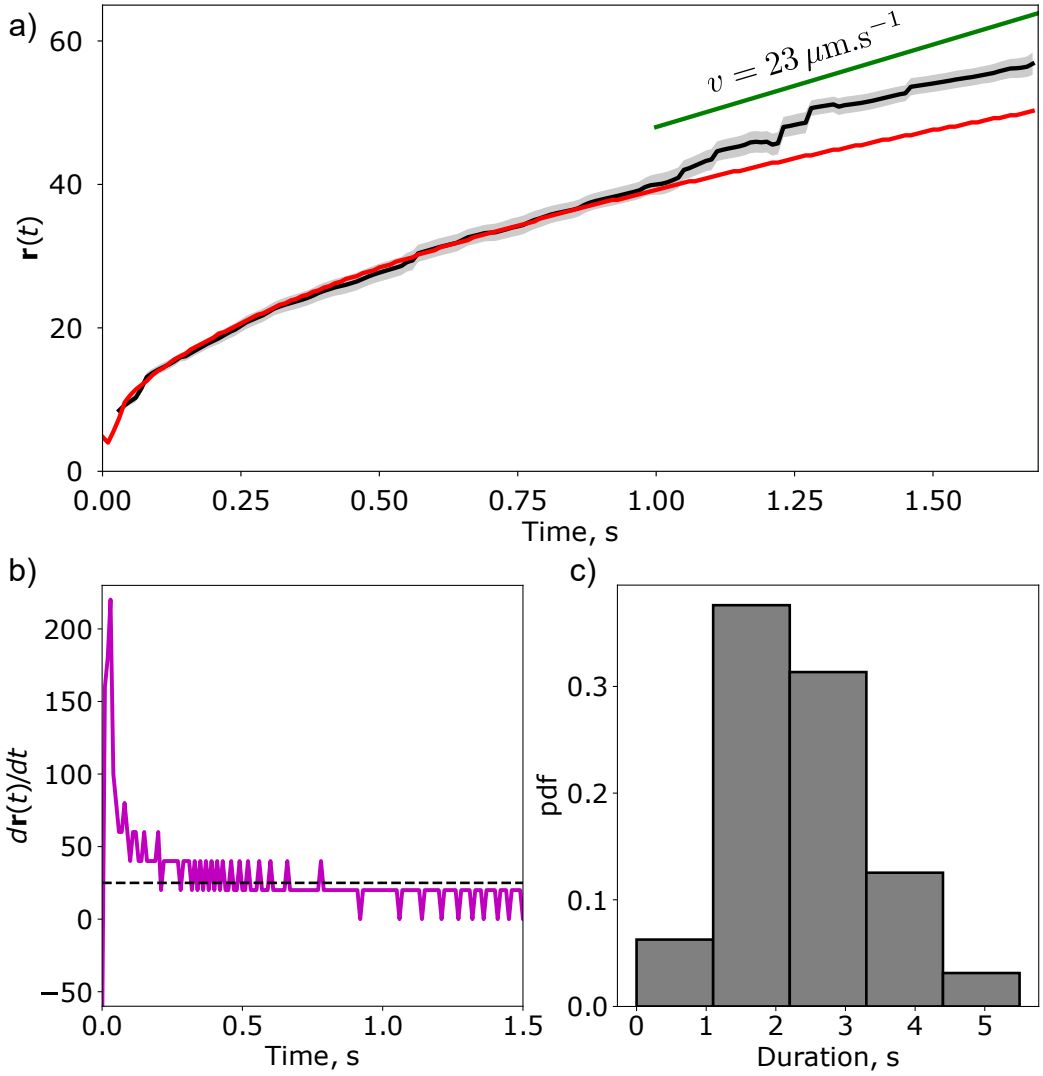


Figure 5.10: **Evolution of the radius of a burst event. a).** The average tracked event front for 18 independent events (black) with a standard error shaded. This is fitted (red) by the solution of the spherical diffusion equation (Eq 5.13), leaving the diffusion as a free-fitting parameter and setting the other variables to biologically relevant quantities: $M = 4.6 \times 10^{-18}, \Gamma = 10^{-6}\,\text{M}$ and fitting a diffusion coefficient of $D = 1.1 \times 10^{-11}\,\text{m}^2\text{s}^{-1}$. There is a breakdown in the model after approximately 1 s due to the swimming speed of the cells exceeding the diffusive speed of the patch, marked in green. **b).** The speed of diffusion, taken as the numerical derivative of the model solution in (a), with the average cell speed marked as the black line. **c).** Duration of events, where we see on average events last between $1 - 2\,\text{s}$.

once, we can then set our initial mass condition of $M = 4.6 \times 10^{-17}\,\text{kg}$. Setting the detection threshold is trickier, literature suggests that for bacteria the threshold

concentration is in the range of $10^{-8} - 10^{-6}$ M [213], so we choose the upper bound here for $\Gamma$. Finally the diffusion coefficient is left as a free-fitting parameter, but based on other particulates such as DMSP we expect a value in the range of $10^{-11} - 10^{-9}\,\mathrm{m^2 s^{-1}}$ [214]. We assume all the mass is released instantaneously (not a slow release) and we ignore any impact the movement of the cells has on the diffusion of the pollutant and absorb these effects into the diffusion coefficient of the pollutant since the size/shape of the pollutant particles are unknown, making it effectively impossible to decouple these effects from each other.

**Experimental results and fitting to the solution**

Hundreds of events were counted during the analysis of the rates of events, however when it comes to studying the single event the data collection rate drops drastically. This is since the events are apparently random (with some time dependence on the frequency as seen previously) so capturing events on camera is not an efficient process. During these experiments we were able to capture approximately 50 events but less than half of these were of sufficient quantity to be analysed for the radius of the event. Fig 5.10a shows the average experimentally measured radius of the burst events (blue) with a standard error shaded on the curve. Fitting this with the spherical diffusion model discussed above, setting the values of $M, \Gamma$ as described we obtain the red curve on Fig 5.10a. During the first second of the event the model describes the expansion of the event extremely well before diverging from the experimentally measured radius. This is to be expected since as the patch spreads further the speed of diffusion will decrease. This speed of diffusion can be obtained by differentiating the fitted curve, shown in Fig 5.10b as the magenta line. Initially the patch spreads faster than the average swimming speed of the cell (approximately $23\,\mu\mathrm{ms}^{-1}$) plotted as the horizontal dashed black line (from Chapter 4) However, there becomes a point where the speed of the patch is less than the speed of the swimming cells, so the cells activated at this point on the edge of the patch are able to swim away faster than the patch expands. This causes the perceived event front to move faster than expected at a speed closer to the swimming speed of the cells, creating the divergence away from the model solution. Plotted in black in Fig 5.10a is the experimental radius speed which we see tends to a value closer to the swimming speed of the cell (shown in green) than the diffusive speed of the patch. Finally, Fig 5.10c shows the distribution of the event durations which are measured from a larger subset of events since it is relatively simple to measure the event duration based on the correlation techniques described in Fig 5.8.

From the fitting of the spherical diffusion model, the diffusion coefficient

of the patch is estimated as being $D = 1.14 \times 10^{-11}\,\mathrm{m^2 s^{-1}}$. For comparison the diffusion coefficient of DMSP is estimated to be around $7.2 \times 10^{-10}\,\mathrm{m^2 s^{-1}}$ [215], showing that the estimate of $D$ is not an unrealistic value for this physical problem.

## 5.5 Triggering the chemical response of the cells

To this point the studied burst events have been treated as random, independent events where cells flee from a chemical source. To complete this section we now attempt to trigger this behaviour in a population of cells, similar to triggering the photo-avoidance discussed earlier in this chapter. Some brief work was attempted with optical tweezers to burst cells in a dense population of cells but unfortunately due to the colour of the laser used we were unable to burst the cell optically which should remain a goal of future studies into this phenomenon. What is possible however is to use microfluidic techniques to dynamically control the chemical composition of the media surrounding the cells and measure the cell activity as the media composition changes.

### 5.5.1 Initial agar device

The principle required is relatively simple - a device with multiple channels separated by a diffusive membrane, where one channel contains cells (and is sealed to prevent flows) and the surrounding channels containing some pollutant source. This will then diffuse through the membrane to the cell channel, modifying the chemical composition surrounding the cells without creating any external flows in the channel itself. The diffusive gradient established by this method can then be altered by changing the media composition of the outside channels - for example, by alternating between pollutant and fresh media in the outside channels we can subsequently expose the cells to the pollutant then return the media composition to a "normal" state without flowing in the cell channel.

A promising example of this type of system was presented by Ieong Wong [216] and is shown in Fig 5.11. A few drops of liquid culture is trapped between a glass cover slide and an thin layer ($250\,\mu$m) of agar. A PDMS chip containing a simple microfluidic channel is placed on top of the layer of agar. The authors were able to studied the growth of a confined monolayer of *E. coli* and track single cells for over 24 hours by maintaining a constant supply of nutrients diffusing through the agar membrane from the media channel. This also allowed for the diffusion of metabolic waste out of the cell layer, maintaining a homogeneous chemical environment for the cell monolayer to develop in. The paper describes how this

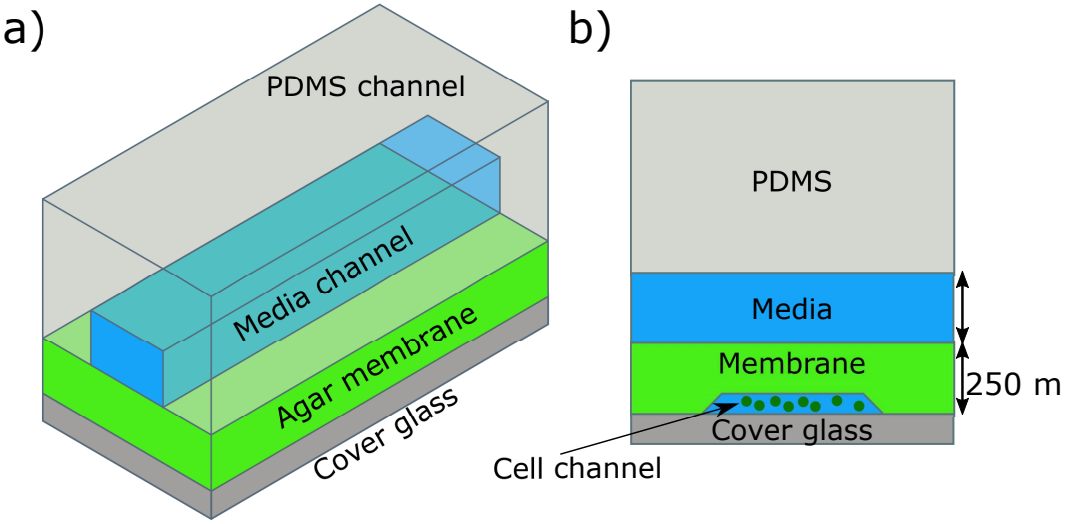


Figure 5.11: **Sketch of hybrid agar-PDMS device used by Wong et al.** (Not to scale, adapted from [216]). **a).** The fully assembled device: an agar membrane (approximately 250 $\mu$m) is sandwiched between a glass cover slide and a PDMS chip with a single microfluidic channel (cuboid with a height of 200 $\mu$m). Media is flowed through the media channel, which establishes a diffusive gradient through the agar membrane. **b).** Cross-section of the device. A few drops of liquid culture are pipetted onto the cover glass then covered with the membrane to trap a cell population under the agar. The media composition around the cells can then be controlled with the diffusion of nutrients from the media channel through the membrane to the cells.

device can be assembled in as little as 30 minutes and does not require any form of clamping/plasma bonding etc. to maintain the bond between the PDMS and agar layers.

Reality however proved very different from this description of the device, with a number of practical problems arising when attempting to replicate this device independently. The main source of problems was the agar layer, starting with consistency in the device. The time taken for diffusion to occur over a length $L$ scales as $L^2$ which means any inconsistencies in the thickness of the agar layer will have a significant impact on the diffusive times through the membrane, and ensuring a constant thickness/agar gel strength of the device is not straightforward for thin layers in particular. More practically the agar membrane used in this example has a gel strength of approximately 1.5%, meaning that simply manipulating this very thin and weak layer is an extremely delicate and difficult task. Whilst this was eventually overcome the main technical difficulty with the device that arose was bonding the agar and PDMS. Following the instructions and methodology laid out

in the source material led to a device that was extremely temperamental - there was such a weak bond at the agar/PDMS boundary (in part to a limited surface area) that the device would inevitably leak, if it sealed at all. If the device did seal (which was an extremely rare event), filling the large media channel without trapping significant bubbles in the device was almost impossible. The seal between the agar and PDMS was never strong enough that negative pressure could be used to pull the media through - in contrast to the usual method of pushing the liquid through the device - which would have improved the success rate of the device significantly.

### 5.5.2 Three-channel agarose device

The solution to this problem comes from in fact an earlier device developed by Cheng et a [217] - a three channel agarose device as shown in Fig 5.12a. Fluid flows through the two outside channels with the cells contained in the central channel (which does not have any flow). Most of the nutrients available to cells are able to diffuse through agarose and the diffusivity of solutes in agarose is similar to that of water [218], meaning it only requires a short period of time to establish a chemical gradient across the hydrogel. By flowing a fluid with constant chemical concentration through the top channel of the device, and flowing the same buffer without the chemical through the bottom channel, a linear chemical gradient can be established and maintained indefinitely across the device. This allows the long-term study of chemotactic cells in the main channel without the introduction of flows into the cell channel.

An exploded view of the device is shown in Fig 5.12b. A layer of 3% agarose cast into a PDMS mould with positive features of the channel design, which when peeled away leaves a thin agarose layer with imprints of the channels on the surface. This is placed onto a glass slide, then covered with a layer of plasma cleaned PDMS with the inlet/outlet holes already punched. It is important that the PDMS is extremely clean and flat as this will determine the strength of the bond between the agarose and PDMS. Fluid can then be drawn through the channels (i.e. using negative pressure) to fill the channels, then provided a sufficient source of buffer/chemical stimulus the gradient can be maintained almost indefinitely.

#### Methods

An initial silicon master mould for the device was generously provided by Dr. Òscar Guadayol i Roig, which was used to pattern the agarose layer. 3% agarose using f/2 medium was prepared by repeatedly heating 0.75 g agarose powder mixed into 25 ml

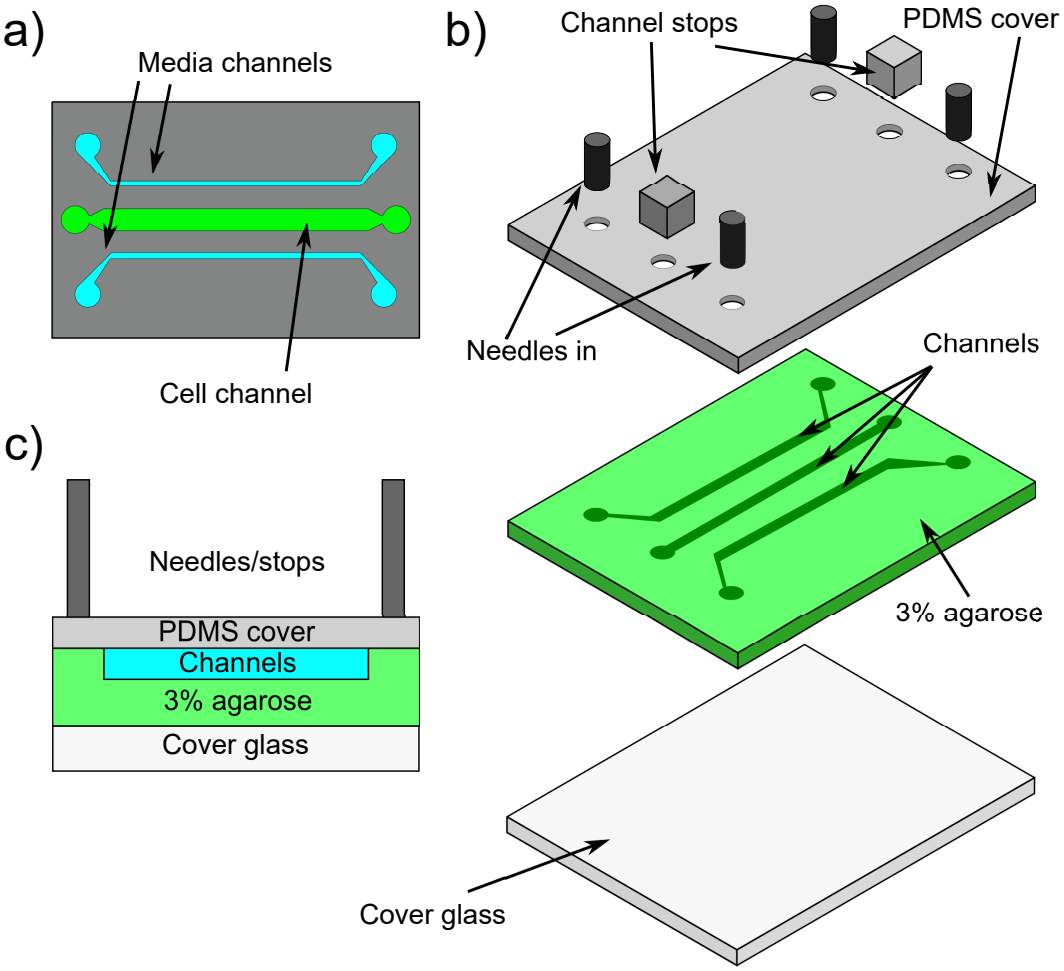


Figure 5.12: **An agarose device to produce steady chemical gradients across a cell channel. a).** Channel design. Two outside media channels with flowing media flanking a flow-isolated cell channel. **b).** Exploded view demonstrating the assembly of the device. The patterned agarose is placed on a glass slide and covered with layer of extremely flat PDMS with the inlet/outlet holes pre-punched. The PDMS is exposed to an oxygen plasma before being brought into contact with the agarose which seals the device. Media is then flowed through the outside channels using negative pressure and the cells are loaded into the central channel using capillary action before the channels are blocked to prevent flow. **c).** Side profile of the device, highlighting how the channels are imprinted into the agarose layer and not the PDMS cover.

of f/2 media until the agarose had fully dissolved. The agarose was then poured over a the mould and immediately covered and compressed with a glass slide then left to cool to room temperature. Once cooled the agarose layer was peeled away from the mould and placed on a glass slide for immediate use. The PDMS layer was made

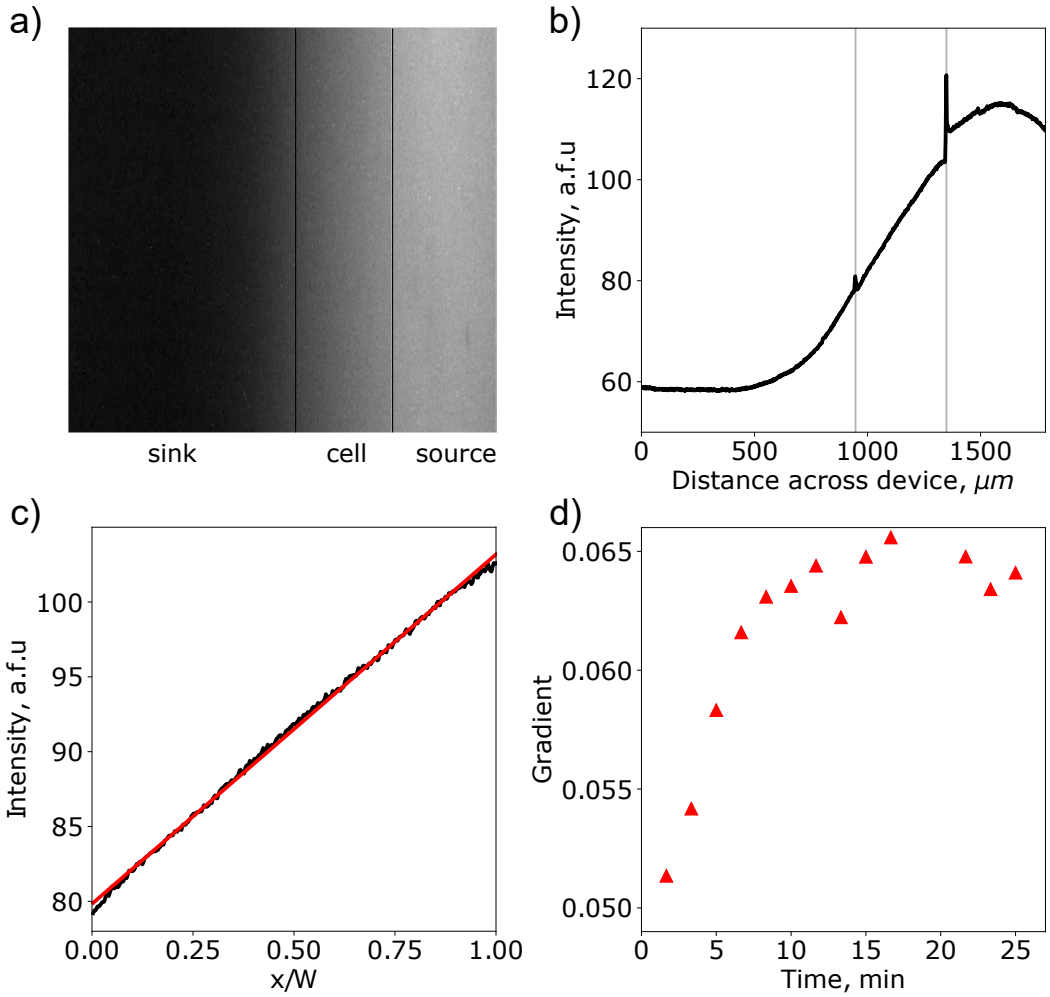


Figure 5.13: **Testing the agarose device. a).** The agarose device was setup as previously described with the three channels as follows: f/2 media in the sink channel, f/2 media in the "cell channel" and 100 $\mu$M fluoroscein (prepared in f/2) in the source channel. The device was then recorded using fluorescent microscopy, with a FITC cube being used to select the excitation/emission wavelengths. **b).** The device is then run with a flow rate of 0.75 $\mu$l.min$^{-1}$ in the source/sink channels, and after a short period of time ($<$ 15 mins) diffusion across the device is apparent. **d).** Evolution of the linear gradient over time which quickly stabilises to a steady gradient across the device. Noise in the plateau is most likely due to the flow rates in the outside channels not being high enough to fully stabilise the gradient in this case.

by pouring a 10 : 1 mixture of degassed PDMS into a large petri dish contained multiple clean slides that had been cleaned in 30% hydrogen peroxide and rinsed with DI water. When the PDMS had cured it was cut and peeled away and the inlet

holes punched in alignment with the agarose layer. The bottom of the PDMS was exposed to an oxygen plasma (Harrick Plasma, UK) for 2 mins, removed, the needles inserted then aligned and placed onto the agarose layer where it immediately seals (and visibly) with the agarose. The outside channel inlets were then connected to tubing in the buffer/chemical mixture. Cells were micropippetted onto the outside of the device then pulled through with a gastight syringe before sealing the open end of the channel to reduce flow through the channel as much as possible. Two 500 ml gastight syringes were used with a syringe pump (kD Scientific) to produce the negative pressure required to introduce flow into the outside channels. For characterising the device we used $10^{-4}$ M fluorescein and a FITC filter cube to measure the diffusion of fluorescein across the agarose layer, with a flowrate of $0.75\,\mu\text{l.min}^{-1}$.

**Device testing**

A simple method of testing the device is demonstrated in Fig 5.13. The device is prepared as above, but instead of loading the central channels with cells it is instead loaded with purely the cell medium f/2. The sink channel is loaded with f/2, and the source channel $100\,\mu$M fluorescein prepared in f/2 medium. The outside channels are subject to a constant flow rate of $0.75\,\mu\text{l.min}^{-1}$, and after a short period of time ($< 15$ mins) the presence of fluorescein across the device due to diffusion becomes apparent (Fig 5.13b). Leaving the flow running in the outside channels we observe a linear gradient established across the device (Fig 5.13c) as expected from solving the one-dimensional diffusion equation. The time taken for a chemical gradient to ready a steady state is given by $\tau_{\text{Diff}} = L^2/2D$, which should be approximately 10 mins in this case. Fig 5.13d confirms this - we see the gradient across the device begins to stabilise at the 10 min mark, with noise in the plateau afterwards suggesting a higher flow rate is needed to improve the diffusion efficiency across the device.

**Device utilization**

Initial experiments with this three-channel device are promising - there are signs of the motility increasing in response to the change in chemical conditions around the cells. However we have not yet observed the dramatic behaviour of motility during a burst event. We believe this is due to the difficulty in identifying the chemical source that is triggering the events - to date the pollutant has been produced by centrifuging cells into an extremely dense pellet then attempting lyse the cells mechanically. The current experiments now rely on doing this mechanical lysis to extremely old cell

cultures to produce a pollutant, for which the experiments are ongoing.

## 5.6 Conclusion

The study of any form of taxis in *M. pusilla* is limited to a single chemotaxis study [133] and the novel mobility/phototaxis study presented in Chapter 4. Neither of this however address any form of phobic/avoidance response of the organism to either a chemical or light stimulus.

By exposing *M. pusilla* to sharp changes in light intensity, it was found that the organism has both a step-up and a step-down response in these conditions. During the step-up response cells are activated on at an intensity-dependent rate, once activated cells swim almost continuously to escape the field of view. This photophobic response is shown to have a clear intensity dependence, and is exhibited by just over half of the population. In contrast nearly the entire population demonstrate the step-down response, where all cells swim continuously for $5 - 10\,\mathrm{s}$ before the activity in the sample returns to normal levels. The presence of the step-up response is, whilst novel, not an unexpected discovery since it can be expected that *M. pusilla* has developed some rudimentary photoprotection mechanism, the most basic of which is to simply escape from the harmful light source. More puzzling is the step-down response which is exhibited by almost the entire population and has a clear dependence on the stimulation duration. It is currently unclear why this organism would require a step-down response in the wild. One possible reason is that *M. pusilla* is found in most coastal environments so this could be a means of escaping a rocky outcrop back into more favourable light conditions, but this is something that warrants much further investigation. Future studies of these novel studies plan to examine the response for more wavelengths as well as confining the cells to prevent population depletion during the photophobic step-up response, and continue the development of a mathematical description of the response in terms of cell activation rates.

A more bizarre response revealed itself when cells were confined for several hours in a millifluidic device, where cells appear to spontaneously attempt to escape a local chemical change in their environments. It is proposed that a cell death releases a pollutant patch into the surrounding media which triggers an avoidance response in nearby cells. The patch diffuses radially outwards and continues to trigger responses in cells until the concentration of pollutant drops below the cells detection threshold, signalling the end of the event. The radius of these events was tracked and fitted to a spherically symmetric diffusion equation which verified

that the cell is capable of releasing sufficient material to produce the observed "cell explosion" in the sample. This response most likely was developed as an avoidance response to the presence of cell dying through viral lysis and/or a predator, where cells detect there is a hazard in the immediate vicinity and attempt to escape the situation. Attempts were made to manually trigger such an event using an optical tweezer as well as an agarose hybrid microfluidic device capable of dynamically controlling the chemical environment surrounding the cells without creating a flow in the cell channel, but more work is required to conclusively prove that a cell death is responsible for these events.

### 5.6.1 Key points

The key points from this chapter are:

- *M. pusilla* is capable of both a step-up and step-down response to a sudden change in light intensity. The step-up response has a clear intensity dependence and acts photophobically to reduce the population of cells in the affected region. During this response the cells change from run-tumble styles of swimming to continuous swimming, with over half of the population displaying this response.

- The step-down response is briefer than the step-up response where in the step-up response the cells remain active until they leave the field of view. The step-down response is shorter (lasts approximately $5 - 10\,\mathrm{s}$) but during this nearly all of the population becomes active, contrasting with only half of the population during the step-up response. The strength of the step-down response also has a clear dependence on the duration of exposure, plateauing after an exposure of $15\,\mathrm{s}$ to the light source.

- Confined cultures of *M. pusilla* will, after reasonably long timescales, begin to undergo "burst events" where cells will begin to rapidly swim away from some local change in the environment. During these events the cells swim continuously as in the step-up photoresponse and the motion appears to spread radially from some central point.

- An absence of external stimulus suggest these events are triggered by some local chemical change in the cell medium due to cell death/lyses, which is validated by tracking the event front and comparing to a spherically diffusing patch.

- Preliminary experiments with the three-channel agarose device are inconclusive so far but the problem is believed to be related to the production of the pollutant which is currently being addressed in ongoing experiments.

This chapter concludes the experimental work with *M. pusilla* for this thesis. Future studies should look at mechanically/optically bursting a cell to validate our hypothesis that these trigger the burst events, as well as more work to fully model the step-up/down photoresponses. We now move to the final experimental chapter of this thesis which will focus on phototaxis of the model green algae *Chlamydomonas reinhardtii* and its phototaxis in more complicated photolandscapes.

# Chapter 6

# Phototaxis of *Chlamydomonas reinhardtii* in complicated photolandscapes

Note: As mentioned in the Declarations, this chapter presents the recent results of a new collaboration with the group of Dr. Giogio Volpe (UCL), investigating the phototaxis of *Chlamydomonas reinhardtii* in complicated photolandscapes. In this collaboration I was responsible for preparing the experiments, carrying them out with Manish Trivedi (UCL), analysing the results and presenting them to the group. The optical setups described here were built by Manish Trivedi, and I would like to take this opportunity to again thank both Manish and Giorgio for making this exciting project possible.

## 6.1 Introduction

To date phototaxis has been studied in relatively simple terms - does the organism swim towards the light, and if so does this depend on the intensity/wavelength of the stimulus? More interesting and biologically relevant however is to ask how would a cell behave in a more complicated light environment - a marine organism will not "see" a single collimated light source but rather swims through a photolandscape that will be constantly varying in intensity. In the past few years there has been some work with synthetic swimmers in more complicated optical environments [219] but very little work has been done with biological microswimmers. In this chapter we present a novel experimental system developed in collaboration with the group of Dr. Giorgio Volpe (UCL) to investigate how biological swimmers navigate in more

complicated photolandscapes.

## 6.2 *Chlamydomonas reinhardtii*

*Chlamydomonas reinhardtii* was covered in more detail during Chapter 3 but a brief re-introduction of the organism is presented here. *C. reinhardtii* is a unicellular green algae with a cell body of approximately 10 $\mu$m diameter, or roughly five times the size of *M. pusilla*. Contrasting with *M. pusilla*, *C. reinhardtii* has two flagella and swims with a "breaststroke" beat pattern as a puller-type swimmer. *C. reinhardtii* has established itself over the past several decades as being the microswimmer of choice for a variety of experimental systems such as the eukaryotic flagella and photosynthesis [145, 146, 149, 220–222]. It is an extremely easy organism to work with - the cell cycle can be almost perfectly synchronised in a diurnal chamber and a variety of mutants have been isolated into algal collections, making it very easy to obtain a specific strain for different experiments - for example the uniflagellated strain CC1926.

Of more interest to us is the fact that *C. reinhardtii* has established itself as the model eukaryotic microorganism for phototaxis studies. The cell has a single well-defined eyespot on the side of the cell body, and due to the body rotation during swimming the eyespot produces a "lighthouse" style signal to the cell. The signal from this eyespot triggers a response in the beat patterns of the flagella, allowing the cell to swim either towards or away from the light - positive/negative phototaxis respectively. Phototaxis of *C. reinhardtii* was first reported in 1973 by Stavis and Hirschberg [223] and since then there has been work demonstrating flagellar photoresponses [224–226], linking photosynthesis to phototaxis [155,227], and more recently a demonstration of how *C. reinhardtii* can track the curvature of light patches to maximise its exposure to the light stimulus [155] as well as reinforcing the hypothesis that photosynthesis controls how cells navigate their optical environments.

In this chapter we present a series of experiments, alongside proof-of-concept results, designed to probe how the phototaxis of *C. reinhardtii* behaves in different optical environments. Here we considering three specific photolandscapes: a complicated speckle pattern, a Gaussian patch and a striped environment.

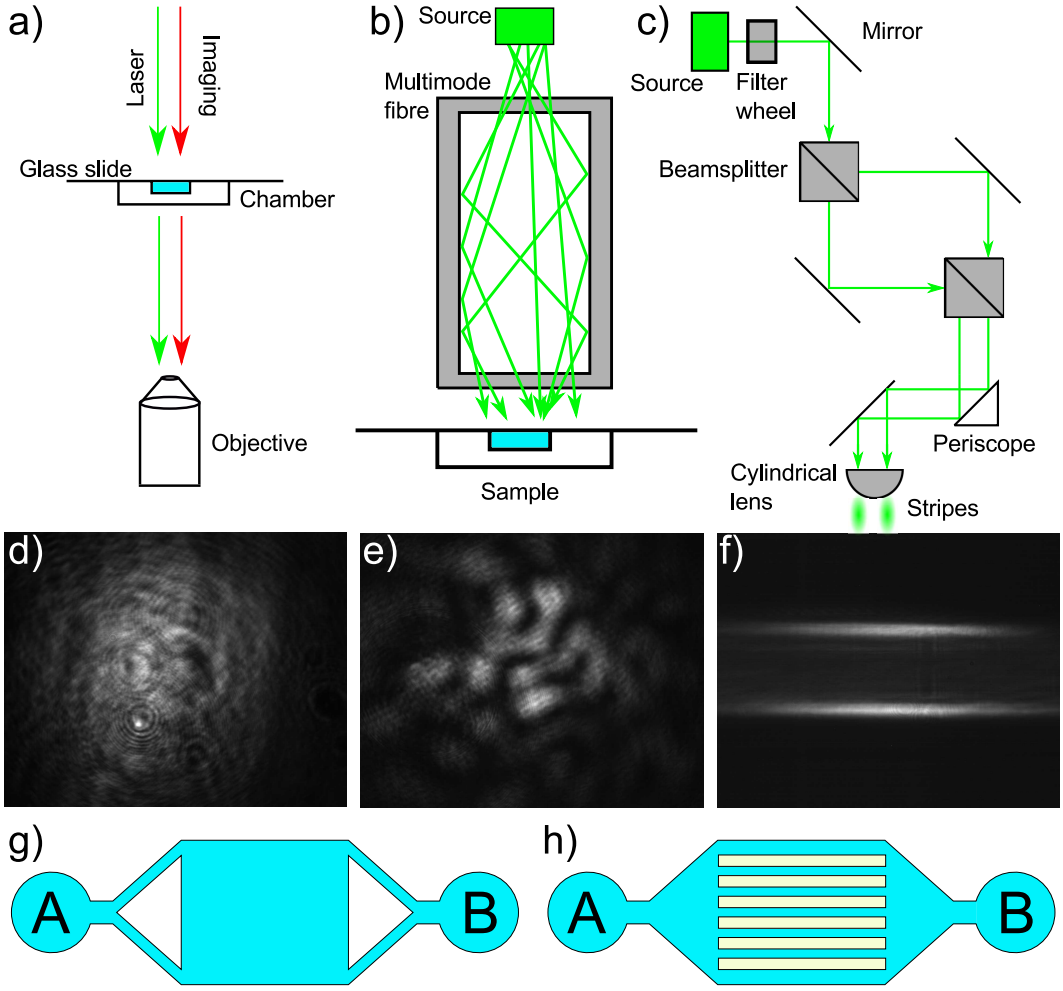


Figure 6.1: **Methods and pattern generation for *C. reinhardtii* phototaxis experiments. a).** General setup. Cells were loaded into a PDMS microfluidic device bonded to a glass cover slip, inverted and mounted onto a microscope. **b).** Speckle pattern was formed by focussing the laser into a multimode fiber then focussing the output onto the sample. **c).** The stripes were formed by using beamsplitters to form two beams which were then focussed through a cylindrical lens to form two-stripes with Gaussian profiles. **d).** Example of the Guassian patch. **e).** Example of a speckle pattern, where the pixel intensity distribution has an exponential profile. **f).** Generation of two stripes. **g).** Sketch (not-to-scale) of the open microfluidic device. **g).** Sketch (not-to-scale) of the channels used for the two-stripe accumulation experiments, with marked inlet/outlets A/B respectively. For both devices, blue marks areas of the device cells can swim in.

## 6.3 Experimental methods

### Cell culturing

Cultures of *Chlamydomonas reinhardtii* strain CC125 (wild-type) were grown in tris-acetate-phosphate (TAP) medium in a diurnal chamber at 20° C with a 16/8 hr

light/dark cycle, with an illumination intensity of $\approx 100\,\mu\mathrm{Em}^{-2}\mathrm{s}^{-1}$ provided by fluorescent strips. The TAP medium was prepared in 500 ml quantities with the phosphate solution added after autoclaving to prevent precipitation. The cells were counted daily using a haemocytometer and maintained at a cell concentration of $2 \times 10^6$ cell/ml.

#### General experiment protocol

Cultures of *C. reinhardtii* were harvested in their exponential growth phase ($\approx 10^6$ cell/ml), then for the initial Gaussian/speckle experiments these were used in their current concentration to enable single-cell tracking. For the phototactic accumulation experiments involving two stripes, these cells were centrifuged gently in 1 ml eppendorf tubes for 12 mins at 1000 RPM to form a dense pellet of cells. The supernatant was carefully removed to leave an extremely dense cell population. Microfluidic devices were passivated by filling the device, and left under pressure from a gravity feed, a 5% mixture of pluronic f-127 dissolved in TAP medium for at least 40 mins before being rinsed with TAP and then filled with the cell suspension. By leaving the device under pressure any trapped air bubbles in the device is pushed out through the PDMS due to its gas permeability. Once the chambers had been loaded they were sealed with petroleum jelly to prevent flows due to evaporation.

The experimental setup is sketched in Fig 6.1a. Once the devices were loaded they were inverted and mounted on a Leica DMI4000B inverted microscope. The samples were inverted to ensure that the laser pattern would be consistent between experiments, as the thickness of the cover slips the devices were bonded to is roughly constant whereas the thickness of the PDMS device will vary significantly between devices. A variety of objectives were used, ranging between 2× and 20×, which will be indicated during the discussion for the different experiments. Experiments were filmed using a monochrome CMOS camera (Thorlabs), brightfield illumination provided by an IR source (850 nm, Thorlabs) and a Y5 filter cube ($620 - 660$ nm, Leica) used to remove the laser pattern before imaging.

### 6.3.1 Pattern generation

A 532 nm (green) wavelength laser was used as the stimulation source for all of the experiments. Three main light patterns were used in these experiments. First, a Gaussian patch (Fig 6.1d) is generated by simply focussing the laser onto the sample, the width of which can be easily adjusted by adjusting the focus of the lens. The speckle patterns were formed by focussing the laser through a 50 mm focal length

lens into a multimode fibre, the output of which was refocussed onto the sample using a 25.4 mm focal length lens (Fig 6.1b). Finally, two-stripes with Gaussian profiles (Fig 6.1cf) were generated by splitting the laser into two beams and focussing onto the sample using a cylindrical lens to focus two stripes onto the sample, both with a Gaussian profile. Initially the laser was blocked from the sample and left to stabilise before the sample was exposed to the stimulus. In the later experiments (two-stripe accumulation), a continuous ND filter wheel (Thorlabs) was used to gradually expose the laser smoothly to the sample over a 30 s period to eliminate any photoshock responses of the cells.

### 6.3.2 Microfluidic devices

Two different microfluidic devices were used in these experiments. For experiments using the Gaussian patches/speckle patterns an open microfluidic chamber (sketched in Fig 6.1g) was used - a simple device with a large open observation window with one inlet/outlet pairing. The device has a thickness of 26 $\mu$m, confining the swimming cells to a 2D plane. For the later experiments involving two-stripes a modified device was used which contains parallel channels with again a single inlet/outlet pair (Fig 6.1h). Channels had a width of either 200 $\mu$m or 250 $\mu$m depending on the experiment, which will be indicated in the results discussions below. Devices were bonded to No. 1 cover slips ($\approx$ 170 $\mu$m thickness) to improve consistency in the laser pattern focussed onto the sample.

## 6.4 Results

**Speckles**

The initial photolandscape used was a "speckle" pattern, an example of which is shown in Fig 6.1c. The pattern results from random scattering of coherent light by a complex media, and the probability density function of the speckle pattern intensity follows an exponential distribution:

$$P(I) = \frac{1}{\langle I \rangle} \exp\left( - \frac{I}{< I >} \right) \tag{6.1}$$

Where $\langle I \rangle$ is the average speckle pattern intensity. A number of experiments were carried out with a variety of speckle patterns, and changes in the swimming patterns of *C. reinhardtii*. However it was found at a later date that the speckle pattern was in fact unstable - the patches would oscillate between bright and dark with a time scale of tens of minutes. Also, cells that moved in a speckle region would autofluoresce

under the effects of the laser, making the cells appear bright in these regions. This makes particle location/particle tracking extremely difficult as the features are a mixture of bright and dark across the image.

These experimental barriers have now been solved - firstly the stability of the speckle has been sorted by improving the stability of the optical components and environmental conditions. Another filter has been installed before imaging to fully remove any fluorescent effects from the image. This ensures the cell "appearance" in the image remains constant across the field of view. In terms of analysing this data, tools have been developed, and tested, to measure quantities such as the curvature of the cell trajectory against the intensity and curvature of the speckle pattern local to the cell, which can be used to build a more complete picture of how *C. reinhardtii* navigates photolandscapes.

#### Gaussian patches

Due to the original experimental difficulties with the speckle pattern we moved back to a simpler landscape - a Gaussian patch, an example of which is shown in Fig 6.1d. Before continuing with this project we needed to confirm that the cells would respond phototactically to the stimulating wavelength - 532 nm. Another consideration was whether the cells were subject to any optical forces that could be misinterpreted as a phototactic influence on their trajectories.

In these experiments we observed similar phenomena to [155], where the cells would trace out the edge of the patch in order to remain in the illuminated region for the maximal amount of time as well as phototshock behaviour in the middle of the most intense patches. In order to test the optical forces the chamber was filled with a suspension of dead cells and applied the laser to the cells. During these experiments there was no noticable influence of the laser on the particles, so it can be safely assumed any changes in the cells trajectories are solely due to phototaxis induced by the light stimulus.

### 6.4.1 Two stripes

#### Image balancing

After repeated testing of a variety of optical systems we decided to start at a more fundamental level than the complicated speckled environment - if the cells are confined to a long straight channel, can the laser be used as a "valve" to block/hinder cell transport along the channel?

For these experiments microfluidic devices such as the one shown in Fig 6.1g

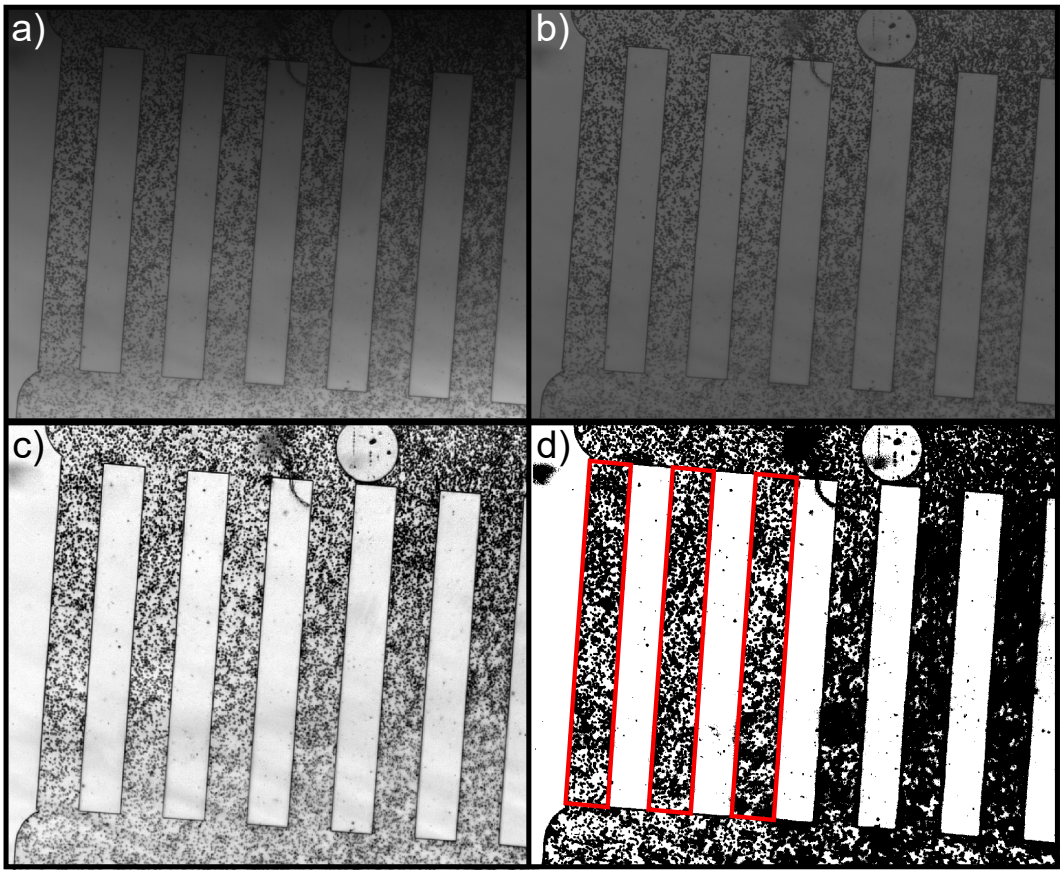


Figure 6.2: **Normalizing the images from the cylindrical lens. a).** The original image $I(x, y)$, where there is a clear uneven background illumination down the length of the channel. **b).** The normalized image $N(x, y)$ where the background intensity has been balanced along the whole image. **c).** $N(x, y)$ is then contrast stretched, highlighting the empty space more clearly than in (b). **d).** A threshold is then applied to the image, producing a binary image where black indicates space occupied by a cell.

were used: a device with a single inlet/outlet pair with numerous parallel channels of the same width - here 250 $\mu$m. Devices were imaged with a 2$\times$ objective, with two laser stripes projected perpendicular to the channel length using a cylindrical lens (Fig 6.1). Fig 6.2a shows a sample frame with the laser blocked from view. The channel boundaries are clearly visible, and each black speck is a single *C. reinhardtii* cell. To analyse this we look at the light density along the length of the channel, which will be lower for higher density regions of cells. However, due to the combination of the 2$\times$ objective to increase our field of view, and the cylindrical lens to produce the stripes, there is a clearly uneven background illumination which will skew any intensity-based analysis. To balance this the normalized image $N(x, y)$ is

produced from the initial image $I(x, y)$ and the background image $B(x, y)$:

$$N(x,y) = \text{mean}(I(x,y)) \cdot \frac{1}{\text{mean}\left(\dfrac{I(x,y)}{B(x,y)}\right)} \frac{I(x,y)}{B(x,y)} = C \cdot \frac{I(x,y)}{B(x,y)} \tag{6.2}$$

For each individual frame the value of $C$ will vary slightly (due to different particle positions etc.) so is fixed at $C = 0.4$ for all of the analysis to ensure consistency in the image processing. The normalized image $N(x, y)$ is shown in Fig 6.2b, where the background illumination is more constant. The image contrast is then stretched (Fig 6.2c) then finally the image is thresholded. This effectively normalises the particle sizes along the length of the channel, producing Fig 6.2d. The stripes are constant only over the highlighted channels, hence the thresholding outside of this region is not important. This processing produces a binary image where black (pixel = 0) corresponds to a space occupied by a cell, and white to empty space. The photolandscape used here was a pair of Gaussian stripes similar to the image shown in Fig 6.1e, but the stripes are slightly shifted to the left and the top stripe is half the thickness (and therefore power) of the lower stripe due to a misalignment issue during the experiments.

### Accumulation to both stripes

Fig 6.3 summarises the phototactic behaviour of *C. reinhardtii* in these experiments. For the range of laser powers tested ($50\,\text{mW} - 500\,\text{mW}$) - the power are summarised in Table 6.1 - there is significant accumulation in both the regions illuminated by the stripes. In fact, for the higher powers ($250\,\text{mW}, 500\,\text{mW}$), the accumulation is so strong that the red autofluorescence of the cells bleaches out the middle of the accumulation region. It is not until the laser is switched off that the scale of the accumulation becomes clear. Similar, but slower, accumulation is observed as the laser power is decreased. Decreasing the power to 50 mW eliminates this red bleaching signal from the image, enabling analysis of the accumulation and dispersal

Table 6.1: Laser powers for the pair of stripes at three different input powers

| Stripe | 50 mW | 250 mW | 500 mW |
|---|---|---|---|
| Top Stripe | 17 mW | 83 mW | 167 mW |
| Bottom Stripe | 37 mW | 167 mW | 333 mW |

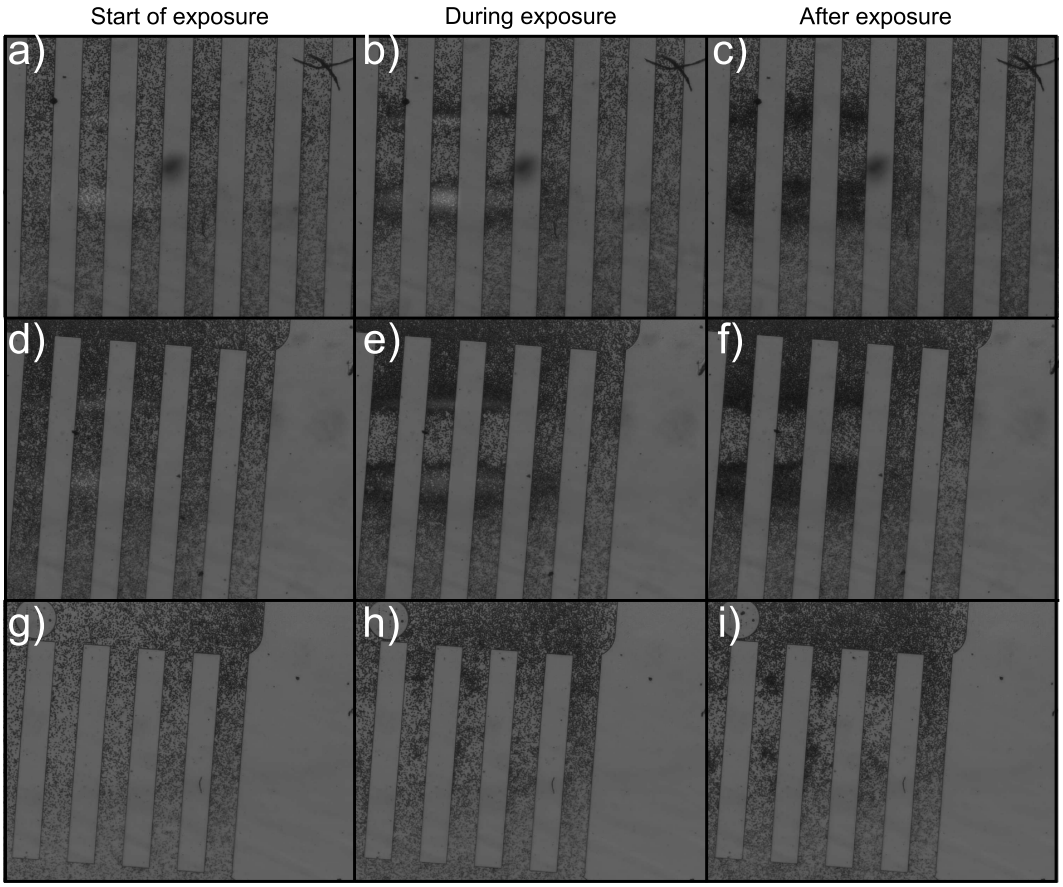


Figure 6.3: **Accumulation to different laser powers.** Three different times (laser on at $t = 0$, accumulation with the laser on, laser off) for three different laser powers ($500\,\mathrm{mW}, 250\,\mathrm{mW}, 50\,\mathrm{mW}$). For the $500\,\mathrm{mW}, 250\,\mathrm{mW}$ cases with the laser on ((a-b),(d-e) resp.) the accumulation appears reduced in the centre of the stripes but this is actually due to red autofluorescence of the cells, made apparant when the laser is switched off (c,f resp.). We see across the range of powers the accumulation is sufficient to block/impede progress through the channels, highlighted by the increasing density outside of the channels (e.g. $50\,\mathrm{mW}$ example).

dynamics.

The first feature apparent is that the accumulation is sufficient to block/impede cell movement through the affected channels, for example Fig 6.3e. Examining the accumulation region in the higher powers with the laser off (Fig 6.3cf) the accumulation is strongest on the outside of the affected zone, with cells freer to move in the middle of the patches. This is an interesting phenomena that warrants further experiments to clarify the transport dynamics inside of these accumulation regions.

For the $50\,\mathrm{mW}$ experiments the development and dispersal of the accumu-

lation was able to be analysed due to the lack of the autofluorescence. Fig 6.4ab plots the accumulation (resp. dispersal) heatmaps for a 50 mW channel experiment, with bright values indicating a full saturation of cells at that channel position. The accumulation zones clearly emerge over time and in the space between the zones the population is severely depleted. This suggests that even at such low powers cells are unable to escape from the accumulation zones to replenish the area marked out by the laser. Releasing the laser (Fig 6.4b) shows that in less than a minute the zones have begun to disperse and the population becomes more homogenous along the length of the channel. However the overall cell density is now significantly higher than before the laser exposure and remains at this higher density.

For the other tested powers, we are unable to produce similar analysis for the accumulation due to the bleaching effect, but we can still analyse the density profiles immediately after the laser is switched off. Fig 6.4cd plots the density profile down the length of the channel for the 250 mW and 500 mW experiments respectively. These follow the expected behaviour - regions of high cell density trapping a region of significantly lower cell density as transport through the region is now blocked by the photoresponses of the cells.

## 6.5 Future work

The preliminary results presented here act as a proof-of-concept that the phototaxis of *C. reinhardtii* in more complicated photolandscapes is a viable and experimentally achievable goal that raises a number of interesting open questions. During these studies we have now developed and refined the experimental apparatus and analytical tools required to pursue this topic further, and leaves a variety of directions that future work could take this project in.

Having shown accumulation to the two stripes, the next experiment is to introduce a second light stimulus but this time along the length of the channel. The aim of this is to determine whether the laser will completely block the channel with the accumulation, or if the presence of a second light source will produce a phototactic response strong enough to "break" the accumulation zones open. This has several potential ecological implications, for example considering phototaxis in porous media where cells could accumulate near a pore opening and use phototaxis to navigate into/out of the pore. We also observed in the accumulation patches a higher density around the edges of the region of accumulation with cells moving more freely inside the patch - high-magnification experiments at the edge of the patch should be carried out in order to model the flux of particles into and out of

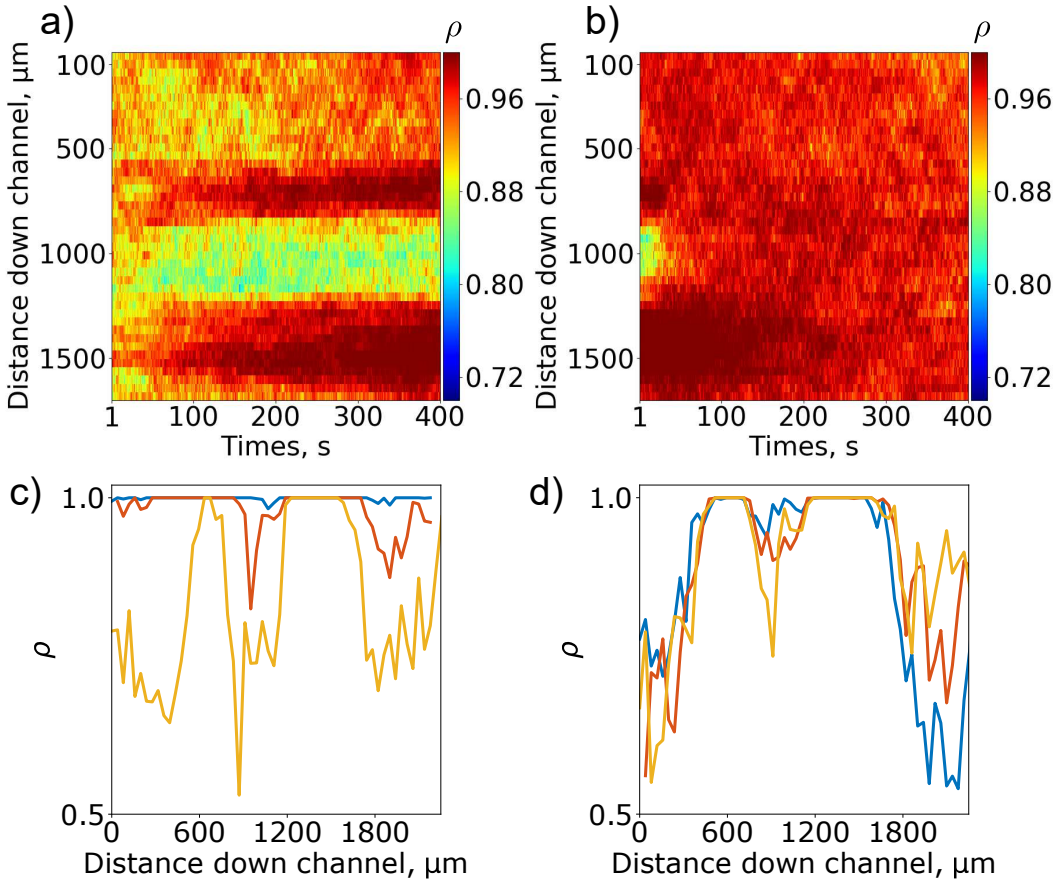


Figure 6.4: **Accumulation profiles of *C. reinhardtii* to the stripe pattern. a).** Accumulation in the 50 mW experiments, where the development of the accumulation zones is clearly visible along with the very low density region between the stripes. **b).** Switching the laser off results in dispersal of the accumulation zones but also a significant increase in the average cell density along the channel for a long period of time. **c-d).** Density profiles for 250 mW, 500 mW respectively, with three channels plotted for each case. These profiles are taken immediately after the laser is switched off to eliminate the bleaching effect.

the patch and whether this too can be influenced by phototaxis from a parallel light source.

The speckle experiments should be repeated now the instabilities in the speckle pattern identified and solved as well as having adapted the optical setup to remove the autofluorescence of the cells in the illuminated portions of the pattern. With methodology this a number of phenomena can now be investigated such as the behaviour of passive colloids in this active system and the use of phototaxis to navigate clogged environments.

## 6.6 Key Points

In this chapter we have discussed a new experimental system designed to probe phototaxis of the model green alga *C. reinhardtii* in different photolandscapes. The key points from this chapter are:

- *C. reinhardtii* is the model eukaryotic microswimmer for investigating phototaxis, due to its well-defined eyespot and clear phototactic swimming behaviour. This behaviour can switch between positive and negative phototaxis, as well as photoshock/photophobic responses when the cell encounters a sudden change in light intensity.

- Previous work with *C. reinhardtii* and other biological phototactic swimmers has been limited to simple photolandscapes - normally a steady uniform light source or a simple light pattern such as a Gaussian patch. Some recent work has been done with more complicated patterns but this has been limited so far to artificial swimmers [219].

- Here we present a model experimental system to investigate phototaxis in more complicated photolandscapes using *C. reinhardtii* as a model swimmer. In a simple case, photoaccumulation to a pair of Gaussian stripes is shown to be sufficient to prevent cell movement down the length of the channel. These accumulation zones are denser at their edges with cells able to remain more motile inside the patch itself. When the laser is switched off the zones begin to disperse, but the overall cell density in the channel remains significantly higher in the entire channel than before exposure.

- Future experiments should start with experiments at higher magnification to investigate the transport properties of the patches. These channel experiments can also be extended to include a second light stimulus along the length of the channel to determine if a second phototactic response can re-enable cell transport down the channel. Finally, passive colloids could be introduced and the laser used as a "valve" to control the flow of colloids down the channel due to the motion of the swimmers.

# Chapter 7

# Conclusion

## 7.1 Thesis overview

Phytoplankton form the basis of major food webs in marine ecosystems and have huge ecological significance - for example over half of the global oxygen production is attributed to phytoplankton. Many of these photosynthetic microorganisms are able to regulate and direct their motion in response to an external light stimulus in a poorly understood processes called phototaxis. Prominent amongst these organisms is the pico-eukaryote *Micromonas pusilla*: a 2 micron comma-shaped cell with a single 5 micron flagellum. *M. pusilla* is perhaps the most globally dominant phytoplankton since it has been found in both marine and coastal environments across the globe such as: Plymouth, the Caribbean and Arctic. Despite its obvious ecological significance, the motility of *M. pusilla* has not been studied before and the presence of phototaxis has only been anecdotally reported before. It is particularly interesting that *M. pusilla* has been reported to be phototactic since that, unlike other organisms classically studied for phototaxis such as *Chlamydomonas reinhardtii*, *M. pusilla* does not have a dedicated eyespot to directly detect the light direction. Using particle tracking velocimetry (PTV) techniques, over a million swimming trajectories of *M. pusilla* were analysed to characterise the motility pattern of this organism which was found to move in a novel form of run-tumble motion. Similar to 70% of marine isolates *M. pusilla* undergoes a run-reverse style of motion, where the next run will preferentially be directed either in the previous run direction or in the opposite direction. In the case of *M. pusilla* there is a difference to the classical run-reverse motion where *M. pusilla* can stop for extremely long periods of time  a tumble can last up to hundreds of seconds, though the majority are under 5 s in duration. Hence this novel motility strategy was called: "stop, run

or reverse" to reflect this novel behaviour.

The phototaxis of *M. pusilla* was then characterised for the first time, with the population response tested across the visible spectrum and a wide range of intensities. It was found that *M. pusilla* is able to respond positively across the visible spectrum by producing a slow net drift towards the light on the order of a few microns per minute. This was supported by investigating the single-cell phototaxis responsible for the net population drift. By considering the full run-reorient-run process, it was shown that *M. pusilla* extends its run length on runs that are reorientated towards the light source which was confirmed by a series of jump-diffusion simulations based on the experimental motility parameters for *M. pusilla*, showing that these subtle asymmetries in the cell trajectories are sufficient to reproduce the observed experimental population drifts.

The phototactic responses tested to this point were in response to a uniform collimated source, but notably across the wide spectrum and intensities that were tested only positive responses were discovered. Under strong epi-illumination however, it was found that *M. pusilla* has extremely strong step-up and step-down responses to sudden changes in the illumination. These responses involve the organism changing its motility pattern from the stop, run-reverse pattern to more continuous swimming, the effect of which rapidly depletes the cell population in the affected field of view. As such, this response is labelled as a photophobic response though it should be noted that this is but one of the possible responses displayed here, with the population depletion being a result of the increased local cell motility the main motivation behind labelling these responses as photophobic. The step-up response is shown to be intensity dependent, with approximately half of the population evacuating the field of view in response to the light stimulus. A more intriguing response is the step-down response to the light source being removed where a high proportion of cells in the field of view become active as per the step-up response, but the response is limited to a few seconds in duration. This response duration is shown to be dependent on the length of time the cells are exposed to the light stimulus, with the response plateauing after an exposure of 15 s.

A similar type of response was observed with a completely different phenomena, where cells would be "activated in a radial manner from a specific point in a so-called "burst event". These activated cells would then change their swimming mode to the same continuous mode observed in the step-up/down responses in an active attempt to escape a local change in the environment. Contrasting to the photoresponses this new response was not directly triggered by an external light source, but rather in response to an apparent sudden release of a chemical

signal/death. New tools were developed to track the front propagation of these burst events, and it was hypothesised that these events were in response to a single cell death which would release a dense pollutant patch into the immediate vicinity. This patch will then diffuse outwards radially and cells will become activated as the patch reaches them. Modelling this problem as a spherically diffusing patch with biologically relevant parameters confirms that this is a viable mechanism, with the theoretical patch radius matching that of the experimentally measured radius of the burst events. Given the similarities between the burst events and the step-up/down responses, in particular the single cell behaviour, it suggests *M. pusilla* has developed an universal avoidance response to harmful conditions including harmful light intensities and cell death triggered by viral lysis for example.

To date, biological phototaxis has been limited to a few model organisms, principally the green alga *C. reinhardtii*, and simple light stimuli such as uniform illumination or Gaussian patches. Indeed, there are only a couple of examples of phototaxis in more complicated photolandscapes which are mostly limited to synthetic microswimmers. The final experimental chapter presents work on a new experimental system designed to investigate biological phototaxis in more complicated photolandscapes. Using *C. reinhardtii* as the target organism: a 10 micron cell with a single eyespot on the side of the cell and swims by beating two flagella in a breaststroke pattern. Using a combination of microfluidics and lasers, a system is developed which is capable of exposing the cells to a variety of photolandscapes including an exponentially distributed speckled pattern. The system was tested by confining the cells in parallel channels and exposing them to two Gaussian stripes perpendicular to the channels. Accumulation to the laser stripes was observed across a range of laser powers, with the photoaccumulation strong enough to effectively block cell transport through the affected channels. Dispersal to a uniform distribution occurs when the stimulus is removed but it is noted that the cell populations in the channel remains significantly higher than prior to exposure.

## 7.2 Future studies

Whilst this thesis has uncovered and addressed many questions, many new questions have been opened up as a result of it. Firstly, the motility of *M. pusilla*. This thesis presents the first substantial work on the cell motility of this organism but it has not addressed the behaviour of the flagellum responsible for the swimming of the cell. There has been some brief work focussing on the flagellum of *M. pusilla*, as discussed in Chapter 3, but it still remains unclear how this unusually structured

appendage works. In particular the reports of Manton and Parke which describe the cell as being able to swim as both a pusher and a puller class of swimmer, which if true could help to explain the stop, run-reverse strategy of this organism. A new collaboration with the group of Eric Lauga is being established to address this topic which will initially focus on mapping and modelling the flagellum beat pattern to determine which parts of the flagellum are actively involved in the beat pattern, moving then to address the apparent pusher/puller nature of this organism. It is also hoped that this will address the nature of the reorientation events - whether they are classical reversals or simply 180° turns (or some combination of the two).

The work presented here focussed on a series of novel photoresponses of *M. pusilla*: the slow positive phototactic drift towards a uniform light source and the apparent photophobic step-up/down responses to a sudden intensity change in the light stimulus. An interesting question to consider is if these responses form parts of a continuim of responses or if they are almost step-responses to different illumination conditions. To test this, future studies should take the two experimental setups described here - the first population experiments and the later photophobic responses - as two ends of the response spectrum then work towards the opposite response with each of them. The idea here is to determine if the transition between the slow drift and the photophobic responses is a smooth one or a sudden switch in response.

The burst events provide what could be considered the simplest extension of the presented work - the principal open topic left here is the triggering mechanism itself. Previous attempts to manually trigger the events have been unsuccessful but there are now plans to test this using a laser ablation setup. This would be the final step in fully characterising the event dynamics, further work should then look to identify the chemical trigger responsible for these events and then perhaps test the theory that cell death by viral lysis could be sufficient to trigger an event by introducing the *Micromonas pusilla* virus into the experimental mix.

Finally, the new experimental system designed to probe phototaxis in complicated geometries and photolandscapes. There are a number of planned future studies involving this setup, the first of which is to introduce a second light stimulus along the length of the channel to determine if the photoaccumulation to the stripes can fully block cell transport through the channel when the cells are directed along it. By modifying the design of the microfluidic device this setup could also be used to investigate how phototaxis influences the motility of cells in clogged porous media. Recent work has shown that *C. reinhardtii* is capable of entraining passive particles so another avenue for exploration for this setup could be to study the effects of

phototaxis on the transport of passive particles in confined environments.

## 7.3 Conclusion

In conclusion, this work has presented a series of novel works focussed on the phototaxis of dominant marine pico-eukaryote *M. pusilla*. The motility of the organism has been characterised for the first time, and a series of photoresponses to different light stimuli have been reported. It was also shown that single cell death is apparently able to trigger an avoidance response in the surrounding local population, which in parallel with the photophobic responses suggests the existence of a universal avoidance response for *M. pusilla* to harmful environmental conditions. Finally, a new experimental system involving *C. reinhardtii* was developed to enable the investigation of biological phototaxis in complicated geometries and photolandscapes. This thesis therefore represents a significant step forward in our understanding of phototaxis and its ecological significance, and provides the field with a broad range of developed tools and systems to continue studying this important phenomenon which drives motility changes at the base of the food web.

# Bibliography


[1] Meet the challenge of interdisciplinary science. *Nature*, 534(7609), 2016.

[2] Olaf S. Andersen. Introduction to Biophysics Week: What is Biophysics? *Biophysical Journal*, 110(5), 2016.

[3] Bart W. Hoogenboom and Mark C. Leake. The case for biophysics supergroups in physics departments. *Physical Biology*, 15(6):60201, Nov 2018.

[4] V. Hensen. *Ueber die Bestimmung des Plankton's oder des im Meere treibenden Materials an Pflanzen und Thieren.* Parey, 1887.

[5] Elisa Schaum, Bjorn Rost, Andrew J. Millar, and Sinead Collins. Variation in plastic responses of a globally distributed picoplankton species to ocean acidification. *Nature Clim. Change*, 3(3):298–302, Mar 2013.

[6] Jörn Dunkel. Rolling sound waves. *Nature Materials*, 17(9):759–760, 2018.

[7] D. J. Acheson. Elementary Fluid Dynamics, 1991.

[8] A. J. Majda and A. L. Bertozzi. *Vorticity and Incompressible Flow.* Cambridge Texts in Applied Mathematics. Cambridge University Press, 2002.

[9] L. Caffarelli, R. Kohn, and L. Nirenberg. Partial regularity of suitable weak solutions of the Navier-Stokes equations. *Communications on Pure and Applied Mathematics*, 1982.

[10] O. A. Ladyzhenskaya. *The Mathematical Theory of Viscous Incompressible: Flow.* Mathematics and Its Applications. Gordon and Breach Science Publishers, 1963.

[11] George Gabriel Stokes. On the Effect of the Internal Friction of Fluids on the Motion of Pendulums. *Transactions of the Cambridge Philosophical Society*, 9, 1851.

[12] Arnold Sommerfield. Ein Beitrag zur hydrodynamischen Erkläerung der turbulenten Flüssigkeitsbewegüngen (A Contribution to Hydrodynamic Explanation of Turbulent Fluid Motions). *International Congress of Mathematicians*, 3:116–124, 1908.

[13] Derek Jackson and Brian Launder. Osborne Reynolds and the Publication of His Papers on Turbulent Flow. *Annual Review of Fluid Mechanics*, 2006.

[14] Richard Foch and Kevin Ailenger. Low Reynolds number, long endurance aircraft design. In *Aerospace Design Conference*, Meeting Paper Archive. American Institute of Aeronautics and Astronautics, Feb 1992.

[15] Robert W. Deters, Gavin Kumar Ananda Krishnan, and Michael S. Selig. Reynolds Number Effects on the Performance of Small-Scale Propellers. 32nd AIAA Applied Aerodynamics Conference, 2014.

[16] Shubham Jain, Nekkanti Sitaram, and Sriram Krishnaswamy. Effect of Reynolds Number on Aerodynamics of Airfoil with Gurney Flap. *International Journal of Rotating Machinery*, 2015.

[17] Dong Ha Kim and Jo Won Chang. Low-Reynolds-number effect on the aerodynamic characteristics of a pitching NACA0012 airfoil. *Aerospace Science and Technology*, 2014.

[18] J. C. M. Lin and Laura L. Pauley. Low-Reynolds-number separation on an airfoil. *AIAA Journal*, 34(8):1570–1577, Aug 1996.

[19] Gary Settles. Schilieren photograph of smoke from a candle. `https://commons.wikimedia.org/wiki/File:Laminar-turbulent_transition.jpg`.

[20] Em Purcell. Life at low Reynolds number, 1977.

[21] T. Kiorboe, H. Jiang, R. J. Goncalves, L. T. Nielsen, and N. Wadhwa. Flow disturbances generated by feeding and swimming zooplankton. *PNAS*, 111(32):11738–11743, 2014.

[22] André W. Visser. Motility of zooplankton: Fitness, foraging and predation. *Journal of Plankton Research*, 2007.

[23] M. Murase, M. Hines, and J. J. Blum. Properties of an excitable dynein model for bend propagation in cilia and flagella. *Journal of Theoretical Biology*, 139(3), Aug 1989.

[24] B. M. Friedrich and F. Julicher. Chemotaxis of sperm cells. *Proceedings of the National Academy of Sciences*, 104(33), 2007.

[25] C. Metz. *Biology of Fertilization V2: Biology of The Sperm*. Elsevier Science, 2012.

[26] Elio Poggi and Jean-François Gohy. Janus particles: from synthesis to application. *Colloid and Polymer Science*, 295(11):2083–2108, 2017.

[27] Alexander A. Solovev, Yongfeng Mei, Esteban Bermúdez Ureña, Gaoshan Huang, and Oliver G. Schmidt. Catalytic microtubular jet engines self-propelled by accumulated gas bubbles. *Small*, 5(14), Jul 2009.

[28] Jonathan Moran, Paul G. McKean, and Michael L. Ginger. Eukaryotic Flagella: Variations in Form, Function, and Composition during Evolution. *BioScience*, 64(12):1103–1114, 2014.

[29] J. Gray and G. J. Hancock. The Propulsion of Sea-Urchin Spermatozoa. *Journal of Experimental Biology*, 32(4):802–814, 1955.

[30] Robert Dautray and Jacques-Louis Lions. The Linearised Navier-Stokes Equations BT - Mathematical Analysis and Numerical Methods for Science and Technology: Volume 6 Evolution Problems II. pages 1–34. Springer Berlin Heidelberg, Berlin, Heidelberg, 2000.

[31] Brian J. Kirby. *Micro- and Nanoscale Fluid Mechanics, Transport in Microfluidic Devices*. Cambridge University Press, 2010.

[32] G. J. Hancock. The Self-Propulsion of Microscopic Organisms through Liquids. *Proceedings of the Royal Society A: Mathematical, Physical and Engineering Sciences*, 217(1128), 1953.

[33] Allen T. Chwang and T. Yao Tsu Wu. Hydromechanics of low-Reynolds-number flow. Part 2. Singularity method for Stokes flows. *Journal of Fluid Mechanics*, 67(4), 1975.

[34] Takuji Ishikawa. Suspension biomechanics of swimming microbes. *Journal of the Royal Society Interface*, 6(39):815–834, 2009.

[35] Žiga Kos and Miha Ravnik. Elementary Flow Field Profiles of Micro-Swimmers in Weakly Anisotropic Nematic Fluids: Stokeslet, Stresslet, Rotlet and Source Flows. *Fluids*, 3(1), 2018.

[36] Knut Drescher, Jörn Dunkel, Luis H. Cisneros, Sujoy Ganguly, and Raymond E. Goldstein. Fluid dynamics and noise in bacterial cell - cell and cell - surface scattering. *Proceedings of the National Academy of Sciences*, 108(27):10940–10945, 2011.

[37] Jens Elgeti, Roland G. Winkler, and Gerhard Gompper. Physics of Microswimmers - Single Particle Motion and Collective Behavior. *Reports on Progress in Physics*, 78(5), 2015.

[38] Eric Lauga, Willow R. DiLuzio, George M. Whitesides, and Howard A. Stone. Swimming in Circles: Motion of Bacteria near Solid Boundaries. *Biophysical Journal*, 90:400–412, 2006.

[39] Eric Lauga and Thomas R. Powers. The hydrodynamics of swimming microorganisms. *Reports on Progress in Physics*, 72(9):096601, Sep 2009.

[40] Allison P. Berke, Linda Turner, Howard C. Berg, and Eric Lauga. Hydrodynamic attraction of swimming microorganisms by surfaces. *Physical Review Letters*, 101(3), 2008.

[41] Robert Brown. XXVII. A brief account of microscopical observations made in the months of June, July and August 1827, on the particles contained in the pollen of plants; and on the general existence of active molecules in organic and inorganic bodies. *The Philosophical Magazine*, 4(21):161–173, Sep 1828.

[42] Albert Einstein. On the Motion of Small Particles Suspended in Liquids at Rest Required by the Molecular-Kinetic Theory of Heat. *Annalen der Physik*, 17(549), 1905.

[43] M. F. M. Osborne. Brownian Motion in the Stock Market. *Operations Research*, 7(2), 2008.

[44] Norbert Wiener. Differential-Space. *Journal of Mathematics and Physics*, 2(1-4):131, 1923.

[45] Don S. Lemons and Anthony Gythiel. Paul Langevin's 1908 paper "On the Theory of Brownian Motion" (Sur la théorie du mouvement brownien), C. R. Acad. Sci. (Paris) 146 , 530533 (1908)]. *American Journal of Physics*, 65(11):1079–1081, Nov 1997.

[46] Albert Einstein. *Investigations On the Theory Brownian Movement*. Courier Corporation, 1956.

[47] Harvey Scher and Elliott W. Montroll. Anomalous transit-time dispersion in amorphous solids. *Physical Review B*, 12(6), 1975.

[48] Aubrey V. Weigel, Blair Simon, Michael M. Tamkun, and Diego Krapf. Ergodic and nonergodic processes coexist in the plasma membrane as observed by single-molecule tracking. *Proceedings of the National Academy of Sciences of the United States of America*, 108(16):6438–6443, Apr 2011.

[49] Lewis Fry Richardson and Walker Gilbert Thomas. Atmospheric diffusion shown on a distance-neighbour graph. *Proceedings of the Royal Society of London. Series A, Containing Papers of a Mathematical and Physical Character*, 110(756):709–737, Apr 1926.

[50] Eric R. Weeks, T. H. Solomon, Jeffrey S. Urbach, and Harry L. Swinney. Observation of Anomalous Diffusion and Levy Flights. In *Levy Flights and Related Topics in Physics*, pages 51–71, 1995.

[51] Jake P. Taylor-King, E. Emiel van Loon, Gabriel Rosser, and S. Jon Chapman. From Birds to Bacteria: Generalised Velocity Jump Processes with Resting States. *Bulletin of Mathematical Biology*, 77(7):1213–1236, 2015.

[52] Mikhail Lifshits. *Random Processes by Example*. World Scientific, 2014.

[53] G K Miller. *Probability: Modeling and Applications to Random Processes*. Wiley, 2006.

[54] Floyd B. Hanson. Stochastic Processes and Control for Jump-Diffusions. 2007.

[55] W. B. Carpenter and W. H. Dallinger. *The microscope and its revelations*. Henry Ford Estate collection. P. Blackiston's Sons and Co., 1901.

[56] Nanguang Chen, Shakil Rehman, and Colin J. R. Sheppard. Recent advances in optical microscopy methods for subcellular imaging of thick biological tissues. *Critical reviews in biomedical engineering*, 41(4-5):393–403, 2013.

[57] Rory M. Power and Jan Huisken. A guide to light-sheet fluorescence microscopy for multiscale imaging. *Nature Methods*, 14:360, Mar 2017.

[58] Joseph S. Boyd, Mary Rose Lamb, and Carol L. Dieckmann. Miniature- and Multiple-Eyespot Loci in *Chlamydomonas reinhardtii* Define New Modulators of Eyespot Photoreception and Assembly. *Genes Genomes Genetics*, 1(6), 2011.

[59] Steve L'Hernault. Phase contrast image of *Chlamydomonas reinhardtii*. `http://cellbio.emory.edu/lab/sale/`.

[60] Lynn Quarmby. Fluorescent image of Fa2p enzyme at the base of the flagellum. `https://scienceandbelief.org/tag/scientific-art/`.

[61] A. K. J. V Köhler. New method of illumination for phomicrographical purposes. *Journal of the Royal Microscopical Society*, 14, 1894.

[62] F. Zernike. How I discovered phase contrast. *Science*, 121(3141), 1955.

[63] Jurek W. Dobrucki and Ulrich Kubitscheck. Fluorescence Microscopy. In *Fluorescence Microscopy: From Principles to Biological Applications: Second Edition*. 2017.

[64] Ionita C. Ghiran. Introduction to Fluorescence Microscopy. 2010.

[65] Irina Semenova and Vladimir Rodionov. Fluorescence microscopy of microtubules in cultured cells. *Methods in molecular medicine*, 137:93–102, 2007.

[66] G. H. Krause and E. Weis. Chlorophyll Fluorescence and Photosynthesis: The Basics. *Annual Review of Plant Physiology and Plant Molecular Biology*, 42(1):313–349, 1991.

[67] R. I. Ghauharali and G. J. Brakenhoff. Fluorescence photobleaching-based image standardization for fluorescence microscopy. *Journal of Microscopy*, 198(2), 2000.

[68] H. Bruus. *Theoretical Microfluidics*. Oxford Master Series in Physics. OUP Oxford, 2008.

[69] Stephen C. Terry, John H. Herman, and James B. Angell. A Gas Chromatographic Air Analyzer Fabricated on a Silicon Wafer. *IEEE Transactions on Electron Devices*, 26(12), 1979.

[70] Lisa R. Volpatti and Ali K. Yetisen. Commercialization of microfluidic devices. *Trends in Biotechnology*, 32(7):347–500, 2014.

[71] Shagun Gupta, Kritika Ramesh, Suhaib Ahmed, and Vipan Kakkar. Lab-on-chip technology: A review on design trends and future scope in biomedical applications. *International Journal of Bio-Science and Bio-Technology*, 8(5), 2016.

[72] Christopher Prohm and Holger Stark. Feedback control of inertial microfluidics using axial control forces. *Lab on a Chip*, 14(12):2115–2123, 2014.

[73] S. M. Richardson. *Fluid mechanics*. Series in Chemical and Mechanical Engineering. Hemisphere Publishing Corporation, 1989.

[74] David C. Duffy, J. Cooper McDonald, Olivier J.A. Schueller, and George M. Whitesides. Rapid prototyping of microfluidic systems in poly(dimethylsiloxane). *Analytical Chemistry*, 70(23):4974–4984, 1998.

[75] Julius B. Kirkegaard, Ambre Bouillant, Alan O. Marron, Kyriacos C. Leptos, and Raymond E. Goldstein. Aerotaxis in the closest relatives of animals. *eLife*, 5(e18109), 2016.

[76] Jan Krajniak and Hang Lu. Long-term high-resolution imaging and culture of C. elegans in chip-gel hybrid microfluidic device for developmental studies. *Lab on a Chip*, 10(14), 2010.

[77] D. R. Gossett et al. Hydrodynamic stretching of single cells for large population mechanical phenotyping. *Proceedings of the National Academy of Sciences*, 109(20):7630–7635, 2012.

[78] Kwanghun Chung, Matthew M Crane, and Hang Lu. Automated on-chip rapid microscopy, phenotyping and sorting of C. elegans. *Nature Methods*, 5:637, Jun 2008.

[79] Maria Cristina Letizia, Matteo Cornaglia, Raphaël Trouillon, Vincenzo Sorrentino, Laurent Mouchiroud, Maroun S. Bou Sleiman, Johan Auwerx, and Martin A. M. Gijs. Microfluidics-enabled phenotyping of a whole population of C. elegans worms over their embryonic and post-embryonic development at single-organism resolution. *Microsystems & Nanoengineering*, 4(1):6, 2018.

[80] Jindan Wu, Zhengwei Mao, Huaping Tan, Lulu Han, Tanchen Ren, and Changyou Gao. Gradient biomaterials and their influences on cell migration. *Interface focus*, 2(3):337–355, Jun 2012.

[81] J.R Seymor, T. Ahmed, Marcos, and Roman Stocker. A microfluidic chemotaxis assay to study microbial behaviour in diffusing nutrient patches. *Limnology and Oceanography*, 6(9):477–488, 2008.

[82] J. W. Foster and J. Slonczewski. *Microbiology: An Evolving Science*. W.W. Norton, 2017.

[83] David W. Lawlor. *Photosynthesis: Molecular, Physiological and Environmental Processes*. Longman Scientific & Technical, Hong Kong, 2nd edition, 1993.

[84] Hans J. Trurnit and Germille Colmano. Chloroplast studies: I. Absorption spectra of chlorophyll monolayers at liquid interfaces. *Biochimica et Biophysica Acta*, 31(2):434–447, 1959.

[85] J.M. Berg, J.L. Tymoczko, and L. Stryer. The Light Reactions of Photosynthesis. In *Biochemistry*, chapter 19. W H Freeman, New York, 5th edition, 2002.

[86] Suliman Khan, Rabeea Siddique, Wasim Sajjad, Ghulam Nabi, Khizar Mian Hayat, Pengfei Duan, and Lunguang Yao. Biodiesel Production From Algae to Overcome the Energy Crisis. *HAYATI Journal of Biosciences*, 24(4):163–167, 2017.

[87] Gary B. Collins and Cornelius I. Weber. Phycoperiphyton (Algae) as Indicators of Water Quality. *Transactions of the American Microscopical Society*, 97(1), 1978.

[88] I. Rawat, R. Ranjith Kumar, T. Mutanda, and F. Bux. Dual role of microalgae: Phycoremediation of domestic wastewater and biomass production for sustainable biofuels production. *Applied Energy*, 88(10):3411–3424, 2011.

[89] Ida Akkerman, Marcel Janssen, Jorge Rocha, and René H Wijffels. Photobiological hydrogen production: photochemical efficiency and bioreactor design. *International Journal of Hydrogen Energy*, 27(11):1195–1208, 2002.

[90] Hui-Min David Wang, Ching-Chun Chen, Pauline Huynh, and Jo-Shu Chang. Exploring the potential of using algae in cosmetics. *Bioresource Technology*, 184:355–362, 2015.

[91] Leanne J Flewelling et al. Red tides and marine mammal mortalities. *Nature*, 435:755–756, 2005.

[92] L. C. Bowling and P. D. Baker. Major cyanobacterial bloom in the Barwon-Darling River, Australia, in 1991, and underlying limnological conditions. *Marine and Freshwater Research*, 47(4):643–657, 1996.

[93] T. H. Donnelly, M. R. Grace, and B. T. Hart. Algal blooms in the Darling-Barwon River, Australia. *Water, Air, and Soil Pollution*, 99:487–496, 1997.

[94] G. Harris. *Phytoplankton Ecology: Structure, Function and Fluctuation*. Springer Netherlands, 2012.

[95] Nathan S. Hall and Hans W. Paerl. Vertical migration patterns of phytoflagellates in relation to light and nutrient availability in a shallow microtidal estuary. *Marine Ecology Progress Series*, 425, 2011.

[96] Daniel C.O. Thornton. Dissolved organic matter (DOM) release by phytoplankton in the contemporary and future ocean. *European Journal of Phycology*, 49(1), 2014.

[97] Paul G. Falkowski. Rationalizing elemental ratios in unicellular algae. *Journal of Phycology*, 36(1):3–6, 2001.

[98] Paul G Falkowski and John A Raven. *Aquatic Photosynthesis*. Princeton University Press, student edition, 2007.

[99] Steven Emerson and John Hedges. *Chemical Oceanography and the Marine Carbon Cycle*. Cambridge University Press, Cambridge, 2008.

[100] H. Londish, A. Berk, S.L. Zipursky, P. Matsudaira, D. Baltimore, and J. Darnell. *Molecular Cell Biology*. W. H. Freeman, New York, 4th edition, 2000.

[101] The Biology Project. Cut-through of an eukaryotic flagellum.

[102] Thomas Gensrch. Sketch of a mammalian sperm celll. `http://worms.zoology.wisc.edu/dd2/echino/fert/sperm/sperm.html`.

[103] Gaia Pigino and Takashi Ishikawa. Axonemal radial spokes: 3D structure, function and assembly. *Bioarchitecture*, 2(2):50–58, Feb 2012.

[104] Anton Bukatin, Igor Kukhtevich, Norbert Stoop, Jörn Dunkel, and Vasily Kantsler. Bimodal rheotactic behavior reflects flagellar beat asymmetry in human sperm cells. *Proceedings of the National Academy of Sciences*, 112(52), 2015.

[105] Chih Kuan Tung, Chungwei Lin, Benedict Harvey, Alyssa G. Fiore, Florencia Ardon, Mingming Wu, and Susan S. Suarez. Fluid viscoelasticity promotes collective swimming of sperm. *Scientific Reports*, 7(3152), 2017.

[106] J. Elgeti and G. Gompper. Emergence of metachronal waves in cilia arrays. *Proceedings of the National Academy of Sciences*, 110(12), 2013.

[107] Alicia Guemez-Gamboa, Nicole G Coufal, and Joseph G Gleeson. Primary cilia in the developing and mature brain. *Neuron*, 82(3):511–521, May 2014.

[108] Sarah C. Goetz and Kathryn V. Anderson. The primary cilium: A signalling centre during vertebrate development. *Nature Reviews Genetics*, 11(5), 2010.

[109] The prokaryote flagellum. `https://en.wikipedia.org/wiki/File:Flagellum_base_diagram-en.svg`.

[110] Hong Sun, David R. Zusman, and Wenyuan Shi. Type IV pilus of *Myxococcus Xanthus* is a motility apparatus controlled by the frz chemosensory system. *Current Biology*, 10(18), 2000.

[111] Swarming bacteria.

[112] Vladimir M. Fomin, Markus Hippler, Veronika Magdanz, Lluís Soler, Samuel Sanchez, and Oliver G. Schmidt. Propulsion mechanism of catalytic microjet engines. *IEEE Transactions on Robotics*, 30(1), 2014.

[113] F .A Samatey, H Matsunami, S Nagashima, T.R Shaikh, D.R Thomas, J.Z Chen, D.J Derosier, A. Kitao, and K. Namba. Structure of the bacterial flagellar hook and implication for the molecular universal joint mechanism. *Nature*, 431(7012):1062–1068, 2004.

[114] Daniel B. Kearns. A field guide to bacterial swarming motility. *Nature reviews. Microbiology*, 8(9):634–644, Sep 2010.

[115] J. Henrichsen. Bacterial Surface Translocation: a Survey and a Classification. *Bacteriological Reviews*, 36(4):478–503, 1972.

[116] R.B. Morrison and A. Scott. Swarming of Proteus - A Solution to an Old Problem? *Nature*, 211(5046):255–257, 1966.

[117] B.D. Holye and J.W. Costerton. Bacterial resistance to antibiotics: the role of biofilms. *Prog Drug Res*, 37:91–105, 1991.

[118] Mark J. McBride. Bacterial Gliding Motility: Multiple Mechanisms for Cell Movement over Surfaces. *Annual Review of Microbiology*, 2002.

[119] H. Lautrop. Bacterium anitratum transferred to the genus Cytophaga. *Int. Bull. Bacteriol. Nomencl*, 11:107–108, 1961.

[120] John S. Mattick. Type IV Pili and Twitching Motility. *Annual Review of Microbiology*, 2002.

[121] Ahmad Al Atrouni, Marie-Laure Joly-Guillou, Monzer Hamze, and Marie Kempf. Reservoirs of Non-baumannii Acinetobacter Species. *Frontiers in microbiology*, 7:49, Feb 2016.

[122] Epler Barbercheck, Chelsea R, Esther Bullitt, and Magnus Andersson. Bacterial Adhesion Pili BT - Membrane Protein Complexes: Structure and Function. pages 1–18. Springer Singapore, 2018.

[123] Oliver G. Schmidt and Karl Eberl. Thin solid films roll up into nanotubes. *Nature*, 410:168, Mar 2001.

[124] NIH Rocky Mountain Laboratories, NIAID. SEM image of *E. coli*. `https://en.wikipedia.org/wiki/File:EscherichiaColi{\_}NIAID.jpg`.

[125] H.C. Berg and D.A. Brown. Chemotaxis in Escherichia coli analysed by three-dimensional tracking. *Nature*, 239:500, 1972.

[126] Linda Turner, William S. Ryu, and Howard C. Berg. Real-time imaging of fluorescent flagellar filaments. *Journal of Bacteriology*, 182(10), 2000.

[127] P.S. Mead, L. Slutsker, V. Dietz, L.F. McCaig, J.S. Bresee, C. Shapiro, P.M. Griffin, and R.V. Tauxe. Food-related illness and death in the United States. *Emerging infectious diseases*, 5(5):607–625, 1999.

[128] Gloria Córdoba, Anne Holm, Frank Hansen, Anette M Hammerum, and Lars Bjerrum. Prevalence of antimicrobial resistant *Escherichia coli* from patients with suspected urinary tract infection in primary care, Denmark. *BMC infectious diseases*, 17(1):670, Oct 2017.

[129] R.M Macnab. Bacterial flagella rotating in bundles-study in helical geometry. *Proceedings of the National Academy of Sciences of the United States of America1*, 74:221–225, 1977.

[130] Peter Delves and Ivan Roitt, editors. *Encyclopedia of Immunology*. Academic Press, 2nd edition, 1998.

[131] J. T. Locsei. Persistence of direction increases the drift velocity of run and tumble chemotaxis. *Journal of Mathematical Biology*, 55(1), 2007.

[132] TEM image of *Vibrio alginolyticus*. `https://microbewiki.kenyon.edu/index.php/Vibrio{\_}alginolyticus`.

[133] Roman Stocker. Reverse and flick: Hybrid locomotion in bacteria. *Proceedings of the National Academy of Sciences of the United States of America*, 108(7):2635–6, Feb 2011.

[134] Jens Efsen Johansen et al. Variability in motility characteristics among marine bacteria. *Aquatic Microbial Ecology*, 28(3):229–237, 2002.

[135] James G. Mitchell, Lynette Pearson, and Simon Dillon. Clustering of marine bacteria in seawater enrichments. *Applied and Environmental Microbiology*, 62(10), 1996.

[136] Longo Dan, Fauci Anthony, Kasper Dennis, Hauser Stephen, Jameson J., and Loscalzo Joseph. *Harrison's Principles of Internal Medicine: Volumes 1 and 2*. 2011.

[137] R.H. Luchsinger, B. Bergersen, and J.G. Mitchell. Bacterial swimming strategies and turbulence. *Biophysical Journal*, 77(5):2377–2386, Nov 1999.

[138] Th. W. Engelmann. Bacterium photometricum. *Pflüger, Archiv für die Gesammte Physiologie des Menschen und der Thiere*, 1883.

[139] Gáspár Jékely. Evolution of phototaxis. *Philosophical Transactions of the Royal Society B: Biological Sciences*, 364(1531), 2009.

[140] Knut Drescher, Raymond E Goldstein, Nicolas Michel, Marco Polin, and Idan Tuval. Direct Measurement of the Flow Field around Swimming Microorganisms. *Phys. Rev. Lett.*, 105(16):168101, Oct 2010.

[141] Noriko Ueki et al. Eyespot-dependent determination of the phototactic sign in *Chlamydomonas reinhardtii*. *Proceedings of the National Academy of Sciences*, 113(19), 2016.

[142] Ken Ichi Wakabayashi and Stephen M. King. Modulation of *Chlamydomonas reinhardtii* flagellar motility by redox poise. *Journal of Cell Biology*, 173(5), 2006.

[143] P.A Dangeard. Recherches sur les algues inférieures. *Annales des Sciences Naturelles, Botanique*, 7(7):105–175, 1888.

[144] Sabeeha S. Merchant et al. The Chlamydomonas genome reveals the evolution of key animal and plant functions. *Science*, 318, 2007.

[145] Raphaël Jeanneret, Matteo Contino, and Marco Polin. A brief introduction to the model microswimmer *Chlamydomonas reinhardtii*, 2016.

[146] Elizabeth S Harris, David B. Stern, and George B. Witman. *The Chlamydomonas sourcebook*. Academic Press, 2nd edition, 2009.

[147] Karl Deisseroth and Peter Hegemann. The form and function of channelrhodopsin. 357(6356), 2017.

[148] Kenneth W Foster and Robert D Smyth. Light Antennas in Phototatic Algae. *Microbiological Reviews*, 44(4):572–630, 1980.

[149] Kirsty Y. Wan and Raymond E. Goldstein. Coordinated beating of algal flagella is mediated by basal coupling. *Proceedings of the National Academy of Sciences*, 113(20):2784–2793, mMy 2016.

[150] D. L. Ringo. Flagellar motion and fine structure of the flagellar apparatus in *Chlamydomonas*. *The Journal of cell biology*, 33(3), 1967.

[151] Rachel R. Bennett and Ramin Golestanian. A steering mechanism for phototaxis in Chlamydomonas. *Journal of the Royal Society Interface*, 12, 2015.

[152] Marco Polin, Idan Tuval, Knut Drescher, J.P. Gollub, and Raymond E. Goldstein. Chlamydomonas swims with two "gears" in a eukaryotic version of run-and-tumble locomotion. *Science (New York, N.Y.)*, 325(5939):487–90, 2009.

[153] Erika Erickson, Setsuko Wakao, and Krishna K. Niyogi. Light stress and photoprotection in Chlamydomonas reinhardtii. *Plant Journal*, 82(3), 2015.

[154] Mary Ella Harman Feinleib and George M. Curry. The Relationship between Stimulus Intensity and Oriented Phototactic Response (Topotaxis) in Chlamydomonas. *Physiologia Plantarum*, 25(3):346–352, Dec 1971.

[155] Jorge Arrieta, Ana Barreira, Maurizio Chioccioli, Marco Polin, and Idan Tuval. Phototaxis beyond turning: persistent accumulation and response acclimation of the microalga Chlamydomonas reinhardtii. *Scientific Reports*, 7(1):3447, 2017.

[156] Gregory J. Pazour, Oleg A. Sineshchekov, and George B. Witman. Mutational analysis of the phototransduction pathway of Chlamydomonas reinhardtii. *Journal of Cell Biology*, 131(2), 1995.

[157] Fabrice Not, Mikel Latasa, Dominique Marie, Thierry Cariou, Daniel Vaulot, and Nathalie Simon. A single species, Micromonas pusilla (Prasinophyceae), dominates the eukaryotic picoplankton in the Western English Channel. *Applied and Environmental Microbiology*, 70:4064–4072, 2004.

[158] Irene Manton. Electron Microscopial Observations On A Very Small Flagellate: The Problem of Chromulina pusilla Butcher. *Journal of Marine Biology association UK*, 38:319–333, 1959.

[159] R W Butcher. Contributions to our knowledge of the smaller marine algae. *Journal of the Marine Biological Association of the United Kingdom*, 31(1):175–191, 1952.

[160] E.W. Knight-Jones and Peter R. Walne. Chromulina pusilla Butcher, a Dominant Member of the Ultraplankton. *Nature*, 167:445, mar 1951.

[161] I Manton and M Parke. Further observations on small green flagellates with special reference to possible relatives of Chromulina pusilla Butcher. *Journal of the Marine Biological Association of the United Kingdom*, 39:275–298, 1960.

[162] C.K. Omoto and G.B. Witman. Functionally significant central-pair rotation in a primitive eukaryote flagellum. *Nature*, 290:708–710, 1981.

[163] Charlotte K Omoto, I.R. Gibbons, Ritsu Kamiya, Chikako Shingyoji, Keiichi Takahashi, and George B. Witman. Rotation of the Central Pair Microtubules in Eukaryotic Flagella. *Molecular Biology of the Cell*, 10(1):1–4, Jan 1999.

[164] J. Throndsen. Motility in some marine nanoplankton flagellates. *Norw J Zool*, 21:193–200, 1973.

[165] E. Bauerfeind, M. Elbrachter, R. Steiner, and J. Throndsen. Application of Laser Doppler Spectroscopy (LDS) in determining swimming velocities of motile phytoplankton. *Marine Biology*, 93(3).

[166] Justin R Seymour, Rafel Simo, Tanvir Ahmed, and Roman Stocker. Chemoattraction to Dimethylsulfoniopropionate Throughout the Marine Microbial Food Web. *Science*, 329:342–345, 2010.

[167] Jacqueline Stefels, Michael Steinke, Suzanne Turner, Gill Malin, and Sauveur Belviso. Environmental constraints on the production and removal of the climatically active gas dimethylsulphide (DMS) and implications for ecosystem modelling. In *Phaeocystis, Major Link in the Biogeochemical Cycling of Climate-Relevant Elements*. 2007.

[168] Kerri A. Fredrickson and Suzanne L. Strom. The algal osmolyte DMSP as a microzooplankton grazing deterrent in laboratory and field studies. *Journal of Plankton Research*, 2009(2), 2009.

[169] Boris Culik. Finding food in the open ocean: Foraging strategies in Humboldt penguins. *Zoology*, 104(3–4), 2001.

[170] Jan Slapeta, Purificación López-García, and David Moreira. Global dispersal and ancient cryptic species in the smallest marine eukaryotes. *Molecular biology and evolution*, 23(1):23–9, Jan 2006.

[171] Clara Jule Marie Hoppe, Clara M. Flintrop, and Björn Rost. The arctic picoeukaryote micromonas pusilla benefits synergistically from warming and ocean acidification. *Biogeosciences*, 15(14):4353–4365, 2018.

[172] Zaid M. McKie-Krisberg and Robert W. Sanders. Phagotrophy by the picoeukaryotic green alga Micromonas: implications for Arctic Oceans. *The ISME Journal*, 8:1953–1961, 2014.

[173] Ken Furuya and Ryuzo Marumo. The structure of the phytoplankton community in the subsurface chlorophyll maxima in the western North Pacific Ocean. *Journal of Plankton Research*, 5:393–406, 1983.

[174] J Throndsen and S Kristiansen. Micromonas-pusilla (prasinophyceae) as part of picplankton and nanoplankton communities of the Barents Sea. *Polar Research*, 10:201–207, 1991.

[175] Daniel Vaulot, Wenche Eikrem, Manon Viprey, and Hervé Moreau. The diversity of small eukaryotic phytoplankton (=3 $\mu$m) in marine ecosystems. *FEMS Microbiology Reviews*, 32(5):795 LP – 820, Aug 2008.

[176] Marli Bergesch, Clarisse Odebrecht, and Øjvind Moestrup. Nanoflagellates from coastal waters of southern Brazil (32S). *Botanica Marina*, 51(1), 2008.

[177] J. A. Mayer and F. J.R. Taylor. A virus which lyses the marine nanoflagellate Micromonas pusilla. *Nature*, 281(5729):299–301, 1979.

[178] R.N Pienaar. Virus-like particles in three species of phytoplankton from San Juan Island, Washington. *Phycologia*, 15(2):185–190, 1976.

[179] R. E. Waters and A. T. Chan. Micromonas pusilla Virus: the Virus Growth Cycle and Associated Physiological Events Within the Host Cells; Host Range Mutation. *Journal of General Virology*, 63(1):199–206, Nov 1982.

[180] M. T. Cottrell and C. A. Suttle. Wide-spread occurrence and clonal variation in viruses which cause lysis of a cosmopolitan, eukaryotic marine phytoplankter, Micromonas pusilla. *Marine Ecology Progress Series*, 78:1–9, 1991.

[181] Matthew T. Cottrell and Curtis A. Suttle. Dynamics of lytic virus infecting the photosynthetic marine picoflagellate Micromonas pusilla. *Limnology and Oceanography*, 40:730–739, 1995.

[182] Christian Lønborg, Mathias Middelboe, and Corina P D Brussaard. Viral lysis of Micromonas pusilla: Impacts on dissolved organic matter production and composition. *Biogeochemistry*, 116:231–240, 2013.

[183] Saeed Roshan and Timothy DeVries. Efficient dissolved organic carbon production and export in the oligotrophic ocean. *Nature communications*, 8(2036), 2017.

[184] Deqiang Duanmu et al. Marine algae and land plants share conserved phytochrome signaling systems. *Proceedings of the National Academy of Sciences*, 111(44):15827–15832, Nov 2014.

[185] Nathan C Rockwell et al. Eukaryotic algal phytochromes span the visible spectrum. *Proceedings of the National Academy of Sciences of the United States of America*, 111(10):3871–6, Mar 2014.

[186] Kimberly H Halsey, Allen J Milligan, and Michael J Behrenfeld. Contrasting Strategies of Photosynthetic Energy Utilization Drive Lifestyle Strategies in Ecologically Important Picoeukaryotes. *Metabolites*, 4:260–280, 2014.

[187] Kimberly H. Halsey, Robert T. O'Malley, Jason R. Graff, Allen J. Milligan, and Michael J. Behrenfeld. A common partitioning strategy for photosynthetic products in evolutionarily distinct phytoplankton species. *New Phytologist*, 198(4), 2013.

[188] Kay D. Bidle. Programmed Cell Death in Unicellular Phytoplankton. *Current Biology*, 26(13), 2016.

[189] Mohammad Hassan Kamani, Ismail E?, Jose M. Lorenzo, Fabienne Remize, Elena Rosell-Soto, Francisco J. Barba, James Clark, and Amin Mousavi Khaneghah. Advances in plant materials, food by-products, and algae conversion into biofuels: use of environmentally friendly technologies. *Green Chem.*, 2019.

[190] Roman Stocker, Justin R Seymour, Azadeh Samadani, Dana E Hunt, and Martin F Polz. Rapid chemotactic response enables marine bacteria to exploit ephemeral microscale nutrient patches. *Proceedings of the National Academy of Sciences*, 105(11):4209–4214, Mar 2008.

[191] G. E. Kaiser and R. N. Doetsch. Enhanced translational motion of Leptospira in viscous environments. *Nature*, 255, 1975.

[192] Vasily Kantsler, Jörn Dunkel, Martyn Blayney, and Raymond E Goldstein. Rheotaxis facilitates upstream navigation of mammalian sperm cells. *eLife*, 3:e02403, 2014.

[193] Kenjiro Yoshimura, Yudo Matsuo, and Ritsu Kamiya. Gravitaxis in Chlamydomonas reinhardtii Studied with Novel Mutants. *Plant and Cell Physiology*, 44(10), 2003.

[194] C P D Brussaard, a a M Noordeloos, R-a Sandaa, M Heldal, and G Bratbak. Discovery of a dsRNA virus infecting the marine photosynthetic protist Micromonas pusilla. *Virology*, 319(2):280–91, Feb 2004.

[195] Alexandra Z. Worden et al. Green evolution and dynamic adaptations revealed by genomes of the marine picoeukaryotes Micromonas. *Science (New York, N.Y.)*, 324:268–272, 2009.

[196] Maureen D. Keller, Rhonda C. Selvin, Wolfgang Claus, and Robert R.L. Guillard. Media for the culture of oceanic ultraphytoplankton. *Journal of Phycology*, 23(4):633–638, 1987.

[197] Robert Guillard and John Ryther. Studies of marine planktonic diatoms. I. Cyclotella nana Hustedt and Detonula confervacea. *Canadian Journal of Microbiology*, 8(1140):229–239, 1962.

[198] Daniel Blair and Eric Dufresne. The Matlab Particle Tracking Code Repository, 2008.

[199] John C Crocker and David G Grier. Methods of digital video microscopy for colloidal studies. *Journal of Colloid and Interface Science*, 179:298–310, 1996.

[200] T van Erven and P Harremos. Rényi Divergence and Kullback-Leibler Divergence. *IEEE Transactions on Information Theory*, 60(7):3797–3820, 2014.

[201] Seymour H. Koenig. Brownian motion of an ellipsoid. A correction to Perrin's results. *Biopolymers*, (11), 1975.

[202] Gabriel Rosser, Ruth E. Baker, Judith P. Armitage, and Alexander G. Fletcher. Modelling and analysis of bacterial tracks suggest an active reorientation mechanism in Rhodobacter sphaeroides. *Journal of The Royal Society Interface*, 11(97), May 2014.

[203] Teuta Pilizota, Mostyn T Brown, Mark C Leake, Richard W Branch, Richard M Berry, and Judith P Armitage. A molecular brake, not a clutch, stops the Rhodobacter sphaeroides flagellar motor. *Proceedings of the National Academy of Sciences of the United States of America*, 106(28):11582–7, 2009.

[204] Felix Thiel, Lutz Schimansky-Geier, and Igor M. Sokolov. Anomalous diffusion in run-and-tumble motion. *Phys. Rev. E*, 86(2), Aug 2012.

[205] Y. Leroyer and A. Würger. Drift - diffusion kinetics of a confined colloid. *Journal of physics. Condensed matter : an Institute of Physics journal*, 22(9):195104, 2010.

[206] Raphaël Jeanneret, Dmitri O. Pushkin, Vasily Kantsler, and Marco Polin. Entrainment dominates the interaction of microalgae with micron-sized objects. *Nature Communications*, 7:12518, 2016.

[207] Nils Schuergers et al. Cyanobacteria use micro-optics to sense light direction. *eLife*, 5:e12620, Feb 2016.

[208] Ó Guadayol, K Thornton, and S Humphries. Cell morphology governs directional control in swimming bacteria. *Scientific Reports*, 7:1–13, May 2017.

[209] Susan B. Watson. Cyanobacterial and eukaryotic algal odour compounds: signals or by-products? A review of their biological activity. *Phycologia*, 42(4), 2010.

[210] Frank W. Haight. *Handbook of The Poisson Distribution*. Wiley, 1968.

[211] Fatih Dikbas. A novel two-dimensional coreelation coefficient for assessing associations in time series data. *Int. J. Climatol*, 37(11), 2017.

[212] M.D. Keller, R.P. Kiene, G.O. Kirst, and P.T. Visscher. *Biological and Environmental Chemistry of DMSP and Related Sulfonium Compounds*. Springer US, 2012.

[213] J. Adler. A Method for Measuring Chemotaxis and Use of the Method to Determine Optimum Conditions for Chemotaxis by Escherichia coli. *Journal of General Microbiology*, 74(1):77–91, Jan 1973.

[214] Mark N. Breckels, Daniel E. Boakes, Edward A. Codling, Gill Malin, Stephen D. Archer, and Michael Steinke. Modelling the concentration of exuded dimethylsulphoniopropionate (DMSP) in the boundary layer surrounding phytoplankton cells. *Journal of Plankton Research*, 32(2), 2010.

[215] Christopher E. Spiese, Triet Le, Robert L. Zimmer, and David J. Kieber. Dimethylsulfide membrane permeability, cellular concentrations and implications for physiological functions in marine algae. *Journal of Plankton Research*, 38(1), 2015.

[216] Ieong Wong et al. An agar gel membrane-PDMS hybrid microfluidic device for long term single cell dynamic study. *Lab on a Chip*, 10(20):2710, 2010.

[217] Shing-Yi Cheng, Steven Heilman, Max Wasserman, Shivaun Archer, Michael L. Shuler, and Mingming Wu. A hydrogel-based microfluidic device for the studies of directed cell migration. *Lab on a Chip*, 7(6):763, 2007.

[218] Edward J. Schantz and Max A. Lauffer. Diffusion Measurements in Agar Gel. *Biochemistry*, 1(4), 1962.

[219] Celia Lozano, Borge Ten Hagen, Hartmut Löwen, and Clemens Bechinger. Phototaxis of synthetic microswimmers in optical landscapes. *Nature Communications*, 7(12828), 2016.

[220] Jean-David Rochaix. Assembly, Function, and Dynamics of the Photosynthetic Machinery in Chlamydomonas reinhardtii. *Plant Physiology*, 127:1394–1398, 2001.

[221] Vasily Kantsler, Jorn Dunkel, Marco Polin, and Raymond E. Goldstein. Ciliary contact interactions dominate surface scattering of swimming eukaryotes. *PNAS*, 110(4), 2012.

[222] Donat-peter Häder and Michael Lebert. Photoorientation in Photosynthetic Flagellates. In Tian Jin and Dale Hereld, editors, *Chemotaxis: methods and protocols*, volume 571 of *Methods in Molecular Biology*, chapter 3, pages 51–65. Humana Press, 2009.

[223] Robert L. Stavis and Rona Hirschberg. Phototaxis in Chlamydomonas reinhardtii. *Journal of Cell Biology*, 59:367–377, 1973.

[224] U. Rüffer and Wilhelm Nultsch. Flagellar photoresponses of Chlamydomonas cells held on micropipettes: I. Change in flagellar beat frequency. *Cell Motility and the Cytoskeleton*, 15(3):162–167, 1990.

[225] U. Rüffer and Wilhelm Nultsch. Flagellar photoresponses of Chlamydomonas cells held on micropipettes: II. Change in flagellar beat pattern. *Cell motility and the cytoskeleton*, 18(4):269–278, 1991.

[226] U. Rüffer and Wilhelm Nultsch. Flagellar photoresponse of Chlamydomonas cells held on micropipettes: III. Shock response. *Botanica Acta*, 108:255, 1995.

[227] Tetsuo Takahashi and Masakatsu Watanabe. Photosynthesis modulates the sign of phototaxis of wild-type Chlamydomonas reinhardtii. *Federation of European Biochemical Societies*, 336(3):516–520, 1993.